A THESIS SUBMITTED TO THE UNIVERSITY OF SHEFFIELD
FOR THE DEGREE OF

DOCTOR OF PHILOSOPHY

UNIVERSITY OF SHEFFIELD

SCHOOL OF MECHANICAL, AEROSPACE AND CIVIL ENGINEERING

An Acoustic Velocity Vector Based Approach to Robotic Pipeline Inspection

Author:
Joanna Watts

Supervisors:
Prof. Kirill Horoshenkov
Dr. Anton Krynkin
Prof. Simon Tait

January 31, 2026

Publications

The following publications have arisen from the work presented in this thesis:

Journal Publications

J. Watts and K. V. Horoshenkov, "Detecting defects in rising mains using the acoustic fluid velocity", *Measurement*, vol. 253, p. 117702, 2025
DOI: 10.1016/j.measurement.2025.117702

P. Shi, Y. Yu, J. Watts, G. Zhang, and K. V. Horoshenkov, "An application of a MEMS vector hydrophone for condition assessment of a water supply pipe", *Applied Acoustics*, vol. 231, p. 110449, 2025
DOI: 10.1016/j.apacoust.2024.110449

K. F. Makris, J. G. Langeveld, F. H. L. R. Clemens-Meyer, J. Watts, H. Begum, and K. V. Horoshenkov, "Sonic assessment of physical ageing of plastic pipes", *Journal of Sound and Vibration*, vol. 544, p. 117393, 2023
DOI: 10.1016/j.jsv.2023.117393

Conference Proceedings

J. Watts, M.-D. Johnson, and K. V. Horoshenkov, "Using the acoustic velocity vector to assess the condition of buried water pipes", *Engineering Proceedings*, vol. 69, no. 1, article 187, 2024
DOI: 10.3390/engproc2024069187

J. Watts, K. V. Horoshenkov, N. Carter, and N. Edwards, "A novel acoustic sensor for condition assessment and early leak detection in water pipes", in *Pipelines 2023*, pp. 107–114, 2023
DOI: 10.1061/9780784485033.012

Declaration

I hereby declare that all of the work contained here is my own, except where specific reference is made to the work of others. The contents of this thesis are original and have not been submitted, in whole or in part, for consideration for full or partial fulfilment of any other degree or qualification at this or any other university.

January 31, 2026

Copyright declaration

Acknowledgements

I would like to express my sincere gratitude to my principal supervisor, Professor Kirill Horoshenkov, for his guidance, support and patience throughout the course of this research. I am also grateful to my secondary supervisors, Dr Anton Krynkin and Professor Simon Tait, for their advice and constructive feedback.

I wish to thank Paul Osborne for his invaluable assistance and advice in designing the experiments at ICAIR, as well as Mathew Hall for his technical help and enthusiasm in the design and creation of the test equipment. I am indebted to Gavin Sailor, whose guidance on numerous occasions helped me to resolve problems and move the work forwards. I would like to thank Yicheng Yu and Hasina Begum for their introductions to the university and the technical aspects of acoustics and Michael-David Johnson for much good advice and encouragement.

Finally, I am grateful to my family and friends for their unwavering support and positivity throughout my doctoral studies.

Abstract

Water loss due to damaged, pressurised pipelines is a significant and ongoing problem in the UK and across most of the world. As of 2022, over 20% of treated water in the UK was lost due to leaks, barely improving on loss rates in 1995. This thesis aims to diagnose some of the causes of current issues with leak detection and suggest an improved methodology.

A comprehensive review identified several areas within the leak detection sphere worth investigation: acoustic propagation and attenuation in plastic pipes, the variability in leak-generated noise, and moving beyond monoaxial sensing, given that this captures only a fraction of the available acoustic information. Motivated by these findings, experimental and numerical studies were undertaken considering the propagation and attenuation of sound in plastic pipes and examining the influence of features such as joints, corners, and burial conditions. Results showed that attenuation was strongly frequency dependent, with higher frequencies attenuating considerably over short distances, limiting the viability of traditional correlation-based leak localisation methods for plastic networks.

To address these challenges, this work explores the novel use of acoustic velocity vector sensors (AVVSs) on an in-pipe platform for defect detection. Numerical models demonstrated that radial components of the acoustic velocity are particularly sensitive to small wall defects, while the pressure and axial velocity showed no deviation from background levels close to the defects. This prediction was confirmed experimentally using an AVVS on a test pipe. A robotic platform carrying multiple AVVSs further validated the feasibility of this approach.

This research establishes acoustic vector sensing as a promising new diagnostic method for pressurised water pipes, allowing smaller and incipient leaks to be detected and laying the groundwork for intelligent, mobile in-pipe monitoring systems that can enhance predictive and preventative maintenance of critical infrastructure.

Nomenclature

a	acceleration
a_i	$i \in \{x, y, z, ref\}$, acceleration in direction specified (x, y, z) or at reference accelerometer (ref)
A	leakage area
B	fluid bulk modulus
c	speed of sound
c_f	speed of sound in a free fluid
c_s	compressional wave velocity of soil/sand
C_d	discharge coefficient
C_L	leakage coefficient (Eq. 2.2)
$C_{xy}(\tau)$	cross correlation between signals $x(t)$ and $y(t)$ for lags τ
d	distance
E	Young's modulus
f	frequency
f_R	ring frequency
f_s	sampling frequency
g	standard acceleration of gravity
G_s	shear modulus of sand/soil
h	pipe wall thickness
i	$\sqrt{-1}$, also used within this list to denote a generic variable
k	wave number
k_f	wave number of a fluid in free space
k_L	wave number of a compressional wave
$k_{(n,s)}$	wave number labelled by mode
K_s	bulk modulus of sand/soil
M_{rad}	radiation mass of a medium

n	circumferential mode order
N_L	leakage exponent (Eq. 2.2)
N	signal length i.e. number of samples
p	pressure
Q	leak flow rate
r	pipe radius
R_{rad}	radiation resistance of a medium
s	radial mode order
$s_j(t)$	example time domain signal recorded using testing by instrument j (j is specified in the main text)
$S_j(\omega)$	example frequency domain signal corresponding to $s_j(t)$
t	time
T_{ij}	frequency response function between signals $s_i(t)$ and $s_j(t)$
v_i	$i \in \{x, y, z\}$, fluid velocity in direction specified
$x(t), y(t)$	generic time domain signals
$\bar{x}, \bar{y}$	average of time domain signals
$X(\omega)$	generic frequency domain signal
α	attenuation
α_i	attenuation in parameter i, where i is replaced by the parameter of interest in the main text
α_T	shape parameter of the Tukey window, representing the fraction of the window inside the cosine tapered region
Δ	(operator) change in a variable
ϵ_i	error in variable i
η	material loss factor/damping coefficient
χ_n	$n \in 1, 2$, leakage fitting parameters (Eq. 2.3)
ν	material Poisson ratio
ρ	material density, of pipe unless otherwise specified
ρ_f	density of fluid
ρ_s	density of soil/sand
ω	angular frequency

Axis definitions

x	axial
y	horizontal
z	vertical
r	'radial' - the magnitude of the combination of the vertical and horizontal components, e.g. $v_r = \sqrt{v_y^2 + v_z^2}$

Abbreviations

AVVS Acoustic Velocity Vector Sensor

DFT Discrete Fourier Transform

DMA District Metering Area

DMA Dynamic Mechanical Analysis

EMD Empirical Mode Decomposition

EPA Environmental Protection Agency (US)

FFT Fast Fourier Transform

FRF Frequency Response Function

GWU Guided Wave Ultrasonic

IH Impact Hammer

ML Machine Learning

NRW Non-Revenue Water

PML Perfectly Matched Layer

PSD Power Spectral Density

RMS Root Mean Squared

SNR Signal-to-Noise Ratio

TRL Technology Readiness Level

VAE Vibro-Acoustic Emission

WDN Water Distribution Network

Contents

List of Figures

List of Tables

Chapter 1

Introduction

20% of potable water in the UK is lost due to leakage [1] and in 2018 the National Infrastructure Commission recommended that this be halved by 2050 in order to improve the UK's water resilience [1]. This issue, where a significant proportion of potable water is being lost as Non-Revenue Water (NRW) is not unique to the UK: Figure 1.1 shows that the UK is average in terms of water loss levels in the EU. Leakage reports from OfWat [2], show that there has been little reduction in leakage volumes since 2000, even with advances in leak detection technology [2–4]. This lack of progress indicates that a paradigm shift is required in how leaks are detected.

Currently, the most common leak detection technologies take a surface-down approach, utilising existing above-ground fixed assets on the water distribution network (WDN) to listen for leaks in buried sections of pipe [5]. Consequently, leaks close to fixed assets, such as hydrants, are disproportionately easy to detect, while more distant or multiple leaks continue undetected. These remote acoustic methods are reliant on the acoustic properties of the pipe material, with plastic pipes proving more difficult to detect leaks on due to the increased attenuation of sound in plastic as opposed to metal pipes. As more metal pipes are replaced with plastic pipes, and as more plastic pipes reach the expected end of their service life, this will become an increasing issue.

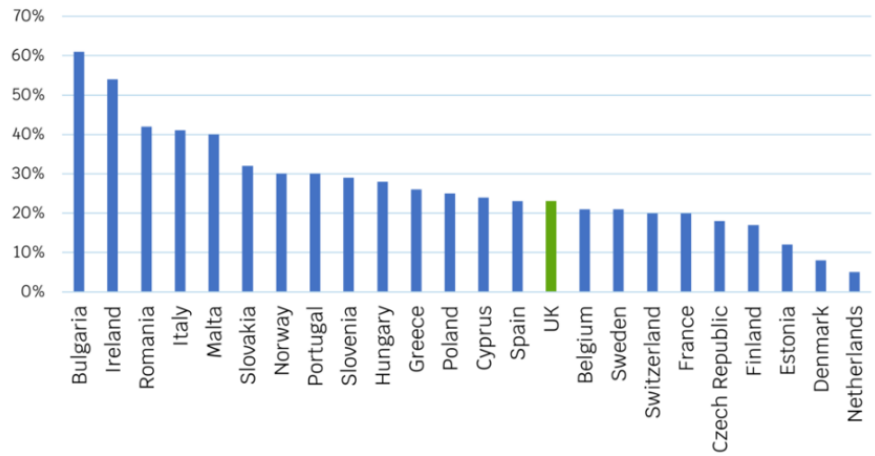

Figure 1.1: Percentage of treated water lost as NRW by country for a selection of EU countries. The figure has been reproduced from OfWat's 2022 report on leakage in the water industry [2] and is based on data from the EU's 2021 report on the European drinking water and waste water sectors [3].

A possible means of solving this issue is inserting autonomous robots into the pipe network. Such robots would allow an unbiased survey of all areas of the network that is less reliant on strong long-distance acoustic propagation through the pipe wall. Building such an in-pipe robotic platform is the objective of the Pipebots Grant [6], of which this research forms a part.

Existing pipe maintenance is commonly reactive rather than proactive, given that existing methods mainly aiming to detect leaks, pipe bursts etc., rather than the onset of defects in the pipe wall itself. A robotic platform allows closer access to the pipe wall, enabling a far more detailed inspection, including searching for defects on the pipe wall as well as leaks. In future, this could be further extended to robotic in-pipe fixing of defects, as proposed by OfWat's no-dig repair project [7].

An additional benefit of a robotic platform is that it is not limited to pipes within the WDN; rising mains are similar acoustically, in that they are pressurised pipelines filled with (mostly) water. There is currently a lack of inspection methods for rising mains, beyond CCTV on robots. CCTV inspection requires the system to be emptied and can only see issues on the inside surface of the pipe. Rising mains offer a readily available environment for testing a prototype platforms given the lower regulatory barriers for access, while allowing transferability of technology to the WDN. Consequently, while the methods proposed in this thesis have been primarily designed for the WDN, they have been tested on rising mains.

Aim and objectives

Based on the shortcomings of existing pipeline inspection methods in terms of the size and range of leaks detectable, lack of visibility of incipient leaks in the form of defects in the pipe wall and the advent of advanced pipeline inspection robots, this thesis aims to develop a novel method for detecting leaks and pipe wall defects appropriate for use on an in-pipe robotic platform.

This can be broken down into the following objectives:

(i) Investigate the variability of leak noise in water-filled pipes and its influence on leak detectability.

(ii) Investigate the efficacy of existing methods for leak detection in water-filled pipelines. In particular, evaluate the range limitations of acoustic leak detection on plastic pipes and the extent of the need for an alternative.

(iii) Investigate the novel sensing options available for pipeline inspection when a robotic platform is used in order to determine the most sensitive method. This should move beyond on-pipe accelerometers and hydrophones to consider the benefits of vector based sensing, measuring the directional effect of defects and leaks.

(iv) Deploy this sensing approach on a robotic platform to test its efficacy and offer recommendations for optimal sensor deployment on a mobile robotic platform.

Thesis organisation

This thesis is organised to answer these objectives in order. It starts by considering existing methods of leak detection, particularly in plastic pipes. This begins in Chapter 2 with a review of

existing methods. It continues in Chapters 3 and 4, where the frequency spectra of leaks are investigated along with the transmission of acoustic waves through plastic pipes. These chapters serve to demonstrate the complexities of leak noise detection, which is compounded by the intricacies of sound propagation in plastic pipes.

Current methods of leak detection are strongly focused on accelerometer-based measurements collected from the outside of the pipe. With an in-pipe robotic platform there are many more opportunities available in terms of sensors. Models of a plastic pipe were developed to see whether any measurable parameters within the pipe were particularly sensitive to leaks and defects within the pipe wall, this is reported in Chapter 5. With this as a basis, a triaxial accelerometer was adapted into an acoustic velocity vector sensor (AVVS) to measure the acoustic velocity of the fluid, since this was determined to be particularly sensitive to variations in the pipe wall.

This novel sensing approach has been tested in a series of experiments of increasing complexity, the results of which are reported in Chapters 6 and 7. These experiments show considerable promise, and a vector-based sensor is now being fitted to robots for Pipebots to use in follow-on projects. It has the potential to transform pipeline surveying by allowing an inspection of the pipe condition that is fast, long range and more sensitive to developing defects than existing technologies. Preventative maintenance is the best method for pipe longevity, cost efficiency and limiting disruption to the water supply. Using the improved methods proposed in this thesis to detect developing defects will allow the use of modern pipe repair techniques, which are effective when a pipe's condition is deteriorating but is not yet structurally compromised. This will allow for highly efficient, proactive pipe maintenance to maintain hydraulic efficiency.

Chapter 2

Literature Review

This chapter presents a review of the most relevant literature pertaining to this thesis. It is intended to give the reader a representation of the current state of research in this field and not to be a full review of all the literature: the reader is directed to section-specific reviews during the course of the chapter, with [8–10] being the most relevant to this thesis as a whole.

This chapter begins with an overview of the causes of leaks and the relative prevalence of different types of leaks on different pipe materials. It moves onto a summary of some of the work conducted looking at the acoustic signatures of leak noise followed by an introduction to the propagation of waves along pipes, with a focus on the influence of this on acoustic leak detection. The review then provides an overview of existing technology for leak and defect detection in the WDN, starting with the most common techniques and progressing to those techniques currently in a more developmental stage. This section of the review focuses on commercial options for leak detection and localisation more than the theory behind leak detection in pipes. It considers previous work on leak noise in pipes and its propagation, including areas where university-led research has progressed further than (or in a different direction to) commercially available technology. Finally, the direction of travel for research into leak detection in pipes is considered.

2.1 Causes and prevalence of leaks

Leakage is a broad term, often used to describe any water escaping from the pipe network unintentionally. The two main classes of this are pipe bursts and background leakage due to unsatisfactory joins, cracks, etc. [11]. Either of these may develop in pipes for a variety of reasons [11, 12]. The type of leak has ramifications for its detection and rectification, with different types of leak having different behaviours which may make them easier or more difficult to detect. Conversely, these differences in behaviour should make it possible to classify a leak remotely.

The material of the pipe is the largest factor in determining which failure modes are most likely [12]. A summary of the most common failure modes for various pipe materials is given in Table 2.1. The abbreviations for the different pipe materials and their prevalence in the UK water network are given in Table 2.2. It should be noted that the UK is not representative of all WDNs, although in general more plastic (PVC and PE) pipes are being installed worldwide [13].

Different types of leak are also caused by different factors. These include: excessive loads beyond the specification of the system, caused by poor design, deterioration or unexpected loading;

Table 2.1: Most common failure types by pipe material. In addition to these any pipe may fail due to third party or environmental damage. Information extracted from [14], material abbreviations summarised in Table 2.2. *particularly common.

Failure mode	SCL	DICL	PVC	PE	CICL	AC	GRP	Copper
Piece blown out	-	Y	Y	Y	Y*	Y	Y	-
Perforation	Y*	Y	Y	Y	Y	-	-	Y
Circumferential break	-	-	-	-	Y*	Y*	-	Y
Longitudinal split	-	-	Y	rare	Y	Y*	-	-
Pipe wall rupture/tear	Y	rare	-	-	-	-	Y*	Y
Caused by tapping	-	Y*	Y	-	-	-	-	-
Joint	Y	Y	Y*	Y*	Y	Y	Y	Y

Table 2.2: Pipe material abbreviations and approximate length of UK water network comprised of each material [13], 15,000 km of the network are of unknown pipe material.

Abbrev.	Material	Length in UK water network (km)
SCL	Steel cement (mortar) lined	5,000
DICL	Ductile iron cement (mortar) lined	20,000
PVC	Polyvinyl Chloride	35,000
PE/HDPE/MDPE	Polyethylene (high/medium density)	25,000
CICL	Case iron cement (mortar) lined	-
AC	Asbestos cement	25,000
GRP	Glass reinforced polyester	0
Copper	-	0
Iron	-	105,000
Lead	-	0
Concrete	-	0

temperature variation causing both contraction of the pipe and pressure from the surrounding soil; corrosion; ageing; and geographic conditions, particularly the surrounding soil which has a significant impact on the forces experienced by the pipe [11]. These effects interact and have varying importance depending on the pipe material. For example, for metal pipes there is evidence that ageing has limited effect on pipe deterioration, with [11] concluding from previous work in New York [15], and by Severn Trent [16] that age is not a significant indicator of future leakage in cast iron pipes. This contrasts with findings in [17–19] which find that the age of PVC pipes does have an impact on leakage incidence. This is a product of the properties of plastics [20], which are not in the same state of equilibrium as metals, such that their material properties change over time. A visualisation of this can be found as Figure 1.2 of [18]. Work on the use of PVC in sewer pipes has shown a stronger correlation with lifetime [21]. Some pipe materials also have specific sources of weaknesses, for example early PVC pipes had poor quality control leading to a higher than expected failure rate for pipes of particular vintages [22].

While Ofwat no longer explicitly recommends using a SELL (Sustainable Economic Level of Leakage) approach to leak repair [23], whereby the economic impact of leaks is compared with the cost of fixing them, it should still be a consideration in leak detection. SELL allows small leaks on busy roads to remain unfixed since the cost of fixing them far outweighs the benefits. This pragmatic approach makes determining the size of the leak as important as determining its location.

Part of this calculation comes down to knowing the leak flow rate Q. If there is only one leak in a DMA this can be calculated using low water flow measurements. It can also be calculated from the shape of the leak. The most basic form of this is the orifice equation[24]:

$$Q = C_d A\sqrt{2gp} \tag{2.1}$$

where C_d is a discharge coefficient, A is the leakage area, g is the standard acceleration of gravity and p is the back-pressure of the leak. This is derived from Bernoulli's theorem, which assumes incompressibility and frictionless flow [24], with C_d added to account for friction and compressibility effects. C_d is usually determined empirically [25], with 0.67* used for leakage modelling where the flow is fully turbulent [26, 27].

However, this is considered an over-simplification that poorly describes leakage flow due to a pressure head [28, 29], and it has been found that a power equation

$$Q = AC_L(2gp)^{N_L} \tag{2.2}$$

more accurately reflects the empirical observations [26, 27, 30] even though it has no physical basis. Here C_L is a leakage coefficient, often substituted with C_d [24] and N_L is an empirically determined exponent.

Even this does not well describe all leakage scenarios, with Walski *et al.* [29] reporting such a range (0.4 - 2.5) of values for N in different systems as to make Equation 2.2 unworkable. Experimental work by Braga *et al.* [24] also showed unsatisfactory results using Equation 2.2 for a head of less than 20 m (1.96 bar), finding that an expression of the form

$$Q = A\chi_1 \ln(\chi_2 2gp) \tag{2.3}$$

was more effective, with two empirically determined values χ_1 and χ_2.

In summary, while there are multiple options for determining Q for a given leak, of varying complexity, the relevant parameters that need to be determined are the area of the leak (A) and the back-pressure (p). In principle, the pressure of the water system should be known, although may not be in practice, so the physical size of the leak is the most important factor to determine.

2.2 Understanding leak noise

It is impractical to measure the size of every leak directly, therefore indirect methods are preferable. A common choice is to measure the in-pipe acoustics to find leaks. This requires an understanding of the acoustics of leaks, as well as of noise propagation in pipes.

2.2.1 Leak spectra

Throughout this section, and the thesis as a whole, the frequency spectrum of the leak noise is a core concept. This spectrum represents the distribution of energy within an acoustic (time domain) signal across each frequency. Viewing the data in this way allows for insight into the dominant frequencies in the spectrum as well as its broadband characteristics.

The spectrum is derived by transforming the time domain signal $x(t)$ into the frequency domain,

*This is an empirical formula, with the value of C_d determined experimentally. Consequently dimensionality is not conserved in this equation and C_d does not have meaningful units.

thus finding $X(\omega)$. This is achieved throughout this thesis using the Discrete Fourier Transform (DFT):

$$X_k = \frac{1}{N} \sum_{m=0}^{N-1} x_m \exp\left\{-2\pi i \frac{mk}{N}\right\} \tag{2.4}$$

where x_m time domain signal sampled by $m = 0, ..., N-1$, X_k is the complex amplitude of the k-th frequency bin, corresponding to the frequency $f_k = \frac{kf_s}{N}$ for sampling frequency f_s and signal length N.

In this thesis the NumPy package has been used to calculate the DFT using the Fast Fourier Transform (FFT), using a forward normalisation according to Equation 2.4 [31].

2.2.2 Influences on leak noise

In 2008, Pal wrote their thesis on leakage detection, during the course of which they demonstrated the differences in spectra produced by leaks from different sources [32]. They considered the leak noise from an open hydrant, a loose flange joint and a split pipe, and found that the main similarity in the acoustic emission spectra was an increase in amplitude between 20 and 1000 Hz. Butterfield performed a similar study, looking at the differences in spectrum for leaks produced by a round hole, a longitudinal slit and a compromised electrofusion joint [10]. Here, they found marked differences in the spectra depending on the leak noise source, with the electrofusion joint being most distinct [33]. This was taken further to look at the effect of the surrounding medium on the dynamic behaviour of a leak [34].

The type of leak influences its development over time as well as its response to varying pressure, for example longitudinal slits increase in area with an increase in back pressure [35]. The material can have an impact on the leakage exponent, N_L, from Equation 2.2 and on the discharge relationship [35]. In addition, leak noise propagates differently in different types of material. A study carried out on three comparable sections of the water network, made of different materials, but with the same simulated leak source found considerable differences in the magnitude of leak noise detected at a distance [36].

One of the largest influences on the level of leak noise is the leak flow rate. It has been shown that the amplitude of leak noise relates to the leak flow rate directly [32, 37] and to the hydraulic pressure via Equation 2.1 [32, 37]. The surrounding soil and backfill material have an effect on the leak propagation in the pipe [32, 38], it can also lead to a change in the acoustics of the leak itself as the material next to the leak is fluidised and hits the pipe wall [39].

2.2.3 Frequencies in leak noise

It is important to know at which frequencies leak noise can be seen in the recorded signal spectrum. It allows filtering of signals to remove or reduce non-leakage components from the acoustic signal. There has consequently been a lot of work considering the frequency spectrum of leaks. The consensus is that leak signals in plastic pipes dominate the low frequencies (below the ring frequency, see Section 2.3) [10, 32, 40, 41].

Pal [32] and Humphrey [42] showed a material dependent frequency range for leaks, with Humphrey recommending filtering to $f < 100$ Hz when correlating on plastic pipes, and between

1000 and 2000 Hz on cast iron, steel and asbestos cement (AC) pipes. Similarly [43] found that leak noise was concentrated at about 1 kHz on metal pipes and 200 Hz on plastic pipes.

Part of the reason for this assertion that leak noise is only visible at low frequencies, particularly on plastic pipes, is that the attenuation in pipes is frequency dependant, with higher frequencies being more strongly attenuated. This is seen more in plastic pipes than metal pipes [42]. A simple expression for the attenuation in the pipe wall is given in [44]:

$$\alpha = \frac{1}{c_f} \frac{\frac{\eta B r}{E h}}{1 + (\frac{2Br}{Eh})} \tag{2.5}$$

where η is the damping in the pipe wall, B is the fluid bulk modulus, c_f is the speed of sound in the free fluid, E is the Young's modulus, h is the wall thickness, r is the pipe radius.

2.2.4 Simulating and modelling leaks

The variability in the acoustics of leaks, which depends to a large extent on their configuration, means that synthetic sources of noise in the pipe network are sometimes more useful when aiming to understand the effect of a single change. Some common choices of synthetic leaks during experiments have been:

- drilled holes [32, 33, 45]
- machined rectangular slits [32, 45]
- artificially compromised electrofusion joints [33]
- open spigots [36]
- open stand pipes [46]
- shakers attached to hydrants [43, 47]
- pistons [40]
- underwater loudspeakers [40]

The problem with many of these synthetic leaks is that they bear little relation to the leaks seen on actual pipes [10]. For example, most leaks on plastic pipes are due to leaky joins [14, 48] which are underrepesented on the list above. An alternative is to insert known compromised pipe sections into a controlled pipe, this was done by Hunaidi *et al* [49], who set up compromised joints and a split pipe to test various leakage detection options. This is easier for some kinds of leak sources that others, for example a poorly tightened flange joint, as tested in [32] is much easier to do than forcing a pipe to split.

Extensive work has gone into modelling the flow of fluid through orifices, for example [34, 37, 50–52]. While this is somewhat beyond the scope of this project, the effect of the in-pipe deployment platform on the in-pipe acoustics will need to be considered. This is similar to work carried out in [53], looking at the effect of a spherical device on the fluid flow inside a pipe. Their results for the impact on the velocity distribution inside the pipe are shown in Figure 2.1.

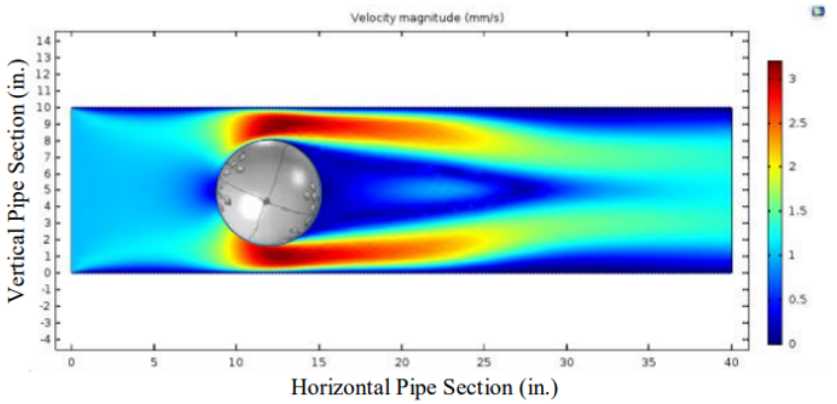

Figure 2.1: Effect of a ball on the fluid flow in a water-filled pipe. Figure reproduced from [53].

2.2.5 Summary of previous experiments on leak noise in pipes

There has been a considerable volume of work investigating the effect of a leak's shape on the ensuent leak noise. A selection of the most relevant experiments to this work is presented in Table 2.3, with an identifier for each, notes on the experimental configuration and the main works based on each experimental rig. This list focuses on those experiments concerning plastic pipes or the effects of complexities in the pipe network and does not include work on transients or non-acoustic techniques for leak detection.

Most of the work summarised in Table 2.3 has considered out-of-pipe monoaxial accelerometer or static hydrophone measurements. The exceptions to this are some of the experiments on rig G (as labelled in Table 2.3) , which considered radial and axial acceleration, and rig I, which used a movable hydrophone. Rig G was only concerned with detecting leaks on small-diameter service connections, and work based on it considered the two acceleration measurements separately, rather than combining them. It also did not compare the additional information they provided with any theoretical treatments of wave propagation in pipes. Rig I was very small, only 14 m in total, and the hydrophone was only moved along 5 m of it. Over that distance, the recorded signal was found to vary by 20 Pa [71], and did not linearly diminish with distance as might be expected, instead reaching a maximum at around 2 m from the noise source.

Most of the work included in Table 2.3 is lab-based, and mostly uses synthetic leaks. This is partly self-selecting; publishable work relies on the repeatability that synthetic, lab-based experiments bring. However when developing any leak-detecting device practical considerations such as water safety and ease of deployment should not be forgotten, even if initial work needs to be conducted in more controlled environs. The synthetic leaks sources are various. Rig B uses opening stand pipe to allow for varying the number and flow rate of leaks at specific points. Similarly, Rig C simulates leaks by opening valves as do rigs I and K. Another common choice is to drill holes in the leak walls, this is used in rigs E, H, I, J and L. Rigs A, G, H and L use actual leaks in a pipe system, with L testing several different leaks by using a replaceable pipe section.

For all of these experiments, a practical consideration is how to pressurise the system reliably. Rigs A, B, E, H, I and K pressurise their systems using the WDN, either because they are testing on live systems (in the case of H and K) or as an easy source of pressure. The other two means of pressurising the system are using a static header tank (rigs D and G) or using a centrifugal pump (rigs C, I, J and L). A header tank or pump allow more control over the pressure, with a pump allowing a variable back pressure at the cost of increased acoustical noise in the experiment.

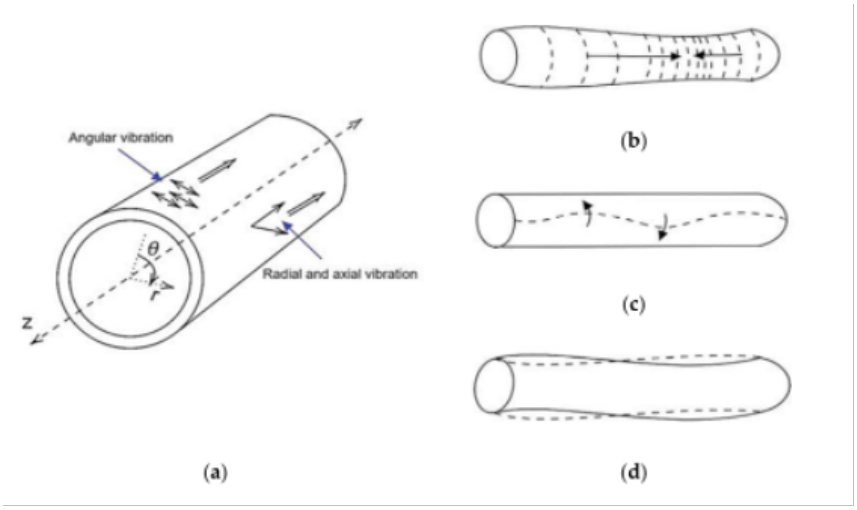

Figure 2.2: Possible motions for a pipe at low frequencies: a) coordinate system, b) longitudinal, c) torsional, d) flexural. Reproduced from [79].

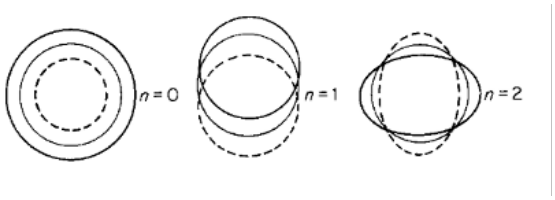

Figure 2.3: Circumferential modes in a pipe, showing the circumferential motion for n=0, 1, 2. Reproduced from [80].

2.3 Wave propagation in pipes

The previous section has mainly considered the leak noise, without explicitly accounting for the distortions inherent in the acoustics being transmitted through the pipe. This section will start by introducing analytical models of waves propagating in pipes, moving upwards through levels of complexity. It will then move onto a review of previous numerical work considering wave propagation in pipes. This work is extended in Chapter 3.

2.3.1 Modes in a fluid-filled elastic pipe

The geometry of a pipe allows for three main wave motions at low frequencies: longitudinal, torsional and flexural [78, 79], these are depicted in Figure 2.2. The cross-sectional modes of waves propagating in a pipe are labelled (n, s) where n describes the circumferential mode order and s describes the radial mode order, the first three circumferential modes are labelled in Figure 2.3.

For a fluid-filled elastic pipe in a vacuum the dispersion relation is analytically tractable and a full treatment of this is given by [81], where the dispersion curves showing how wavenumber varies with frequency are generated for various configurations. Most acoustic analysis in water-filled pipes is performed for frequencies less than the ring frequency [82], this is the frequency at which the wavelength of an extensional wave equals the mean circumference of the pipe wall, i.e. where

$$f_R = \frac{c_f}{2\pi r} \tag{2.6}$$

For frequencies above f_R, the response of the pipe is similar to that of a flat plate, while below f_R the curvature of the wall has more of an effect, adding to increased complexity in the response.

For frequencies below the ring frequency the main modes excited are the $n = 0, s = 0, 1, 2$ and the $n = 1, s = 1$ modes. The $n = 2$ modes are usually ignored since it has been shown that the majority of the energy is contained in the $n = 0$ mode, with some in the $n = 1$ mode and relatively little in higher order modes [80]. To summarise, the expected wave modes in the frequency of interest, labelled as (n, s) are [80]:

$(0, 0)$: axisymmetric motion of pipe, with minimal coupling to the fluid.

$(0, 1)$: axisymmetric, compressional wave in fluid, with some coupled radial shell motion.

$(0, 2)$: axisymmetric, compressional wave in shell, with some coupled motion in fluid, the extent of coupling depends on the relative stiffnesses of the pipe and fluid.

$(1, 1)$: flexural bending of pipe.

A further explanation of exactly how the fluid and shell move for each mode in a fluid filled shell is given in [80].

The axial wavenumbers for the $(0, 1)$ and $(0, 2)$ modes can be approximated [64] analytically as

$$k^2_{(0,1)} = k^2_f \frac{1 + 2B/r}{Eh/r^2 - \rho h\omega^2} \tag{2.7}$$

and

$$k^2_{(0,2)} = k^2_L \frac{1 + \nu^2}{1 - \nu^2} \frac{Eh/r^2}{Eh/r^2 + 2B_f/r - \rho h\omega^2} \tag{2.8}$$

where k_f is the axial wavenumber of a fluid in free space, $k_L = \sqrt{\omega^2\rho(1 - \nu^2)/E)}$ is the wavenumber of a compressional wave in the pipe material and ω is the frequency. The properties of the shell are described by its Poisson ratio, ν, its Young's modulus, E, and its density, ρ. The fluid is described by its bulk modulus, B. The dimensions of the pipe are its radius, r, and wall thickness, h. The above assumes that the wavelength is greater than the fluid diameter, that $k^2_{(0,s)} \gg k^2_L$ and that $k^2_{(0,2)} \ll k^2_f$. (These results are presented in the form used in [83], which is a rearrangement of the original work in [64].) The wave speed, c, can then be predicted using the relations [55]*:

$$c = \frac{\omega}{Re\{k\}} \tag{2.9}$$

It can be shown [81] from Equations 2.7 and 2.8 that $k_{(0,1)}$ is always greater than k_f, i.e. the fluid wave in a pipe is always slower than the wave in an infinite medium, and that its speed decreases with decreasing wall stiffness (increasing β). Similarly, $k_{(0,2)}$ is always greater than k_L, so waves travel more slowly in the pipe wall than in the pipe material, although as the frequency increases so $\omega^2 \gg \nu^2$, and the radial motion of wall is dominated by inertia, the speed approaches

*k has no imaginary component in the subsection, however later sections introduce a loss factor such that k becomes complex-valued.

c_L. It should be noted that by assuming that $k^2_{(0,2)} \ll k^2_f$ it has also been assumed that the wavelength in the pipe wall is always greater than in the fluid, since $k_{(0,1)} > k_f$.

As discussed in Section 2.4.3, an accurate prediction of the sound speed is very useful to locate accurately the leak in a pipe. There are challenges in predicting the speed of sound in plastic pipes, and additional complexities are required for an accurate prediction.

2.3.2 Adding surrounding soil

The first level of complexity considered here is adding the surrounding soil. Incorporating the effect of surrounding soil leads to the following expressions for the wavenumbers [83]

$$k^2_{(0,1)} = k^2_f \frac{1 + (2B/r)}{((Eh/r^2) - \omega^2(\rho h + M_{rad}) + i(\omega R_{rad} + \eta Eh/r^2))} \tag{2.10}$$

and

$$k^2_{(0,2)} = k^2_L \frac{1+\nu^2}{1-\nu^2} \frac{((Eh/r^2))}{(Eh/r^2) + (2B/r) - \omega^2(\rho h + M_{rad}) + i(\omega R_{rad} + \eta Eh/r^2)} \tag{2.11}$$

where, in addition to the parameters and approximations used in Equations 2.7 and 2.8, M_{rad} and R_{rad} describe the radiation mass and resistance of the surrounding medium. The Young's modulus of the pipe wall has been modified to account for losses such that $E_{complex} = E(1 + i\eta)$ where η is the material loss factor.

Considering these, it can be seen that the mass resistance of the soil causes the sound speed of the fluid wave to decrease even further from its free-field value than in the soil-free case. There is also now an imaginary component to both equations, so the wave decays as it propagates because of its interaction with the soil. This imaginary component is determined by $1/i(\omega R_{rad} + \eta Eh/a^2)$ for both waves, so these losses are dominated by radiation into the soil at high frequencies, and losses in the pipe wall at low frequencies.

Let us consider the effect of varying some of these parameters:

- $M_{rad}, R_{rad} \ll \rho h \omega^2$, i.e. the radiation impedences are much less than the mass term for the pipe: the effect of the soil can be ignored. This means that denser materials are less influenced by the surrounding soil.

- ω small (much less than the pipe ring frequency), such that terms in ω^2 can be ignored: the behaviour of the fluid ($s = 1$) wave is dominated by the pipe wall stiffness, Eh/a^2 and its interaction with the stiffness of the contained fluid, while the behaviour of the shell-borne ($s = 2$) wave reverts to that of the soil-free case, with some losses associated with the radiation impedance.

In general, these expressions agree better with experimental results, but are still not a perfect description.

2.3.3 Numerical studies of wave propagation in pipes

The work described above has been continued to account for more of the complexities of a real pipe network, using both analytical and numerical models. A summary of the most significant of these for this work is given in Table 2.4.

Based on this work it has been found that the effect of soil is small for metal pipes, and can usually be neglected [63], a result that is in agreement with the well-established finding that leaks are easier to locate on metal pipes, where the speed of sound is less variable. In contrast, plastic pipes couple more strongly to both the enclosed fluid and surrounding soil, and any variation in soil properties is more influential [63]. It has further been shown that for metal pipes there is very little deformation of the pipe wall, and as such the shell-dominated (0,2) mode carries very little energy and can mostly be neglected [43]. The (0,2) mode is still smaller that the (0,1) mode for PVC pipes, but the difference is less extreme: over the range 10-1000 Hz the ratio of pressure caused by the s=2 mode to that caused by the s=1 modes is 10^{-4} to 10^{-7} for a cast iron pipe as opposed to 10^{-1} to 10^{-6} for a PVC pipe [43].

The coupling of soil to pipes has been investigated, both with a Dirichlet 'no-slip' boundary condition, in which case there is both axial and radial coupling between soil and pipe, and with imperfect bonding between soil and pipe, such that they are only coupled radially [63]. This study showed limited differences between the two cases. Therefore, the relative simplicity of the analytical solution for the imperfect bonding case may be preferable, as suggested for example in [59].

Relatively little work has been conducted looking at the effects of discontinuities on wave propagation in pipes. There has been some work looking at changes of material, including material thickness, for pipes in vacuo [82] and for changes in material, material thickness and channel radius for buried pipes [84], however there has been no experimental validation of this work and it is somewhat dated. Some groups have looked at modelling the effect of bends [85–87] and flanges [88] on wave propagation at ultrasonic frequencies, with mixed success, but none have extended this work to low frequencies in water-filled pipes.

Most of the work discussed above has focused on the axisymmetric modes, as measured by radial displacement and pressure inside the pipe. As already mentioned, the focus on axisymmetric, i.e. n=0, modes is because they carry most of the energy, so have the most effect on observations. The focus on radial motion and pressure appears to have been driven by measurement constraints: the pressure can be measured by hydrophones and the radial acceleration by monoaxial accelerometers. Only one group, [66], have reported using a monoaxial accelerometer perpendicular to the pipe to measure axial acceleration. They found it more sensitive to leak noise excitation than an accelerometer traditionally mounted to record the radial acceleration. However, they did not apply their measurements to any of the theory of wave propagation.

The above is still fairly theoretical. Comparing the predictions with measured results still leads to discrepancies, [89] and [90] propose stochastic methods for understanding the uncertainties in wave speed predictions based on models.

Table 2.4: Summary of analytical and numerical models of wave propagation in pipes.

Accounts for	Basis	Success	Ref	Date
Surrounding soil.	Analytical, (0,1) and (0,2) modes	Reasonable agreement with measurements of wave speed, poor agreement with measured attenuation, predictions grew worse at higher frequencies over range 100-800 Hz.	[40, 83]	2002-2004
Effect of discontinuities in buried pipes: change of radius or material	Analytical (0,1) and (0,2) modes	No experimental validation. Found reflection and transmission behaviour depended on type of discontinuity, with mode conversion for certain types of join.	[84]	2005
Surrounding soil, including shear coupling of pipe with soil	Analytical (0,1) and (0,2) modes	Improved agreement with measurements for both wavenumber and attenuation compared with [40] over range 200-600 Hz.	[38]	2013
Surrounding soil, impact of including shear coupling, vs. only radial coupling, between pipe and soil.	Analytical, (0,1) mode	Good agreement with measurements of wavenumber and attenuation for buried MDPE pipe over frequency range 200-600 Hz for fluid-dominated, (0,1), wave.	[63]	2016
Surrounding soil, effect of soil properties	Numerical (COMSOL)	Good agreement with experiment and showed clearly the large effect of different soil types, including explaining some of the cause.	[59]	2018
Surrounding soil.	Numerical (SAFE), focus on (0,1) mode	Good agreement with measurements of wavenumber and attenuation for buried MDPE pipe over frequency range 200-600 Hz for fluid-dominated, (0,1), wave.	[62]	2018
Effect of bends, Fluid-filled pipe in vacuo, ultrasonic frequencies.	Numerical	Predictions matched experimental results. Comparison performed for ultrasonic frequencies (45-75 kHz).	[85]	2005

Continued on next page

Continued from previous page

Accounts for	Basis	Success	Ref	Date
Effect of right-angle, fluid-filled pipe in vacuo.	Analytical and numerical (COMSOL)	Good agreement between analytical (scattering matrix) and numerical results, no experimental validation. Expect some resonances to occur at corner, influencing transmission and reflection.	[86, 87]	2013
Effect of flanges. Fluid-filled steel pipe in vacuo, high frequency (5-50 kHz)	Analytical and numerical	Some agreement between model and experiment, model may not have encompassed complexity of flange plates enough. Predicted and found mode conversion at flanges, observed more attenuation at flange than predicted.	[88]	2018
Effect of flow. Fluid-filled pipe in vacuo.	Numerical. No experimental validation.	Showed change in flow from v_{flow}=0 to v_{flow}=0.3c leads to small change in wave velocity. C.f. typical water pipe flow, v_{flow}=1E-4 m/s	[91]	2019
Effect of material, burial, internal material	Numerical (DISPERSE model), with experimental validation. Focus on L(0,1) and L(0,2) waves	Modelling and experimental work, moving towards a full defect finding system on large diameter metal pipes: [92]	[93–95]	1998-

ID	Description	Configuration	Ref.
A	Ottawa, Canada	Buried PVC, 200 m long, 75 mm diameter. Pressurised from the WDN. Looking to identify several different leaks using accelerometers and hydrophones.	[43, 49, 54–57]
B	Blithfield, UK	Buried HDPE, 120 m long, 80 mm diameter. Pressurised from the WDN. Looking to identify and localise multiple leaks simulated by opening valves attached to stand pipes. Used accelerometers, hydrophones and geophones at hydrants.	[44, 49, 56, 58]
C	Sao Paolo, Brazil	Buried PVC, pressurised using a centrifugal pump up to 3.4 bar. Leak simulated by open valve. Detection by accelerometers attached to pipe wall.	[56, 59, 60]
D	University of East Anglia, UK	Buried MDPE, 34 m long. Pressurised to 1.5 m using a standing head of water. Looking to validate multiple models of wave propagation in pipes, used loudspeaker and shaker as sound source with hydrophones inserted into the pipe.	[38, 40, 43, 59–63]
E	Papastefanou 2012	Unburied MDPE, 50 m long. Pressurised from the WDN. Looking at cavitation due to leaks simulated by drilling holes in the pipe wall. Measured using hydrophones.	[37]
F	Southampton, UK: vertical piston	Vertical, unburied MDPE, 2 m long. Looking to validate model of wavenumbers in water filled pipe. Used piston in the water column as a sound source, with pressure sensing PVDF wire ring transducers measuring the effect.	[40, 61, 64]
G	Martini 2017	Buried, small diameter HDPE, 28 m long, 16 mm diameter. Pressurised using a static header tank to 3.5 bar. Looked to identify various leaks on the pipe, measured using accelerometers and hydrophones.	[65, 66]
H	Nestleroth	Live test on cast iron WDN pipe. 630 m long, 300 mm diameter, pressure 3.1-3.4 bar. Aiming to compare ability of Sahara [67], SmartBall [68] and LeakfinderRT [69] at locating real and simulated leaks.	[70]
I	MIT	Mixed material, above-ground pipe loop, 14 m long, 50 mm diameter. Pressurised using a centrifugal pump or WDN. Simulated leaks using service connections, valves and drilled holes. Measured using a tethered hydrophone.	[71–73]
J	Sheffield, CID lab	Above ground MDPE pipe loop, 140 m long, 25 mm diameter. Pressurised using a pump. Simulated leaks by machining a longitudinal slit, drilling holes in the pipe and spoiling an electrofusion joint. Measured using accelerometers placed o a flange plate.	[10, 33, 74–76]
K	WDN case study	Live section of the WDN containing PE, CI and AC. Leaks generated by attaching stand pipes to fire hydrants. Measurements using accelerometers at various locations.	[36]
L	Pal 2010	Buried MDPE, 110 m long, 45 mm diameter. Pressurised by pump. Various leaks placed in line using a replaceable pipe section.	[32, 77]

Table 2.3: Summary of experiments for investigating leak detection, the description is based on the location of the experiment if multiple research groups have used results from the same experiment.

2.4 Existing technology for acoustic leak detection

Leak reduction already forms an important part of the water industry management plan, and as such there are already many companies selling leak detection technologies. A large number of these are based on acoustic techniques, but there is also interest in CCTV, laser scanning, electromagnetic and ground penetrating radar-based systems [8]. This section will explore the existing options and discuss where there are opportunities for progress. It will focus on acoustic techniques, although relevant alternatives will also be considered; for more information on these alternatives readers are referred to reviews by Liu and Kleiner [8, 96] and the more recent review by Yu *et al.* [9].

2.4.1 Flow monitoring

The presence of leaks in the water network and their net outflow can be found relatively easily from macroscopic monitoring of flow in the network. This is usually achieved by considering the minimum night flow to give an estimate of the amount of water being lost within a district metering area (DMA) [97]. These are now routine measurements, based on which high loss DMAs are identified for closer inspection. The subtleties of flow monitoring are covered in [98].

This can be combined with hydraulic models to narrow down on the leak location [97].

It has been shown theoretically [99] that it is possible to find the size and location of a leak given flow and pressure readings from each end of a pipe. This has been extended in [100] to find the size of a leak from pressure and flow measurements at specific points on a larger network, which includes branches. Both of these papers show only simulated evidence of these techniques working, with no attempt at localising leaks on a real system.

2.4.2 Standard acoustic devices

The original leak detection device was a listening stick, where an operator places the tip of a stick on the ground, or an appropriate probing point on the network such as a hydrant, and listens for leak noise [5]. The method is very subjective, relying on the operator to decide that a given noise is a leak.

This progressed to more technical listening devices, which are touched onto the pipe or the ground nearby then the noise recorded, e.g. the Guterman Aquascopes [101]. These may be microphones or accelerometers, but still tend to rely on the operator to classify the sound. More recently, many of these have been augmented with machine learning to automatically determine whether the noise detected by these devices comes from a leak, both in academia, e.g. [76] and [102], and commercially [103]. This kind of leak noise classification is covered in more detail in Section 2.4.10, with a summary of AI-based techniques. Currently these commercial platforms report an accuracy of over 90%: a higher success rate than trained operatives [103].

When using these recording devices, the leak can be located either by moving the probe point in small increments (a 'step survey'), or by using two devices and correlating their signals to find the distance to the leak, as is explained in Section 2.4.3. Such 'correlators' were originally used only for manual inspections, with an operator attaching the correlator for a single survey, but they are now predominantly being deployed as noise loggers, e.g. [104]. A noise logger is left installed on an asset, usually a hydrant, for a period of time, from days up to permanent installations. The loggers

turn on for a couple of hours during the night, when the network is quiet, and record noise levels. The recordings can either be sent up to the cloud wirelessly or picked up by operators driving by regularly [8]. Once the recordings have been taken, the same methods described above can be used to determine whether there is a leak in the signal: either frequency-band based techniques or increasingly algorithm-driven/AI based techniques. Once a leak has been identified either cross-correlation is used on data from neighbouring loggers to locate the leak, or operators are sent to investigate.

2.4.3 Cross-correlation for leak detection

A common method for leak localisation is to use spatiotemporal data from a number of receivers at different locations. Sets of data can be compared using cross-correlation to determine whether there is a common noise source, and if so the distance from the receivers to the noise source. The cross-correlation can be calculated using [105]:

$$C_{xy}(\tau) = \frac{\Sigma_t\{(x(t) - \bar{x})(y(t-\tau) - \bar{y})\}}{\sqrt{\Sigma_t(x(t) - \bar{x})^2}\sqrt{\Sigma_t(y(t-\tau) - \bar{y})^2}} \tag{2.12}$$

for two signals $x(t)$ and $y(t)$, where r is evaluated at a range of 'lags' τ between the two signals. $\bar{x}$ and $\bar{y}$ are the average of the time series. In this form it can be seen that C_{xy} is a metric describing the size and direction of the relationship between x and y at a given τ: if the signals are identical then $C_{xy} = 1$, if they are out of phase by π then $C_{xy} = -1$ and if there is no relation between the two $C_{xy} = 0$. In an ideal scenario, where the source signal is perfectly transmitted to both receivers, C_{xy} would equal 1 at the lag corresponding the time delay between the two signals arriving. In practicality, C_{xy} rarely equals 1 and instead the time delay between the two signals is taken as the maximum of $r(\tau)$, τ_{peak}.

Once τ between the two signals has been determined the position of the leak can be calculated as [106]:

$$d_1 = \frac{d - c\tau_{peak}}{2} \tag{2.13}$$

where c is the speed of sound, d is the separation of the two measurement locations and d_1 is the distance from one of the measurement locations to the leak.

It should be noted that the cross-correlation is rarely calculated using Equation 2.12. An automated process is available in most analysis software packages, this author uses Python's SciPy signal processing library [107], which defines the cross-correlation using the general form:

$$r(\tau) = \sum_{i=0}^{N_x - 1} x_i y^*_{i-t+N-1} \tag{2.14}$$

where y^* is the complex conjugate of y, N_x is the number of samples in x and $N = \max(N_x, N_y)$.

Using the cross-correlation is a popular means of locating leaks from outside the pipe. However, the following deficiencies in cross-correlation based techniques are often encountered in a real leak-localisation scenario:

1. **Variable wave speed**: for simple scenarios the wave speed can be looked up in standard

tables. However these rely on consistent wave speed in pipes, which may actually depend on numerous factors, such as the surrounding soil type, the pipe dimensions, the location of joints, etc. An inaccurate wave speed leads to errors in leak location [89]. This is far more of a problem on plastic pipes than metal pipes, with studies [8, 44] investigating the accuracy of correlation on metal vs. plastic pipes finding correlation on a metal pipe to be accurate to 10 cm [8], while on a plastic pipe it is only accurate to 1 m when measuring 20 m away [44]. Furthermore [108] have shown that the speed of sound on plastic pipes is very variable, measuring c between 207 and 582 m/s on PE80 pipes with diameter 110 mm.

2. **Changes in pipe material**: this leads to variation in the wave speed, so complicates the calculation of leak location. This is compounded by the fact that much of the WDN is poorly mapped, this leads to situations such as that in [58], where an unmapped change in pipe material led to a 10 m error in leak location.

3. **Low signal to noise ratio**: noises in pipes may attenuate quickly, particularly in plastic pipes and at high (>1000 Hz) frequencies [54]. Focussing analysis on low frequencies partially solves this, but there is still a finite limit to how far away leaks can be detected. If sensors are mounted on fixed assets, such as hydrants, the distance between sensors may be greater than the noise can travel. It is generally found that sound travels further in the water column than along the pipe wall [43], so accelerometers mounted to the pipe wall are inherently more limited than measurements inside the pipe. In plastic pipes, the search for a good SNR leads to low frequencies being focused on as high frequencies are strongly attenuated [8], [109].

4. **Obfuscating signals**: running taps, for example, may sound very similar to leaks; other noise sources, such as nearby traffic, may obscure leak signals. This can be reduced by running surveys during the early hours of the morning [110] but must still be considered.

Correlation as a leak-detection technique is hardly a new idea, for example [111] discusses the advantages and disadvantages in 1991. It is working through improvements to it that still poses a research question.

2.4.4 A comparison of current conventional techniques

A summary of the capabilities of some of the available acoustic loggers is provided in Table 2.5. Based on this sample, it can be seen that accelerometers are by far the most common sensor used (5/6 of the loggers shown), with a hydrophone included as an optional extra on two of these. The single option that is only a hydrophone (the Gutermann HISCAN) specifies that it is mainly used for trunk mains due to the relatively high cost, such that the higher cost of failure is needed to justify the outlay. All six of these loggers use correlation to determine the location of the leak, and it is presumably this that leads to the material-specific range ratings reported by the Gutermann ZoneScan and the Ovarro Eureka. It is interesting how large the discrepancy in reported range is between these two: the ZoneScan wants 80-140 m intervals while the Eureka specifies a 3,000 m range. This may be due to the differences in approach: the ZoneScan is a permanently deployed option while the Eureka is for targeted searching, so may have a much more sensitive accelerometer.

A comparison of several of these acoustic techniques, including listening sticks and correlators was reported in [58] for a known leak on an MDPE section of the WDN. It found the correlators to be the most effective of the methods studied, able to detect and locate the leak at distances up to

Table 2.5: Comparison of a few of the most common acoustic logging devices currently on the market, this list is far from exhaustive but covers a good range of the options.

Name	Logging type and deployment	Launch date
Echologics, LeakFinder-ST/RT [69], [70]	Piezoelectric accelerometer mounted magnetically with optional additional hydrophones. Deployed manually, for targeted searching. Can be used on most types of pipe, e.g. plastic, metal, concrete including mixed pipe types. The underlying localisation method is correlation-based, and includes noise reduction, frequency selection and a velocity calculator.	ST: 2014, RT: 2003
Gutermann ZoneScan [104]	Accelerometer, magnetically attached to hydrant, valve or pipe. Permanent or semi-permanent deployment, data collected by device nightly, sent to cloud regularly. Appropriate for MDPE/HDPE (60-80 m intervals), asbestos cement (80-100m intervals) and metal (80-140 m intervals). Provides leak likelihood score based on noise level, frequency and history. Correlates loggers to locate.	> 15 yrs.
Gutermann HISCAN [112]	Hydrophone inserted into the water column at a tapping point or hydrant. Permanent deployment with data delivered daily to the cloud. Mainly used for trunk mains (since expensive to deploy). Provides leak likelihood score based on noise level, frequency and history. Correlates loggers to locate.	2018
Ovarro, Phocus [113]	Accelerometer (5 V/g). Placed on access point, e.g. hydrant. Permanent/semi-permanent deployment. Transmits data via local IR (50 cm range) or radio (50 m range). Does not specify the types of pipe it is appropriate for. Uses correlation for localisation.	Phocus3: 2020
Ovarro, Eureka [114]	Accelerometer (10 V/g), placed on access point, e.g. hydrant. Optional hydrophone (-195 dB). Temporary deployment, for targeted searching. Appropriate for iron pipe (3,000 m range), PVC pipe (1,300 m range). Specifies a maximum of 6 materials between correlators. Uses correlation, including velocity correction function. Uses frequencies of 3-5000 Hz for the accelerometer and 0-2400 Hz for the hydrophone.	Eureka5: 2022
Ovarro, Enigma [115]	Accelerometer (30 V/g), magnetic stud attachment. Semi-permanent deployment. Transmits data via 2G/3G. Can be used on any pipe material. Uses correlation for localisation.	Enigma3-BB: 2021

62 m, unlike listening sticks or direct acoustic measurements, which were only effective up to 5 m from the leak. Similar studies, such as those described in [70, 116, 117], looking at the efficacy of cross-correlation based techniques, find them to be reasonably effective at detecting leaks and locating them to within 1 m. Most excavations for leak repair require the leak's location to be within that distance [70].

An excellent review of the various acoustic devices available as of 2013 can be found in [5], this includes matrices showing which methods are most efficacious on which elements of the network.

2.4.5 In-pipe detection in the WDN

One of the most advanced and sensitive options for in-pipe acoustic sensing is a hydrophone inserted into the pipe. This can be done at specific access points, such as hydrants, and a static recording of the in-pipe soundscape taken. Several of the leak detection systems given in Table 2.5 have a static hydrophone as an option for their systems. Using a hydrophone does improve the range of leak detection since noise tends to attenuate less in the water column that in the pipe-wall [43], however the additional benefit is often considered minimal compared with the added technical complexity of inserting a hydrophone into the pipe vs. attaching an accelerometer to the pipe wall. A static hydrophone is also still limited in what it can detect by where the fixed assets are on the network. A mobile platform allows for full inspection of the network. Development of an in-pipe inspection unit is a growing field in the research and industrial communities. In-pipe inspection is far more developed for gas and oil pipelines, for a review see [118], however it operates in a completely different economic and risk environment. Gas and oil leaks lead to loss of revenue and environmental contamination considerably faster than water leakage.

The commercial in-pipe inspection area is dominated by Pure Technologies, who have three different in-pipe inspection platforms for a range of scenarios and at varying levels of development. Aside from these several research groups have attempted to build robots suitable for use inside the WDN, however none have managed to develop a platform to the point of deployment. The capabilities and configurations of these platforms are summarised in Table 2.6, and discussed below. Images of each of the devices are shown in Figure 2.4.

The two main methods of interest are the Sahara [67] and the SmartBall [68] platforms, since these are farthest developed. The Sahara is a tethered hydrophone-based platform while the SmartBall is free-swimming. They seem to often be used in conjunction, for example in the case study in [134]. Both these platforms are passive devices that follow the flow of the pipe. Sahara is a tethered hydrophone, with a parachute to maximise the force exerted by the water column. Being tethered, it is easy to retrieve from the WDN, and it has a high location accuracy since the distance to the leak can be determined by the length of the tether. This is augmented, for both platforms, by the use of an RF transmitter on the platform, which allows it to be tracked in real time from above-ground. The SmartBall is untethered and is retrieved using a net placed downstream of the deployment location. This means its range is limited by the length of pipe before the flow branches, rather than by the length of a tether, although its range can be increased by stopping flow to laterals [119]. Both SmartBall and Sahara can be inserted into live pipelines, using existing access points of minimum diameter 100 mm and 50 mm respectively. Since they are moving passively there are required minimum and maximum flows for deployment. This is particularly true in the case of the SmartBall which rolls along the bottom of pipelines for flows with velocity between approximately 0.15 and 0.6 m/s, but moves in the water column for larger flow velocities, and will

Table 2.6: Comparison of in-pipe leak detection systems for the WDN, separated into commercial platforms in the upper and research platforms in the lower sections.

Name	Logging type and deployment	Status
Sahara [67, 70]	Hydrophone and CCTV Tethered, 1.6 km long tether. Parachute allows water flow to pull it down pipe. Inserted through existing fittings. Fits through valves and bends. Operable in pipe of diameter > 150 mm.	Testing since 1997, 7,200 km scanned, 6,500 leaks found.
SmartBall [68, 70, 119]	Senses using a 'range of acoustic sensors'. Foam ball, inserted into pipeline using existing fittings, extracted using net. Propelled by water. Fits through valves and bends. Operable in pressurised pipelines up to 34bar of diameter >150 mm	Testing since 2004, 11,500 km scanned, 3,000 leaks found.
PipeDiver [120]	Electro-magnetic sensors. Free-swimming, untethered. Requires 300 mm access point installed at either end of inspection section. Fits through most valves and bends. Can scan both pressurised water and waste-water pipelines, including metallic or concrete pipes of diameter >600 mm	Testing since 2007
Chatzigeorgiou et al. 2011 [121, 122]	Hydrophone and DPS. Pushed by water, uses legs to control speed, including capability to anchor in place. Operates in pipe of diameter 100 mm.	Suggested 2011 No publications since 2016 Superseded by PipeGuard?
PipeGuard Mark 0 [123, 124], and Mark 2 [125–127]	Pressure sensor, based on membrane moving due to pressure change on passing leak. Patents: [128], [129] Sensor pulled along by wheeled carrier module, spring-loaded to fill pipe. Operates in pipe of diameter 50 or 100 mm.	Suggested 2015 Last publication 2019 Sensor patented 2020
MIT-MRL robot [130, 131]	Can either move passively with the water or is self-propelled to execute turns at T-junctions. Tested in open water, not yet in pipe. Operates in water-filled pipes of diameter >100 mm	Suggested 2015, further work 2020.
Ultrasonic mote swarm [132, 133]	This work explored putting small (39 mm diameter) 'motes' into a pipe, each equipped with various sensors. The collisions of these with the pipe walls, coupled with ultrasound and magnetic measurements were used to corroborate existing maps of the pipe network. While this sensor looks very interesting, decoupling the complications of the sensor motion from the sensing seems a significant challenge.	Thesis 2019

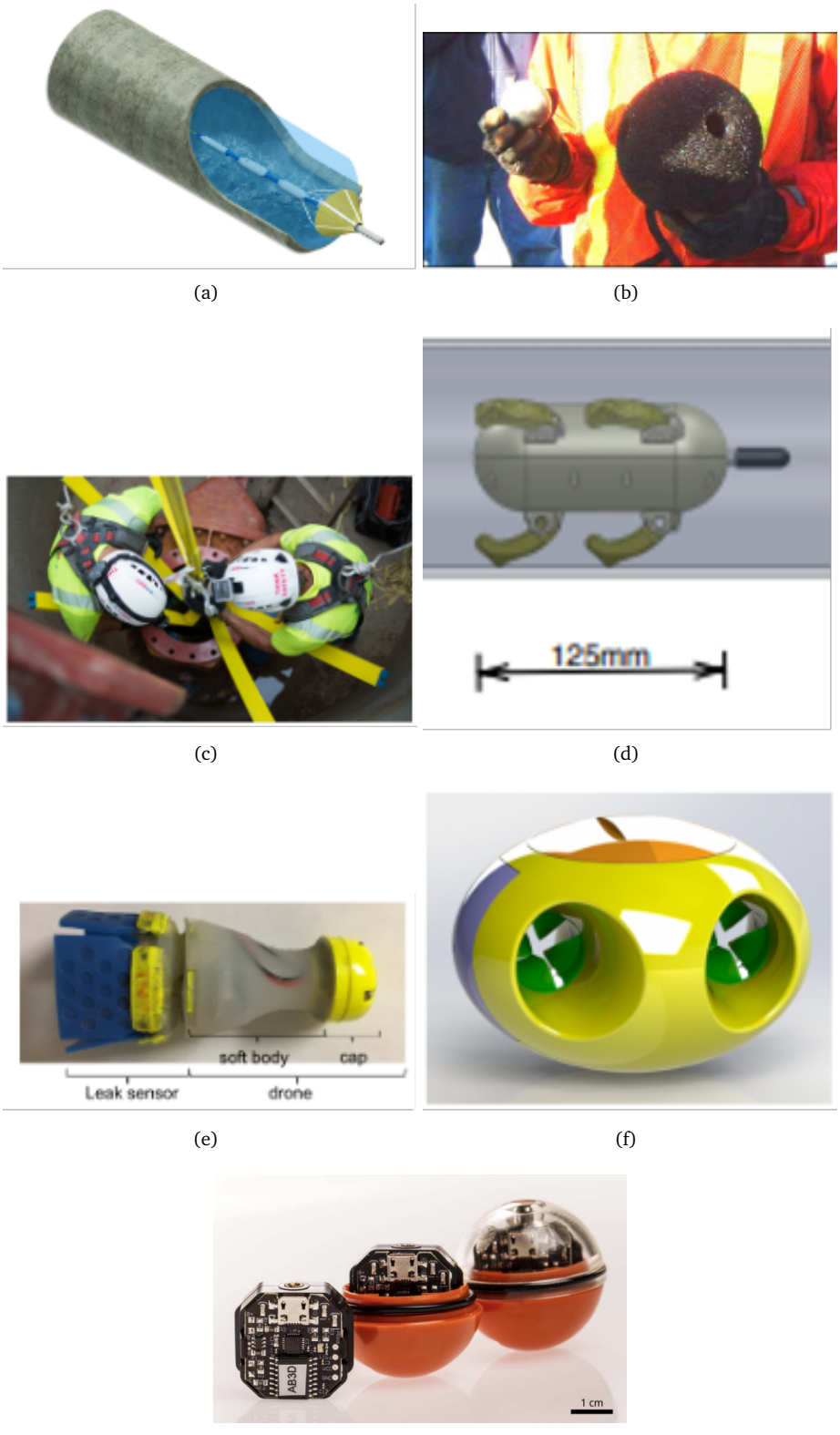

(a) (b) (c) (d) (e) (f) (g)

Figure 2.4: Pictures of each of the in-pipe inspection methods summarised in Table 2.6, showing (a) the Sahara platform [67], (b) SmartBall [68], (c) PipeDiver [120], (d) the robot proposed by Chatzigeorgiou et al. 2011 [121], (e) PipeGuard Mark 2 [126], (f) the MIT-MRL robot [130] and (g) the 'motes' [132].

not move for flows below this range. For reference, the required flow rate in a small housing development is 8 l/s and the typical pipe diameter is around 100 mm [13], giving a typical flow rate of 1 m/s. It is not specified how large a flow rate is required for Sahara to work properly, although a mule line can always be used to pull it through a pipe section with too low a flow rate [67]. Both of these devices are described as being for both leak and air pocket detection.

The Sahara platform predominantly uses a hydrophone to listen for leak noise within the pipe [67]. It is also possible to use Sahara to test the wall thickness of pipes when used in conjunction with another acoustic sensor and a reference sound source [70]. It is less clear how exactly the SmartBall gathers noise information – it is known to contain accelerometers, magnetometers and an ultrasonic transmitter, plus unspecified acoustic sensors. The ultrasonic transmitter is used solely to follow the device from above-ground, and the accelerometer to calculate the position internally [119]. There is some concern that the results from the SmartBall and Sahara are difficult to interpret, due to variations in the surroundings, difficult to distinguish signals and their non-deterministic path [135]. These problems would be particularly apparent for small leaks. The SmartBall aims to mitigate some of these problems by encasing the aluminium shell with foam, to minimise the noise produced by its passage [8], but it is unclear how effective this is.

An early study from 2008 by Galleher and Kurtz [119] detected the location and size of a leak in a large-diameter water transmission pipeline, based on data recorded by the SmartBall. It should be noted that the work performed here was undertaken by the manufacturers of SmartBall, a more even handed study of its performance has been conducted by the US Environmental Protection Agency (EPA) [70] which gave a more mixed review of its performance. The EPA study [70] was conducted in 2012 and compared the accuracies of Sahara, SmartBall and Echologics' LeakfinderRT (a static cross-correlator described in Table 2.5). It utilised 11 simulated leaks on a 0.6 m diameter, 0.6 km cast-iron water main to test how successful the three platforms were at detecting, locating and sizing leaks. It also tested how well each method working 'blind' by excavating other features reported by the devices to be leaks which had not been intentionally compromised. All three platforms detected all 11 synthetic leaks. They correctly quantified the flow rates of 6, 7 and 8 of these respectively. Sahara located the leaks by tracking the platform from above ground and marking leak locations. SmartBall located them by post-processing the on-board accelerometer data to calculate the trajectory. As already mentioned, the LeakfinderRT uses standard correlation-based analysis. LeakfinderRT could locate 3 of the 11 simulated leaks to within 1.5 m, the others were incorrect by up to 5.1 m. The three platforms also reported 5, 6 and 3 real leaks respectively of a total of 6 that were confirmed by excavation or other inspection. This meant that LeakfinderRT correlator had the lowest success rate for finding real leaks, although it did find a relatively large-volume leak that the other two platforms missed. For all of these real leaks all three platforms were within 1 m of locating it, except for one leak which the SmartBall reported at 1.2 m from its actual location, a successful excavation requires an accuracy of 1 m [70].

Based on this survey the three technologies performed comparably well in a metal pipe. However, it was, perhaps, not the best survey for demonstrating the relative strengths of the in-pipe deployment methods. It is known that cross-correlators work considerably better on metal pipes than on plastic [117], since the speed of sound is more predictable and the attenuation lower. It would be interesting to see how the performance of these three devices compare on plastic pipes, particularly where access points were at large intervals. It is noteworthy that the in-pipe detectors were far more successful at picking up small, real leaks than the correlator, although perhaps concerning that they did not detect the largest leak.

A further interesting component of this report was the cost estimates provided for a survey performed using each of the three methods. For a 0.6 m diameter, 3.05 km long steel pipeline the cost estimate for a leak survey was $22,000, $45,000 and $20,000 for a survey using Sahara, SmartBall and LeakfinderRT respectively in 2012.

In terms of the lower Technology Readiness Level (TRL) options, MIT have been working on a pipe inspection robot since about 2010 and have looked at several different configurations. Most of these do not appear to have moved beyond initial prototypes for testing manoeuvring and localisation of the robot. From approximately 2011 to 2016 they worked on a cylindrical robot that uses the water flow for propulsion then deploys legs to control its speed [121], and since around 2015 they have been working on a self-propelled spheroidal robot [130]. Their two iterations of PipeGuard robots have moved beyond this into leak detection [121, 123]. The system uses a patented pressure-sensing skirt to detect the change in pressure as the robot moves past the leak [128, 129]. It has been tested on a commercial test site with small diameter pipes [127] with early trials showing promise.

Some other groups have worked towards building a robot for in-pipe detection, for example Kazeminasab et al. at Texas A&M University [136], where, again, their robot has not moved beyond the early prototype stage and has not been used at all for in-pipe acoustic detection of leaks as far as could be determined from the literature.

2.4.6 Challenges for in-pipe inspection

Clearly there has been interest in deploying robots for pipe inspection for some time, but most work is still at an early stage. Furthermore, it has largely focused on deploying robotic platforms, with little understanding of how to detect leaks from such a platform.

The practicalities of deploying a robot in the water distribution network should also be mentioned here. Obviously, the robot needs to be waterproof under the pressures and velocities found in the network. In addition to this it needs to conform with water quality standards [137], so needs to be sterilisable before deployment, not introduce foreign matter into the network, and, potentially most challenging, not remove sediment from the walls during its passage [97]. Furthermore it must be retrievable.

2.4.7 Improving correlation-based techniques

As was mentioned in Section 2.4.3 there are several short-comings of correlation based methods of leak localisation. One of these is that in Equation 2.13 the accuracy of the leak localisation depends not only on the accurate determination of τ_{peak} from the cross-correlation, but also on an accurate value of c, the speed of the travelling wave. For metal pipes this does not tend to vary much, and the speed of sound for different materials and pipe diameters is available in various tables, often pre-programmed into the device [138], or can be be calculated from Equation 2.15 [138].

$$c = \frac{c_f}{\sqrt{1 + \frac{2Br}{Eh}}} \tag{2.15}$$

Here c_f if the free-fluid wavespeed, B is the fluid bulk density, E is the Young's Modulus, r is the pipe radius and h is the pipe wall thickness.

Table 2.7: Some of the reported variation in the speed of sound calculated for plastic pipes.

source	material	c [m/s]
[143]	MDPE	160
[47]	MDPE	365
[144]	PVC	495±5
[142]	MDPE	375±50
[142]	PVC	540±50

These values are also available for plastic pipes but because the material is often dispersive, so different frequencies arrive at different times, and the speed of sound in the material depends on its surroundings, the quoted values may be very different to those observed [139]. Another issue with using Equation 2.15 is that it does not take into account the surroundings of the pipe, which many studies [140] have found has an impact on the speed of sound, particularly in plastic pipes. Even with these modifications, using an analytical model to find the sound speed still may not include enough of the complexities of the system to give an accurate prediction [32], and the necessary material properties may not be known, particularly those of any surrounding soil.

Instead the speed of sound is usually measured for each new location. It may be calculated from time of flight measurements, comparison of the pressure at three transducers or cross-correlation or phase information. Time of flight measurements use the arrival time difference, Δt, between measurements separated by d, so $c = d/\Delta t$ [32]. These require precise time synchronisation of measurements that may not be practical. For example, for a PVC pipe with $c \approx 500$ m/s, and sensors 1 m apart, $\Delta t = 2$ ms. Alternatively, the relationship between the transfer functions across three sound pressure measurements and the speed of sound can be derived [141] and compared with experiment. Thirdly, by generating a sound at a known distance from two sensors, cross-correlation and a rearrangement of Equation 2.13 can be used to find c [32]. Finally, the speed of sound can be calculated from the phase difference between two measurements [32].

Experiments finding the speed of sound in plastic pipes find a large range of values, a small selection of values found in the literature is provided in Table 2.7. Scussel *et al.*investigated the impact of various factors on c using Monte-Carlo methods to consider how variation in each parameter changed the estimated value of c [142].

Any cross-correlation based sensor method needs to account for the variability in the speed of sound in pipes. Either models need to be improved such that c can be calculated from the pipe material and soil properties, or part of the data processing capabilities of the sensor should include calculating c using one of the techniques described above. The practicality of this is considered in Chapter 3. Alternatively [145] suggests improved statistical approaches to analyse the cross-correlation function which improve its accuracy in estimating τ_{peak}.

The significant attenuation experienced by noise on plastic pipes [44] leads to more issues in locating leaks on plastic pipes. It has been widely reported [32, 42, 146, 147] that correlators are less effective on plastic pipes. As of 2012 [42] interviews with sensor companies indicated that they were well aware of these issues with detection on plastic pipes, and were working to improve their sensors accordingly. Their main focus for doing so was using transients and hydrophones.

2.4.8 Transients

It is beyond the scope of this work to give a full summary of transients. They are an alternative method of leakage detection, which uses active acoustics with induced 'transients' in the pipe system. The transients are short periods of increased pressure, that may be generated by closing a valve. This subsequent increase in pressure can be picked up acoustically on the pipe surface or with a hydrophone. The behaviour of the transient is affected by wall perforation, poor joints, blockages and leaks, making it a viable method of leak detection [9, 148]. However, so far this method has been limited to controlled experimental testing, generally on limited systems [149], and as far as could be identified there is not currently work to commercialise it. For a fuller view of the method readers are directed to Brunone *et al.*'s 2022 review [149].

2.4.9 Ultrasonic methods

There are two main, distinct, types of ultrasonic sensing used in pipe leak detection. Guided wave ultrasonic (GWU) methods generate ultrasonic waves using a ring around the pipe, these waves then propagate for long distances due to the shape and frequency of the waves generated, with any defects or leaks reflecting back the wave to the source. The distance to the feature can then be determined by the time of arrival [150]. Several commercial GWU options exist, including [92, 151].

In long sections of metal pipes with few features, this is an effective technique. In more complex pipes with multiple junctions or material surroundings, the clarity of results is impaired. For example, pipes embedded in concrete or bitumen are much more difficult to inspect [152] as are coated or buried pipes [153]. Plastic pipes also pose more of a challenge, due to the increased guided wave attenuation. Lowe *et al.* show improvements specifically for plastic pipes [154], however these ideas require further work to bring them up to the resolution of other existing methods for metal-pipe inspection.

The second ultrasound-based inspection technique places a single transducer on the pipe wall, and inspects a small region of pipe wall under the transducer [9]. This is very accurate, but requires access to the whole pipe and many scans to inspect a reasonable length of the pipe. It can be extended using phased arrays [155] to scan more of the pipe in one go, and to detect different types of defects. This concept has been commercialised as the UltraScan DUO and EDGE [156] for defect detection in dry pipes, where the scanner surveys the pipe at a speed of between 0 and 5 m/s (no information is available on how much of the time it spends at which end of that speed range). This is only one example of a phased array system, there are others, including [157]. There is also ongoing work to combine ultrasonic detection with a robotic work, for example by Zhang *et al.* [158].

A much more detailed review of these and other acoustic and ultrasonic techniques is available in [9].

2.4.10 Machine learning for leak detection

Leaks lead to complex acoustic signals, with difficult to detect similarities and correlations between data sets. In some ways this makes them a perfect target for machine learning methods and lots of work, especially over the last 5-10 years has looked into this. This thesis does not use machine

learning methods due to a lack of high quality, representative data. However, given the fact that this is a burgeoning field it was felt it could not be ignored.

A good summary of different types of machine learning (ML) models that can be applied to acoustics can be found in [159]. Papers looking at the success of various models when applied to leak detection include [10, 160–166] with a summary of the state of ML for leak detection as of 2020 in [167] and a discussion of some of the challenges when deploying ML for leak detection is in [168].

A consistent issue in training ML models on leaks is a lack of data, Yu *et al* [169] present some interesting work demonstrating a model for leak detection with an accuracy of nearly 95%. This was achieved on a data set collected on the WDN of multiple cities with the presence (or not) of a leak verified by digging next to each logger. This meant the authors could train their models on 821 recordings, 299 of which were known to be leaks and 522 had no active leaks nearby. This is a large amount of high quality data to have found, but still barely enough to prove that the models are not fitting to other parameters of the system, particularly once the variations in pipe material etc. are accounted for.

There is significantly less information on how they work, but there are many commercial ML options, for example Guterman's ZoneScan now has an AI option [170], along with ML specialists FIDO [103].

2.4.11 Other signal processing based techniques

Alternative signal processing based techniques have been proposed for use on acoustic data, particularly for leak detection rather than localisation: there is no point locating a sound source only to discover that it was not caused by a leak. As mentioned previously, the size of the leak is almost as important a metric as its location and many of these methods aim to determine leak size. Common methods include:

1. **Power spectral density (PSD)** based methods: these look for peaks in the PSD, and assume the magnitude of these peaks is proportional to the size of the leak, while the frequencies of the peaks are dependent on the type of leak [75]. Kaewwaewnoi *et al* [171] showed a clear increase in the peak magnitude with flow rate, but ran limited tests and only considered leaks from valves. This method is subjective and more difficult to repeat or automate than other methods, as discussed in [172].

2. **Signal root mean square (RMS):** the RMS is taken, often of the PSD, over either the entire frequency range or sections of it [171]. Both [171] and [172] showed a clear increase in the signal RMS as leak flow rate or pressure were increased. Both were looking at leaks from valves.

3. **Vibro-acoustic emission (VAE) counts:** in this technique a threshold is set for the sensor output, and the number of times this threshold is exceeded is counted [75]. This method is very sensitive to the threshold chosen: both [75] and [172] report a clear correlation for an appropriate threshold. Unfortunately, choosing this value is subjective.

4. **Octave banding:** this can be combined with the previous techniques. In this method the frequency domain is split into octave bands and analysis run separately on each one. Some bands will be of more significance than others. Some automation of the splitting of the

frequency domain allows the important frequencies to be determined in a way compatible with machine learning techniques. A comparison of the magnitude of results for different bands was proposed in [75] to differentiate leak signals from others.

5. **Wavelet analysis:** this is an alternative to the traditional spectral analysis method which combines time and frequency transformation for improved performance [173, 174].

6. **Empirical mode decomposition (EMD):** again, this extracts features present in both and time frequency domains [33].

All of these are extensions to any choice of acoustic recording, and appropriate signal processing is an essential step in analysing leak noise recordings.

2.4.12 Condition assessment in the waste-water network

For a the majority of the waste-water network the problems involved in pipeline inspection are quite different to in the pressurised clean-water water network. This is not the focus of this thesis, instead interested readers are directed to [175] which provides a review of many more techniques than are covered here, including pulsed eddy current testing, magnetic flux leakage and ground penetrating radar.

While there are multiple robotic platforms in development for the inspection of gravity fed wastewater pipes, there has been less work on the pressurised wastewater network, such as rising mains. Most of the existing platforms focus heavily on CCTV-based checks, e.g. [176], [177]. This includes significant work on image detection techniques appropriate for sewers, with much recent effort going into deep-learning based image recognition [178]. Visual scanning can be augmented by LIDAR, as proposed in [179] to gain further information on the surface topography. The main disadvantage of these light-based techniques is that they only show the state of the pipe surface. Another choice is active acoustic sensing whereby the sensor analyses the response from a generated signal [180].

Some work has been done on moving beyond CCTV for waste-water inspection, the largest single piece of work being carried out by the Pipebots grant (of which this thesis forms a part) [6, 181]. During this 5 year project several robotic prototypes were developed intended for deployment in pipes of varying sizes. Key findings during the project concerned robot control [182], localisation and mapping [183] and new methods of pipe inspection. The pipe inspection methods included ultrasonic [184] and acoustic [185] methods.

However, all of the above sensing methods again focus on partially filled, unpressurised systems. A small but significant portion of the waste water network is composed of rising mains. These pipes have received much less interest, given that they are more similar in many ways to the pressurised water network it may be that pressurised water inspection strategies are more appropriate than the aforementioned wastewater inspection technologies.

2.4.13 Acoustic velocity vector sensors as an alternative to hydrophones

Currently, most in-pipe leak detection methods use hydrophones to measure the pressure in the pipe. Outside of the leak detection sphere, acoustic velocity vector sensors (AVVSs) are an established alternative to hydrophones, which measure the particle velocity vector in acoustic waves.

These were first posited in 1956 [186], but were not fabricated reliably until the 1990s [186]. These combine a vector velocity sensor measuring the particle velocity with a hydrophone to measure the pressure [187, 188]. These have been applied in a range of areas, including acoustic imaging [189], near-field sensing from a planar surface [188] and ship tracking [190]. For these purposes an array of AVVSs is often appropriate, and extensive work has been conducted considering the best placement of sensors within an array, e.g. in [191, 192]. The advantages of AVVSs over traditional hydrophones is an increase in information, as the direction of a source can be determined in addition to its magnitude.

2.5 Direction of travel for research in leak detection

Leak detection and localisation remains an active area of research as improvements are still required on existing techniques, since they are not accurate enough when used in all situations, particularly on plastic pipes and in complex situations such as when buried in certain substrates, or when there are many pipe and substrate materials on a single stretch of pipe. The effect of soil type on noise propagation through a pipe is also poorly understood, particularly for plastic pipes, as is the effect of complex transmission paths, e.g. across multiple pipe features.

There is further work to be done on understanding the noise produced by different types of leak, with no current models existing that can predict the acoustic emission from a given leak, and consequently any method of predicting the type of leak from the acoustic emission is statistical rather than analytical. Current research is looking at augmenting these statistical techniques with AI to classify signals more accurately. This is strongly dependent on an extensive, well-labelled dataset, and is in some ways dissatisfying as the underlying cause of the differences in noise produced by different leaks is not understood as part of this process.

Current acoustic methods are focused on monoaxial accelerometers attached to the external pipe wall or pressure measurements in the fluid. Consideration of the modal properties of pipes indicates that externally applied triaxial accelerometers on the outside of the pipe, or AVVSs inside the pipe, may provide an increased level of information about the leak noise. These could aid in detecting leaks on more complicated pipe configurations.

Increasingly, static above-ground sensor development is moving towards in-pipe sensors, such as the SmartBall and Sahara systems. These have the strong advantage of moving past leaks, so the complexities of acoustic wave propagation in pipes does not need to be considered. These can currently only operate in specific circumstances, and mainly operate with pressure sensors. Little work has been done on developing sensors specifically for measurements close to leaks from an in-pipe platform.

Based on this review, it was determined that the propagation of waves on pipes could be understood more comprehensively by measuring a vector acceleration of the pipe wall or vector velocity of the fluid within the pipe. Plastic pipes were determined to be an area of the water network where existing techniques were having most difficulties, with little information available on the measured propagation and attenuation of acoustic waves through plastic pipes. There has also been limited work considering the propagation of acoustics through different features in plastic pipes. Finally, the use of AVVSs for leak detection in pipes has not been considered previously, and seems a natural progression of current interest in in-pipe robotic platforms for leak and defect detection.

Chapter 3

Preliminary Investigations of Leak Noise in Water-Filled Pipes

The previous chapter has provided an introduction to the theory of wave propagation in water-filled pipes. In this chapter the application of this theory to leak detection in an experimental pipe network is presented. The aim of this chapter is to investigate the variability of leak noise in water-filled pipes, including how the basic characteristics of the pipe influence the transmission of acoustic waves through the pipe, and so influence the acoustic detectability of leaks. This acts as the first stage of investigating the efficacy of existing methods, including their range limitations.

The influence of different parameters, such as the pipe dimensions, pipe material and pipe surroundings, on the acoustic propagation in a plastic pipe was initially investigated using a numerical model. This model was built in COMSOL MultiPhysics®, directly building on the work summarised in Section 2.3.3. Experimental work was then undertaken to consider the variations in leak noise over time and due to differences in leak shape. This represents a continuation of previous work, summarised in Section 2.2.4. The ramifications of the measured variability in leak noise and the modelled variability in acoustic propagation are considered in terms of their effect leak detectability and the effectiveness of existing methods.

3.1 Modal analysis of wave propagation in pipes

As a first step to understanding the acoustical pipe environment, modal analysis for some common pipe materials was carried out. As discussed in Chapter 2.3, pipes represent a very constrained acoustical environment such that a few specific modes are usually expected to propagate distances long enough to be detected with traditional sensor technologies. This section serves as a numerical demonstration of the results presented in Section 2.3.

3.1.1 Initial model

Initially, let us consider a 110 mm HDPE pipe, a common element of the modern water network. A basic modal analysis was conducted in COMSOL MultiPhysics® [193] for a 2D axisymmetric model of a pipe cross-section. The mesh is shown in Appendix B where a summary of the mesh sensitivity analysis has been provided. The parameters used within the model are summarised in Table 3.1.

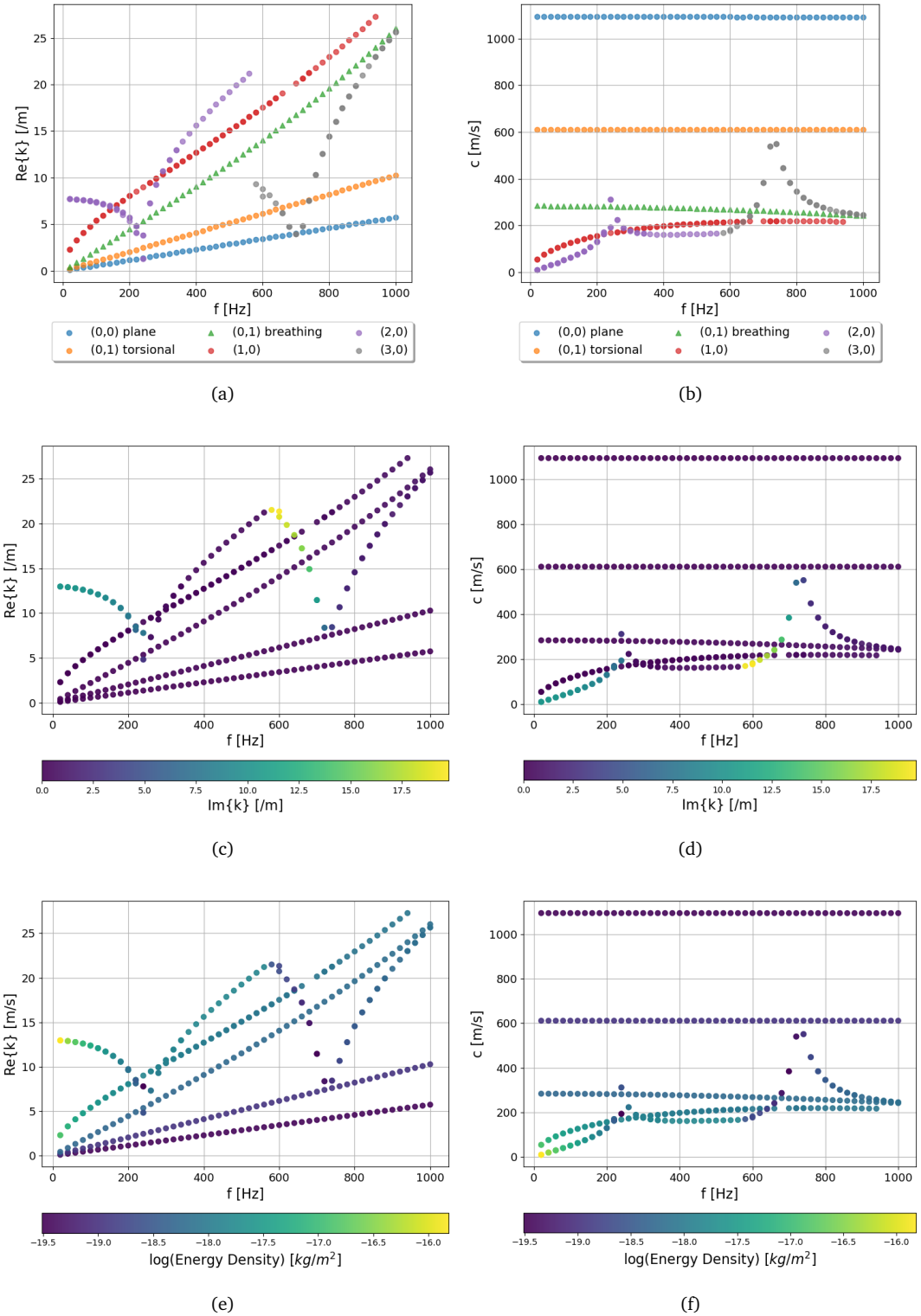

Figure 3.1: The dispersion relations for $f < 1000$ Hz for a 110 mm diameter MDPE pipe showing (a) $Re\{k(f)\}$ and (b) $c(f)$, both labelled by mode, (c) and (d) show $Re\{k(f)\}$ and $c(f)$ respectively coloured by attenuation factor.

Table 3.1: A summary of the pipe properties. Sources for generic values: [194] for sandy soil properties and [195, 196] for water properties. Entries marked with a * were chosen based on generic pipe values.

Element	**Property**	Symbol (units)	Value
Pipe	internal radius*	r (mm)	55
	wall thickness*	h (mm)	10
Fluid (water)	density	ρ_f (kg/m^3)	998
	compressional wave velocity	c_f (m/s)	1482
Soil (sand)	density (bulk)	ρ_s (kg/m^3)	1950±350
	compressional wave velocity	c_s (m/s)	250

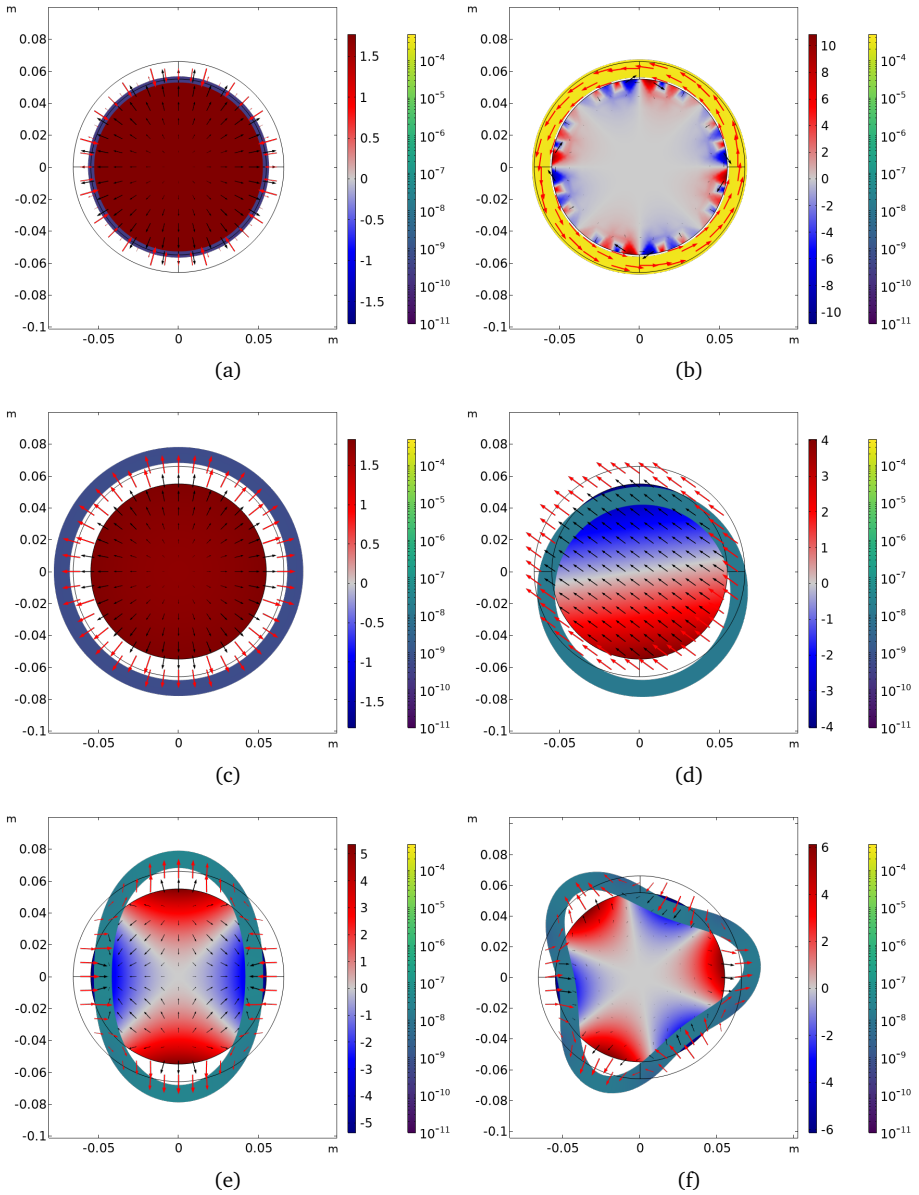

Figure 3.2: Dominant modes in a 110 mm HDPE pipe over the frequency range 0-1,000 Hz. Each of these images has been exported from COMSOL MultiPhysics and shows the pressure inside the pipe in Pa (the scale of which varies between figures), the magnitude of the displacement in the pipe walls in m, as well as showing the shape of the deformation of the pipe walls. The red arrows show the velocity of the pipe walls while the black arrows show the velocity of the fluid. The modes shown are (a) (0,0) acoustic plane wave, (b) (0,1) torsional mode, (c) (0,1) breathing mode, (d) (1,0) mode, (e) (2,0) mode and (f) (3,0) mode.

Material	E (GPa)	ν	ρ (kg/m^3)	η
HDPE	1.0 (0.8)*	0.4	950	0.05
PVC	3.0 (2.4-4.1)*	0.38*	1,400 [a]	0.05
Lead [a]	14 (13-15)	0.44 (0.435-0.445)	11,290 (11,310-11,390)	0.1 (0.065-0.14)
Ductile iron [a]	172 (165-180)	0.275 (0.27-0.28)	7,150 (7,050-7,250)	1.5 (0.6-2.2) $\times 10^{-3}$

Table 3.2: Material properties used in COMSOL model. E is the Young's modulus, ν the Poisson ratio, ρ the density and η the loss factor. Sources: *[198], [a][199]

The modal dispersion curve for such a pipe is shown in Figure 3.1. The legends of Figures 3.1(a) and (b) provide labels for each mode, shown in terms of the wave speed, c, and the wavenumber, k, respectively. c has been calculated as $\omega/Re\{k\}$. Figures 3.1(c) and (d) are coloured by $Im\{k\}$ to show which modes are evanescent, while Figures 3.1(e) and (f) are coloured by the energy density of each mode at each frequency. The energy density has been calculated within COMSOL as the integral across the pipe cross-section of the fluid of [197]

$$\epsilon = \frac{p_{ref}^2}{g\rho_w c^2} \tag{3.1}$$

so as to describe the energy in the the fluid for each of the modes.

Cross-sections of each of these modes are shown in Figure 3.2, where the internal pressure, wall acceleration and wall deformation are shown for each.

Figures 3.1(d) and (f) show which modes dominate the behaviour of the pipe in terms of their ability to propagate with little attenuation and high energy density, and so are of the most interest. Assuming a leak is being detected from some distance away, the most interesting modes are those with a low attenuation factor and a high energy density. It can be seen that the (2,0) and (3,0) modes are evanescent for frequencies less that their resonant frequency (at 250 and 650 Hz respectively), with a low energy density, then are propagating waves for frequencies greater than this. The (0,0) plane wave has a low energy density when compared with the other modes. The (0,0), (0,1) torsional and (0,1) breathing modes all display a constant $c(f)$, making them easier to differentiate within the signal.

The introduction of the (2,0) and (3,0) modes at 250 and 650 Hz add to the complication of the signal, encouraging an analysis at very low frequencies of less than 250 Hz. It should be noted, that based on the pipe diameter of 110 mm and Equation 2.6, the ring frequency is predicted to be 4,280 Hz, well beyond the range shown.

3.1.2 Effect of varying pipe parameters

A similar analysis was conducted for several pipe materials and dimensions, the results of which are summarised in Figures 3.3, 3.4 and 3.5. The material properties used for each pipe material are provided in Table 3.2. When varying the pipe thickness, the pipe diameter was kept at 110 mm. When varying the pipe diameter, the pipe thickness was kept at 10% of the pipe diameter, and for the differing pipe materials the pipe diameter was kept at 110 mm and the pipe thickness at 11 mm.

Neither the pipe thickness nor pipe diameter has a significant impact on the speed of the (0,0) plane wave and the (0,1) torsional wave, with speeds of a consistent 600 and 1100 m/s respectively. The (0,1) breathing mode mode at between 200 and 400 m/s is sensitive to changes in pipe

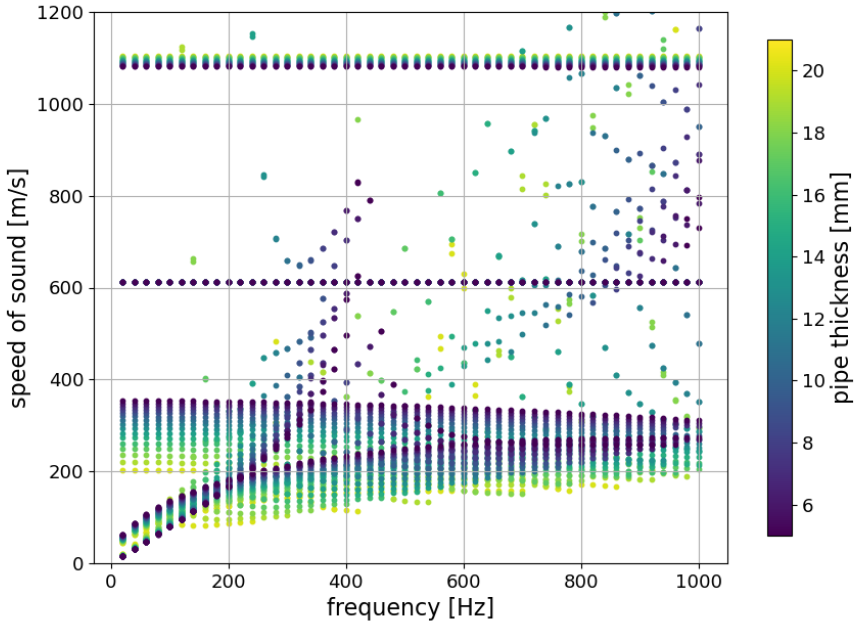

(a)

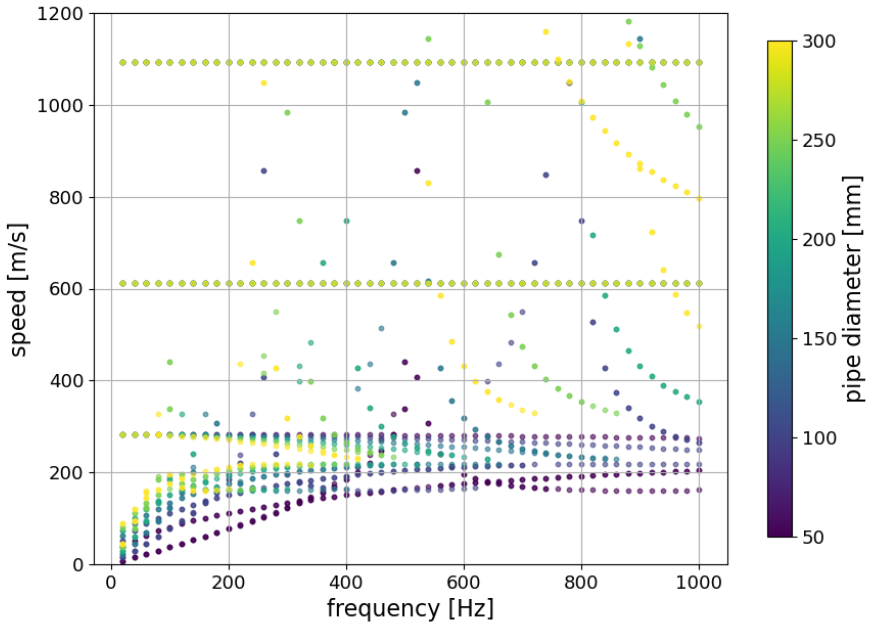

(b)

Figure 3.3: Frequency-wavespeed plots of a 110 mm diameter HDPE pipe, showing the effect of varying (a) pipe wall thickness and (b) pipe diameter. An extended view of (b) is available in Figure 3.4.

thickness, with the speed increasing for thinner pipe walls. This is to be expected since a thinner pipe deforms more readily in the radial direction. Looking at Figure 3.4, it can be seen that this mode has a complex reaction to changes in pipe diameter. The maximum frequency of this mode decreases with increasing pipe diameter, so a 300 mm pipe only supports this mode up to 450 Hz. In addition, the speed of this mode decreases as its cutoff frequency (the maximum frequency at which a mode is supported) is approached. The (1,0) mode decreases in speed with pipe thickness, and has a lower maximum frequency at which it is supported as the pipe thickness increases. It also has a lower maximum frequency as the pipe diameter increases, and the gradient of $c(f)$ at

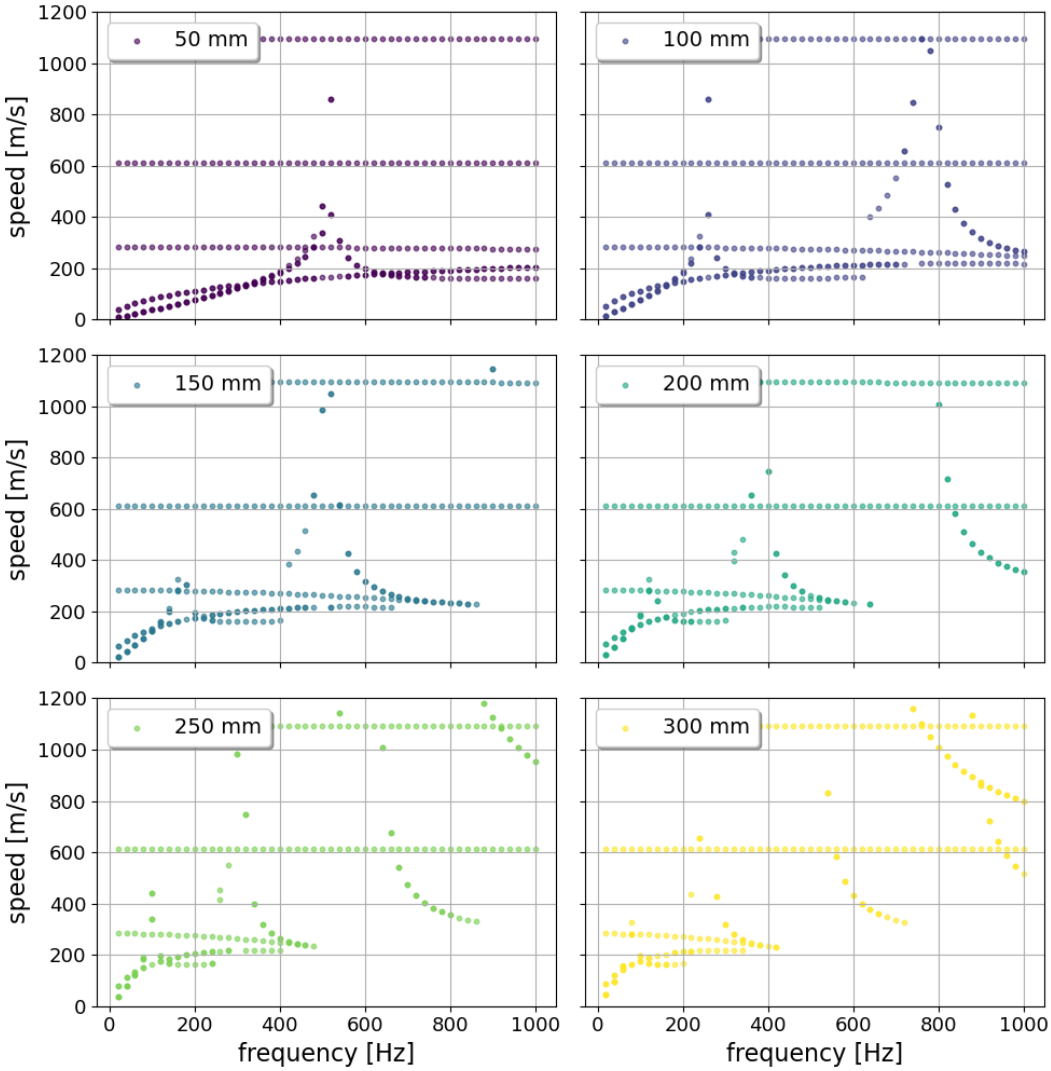

Figure 3.4: Effect of changing pipe diameter on the frequency-wavespeed relation, the diameter of the pipe for each plot is provided in the top-left, the colours of each plot match those from 3.3(b).

low frequencies increases with pipe diameter.

It is difficult to discern the behaviour of the (2,0) and (3,0) modes with changing pipe diameter in Figure 3.3(b): the results for a subset of pipe diameters are separated in Figure 3.4 to make this easier to inspect. With increasing diameter the onset frequency of these modes decreases, such that a 50 mm pipe only has one higher order mode at less than 1,000 Hz, while a 300 mm diameter pipe has five higher order modes present. These two modes show similar behaviour with changing thickness, with the frequency of highest speed of the (2,0) mode (the 'peak frequency') increasing from 620 Hz for a pipe thickness of 10 mm to 840 Hz for a pipe thickness of 6 mm. The (3,0) mode shows a similar decrease in this peak frequency with pipe thickness. This coupling of the behaviour of the pipe thickness (h) and the pipe diameter ($2r$) means many analytical treatments combine these into a dimensionless term of h/r, e.g. [80].

Figure 3.5 shows the effect of changing the pipe material, with Table 3.3 providing a summary of the speed of the three lower order modes for each material. The values shown are for 100 Hz, although the relationship between c and f is flat for these modes. As expected, there is a significant variation in wave speed, with increasing wave speed with material moving from HDPE through PVC

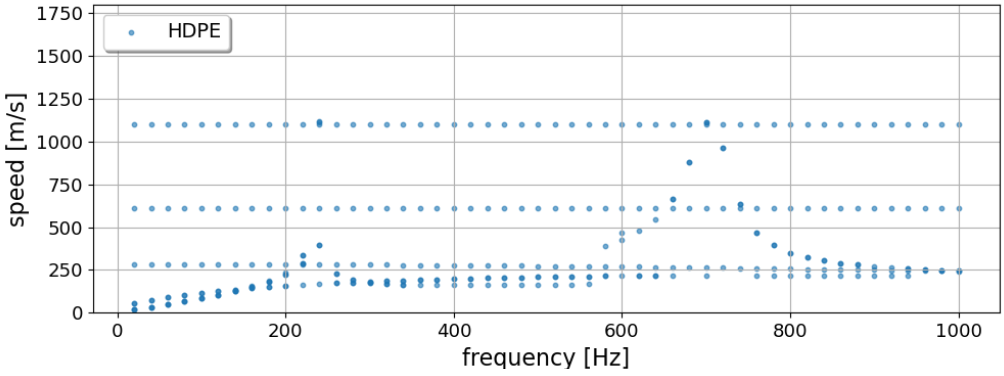

(a)

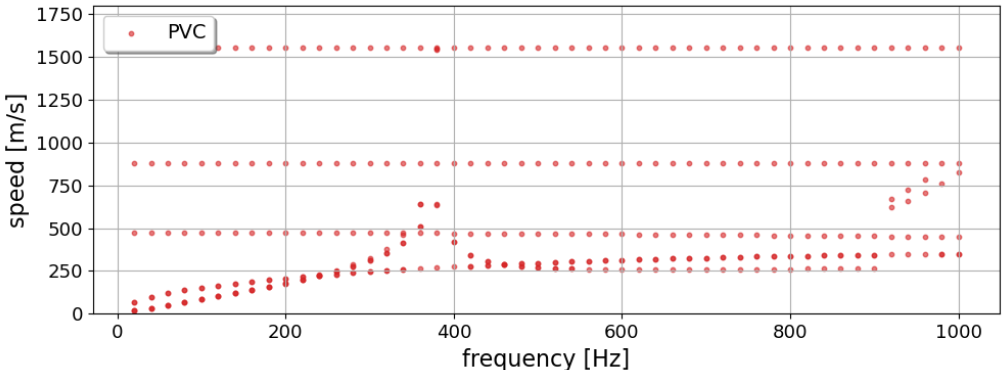

(b)

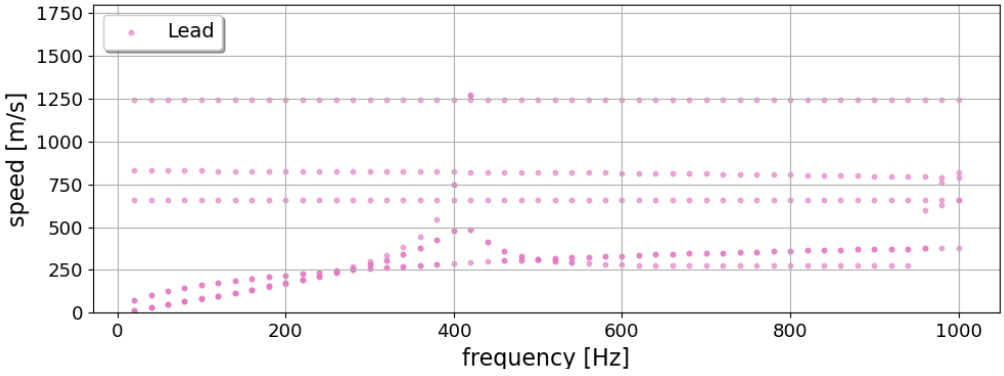

(c)

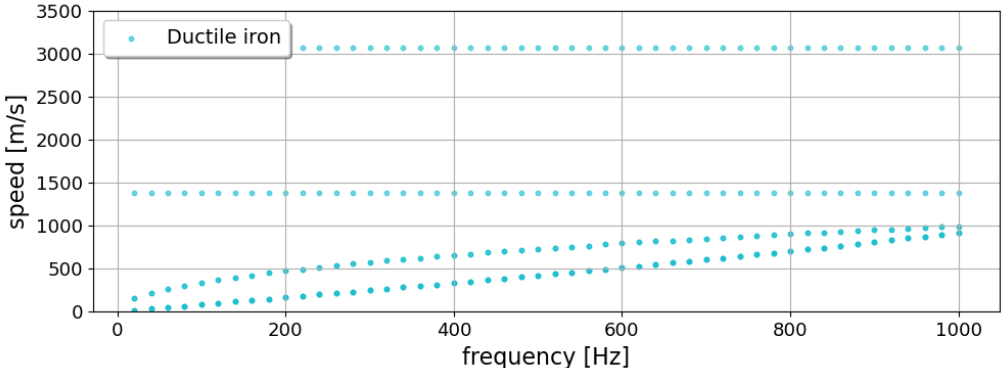

(d)

Figure 3.5: Effect of changing pipe material on the frequency-wavespeed relation, the material in each plot is provided in the top left, note the change in limits for plot (d).

Table 3.3: Wave velocity of the main modes of interest for four materials in m/s at 100 Hz.

mode	HDPE	PVC	Lead	Ductile Iron
(0,0) plane	283	474	659	337
(0,1) torsional	614	882	829	1382
(0,1) breathing	1099	1553	1242	3071

and Lead to Ductile Iron.

For leak localisation in pipes, it is much easier to find the leak location if the speed of sound is consistent both with frequency and between pipes. This analysis has demonstrated the well-established results that variations in pipe material lead to large changes in the sound speed, so unexpected pipe material changes are a significant inhibitor to leak localisation. It has further shown that the (0,0) plane wave mode and the (0,1) torsional mode are least sensitive to changes in pipe diameter and wall thickness. This fact has been previously utilised by [152] whose sensor focuses on the (0,1) torsional wave in the pipe wall. For similar reasons, in-pipe measurements of the plane wave in the fluid would allow for more accurate leak localisation.

Effect of burying pipe

The pipe was 'buried' by added 1 m of sand around the pipe, where the sand was simulated as a linear elastic material, with bulk modulus $5.3 \times 10^7\ N/m^2$, shear modulus $2 \times 10^7\ N/m^2$ and density $2 \times 10^3\ kg/m^3$. These values were based on those used in a similar study conducted by Brennan *et al.* [200]. The outer boundary of the soil was modelled as a free boundary. This means there will be reflections from this surface, however it serves as a starting point for considering the effect of soil on the pipe behaviour. The results of this analysis are shown in Figure 3.6 for ductile iron and HDPE, comparing the results for the below ground, 'buried' pipe, with the previous results for an unburied pipe.

It can be seen that there are a large number of extra modes added for both materials, with the behaviour of these additional modes being less linear in this frequency range than for the unburied pipe. The results for the HDPE pipe are most changed, with the previous modes being completely subsumed by more complex behaviour. The exception to this is at very low frequencies, of less than 100 Hz, where the (0,1) breathing mode is retained at a slightly increased c of 325 m/s. This increase in complexity is caused by strong leakage of energy into the surrounding material due to strong coupling of the soil and plastic.

There is less leakage between the ductile iron and soil due to poorer coupling between the materials. The breathing mode at 1,400 m/s is almost unchanged, with many of the points for the unburied pipe being directly overlaid by those of the buried pipe. The (1,0) and (2,0) modes are more affected by the presence of the soil, inspection of Figure 3.2 shows that these modes have a higher displacement of the pipe wall, which is clearly suppressed by the sand. The (0,1) torsional mode at 3,000 m/s is also significantly affected by the presence of the sand.

These demonstrate the additional complexity of wave propagation in a buried pipe.

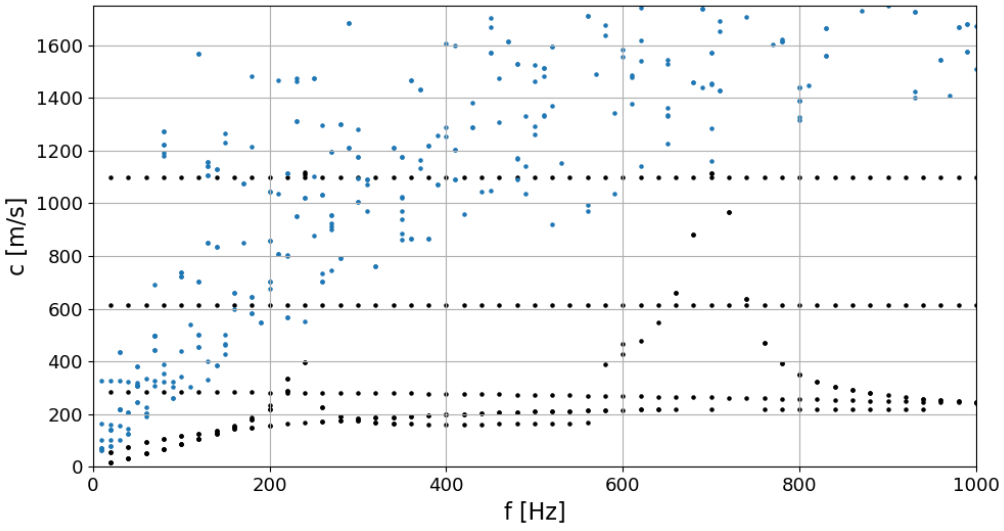

(a)

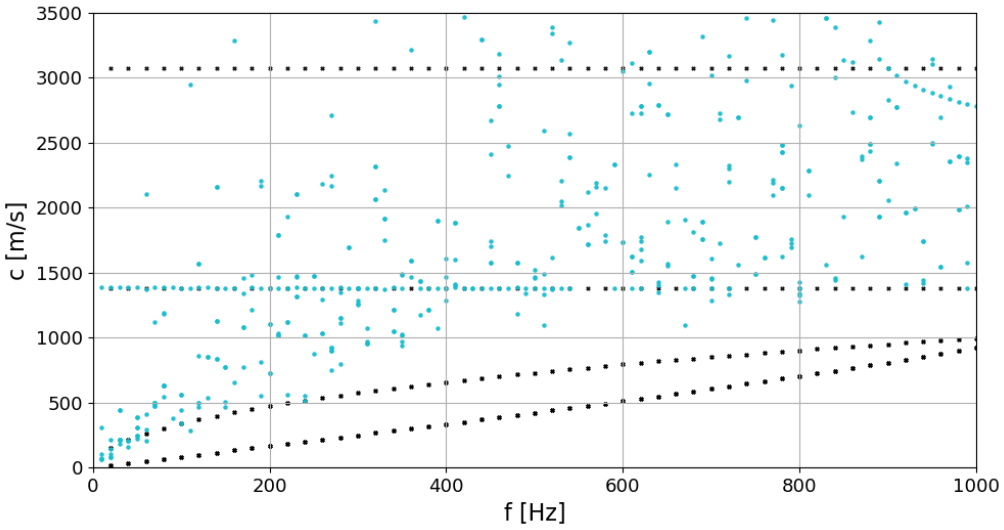

(b)

Figure 3.6: Effect of changing pipe material on the frequency-wavespeed relation for (a) HDPE and (b) ductile iron, when the pipe is surrounded by sand. The black points are for the unburied pipe and match those in Figure 3.5, the coloured points are for the buried pipe. Note the change in limits between the two plots.

3.2 Variations in leak noise in plastic pipes over time

3.2.1 Experimental setup

As a first step towards understanding leak noise in plastic pipes, a leak was set up on a relatively realistic testing rig made of 100 mm PVC pipe, pressurised from mains water to a nominal pressure of 4 bar. Access to the rig was provided by United Utilities and Fido Tech [103]. A schematic of the rig is shown in Figure 3.7(a). A leak was introduced to the system at the point shown in the schematic by drilling a hole and then covering it with a jubilee clip. By loosening the jubilee clip the size (i.e. flow rate) of the leak could be roughly controlled. The leak thus induced is shown in Figure 3.7(c).

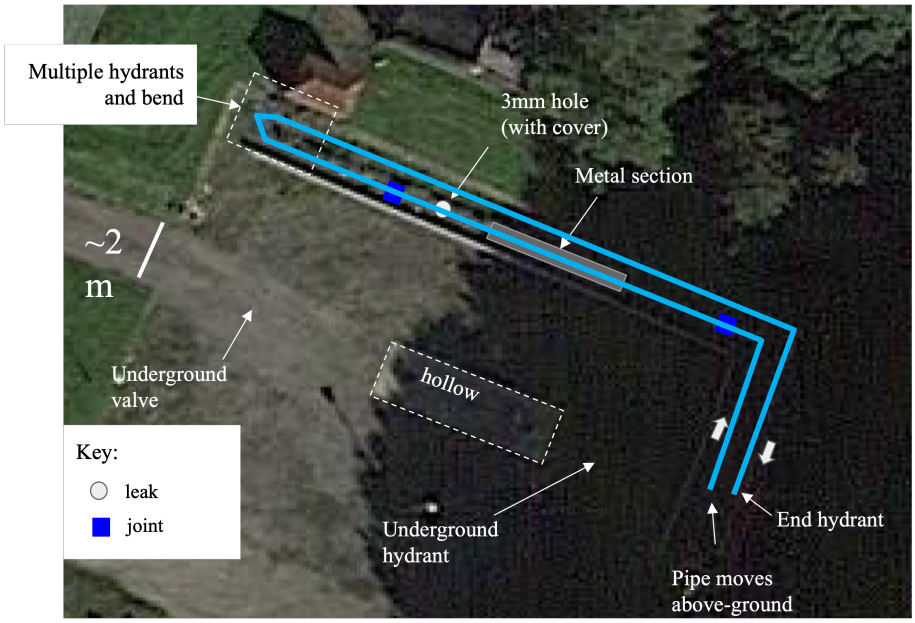

(a)

(b) (c)

Figure 3.7: (a) Schematic of set up at Worthington. (b) picture of pipe section used at Worthington. (c) leak on PVC pipe: the leak is under the jubilee clip in the centre of the picture, the water from the leak is visible coming out to the left of the black spigot, the monoaxial accelerometer used for recordings is shown behind the spigot.

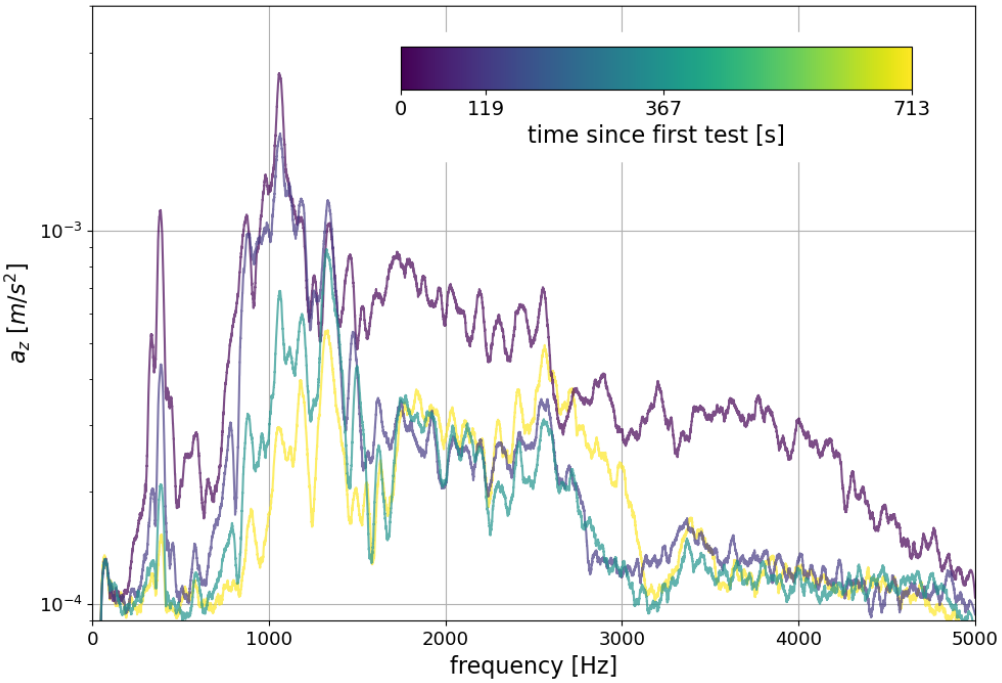

Figure 3.8: Radial acceleration measured 0.05 m from a fading leak. The colorbar shows how the colors relate to time since the start of the test. The data has been smoothed using a 301 point savgol filter.

The leak noise was recorded using a monoaxial accelerometer (PCB 353B04) measuring the radial component of acceleration (a_z). This was connected to a computer recording the output using LabView via a NI DAQ (USB-4431). Full part numbers are provided in Appendix A.

Data was recorded at a sample rate of 12 kHz and each recording lasted 5 s. The accelerometer was located 0.05 m from the leak. The discharge from the leak diminished over time as the back pressure in the pipe reduced, the effect of this on the leak noise was recorded and is shown in Figure 3.7. The data has been filtered using a third order Butterworth filter to between 50 and 5,000 Hz, and smoothed with a 301 point Savitzky-Golay ('savgol') filter [201] to remove very fine detail and aid in comparison. A 301 point filter, corresponding to 60 Hz, was chosen as a balance between maintaining information and clarifying the plot. All data processing here and elsewhere has been achieved using Python.

3.2.2 Results & discussion

The radial acceleration measured 0.05 m from a leak on a PVC pipe is shown in Figure 3.8. The flow rate of the leak diminished across these measurements. While there are similarities between the spectra, for example the peaks at 400, 1,100 and 1,300 Hz, as well as the trend towards higher amplitudes at lower frequencies, there are significant differences. The most noticeable difference in the strong diminution of amplitude of the peak at 1,100 Hz: this is by the far the dominant feature for larger back pressures, but is barely noticeable for the smaller leak.

Based on this information, it is not possible to determine which modes are propagating, since the main modes of interest are frequency-independent. Further data measuring the motion of the pipe in more detail would be required to link this, and the following, leakage measurements with

the modal analysis work conducted in Section 3.1.

This experiment suggested that the amplitude of the acceleration spectra measured in the vicinity of the leak can vary between 0.1-1 $\mathrm{mm/s^2}$ depending upon the hydraulic pressure in the pipe. This information is particularly useful in combination with the numerical data on the mode attenuation presented in the previous chapter because it can guide the choice of the accelerometer sensitivity and signal-to-noise ratio required to detect a typical leak. Calibrated acceleration data for leak signals is difficult to find in the available literature.

It is not known why the back pressure was so unstable, in order to correct this, additional measurements were taken on a more repeatable pipe setup.

3.3 The effect of leak shape on leak noise in pipes

3.3.1 Experimental setup

Measurements were conducted on a pipe loop located at the ICAIR facility [202] at the University of Sheffield. The pipe loop comprises a mixture of 100 and 110 mm diameter HDPE pipes, joined by electrofusion and flange joints. The system can be pressurised using a header tank and pumps, or using a hose pipe. A schematic of the pipe loop is shown in Figure 3.9, showing the section used for this experiment. Section A is a transitionary region of the pipe loop where the pipe goes from above to below ground.

A picture of the above-ground region of pipe section A is shown in Figure 3.10(a). The two protrusions from the pipe are electrofusion tapping points, usually used to join a smaller pipe onto a larger pipe. In this case they have been used as access points to the main pipe loop for adding sensors or other devices to the system. The lower of the two 'ports' visible in Figure 3.10(a) has a hydrophone inserted into the centre of the pipe. The upper 'port' instead has inserts added such that specific shapes and sizes of leaks can be introduced to the system. Pictures of the two inserts used for these experiments are shown in Figure 3.10(b) and (c), with the lower surface of one

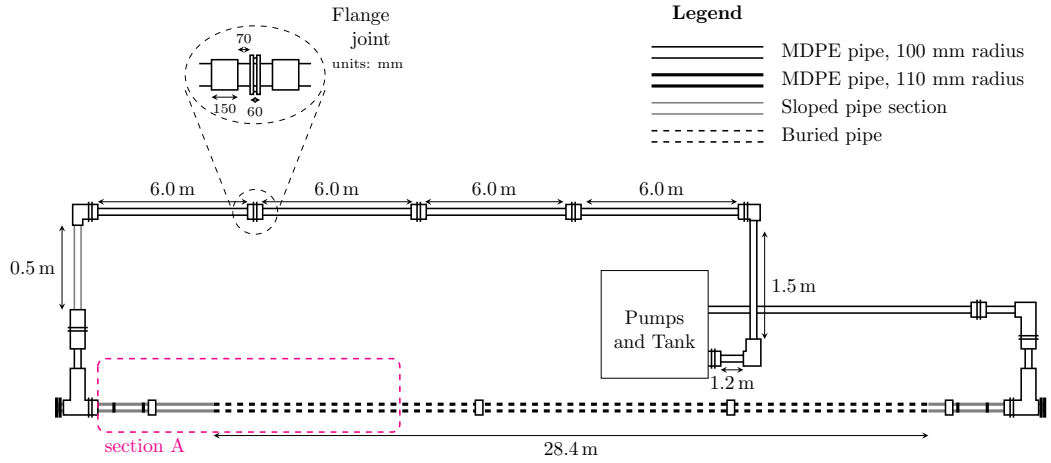

(a)

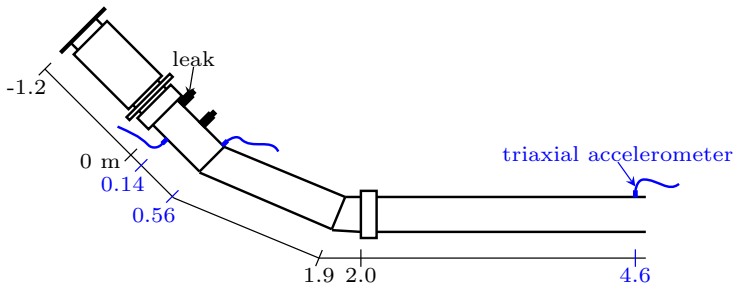

(b)

Figure 3.9: Schematic of pipe loop used for testing, showing (a) a top down view of the entire pipe loop, with the section used for testing circled and (b) a more detailed view of the test section, as viewed from the side, the hydrophones, the three positions for the triaxial accelerometer are all shown, although they were measured one by one.

(a)

(b)

(c)

(d)

(e)

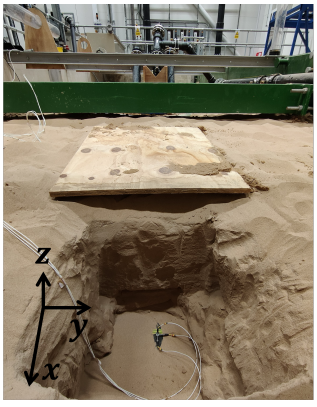

(f)

Figure 3.10: The experimental setup used to investigate the effect of different aperture shapes on the acoustic emission from leaks. (a) a wider view of the testing area, including the catchment system used; (b) the 3 mm leak insert; (c) the 2x2 mm leak insert; (d) the flow from the 3 mm leak when the catchment system has been removed; (e) the attachment method for the triaxial accelerometer; (f) the position of the accelerometer on the buried section of pipe when it is 4 m from the leak, the end of the pipe is just visible in the background of this photograph.

insert shown in (b) and the top view of the other in (c). Figure 3.10(b) is a 3 mm clean hole, while Figure 3.10(c) is two connected 2 mm holes. Each of these holes was drilled in the bottom surface of the insert, with a tapped hole in the top surface such that a screw can be used to stop the leak when required. It was hypothesised that these would lead to quite different leak noises due to the additional turbulence induced by the assymmetry of the '2x2' leak.

The flow shown in Figure 3.10(a) comes from the 3 mm leak. The PVC tube in the photograph is attached purely as a water catchment device, to reduce the impact of the water on the substrate surrounding the pipe, and to allow the flow rate of the leak to be measured. The catchment system has been removed in Figure 3.10(d) to show the flow from the 3 mm leak. During these tests, the pipe loop was pressurised using a hose attached to a header tank, with a pressure head of 8 m. This arrangement was chosen over the pumps due to the large background noise caused by the pumps. The low flow rate of the leaks compared with the volume of the tank, coupled with the short testing times (about 1/2 hour) means the test pressure can be assumed to be constant during testing at approximately 0.8 bar. The flow rate of the leaks was 4.23±0.33 l/min for the 2x2 mm leak and 6.44±0.32 l/min for the 3 mm leak.

The acoustic emission from the leak was measured using a trixial accelerometer (3 x PCB 353B18) attached to the pipe wall using wax. This accelerometer was attached between the two 'port' positions, 0.14 m from the leak as shown in Figure 3.10(e). The accelerometer was oriented such that the x-axis aligned with the pipe axis, measuring the axial acceleration, the y-axis was horizontal, measuring the torsional acceleration and the z-axis was vertical, measuring the radial acceleration perpendicular to the pipe. The accelerometer measurements were processed using LabView on a laptop, with an NI DAQ (USB-4431) connecting the accelerometer to the laptop via USB. The data was collected at a 12 kHz sample rate for 5 s per measurement. For full part details see Appendix A.

3.3.2 Results & discussion

The acceleration spectra for each of the two leak apertures are shown in Figure 3.11, with each axis of acceleration plotted separately. The figure includes background (bg) measurements taken without a leak in the pipe with a background measurement taken immediately before each leak noise measurement and labelled accordingly.

The background measured before each of the leak recordings are similar to each other, in that they are constant with frequency, except for an increase in acceleration in all axes for $f < 200\ \mathrm{m/s^2}$. The background measurement from before the 2x2 leakage recording is consistently higher by approximately $0.1{\times}10^{-}4\ \mathrm{m/s^2}$ (30%). The SNR in these measurements is low, with a maximum SNR of 10 for a_z when $f > 2,000$ Hz and a_x between 2,000 and 2,700 Hz. Given the proximity of the measurement to the leak, this demonstrates some of the challenges in remotely sensing small leaks on plastic pipes.

The acoustic signal emitted by these leaks is complex and tonal, with energy spread up to 4,000 Hz and an acceleration range below 1 $\mathrm{mm/s^2}$. The spectral amplitude of the background noise in the pipe was approximately 0.2 $\mathrm{mm/s^2}$ setting up the threshold of detectability.

The maximum acceleration is in the vertical (z) direction around 100 Hz and the minimum is in the axial (x) direction, with the exception of the large peak in a_x for the 3 mm aperture at 2,500 Hz. There are several points of similarity in the spectra measured at the two apertures. There are very similar peaks in a_z and a_x between 500 and 750 Hz, and some similarities in the peak positions

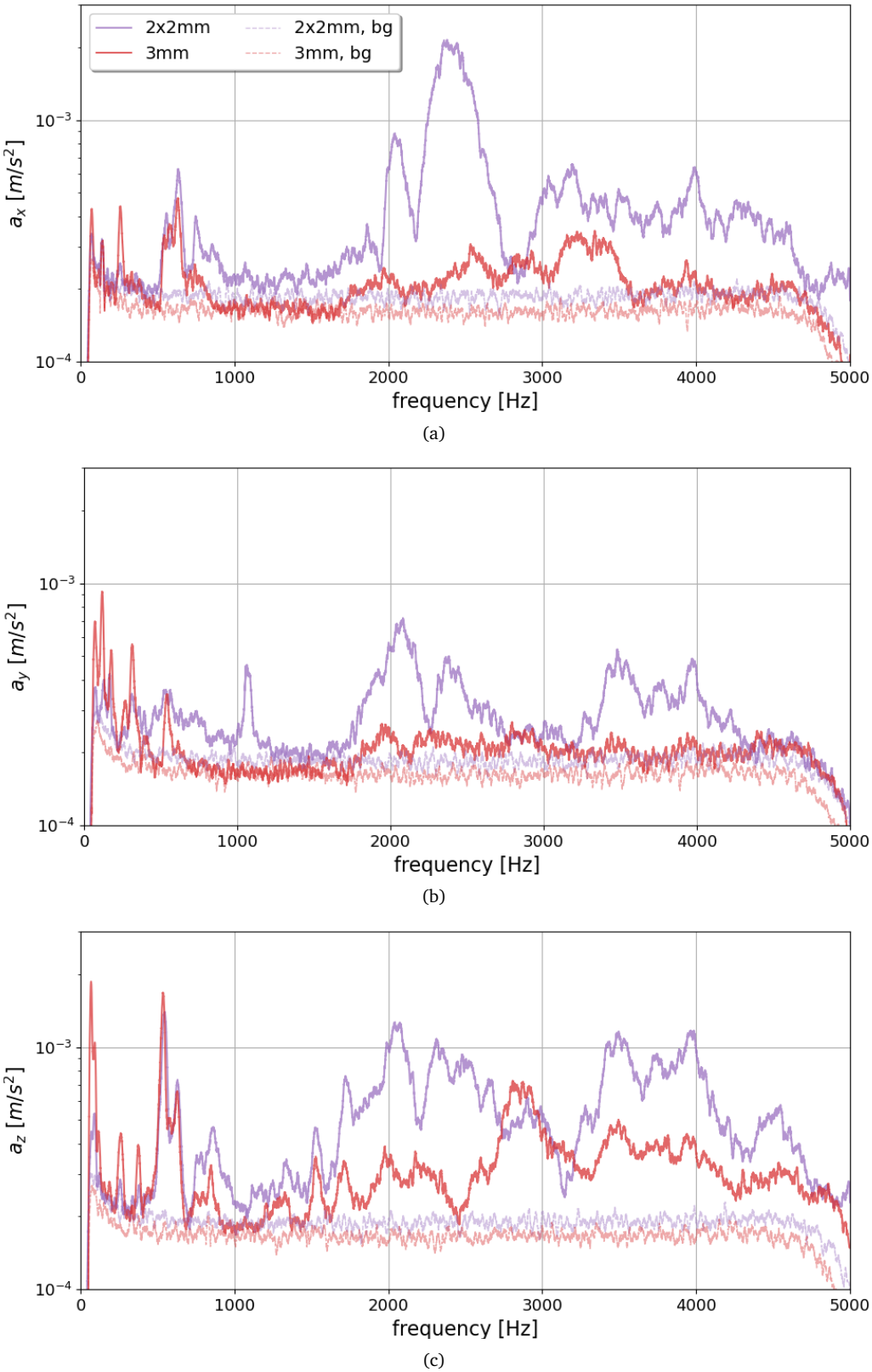

Figure 3.11: The acceleration spectra measured at 0.14 m from a leak, for two different leaks, both on an HDPE pipe. The accelerometer was oriented such that the x-axis was aligned with the pipe axis, the y-axis was horizontal, and the z-axis was vertical, perpendicular to the pipe in the radial direction. Background measurements were taken by closing off the leak immediately prior to each experiment, both of these measurements have been included and labelled with the leak they were measured prior to.

below 500 Hz in the z-acceleration between the two leaks, although the amplitude of these peaks for the 2x2 mm leak is significantly lower. The 3 mm aperture exhibits more features at the lower frequencies, whereas the 2x2 mm leak is generally lower amplitude at these frequencies, with more features at the upper end of the frequency range, including more pronounced features at more than 1,500 Hz.

Based on these results, low frequencies ($f < 1,000$ Hz) display more promise for seeing consistent acoustic responses to a leak source, regardless of the source geometry.

3.4 The effect of attenuation on leak noise in a plastic pipe

3.4.1 Experimental setup

The experiment described above was extended to estimate the attenuation of the leak signals along the HDPE pipe. The experimental setup was the same as described in Section 3.3.1, with additional measurements taken 0.56 m and 4 m from the leak. The recording 4 m from the leak was at a buried section of the pipe and was achieved by excavating a short section of pipe as shown in Figure 3.10(f), with the top of the pipes just visible in the background. The sensor used in this experiment was the same triaxial accelerometer: 3 x PCB 356B21.

3.4.2 Results & discussion

The triaxial acceleration specra measured on the pipe wall at a range of distances from the leak source are shown in Figure 3.12 for each of the leak apertures in the HDPE pipe and for the three axes. It can be seen that there are few similarities in their acoustic spectra save perhaps the peaks at 700 and 2000 Hz. The radial (z) acceleration is largest for each, demonstrating that the accelerometers are mainly detecting the (1,0) breathing mode, with some contribution from the fluid-borne axial (x) waves also being picked up.

For these leaks there is strong attenuation of the accelerometer signals on the pipe, particularly the buried pipe section, such that by 4 m from the leak the spectrum is indistinguishable from the background. The acoustic attenuation is investigated further in Section 4.3.

The specifics of leak spectra was not felt to be a beneficial avenue of exploration at this time, given there is already a significant body of work concerned with characterising the spectra of different leaks, for example in [160] and [77]. Furthermore, it was felt that this kind of classification work was best suited to machine learning work, this is an active field of research, with the main barrier to entry being a lack of data. For example, Yu et al. conducted a study considering the applicability of various machine learning methods for leak detection based on 821 recordings of between 2 and 4 hours, 299 of which contained a leak [169] and Tariq et al. conducted a similar study on 993 recordings [203]. This is a large dataset of leak recordings, but small compared to standard datasets for machine learning. Some researchers have worked around this issue by supplementing their data using simulations, as for example in [204], however this seemed a digression from the main purpose of this thesis.

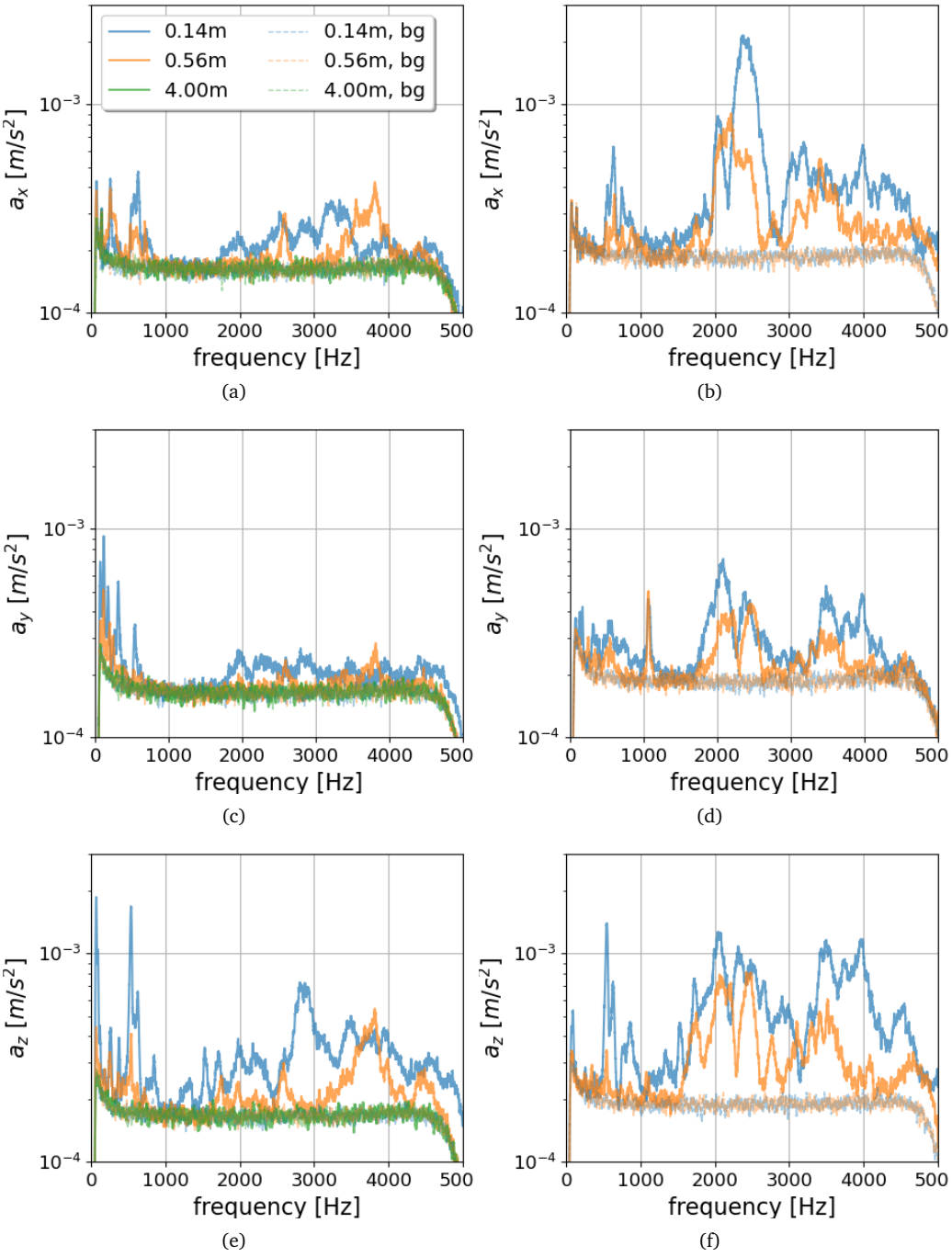

Figure 3.12: Acceleration measured at multiple distances from two different shaped leaks, both on an HDPE pipe. The accelerometer was oriented such that the x-axis aligns with the pipe axis, the y-axis is horizontal and the z-axis is vertical. Figures (a,c,e) show the results for the 3 mm leak, showing the x, y and z components of acceleration respectively, while (b,d,f) show the results for the 2x2 mm leak.

3.5 Summary

This chapter has shown some of the complexities of leak noise propagation in pipes, with a focus on plastic pipes. It has shown experimentally how the sound produced by leaks is highly variable, adding to the difficulties in long-range acoustic leak detection. Modelling work has shown how the pipe dimensions, pipe material and surroundings affect the speed of the low-frequency (<1,000 Hz) acoustic modes.

The acceleration spectrum produced by a leak has been measured, where the leak noise can be seen to extend to 4,000 Hz with several clear tonal components. The maximum acceleration amplitude in the measured spectra was around 1 $\mathrm{mm/s^2}$. The dominant component of the acceleration vector was the radial component. However, the axial and horizontal acceleration components can also be used to detect leak signals in the vicinity of a leak. It has been shown that leak noise rapidly attenuates with distance, with leak noise in a 100 mm HDPE pipe being almost indistinguishable from background noise 4 m away from the leak. The acoustic attenuation has been shown to be frequency dependent for changes in both distance and leak size. The compound effect of this, coupled with the variability in leak spectra by source, would render any leak classification very challenging, since a database of leak spectra would need to be collated with not only the source type changing but also the distance and back pressure. While this could prove interesting, and has been achieved to an extent using machine learning by FIDO Tech [103], a full analysis was considered to form a project in its own right, while the focus of this thesis should be on improved sensors suitable for a robotic platform.

Chapter 4

Investigations of Acoustic Properties of Plastic Pipes

The previous chapter has provided, through numerical simulation and experiments, an introduction to the complexity of wave propagation in water-filled pipes as well as a presentation of the variability of leak noise. In this chapter, the range limitations of existing methods of acoustic leak detection are investigated. This is achieved primarily through experimental measurements of the acoustic attenuation on plastic pipes.

The chapter is split into three sections. The first considers an extension of existing methods to determine the age of pipes acoustically, this is a presentation of published work conducted in collaboration with K. Makris [205]*. The second section considers the best method, as well as the accuracy of methods, for finding the true sound speed in plastic pipes. This was driven by the large errors encountered during the previous experiment, along with anecdotal accounts that the speed of sound is challenging to determine in plastic pipes. Given the importance of an accurate measurement of the speed of sound in determining the location of a leak from acoustic measurements, any uncertainty in this limits the range of acoustic leak detection methods. Finally, attenuation in plastic pipes is considered, including over different features in the pipe network. This culminates in a consideration of the workability of existing logger-based methods of leak localisation in plastic pipes.

It should be emphasised that due to the large difference in material properties between metal and plastic, the findings presented here may not hold for metal pipes. Metal pipes exhibit significantly lower attenuation and as such present a much easier environment for acoustic localisation of leaks using existing methods [9, 181, 206].

4.1 Sonic assessment of physical ageing of plastic pipes

The age of a pipe is the dominant factor in its performance, with older pipes being considerably more likely to fail. This is true for water [207], gas [18] and drainage [21] pipes. For plastic pipes, the focus of this work, older pipes are more brittle and consequently have a lower resistance

*The initial idea of looking to find the age of a pipe from its material properties was some combination of Makris, Langevald, Clemens-Meyer and Horoshenkov. Experimental work on the acoustic pipe measurements was conducted by Makris and myself, with DMA measurements taken by Begum. The modelling work was conducted by Makris and myself. Additional analytical modelling work conducted by Makris is not presented here, but can be found in [205].

to impacts and soil loading [208]. This means more care needs to be taken when inspecting or altering the pipe network in their vicinity. The age of a pipe may not be known from records, and so must be found in-situ. Existing methods used to study aging in thermoplastic materials are often destructive, for example differential scanning calorimetry [208], dynamic mechanical analysis [208, 209] and tensile/torsional creep compliance measurements [210]. For in-situ measurements to aid in pipe maintenance a non-destructive method is essential. Previous work has considered micro-indentation [207] and non-collinear ultrasonics as alternative methods for pipe ageing [211, 212]. However, micro-indentation only provides information about the properties on the surface of the material, while the use of non-collinear ultrasonics requires precise alignment and knowing the acoustic properties of the inspected medium [213, 214]. Finding these to the accuracy required for calculating the age of the pipe has proved challenging within the ultrasonic frequency range [210, 211].

Here, the use of low-frequency acoustics to determine the pipe's age via the storage modulus of its wall material is investigated as an a non-destructive, non-intrusive methodology. Low frequencies were chosen since, as demonstrated in Section 3.1, fewer modes propagate at low frequencies, simplifying analysis. At these frequencies the fluid-borne wave dominates because it attenuates less than other modes in buried pipes and is affected less by joints and fittings [150].

This section will assess the viability of assuming the acoustic properties of a pipe, namely the speed of sound in the pipe that is strongly linked to the pipe wall material storage modulus. The published version of this work [205] achieved this by solving the equations of motion for the problem such that the storage modulus can be determined from the speed of sound. Here similar results are presented using the results of a numerical model to recover the storage modulus. A short summary of the equations of motions from [205] is provided in Appendix C. The results of an experiment aiming to relate the age of a pipe and its acoustical properties are provided along with the estimated error. This is compared with a more direct approach (DMA) and the efficacy of the acoustical approach evaluated.

4.1.1 Numerical model

Alternatively, the problem presented in the previous section can be solved with a numerical model, such as a finite element model. A 2D axisymmetric model of a straight pipe of internal diameter 100 mm was introduced in Section 3.1. In order to consider the effect of changing Young's modulus on the acoustic properties of the pipe, this model has been modified such that the pipe wall material has a range of Young's moduli within the range possible for HDPE, including its variation due to pipe ageing [205]. Table 4.1 presents a summary of the base values of the parameters used in the numerical simulations (this is a reproduction of Table 3.1, with the material parameters of HDPE included).

The results of this analysis are shown in Figure 4.1. Figure 4.1(a) presents the entire frequency-speed plot, showing the effect of the change in the Young's modulus via the colour of the scatter points. The six main modes discussed in Section 3.1 are visible, and it can be seen that these are affected by the variation in E to different extents. It can be seen that there is a clear increase in wave speed with increased Young's modulus for the two main modes of interest (the (0,1) mode with speed around 800 m/s and the fluid-borne (0,0) mode with speed around 1,100 m/s). A more detailed discussion of the modes in this figure has already been covered in Chapter 3. This increase is linear with frequency in this frequency range, making an estimate of E based on c possible from

Element	Property	Symbol (units)	Value
Pipe	internal radius*	r (mm)	44.0±0.5
	wall thickness*	h (mm)	11.0±0.2
	material	-	HDPE
	density*	ρ (kg/m^3)	957.6±1.4
	Poisson ratio	ν (-)	0.40±0.05
	loss factor	η (-)	0.05±0.01
Fluid (water)	density	ρ_f (kg/m^3)	998
	compressional wave velocity	c_f (m/s)	1482
Soil (sand)	density (bulk)	ρ_s (kg/m^3)	1950±350
	compressional wave velocity	c_s (m/s)	250

Table 4.1: A summary of the pipe properties. Sources for generic values: [215] for HDPE properties, [194] for sandy soil properties and [195, 196] for water properties. Entries marked with a * were measured from the experimental setup.

this information, as long as c is known. To aid in the visualisation of this Figure 4.1 has been replotted to show $c(E)$ for $f = 500$ Hz for the two modes of interest in Figure 4.1(b). Based on this it was determined that c is sensitive enough to E that the proposed methodology is viable.

4.1.2 Experimental setup

Two sets of measurements were taken, on two different sections of a pipe loop: an above-ground section surrounded by air and a buried pipe section surrounded by sand. Illustrations of the two sections are provided in Figure 4.2, showing the relative positions of the relevant features and measurement apparatus. The hydrophone mounting for each is shown in Figure 4.3. The pipe loop was situated at the ICAIR facility at the University of Sheffield, in total it is 60 m long, with a straight 30 m section buried to 0.5 m in sand and a return lying on supports above the sand. The pipe properties and dimensions are the same as those shown in Table 4.1, where the density of the pipe material was measured according to ISO 1183-1 [216] and the remaining geometrical properties were measured using a tape measure; the sources of the other parameters are [194–196, 215].

A rubber-tipped impact hammer (PCB 086C03) was used to excite low frequency waves in the pipe. Hydrophones (B&K 8103) connected via a conditioning amplifier (B&K Nexus 2693-0S4) to a data acquisition card (USB 4103) recorded the response of the system. All recordings were performed with a 12 kHz sample rate. The locations of the hydrophones and accelerometers for each of the two pipe sections are shown in Figures 4.2(b) and (c). Full part numbers are provided in Appendix A.

4.1.3 Signal processing

The same signal processing steps were performed on multiple tests conducted as part of this experiment. A representative example is provided here for pipe section B, where the impact hammer was positioned 5.0 m from H0. The following process was applied to the signals from the two hydrophones, the accelerometer and the impact hammer:

1. Record the raw signals $s_j(t)$ where j is the recording for the two hydrophones ($H0$ and $H1$) and the impact hammer (IH).

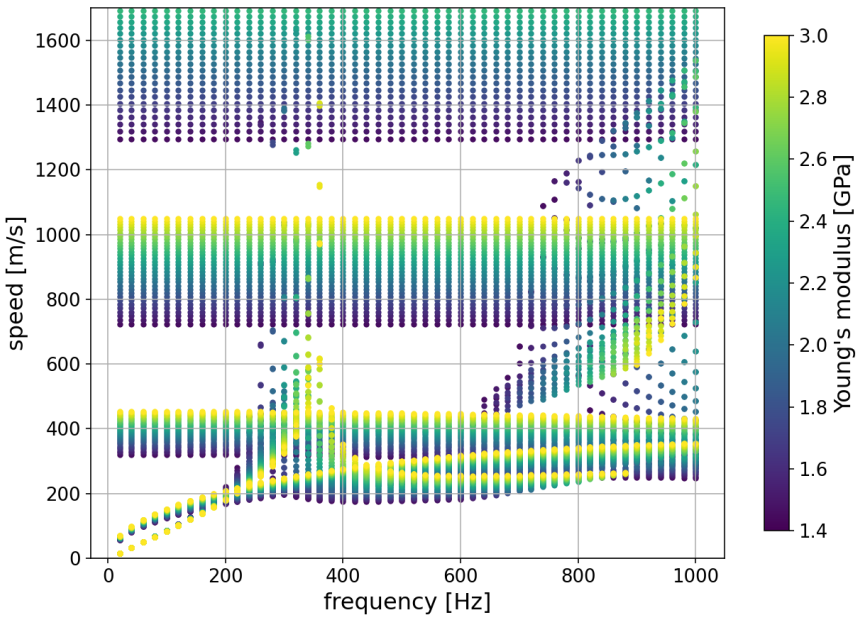

(a)

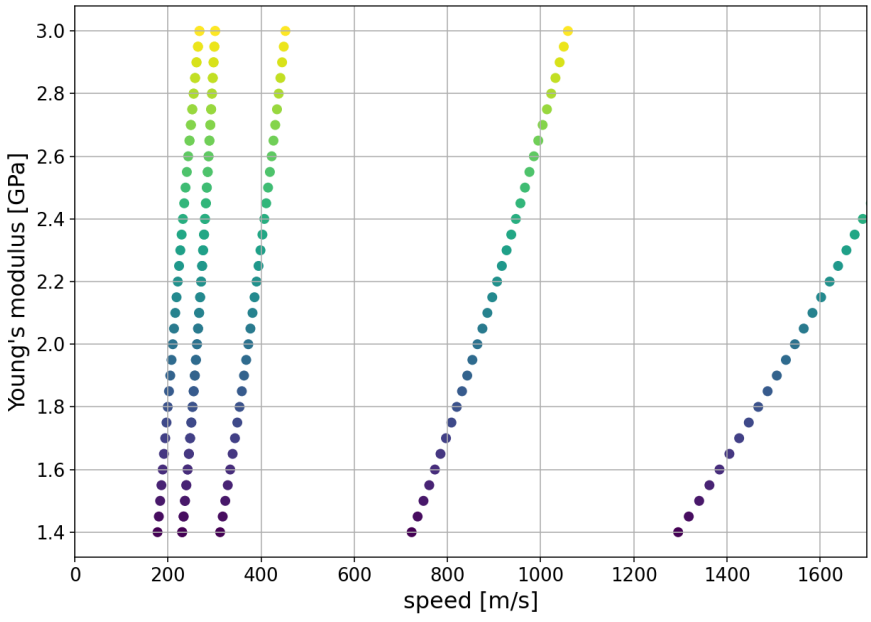

(b)

Figure 4.1: The results of the modal analysis of a 110 mm plastic pipe, showing the variation in $c(f)$ with material property (E) of the pipe. (a) shows the variation for frequencies between 0 and 1000 Hz, (b) shows a slice of $c(f)$ from graph (a) for $f = 500$ Hz.

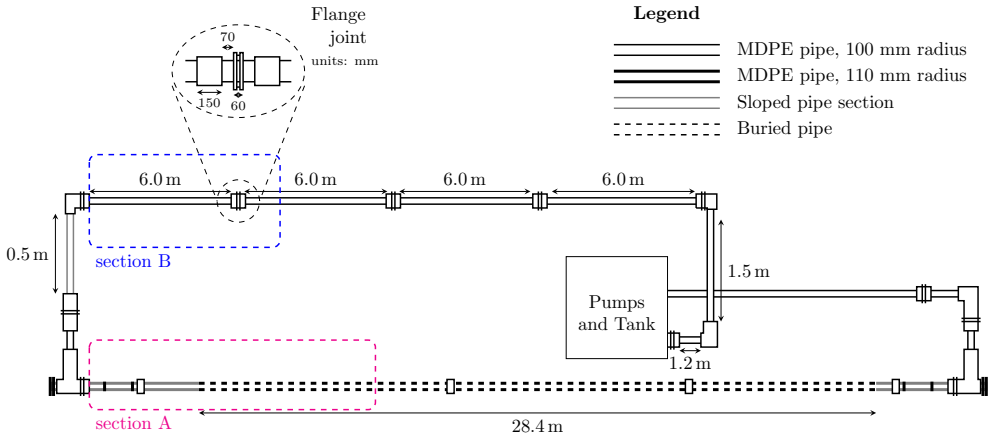

(a)

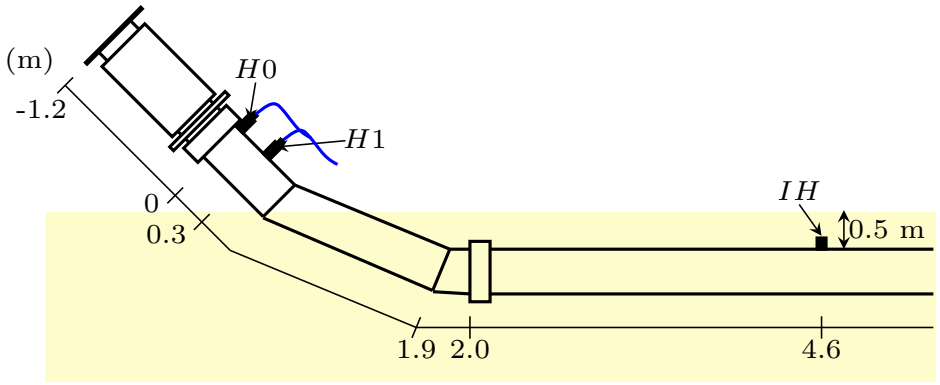

(b)

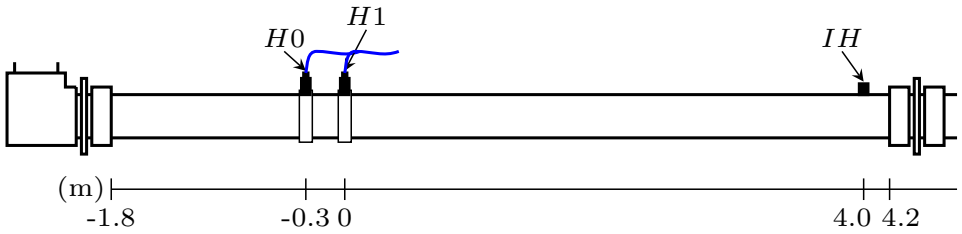

(c)

Figure 4.2: (a) The two pipe sections used for the experiments to determine the age of a pipe from its acoustical properties, (b) a detailed view of section A (below ground measurements) and (c) a detailed view of section B (above ground measurements).

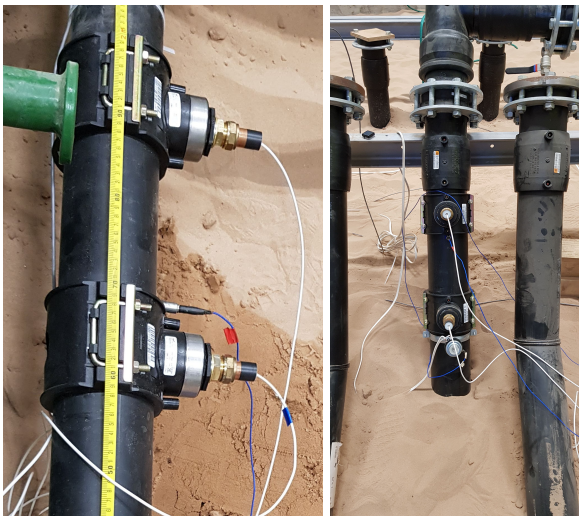

(a) (b)

Figure 4.3: Hydrophone mounting locations for (a) below ground measurements and (b) above ground measurements.

2. Apply a Tukey window [217] to the signals. A shorter window was applied to the impact hammer since the signal of interest was significantly shorter. This is shown in Figure 4.4(a). Both windows are applied relative to the peak of the impact hammer: the impact hammer is windowed from 5 ms before to 5 ms after this peak, the hydrophone measurements are windowed between 10 ms before and 0.2 s after the peak. A tukey window was chosen based on its appropriateness for use with an FFT [218] and the long period over which the original signal is preserved.

3. Apply a filter to the signals. In this case a third order bandpass Butterworth filter, with frequency limits 10-1,000 Hz was used. Here, as elsewhere, the SciPy signal package [107] was used, with the filter generated and applied using the 'second-order section' (sos) framework given its relative numerical stability when compared with other frameworks [219]. The result of this is also shown in Figure 4.4.

4. Inspect the spectrum of the data (calculated using the Fast Fourier Transform) to choose an appropriate frequency range to run calculations over. An example spectrum is shown in Figure 4.5. The spectrum shows that the impact hammer predominantly excites frequencies from 0 to 400 Hz, with the response at the hydrophones extending to 800 Hz.

5. Calculate the speed of sound based on the phase difference between the signals. The signal was more aggressively windowed, as shown in Figure 4.6(a). This acts as a method of peak detection. The speed of sound has then been calculated by considering the phase difference between the combinations of signals using

$$c(\omega) = \frac{\omega d}{\text{Phase}(T_{ij}(\omega))} \tag{4.1}$$

where $T_{ij}(\omega) = \frac{S_i(\omega)}{S_j(\omega)}$ is the frequency response function (FRF) between two signals $s_i(t)$ and $s_j(t)$ recorded by sensors (i and j). $S_i(\omega)$ and $S_j(\omega)$ represent the Fourier Transform of $s_i(t)$ and $s_j(t)$.

The results for $c(f)$ are shown in Figure 4.6(b). It is clear that the sound speed estimates

based on the two hydrophone signals do not make physical sense. This can be explained by a relatively short separation between the two hydrophones. The use of an impact hammer and hydrophone signal leads to a stable speed estimation over the frequency range of 420 ± 20 m/s; the impact hammer and hydrophone hammer have a relatively large (4 m) separation, explaining this stability.

6. Estimate the Young's modulus of the pipe, based on comparison of the measured value of c and comparison with Figure 4.1(b).

These processing steps were carried out for 10 measurements in section B, where the pipe was below ground and 10 in section A where the pipe was above the ground (see Figure 4.2). The average of these measurements was carried forward from step 5 into the calculation of E in step 6.

As a reference point, Dynamic Mechanical Analysis (DMA) was performed to find the viscoelastic properties, specifically the frequency dependent storage modulus, of the pipe material. This is a standard technique, further details of which are given in [205]. A 20 mm x 10 mm x 11 mm sample was milled from a spare length of the same pipe used to construct the main experimental rig. DMA was conducted using a Matravib (VA 2000) analyzer at frequencies between 1 and 50 Hz over a temperature range of -10 to 20^{o}C at 5^{o}C intervals. Time-temperature superposition [220] was used to extend the maximum frequency of the estimations from 50 Hz to 800 Hz. This gives a more standard value of E for the specific pipe used for testing.

4.1.4 Results

The calculated values of c for all these repeats are summarised in Figure 4.8. The results for c calculated based on the comparison between the $H0$ and $H1$ signals have been included for completeness, it was already shown in Figure 4.6(b) that this method does not yield consistent results, which Figure 4.8 corroborates, particularly for the below ground measurements. The results for each hydrophone compared with the impact hammer give more consistent results, with the largest uncertainty in c being 50 m/s for comparing $H1$ and IH below ground and the smallest being between $H0$ and IH below ground, where apart from a single outlier the uncertainty is 15 m/s. The spread of results for the above ground measurements is far more consistent at 30 m/s. This increased repeatability for the above ground measurements makes sense given the improved SNR expected in an above ground pipe. The very low variance (of 15 m/s) in the below ground results based on $H0$-IH is somewhat surprising, especially given the much higher (30 m/s) variance for the $H1$-IH results. Further measurements are required to understand the cause of this.

Combining all of these results leads to a value of c of 470 ± 60 m/s. Based on this value, Figure 4.1(b) gives an estimated value of E of 2.8 ± 0.2 GPa. In contrast, the DMA measurements (Figure 4.7) found the storage modulus to be in the range 1.7 to 1.8 GPa over 150-800 Hz. This indicates a significant over-estimate has been made when measuring the material properties acoustically. Based on this, further work is needed to reduce the error and increase the accuracy of acoustical methods for finding the acoustical properties in buried pipes and relate it to the age of the pipe.

Further work was conducted on the pipe loop, considering alternative methods of finding c, these are presented in the following section, but none achieved a higher level of accuracy than the method used here.

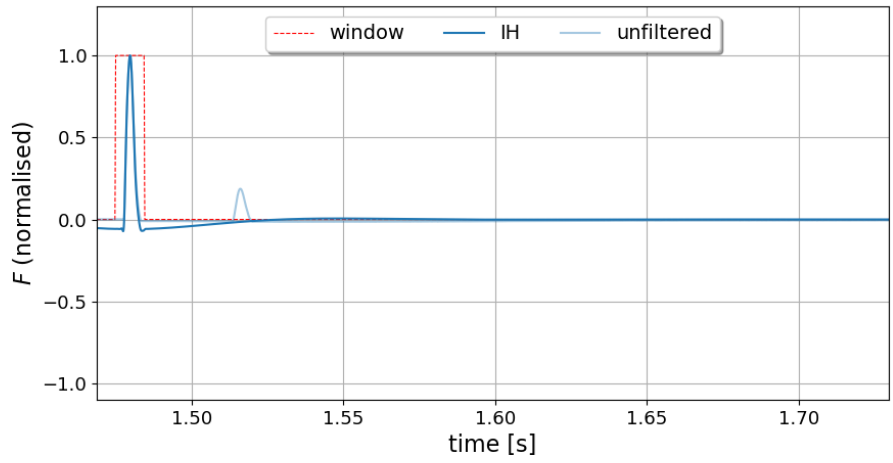

(a)

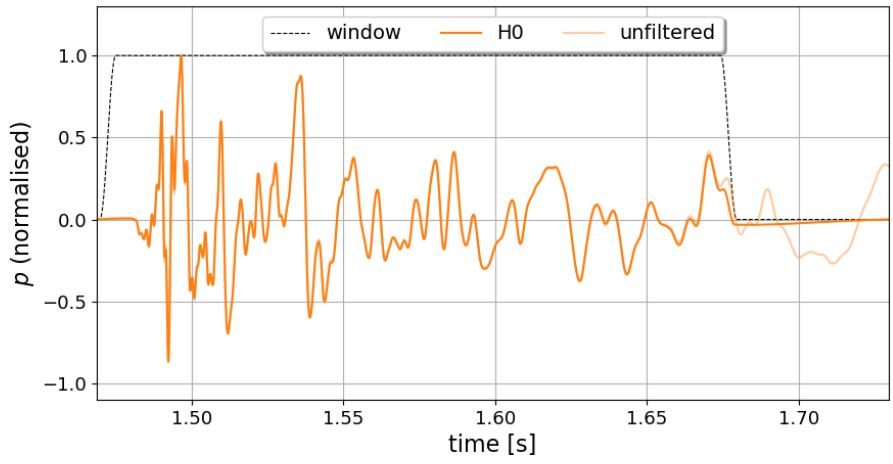

(b)

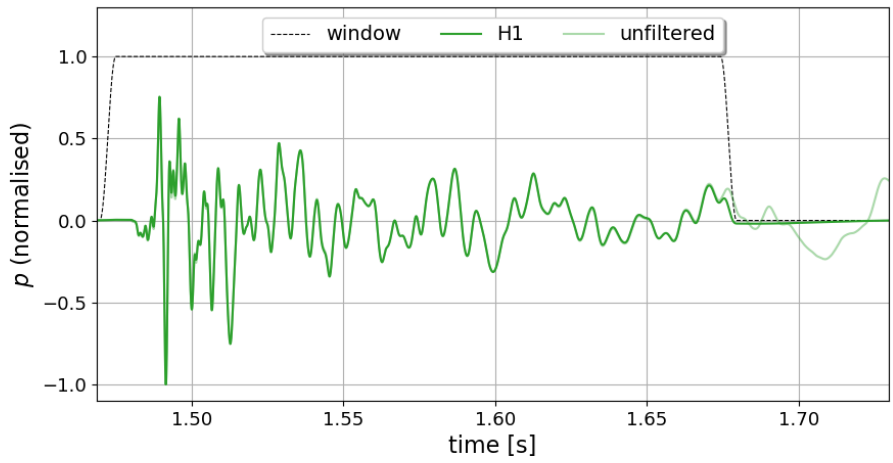

(c)

Figure 4.4: An example of data used to find the pipe material properties, showing the original data and the effect of adding windows and filters. The data, whether pressure, p or force F, has been normalised by the peak of each series over the time range for this plot to aid in comparison. A Tukey window with $\alpha_T = 0.2$ has been applied from -5 ms to 5 ms of the peak for the impact hammer measurements (a) and from -10 ms to 0.2 ms of the peak in the impact hammer measurements for the hydrophone measurements (b, c). The filtered data has been windowed and a third-order, 10-1000 Hz Butterworth filter applied.

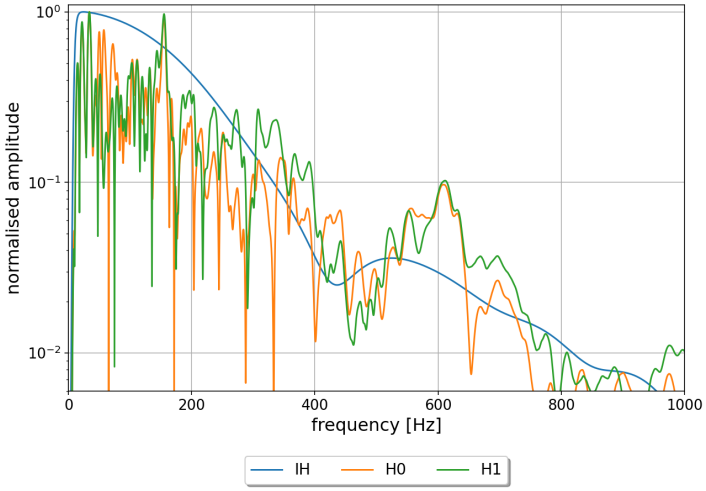

Figure 4.5: The spectra of the example data used to find the pipe material properties. Each data set has been normalised by its maximum value within the range shown to aid in comparison. Truncated at 1,000 Hz due to extreme loss of amplitude for higher frequencies.

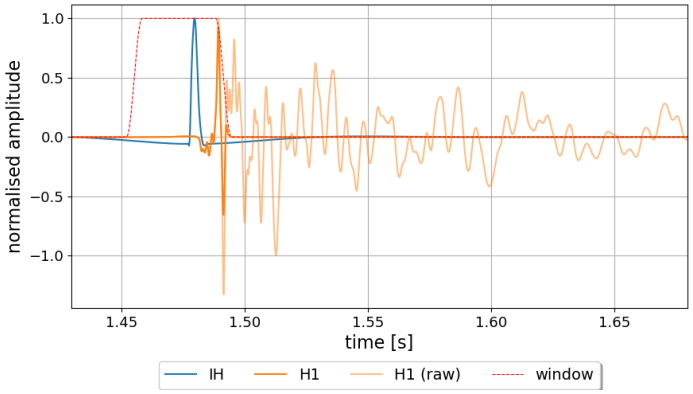

(a)

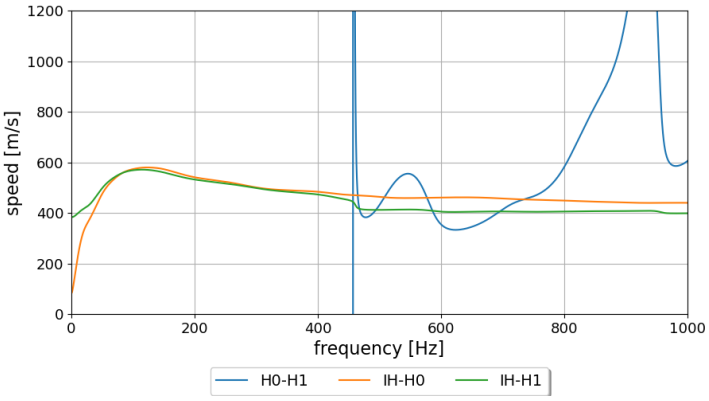

(b)

Figure 4.6: An example of the process for finding the speed of sound from a dataset, showing (a) the windowed and filtered time series and (b) the speed as calculated using the phase difference. Again, the amplitudes of each time series in (a) have been normalised by their maximum value within the time range to aid in comparison between the measurements.

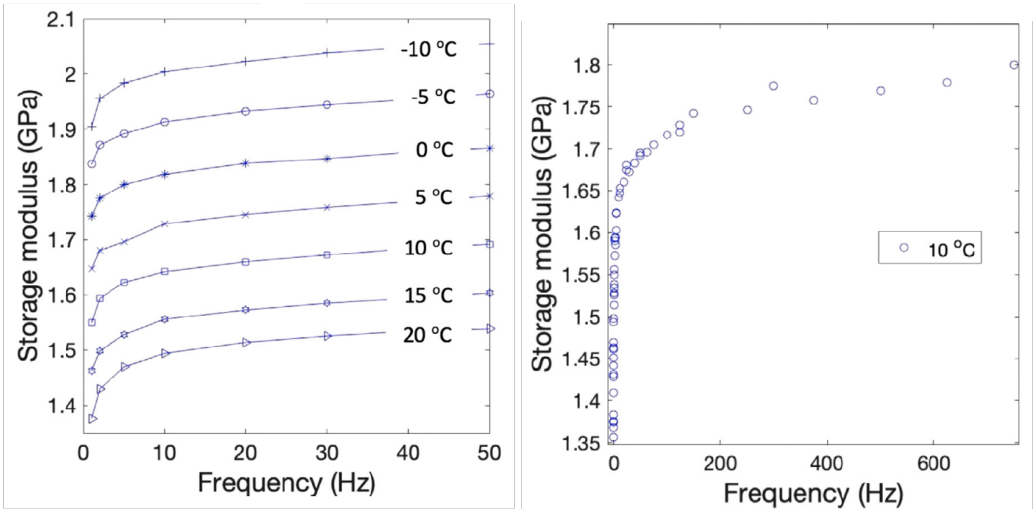

(a) (b)

Figure 4.7: (a) Storage modulus of an HDPE pipe sample as a function of frequency for multiple temperatures as obtained using DMA, (b) the storage modulus calculated for the HDPE pipe sample as a function of frequency after the application of time-temperature superposition for a reference temperature of 10°C. Reproduced from Makris *et al.* 2023 [205].

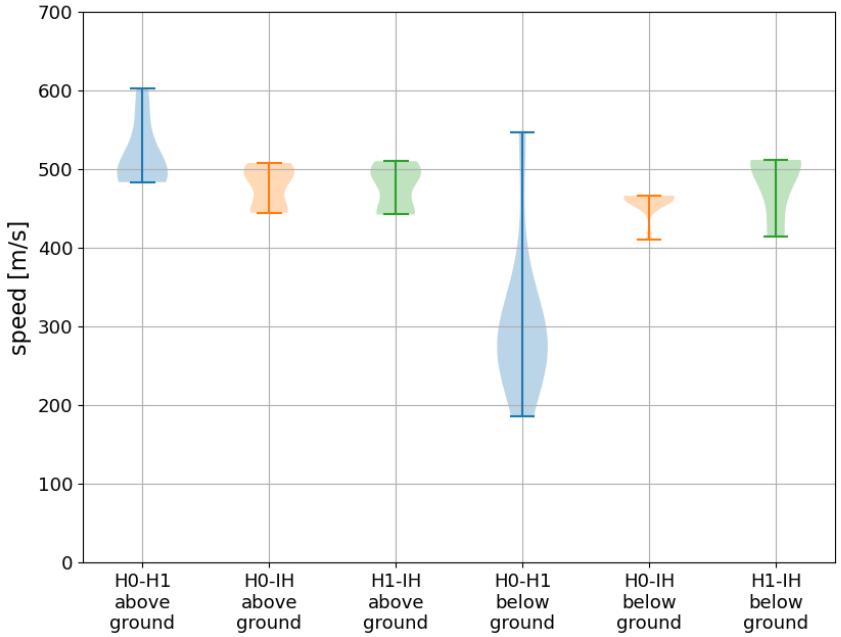

Figure 4.8: Comparison of speed of sound calculated using each combination of measurements above and below ground, showing the range in calculated values over 10 repeats at each location.

4.2 Speed of sound in pipes

As mentioned in Chapter 2, current methods of leak localisation are highly dependent on knowing the speed of sound in the pipe since the leak's location is calculated using Equation 2.13. The previous section has presented some work to determine material properties acoustically. Large errors were found in the acoustic method in comparison with the standard DMA method. This section presents the results of an experiment to find the speed of sound on a straight section of the HDPE pipe with sensors deployed at multiple locations using three different methods for its estimation. These results demonstrate the difficulties in determining the speed of sound in a relatively simple section of a plastic pipe, including a discussion of where these difficulties arise.

4.2.1 Methods for calculating the speed of sound

Three methods were used here to calculate the speed of sound:

1. **From the cross-correlation:** the lag, Δt, between two signals can be found using the cross-correlation, C_{xy} (defined in Equation 2.12. This is a means of finding the travel time between either a source and a receiver or two receivers, at which point $c = d/\Delta t$.

2. **From the phase of the FRF:** if the FRF between two signals s_i and s_j recorded by two sensors (i and j) separated by a distance d, is defined in the frequency domain as

$$T_{ij} = \frac{S_i(\omega)}{S_j(\omega)} \tag{4.2}$$

   then the wave number k is defined by

$$Re\{k(\omega)\} = -\frac{\text{Phase}\{T_{ij}\}}{d} \tag{4.3}$$

   and

$$c = \frac{\omega}{Re\{k\}} = -\frac{\omega d}{\text{Phase}\{T_{ij}\}} \tag{4.4}$$

   as shown previously in Equation 4.4.

3. **From the travel time**: this was suggested to be appropriate for use when an impact hammer is the sound source, in which case the arrival time of the signal is relatively clear since the initial sound is very short. An example of this is shown in Figure 4.11, for a recording of the impact hammer impact and a hydrophone, and for an impact hammer and accelerometer. There is a clear change in the recordings on the hydrophone and accelerometer as the signal from the impact hammer arrives. Once the time difference between the impact hammer and the hydrophone/accelerometer arrival times have been determined, c can again be calculated using $c = d/\Delta t$. This was found to be a problematic method, so is not covered in detail here. Some of the issues encountered are covered in Appendix D.

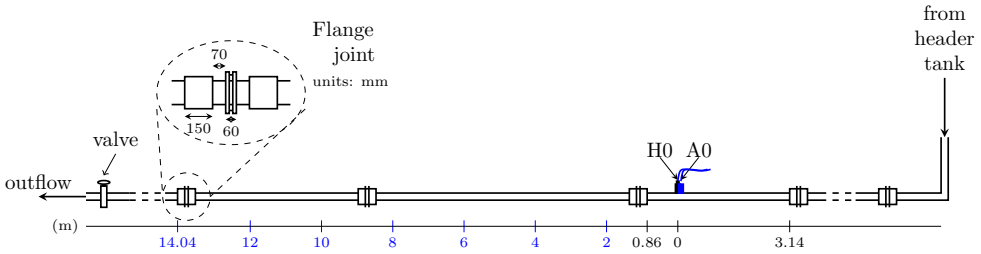

Figure 4.9: Schematic of pipe used for testing methods for calculating c, showing the location of the hydrophone and the accelerometer. The accelerometer is 0.08 m from $H0$. The impact hammer was used to generate an impact at each of the positions shown in blue.

4.2.2 Experimental setup

A schematic of the pipe used for this experiment is shown in Figure 4.9, with pictures of the setup in Figure 4.10. It is a HDPE pipe of diameter 110 mm and wall thickness 10 mm. It is installed above ground, resting on wooden blocks on a concrete base. The pipe wall acceleration was measured using a monoaxial accelerometer, attached such that the measurement was perpendicular to the pipe wall. This was a PCB 353B04 accelerometer, with sensitivity of 10 mV/g, labelled as $A0$. A B&K 8103 hydrophone was inserted into the pipe using similar ports to those described in Section 3.3.1 with the same hydrophones and amplifiers. The impact hammer used was a PCB 086C03. The impact was delivered at 2 m intervals from 2 to 14 m from the hydrophone, i.e. from 2.05 to 14.05 m from the accelerometer. A DAQ (USB-4103) was used to connect these sensors to a laptop, with Labview code used to record the sensor data.

4.2.3 Signal processing

The signal processing steps are provided here for a single example in order to make the process clear, as well as justifying some of the choices made during the process. The time domain results for the accelerometer and hydrophone, unfiltered and unwindowed, are shown in Figure 4.11 for the impact delivered 8 m from the hydrophone. The spectra of these data is shown in Figure 4.12. The time domain results continue for a long period in comparison with the length of the impact delivered. This indicates multiple reflections occur in this relatively simple above-ground pipe setup. Assuming a speed of sound in plastic of approximately 600 m/s and a total pipe length of 30 m, it would be expected for reflections from the end of the pipe to take about 0.1 s to return to the receiver. The signal clearly continues for much longer than this after the impact, and has many features in the intervening time, indicating reflection from various features within the pipe, e.g. joints and supports.

The data was windowed using a Tukey window with $\alpha_T = 0.2$ between 0.02 and 0.5 s, then it was filtered using a 3rd order bandpass Butterworth filter. A selection of frequency ranges were applied, between 25 and 1,000 Hz, the merits of each are discussed shortly. The speed of sound was calculated using each of the three methods listed in Section 4.2.1.

An example of the cross-correlation between the traces is shown in Figure 4.13 for the data between 0.02 and 0.5 s. The maximum of the cross-correlation indicates the point at which the signals are most similar, so should be the point at which the impact is received, taking the time delay of this point and dividing it by the separation of the two signals should give the speed of

(a)

(b)

Figure 4.10: Pictures of the experimental setup used for calculating c. (a) shows the length of the pipe rig, with the empty hydrophone ports in the foreground, (b) shows the hydrophone and accelerometer attachment.

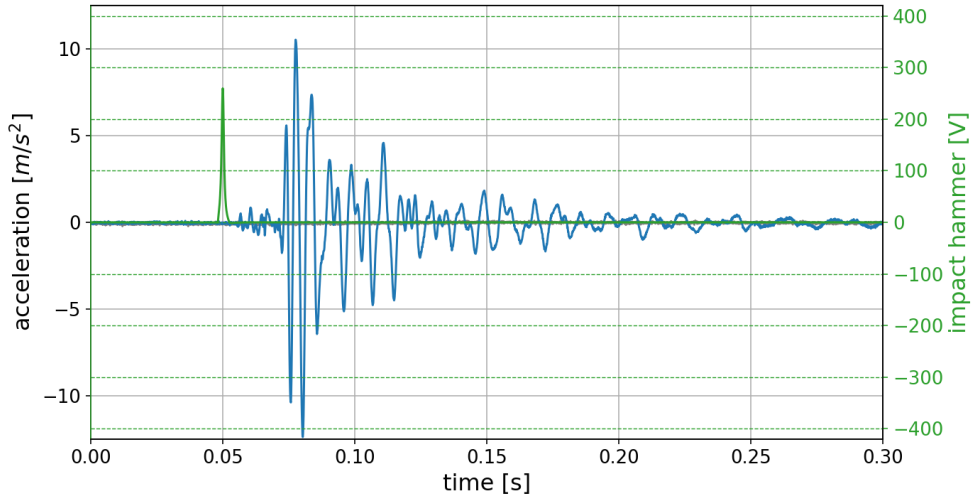

(a)

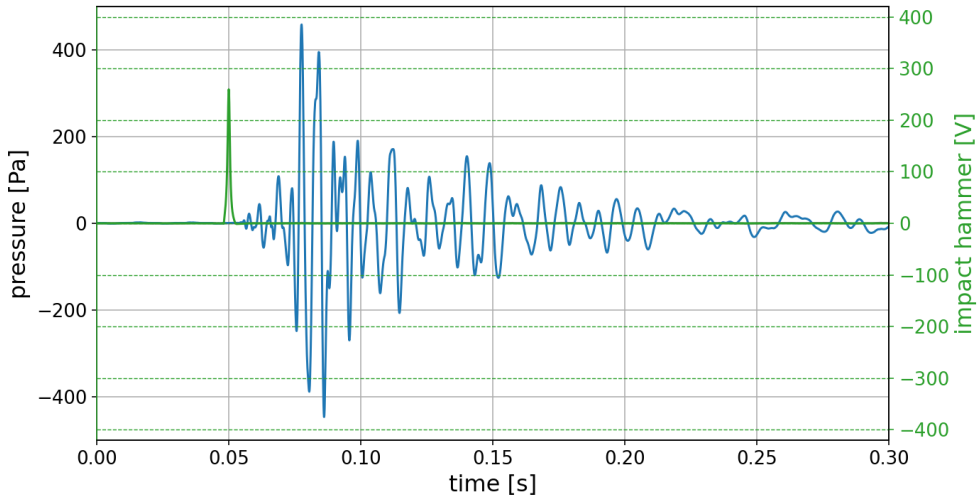

(b)

Figure 4.11: The recording on the (a) accelerometer and (b) hydrophone for to an impact delivered at 8 m from the hydrophone. The impact hammer signal is shown in green on both graphs, with the corresponding scale on the right hand axis.

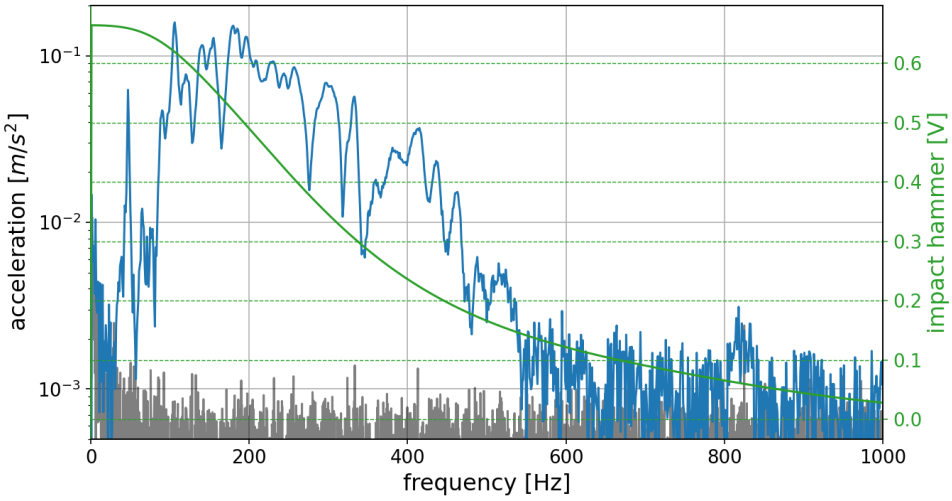

(a)

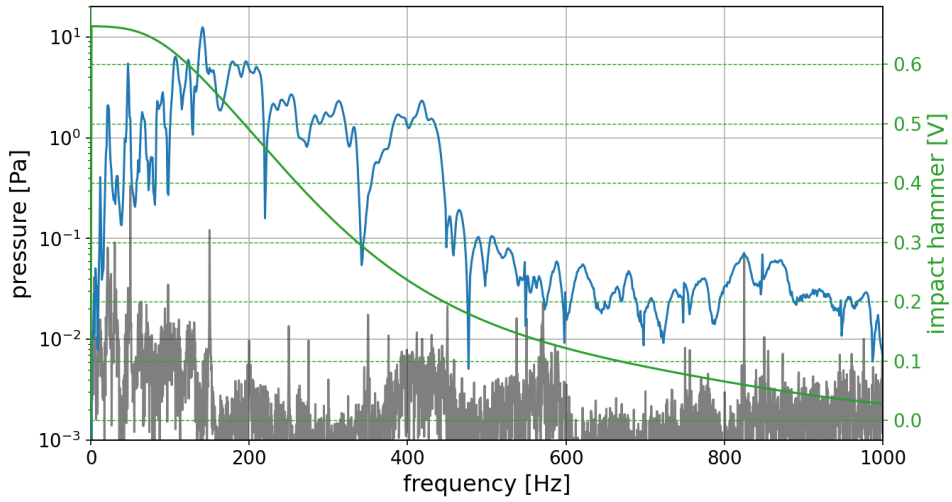

(b)

Figure 4.12: The (a) acceleration and (b) sound pressure spectra corresponding to the time series shown in Figure 4.11. The impact hammer signal is shown in green on both graphs, with the corresponding scale on the right hand axis. The background noise spectra are shown in grey.

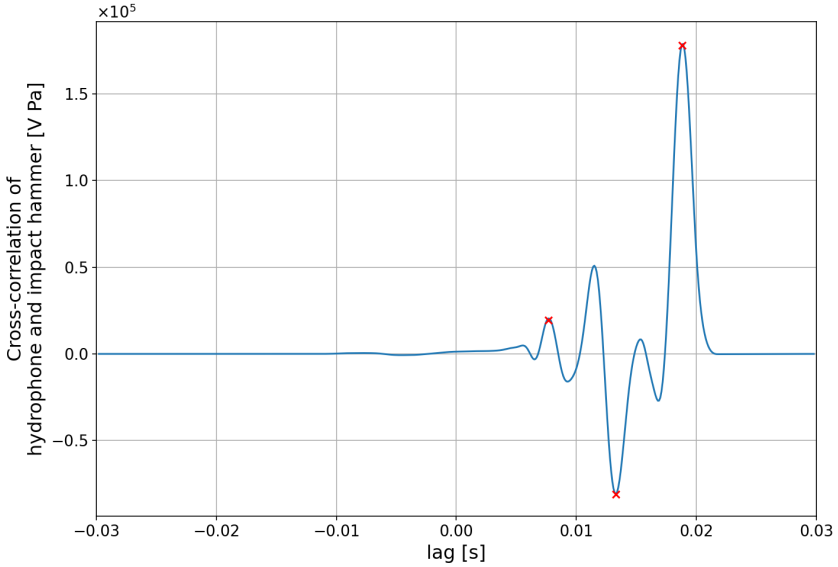

Figure 4.13: Example of finding speed of sound from cross-correlation. This is the cross-correlation between the impact hammer and hydrophone recordings for the impact 8 m from the hydrophone, with the three peaks of interest highlighted.

sound. As an example, here three peaks have been highlighted: the first peak, the largest peak and the peak that gives the most sensible answer. These occur at $\Delta t = 0.00768, 0.188, 0.0133$ s, giving values of c of 40, 1040 and 600 m/s respectively. This result is discussed further in Section 4.2.4 when the results for all datasets are presented.

An example of the process for finding the speed of sound from the phase difference between the signals is shown in Figure 4.14. Figure 4.14(a) shows the short window applied in order to focus on the region of interest in the recorded signal. This segment of data was then converted to the frequency domain using a Fourier Transform and converted to the phase difference shown in Figure 4.14(b). The sound speed was calculated using Equation 4.4, the results of this are shown in Figure 4.14(c). A single value for c over the frequency range 200 to 1,200 Hz was calculated as the average of Figure 4.14(c), with the error as the standard deviation. For this example data set this leads to $c = 480 \pm 40$ m/s from the acceleration and 650 ± 50 m/s from the pressure.

4.2.4 Results

The methods demonstrated in the previous subsection were applied to data filtered using a band-pass filter between a range of frequencies. It was hoped that this might allow the mode shapes to be seen, including ensuring the correct modes are being measured given that the two modes of interest here have constant $c(f)$, c.f. Section 3.1. The values of c calculated for each method with each filter range are shown in Figure 4.15 for each method plotted against the central frequency of the filter applied. The frequency bands used are provided in Table 4.2. The variation in length of filter are to ensure a stable response; more filters than this were tested, these give the most sensible results. The errors in these measurements were calculated across three repeats, with the error for the phase difference measurements being found by combining the error on each individual measurement, while that of the cross-correlation was simply the range of values found across the repeats.

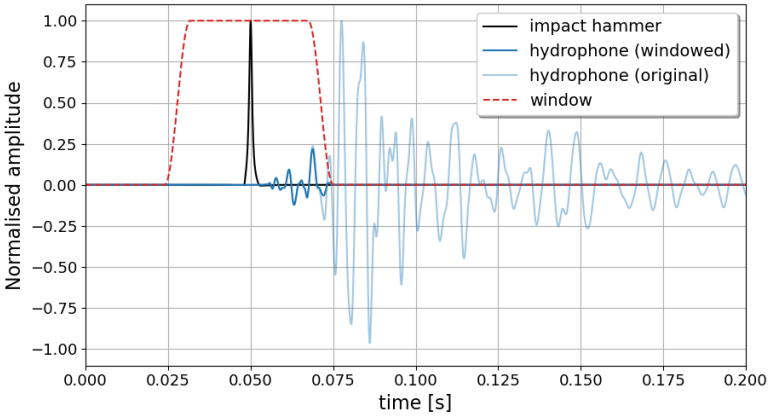

(a)

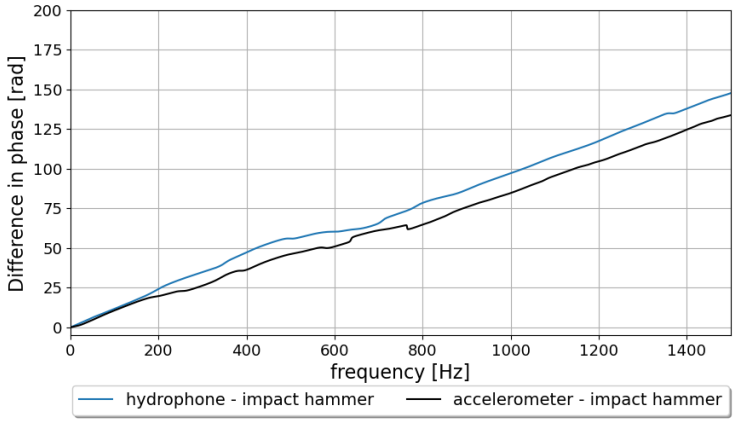

(b)

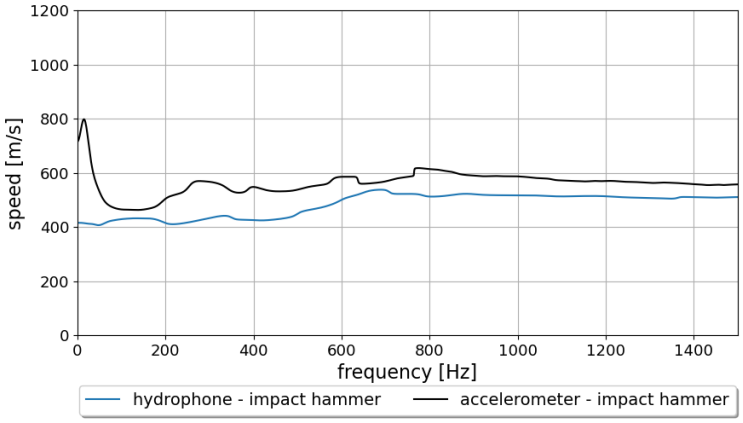

(c)

Figure 4.14: Example of process for calculating speed of sound from the phase difference, showing (a) the original signal in the time domain, (b) the phase difference between the two signals and (c) the speed of sound as calculated for the two signals. This data has not been filtered.

Table 4.2: Frequency ranges used to filter impact hammer measurements. The unfiltered data has been plotted at 0 Hz in order to allow comparison with the filtered data on the same graph.

central [Hz]	0	100	150	200	250	300	350	400	450	500	600
lower [Hz]	None	25	75	125	175	225	275	325	375	400	400
upper [Hz]	None	175	225	275	325	375	425	475	525	600	800

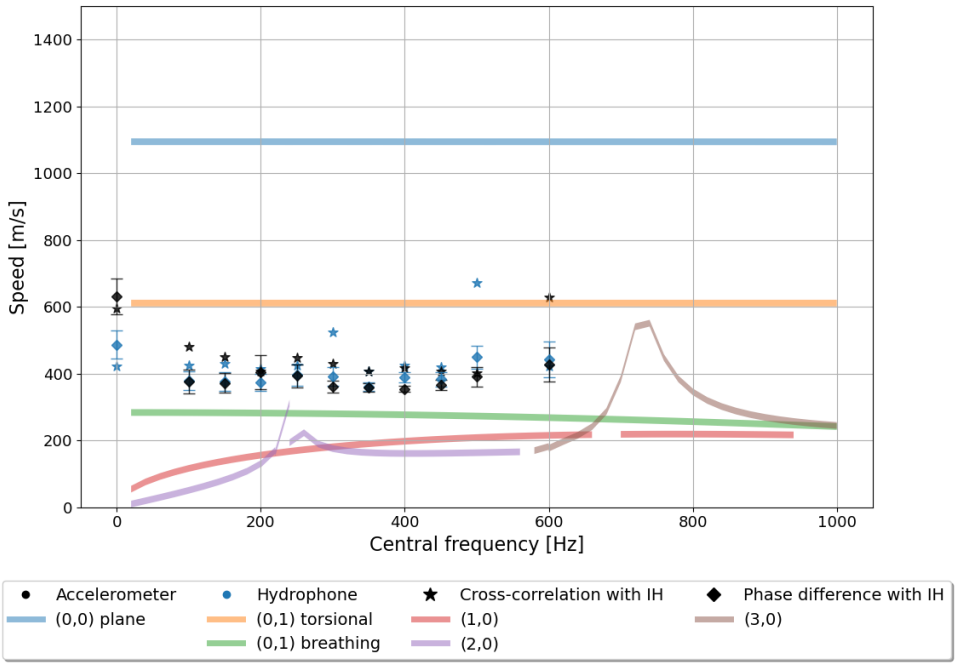

Figure 4.15: A comparison of the speed of sound calculated for an example dataset with the impact 8 m from the hydrophone. The speed of sound is plotted against the central frequency of the filter applied to the data for an array of filters, the exact frequency ranges are provided in Table 4.2. The shaded regions show the predicted values of c from Chapter 3, coloured by mode type as per Figure 3.1.

It can be seen in Figure 4.15 that the results for c calculated using the cross-correlation and phase difference give consistent results to within 50 m/s for $f < 500$ Hz. At frequencies of 500 Hz or greater there is more variability in the results, particularly for the accelerometer measurements. This is reflected in the larger values of c found for the unfiltered data (shown in the figure at 0 Hz). A comparison with the predicted values from Section 3.1, shown as the shaded regions in Figure 4.15, does not identify which mode is being observed: it could be either the (0,1) torsional mode shown in orange or the (0,1) breathing mode shown in blue. Consideration of Figures 3.3 and 4.1, which show the effect of changing the pipe dimensions and material properties respectively, indicates that the Young's modulus used to model the HDPE here may have been an under-estimate. The variations in pipe dimensions (Figure 3.3 cannot explain the discrepancy since changing the pipe diameter has very little impact on these two modes over the frequency range of interest, while the pipe thickness would need to be unbelievably thin for the (0,1) breathing mode to increase to 400 m/s. Figure 4.1 shows that increasing the Young's modulus to 2.8 GPa brings the breathing mode up to a speed of sound of approximately 400 m/s. As discussed previously in Section 4.1.4, this contradicts the value of E measured for this pipe using DMA, which E to be 1.8 GPa.

To investigate the variability in these methods of calculating c further, the speed of sound was calculated using the same method at a range of distances. This is shown in Figure 4.16. The data was filtered between 125-275 Hz since this seemed to lead to some of the lowest errors in Figure 4.15. The calculated values of c found using the phase difference between the impact hammer and the accelerometer/hydrophone are shown in Figures 4.16(a) and (b) respectively. These show a reassuring lack of variability across the different measurement locations, with none of the calculated values of c differing by more than 50 m/s. In contrast, the calculated values of c

found using the cross correlation between the impact hammer and the accelerometer/hydrophone (Figures 4.16(c) and (d) respectively), show values of c varying from 300 to 1,000 m/s; a degree of variation which make them unsuitable to the task. It is mainly at larger distances that the calculated values deviate from the 400 m/s calculated using the phase difference. This will be due to the lower signal to noise ratio as the attenuation of the signals increase.

Even using the phase difference, which here calculated c as 400$\pm$50 m/s, could lead to difficulties in leak localisation. For two measurements separated by 100 m, with a time delay between measurements of 0.1 s, if c is 350 m/s Equation 2.13, the leak is predicted to be 33 m from the first measurement, whereas if c is 450 m/s the leak is predicted to be 27 m from the first measurement. Given that leaks need to be located to within 2 m for a successful dig, this uncertainty in the the measured value of c is not acceptable.

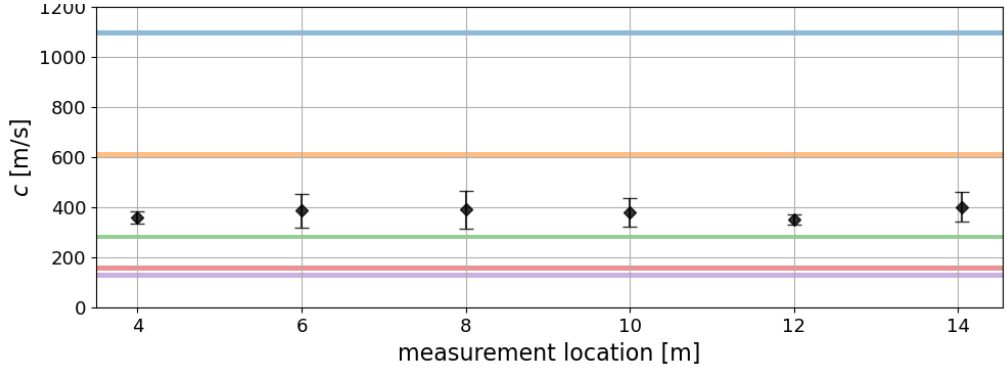

(a)

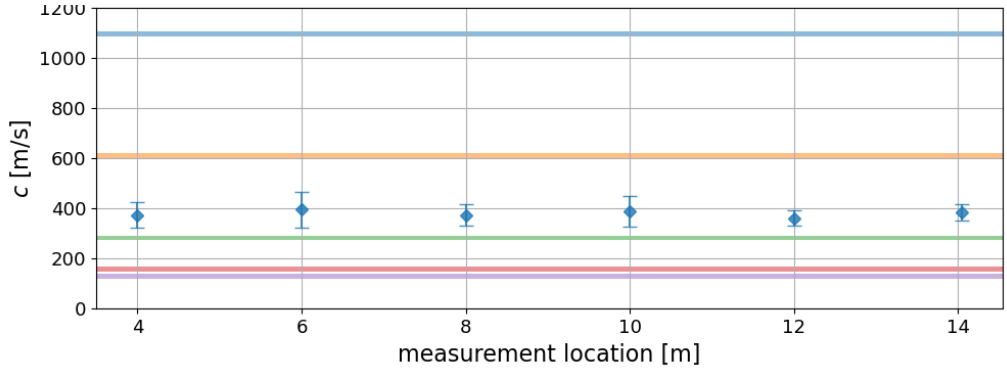

(b)

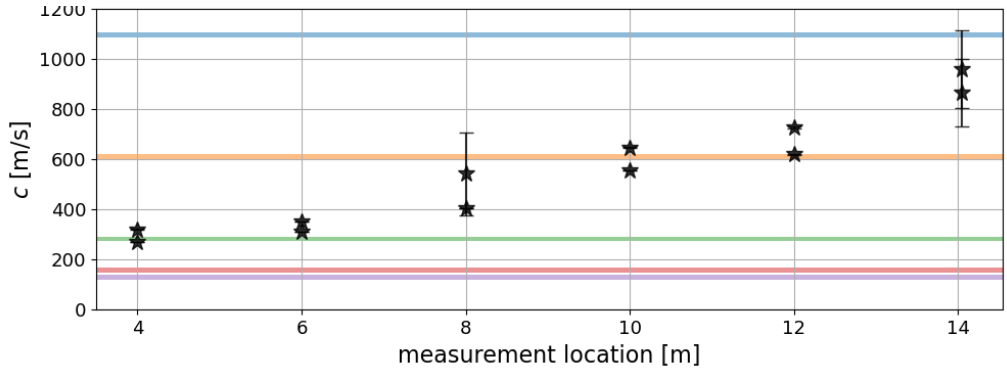

(c)

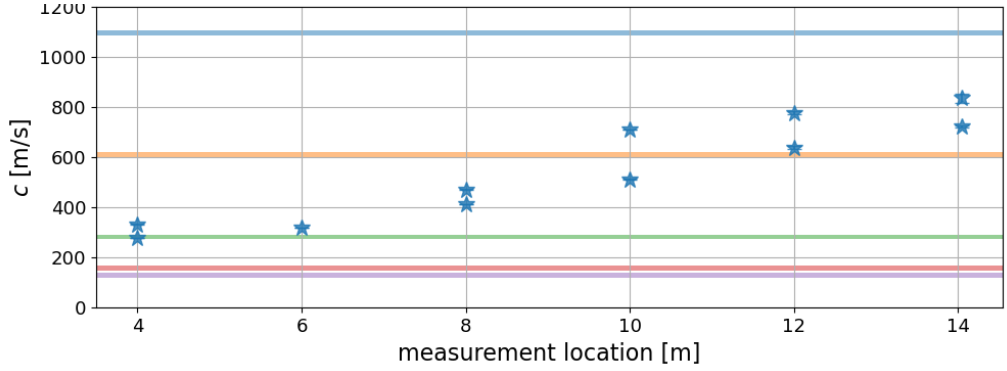

(d)

Figure 4.16: A comparison of the speed of sound calculated using different methods at a range of distances, for a filter of 125-275 Hz applied. The results have been calculated using (a) the phase difference between the accelerometer and the impact hammer, (b) the phase difference between the hydrophone and the impact hammer, (c) the cross-correlation between the accelerometer and the impact hammer and (d) the cross-correlation between the hydrophone and the impact hammer. The shaded regions show the predicted values of c from Chapter 3, coloured as per Figure 3.1.

4.3 Acoustic attenuation in plastic pipes

It is established [8, 44, 49, 203] that successful techniques for locating leaks in metal pipes struggle in plastic pipes. In part this is due to the greater variation in the speed of sound in plastic pipes: plastic pipes couple to surrounding soil in a way that steel pipes do not [89], such that the speed of sound in the pipe wall varies depending on the properties of their surroundings. This can be ameliorated by taking in situ measurements of the speed of sound, as suggested by [108], although the previous section has demonstrated the difficulties in doing so. Another problem for acoustic leak detection is the high attenuation of sound in plastic pipes. Acoustic signals in plastic pipes, including those produced by leaks, attenuate quickly, as already demonstrated in Chapter 3, Section 3.4. In this section we estimate the attenuation in both buried and unburied HDPE pipes, as well as across several features that may be found in a pipe network.

4.3.1 Calculating attenuation

The acoustic attenuation (1/m) can be found using signals recorded on two sensors attached to the pipe and separated by a distance d according to:

$$\alpha = -\frac{\ln |T_{ij}(\omega)|}{d} \tag{4.5}$$

in which the transfer function T_{ij} is defined in Equation 4.2.

4.3.2 Experimental setup

The same pipe setup as described in Section 4.2.2 was used for these experiments. The sections used here are shown in Figure 4.17. To determine the attenuation in a straight section of pipe, both above (pipe sections B and C) and below (pipe section A) ground measurements were taken. Sections D and E were used to investigate the effect of more complex pipe features on the acoustic attenuation in a plastic pipe.

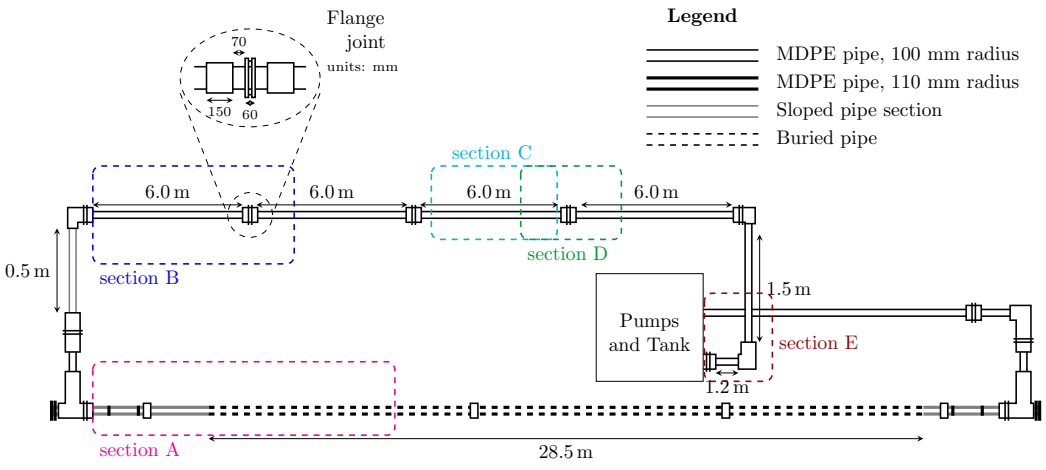

Figure 4.17: The location of the five test sections used to study the acoustic attenuation in HDPE pipes.

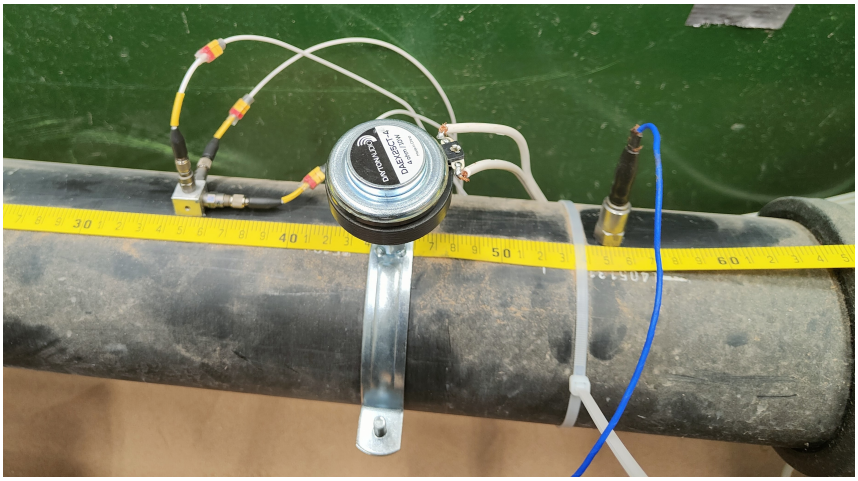

Figure 4.18: The shaker and accelerometer setup on the HDPE pipe used to measure the acoustic attenuation.

A sine sweep excitation signal was used so the frequency dependence of the acoustic attenuation across a broad frequency range could be determined. For these measurements a sine sweep from 100 to 6,000 Hz was used with a ramp up in amplitude for the first 1 s. The minimum frequency was chosen such that the sweep was at its full amplitude by 200 Hz. This signal was introduced into the system using the shaker arrangement shown in Figure 4.18. The shaker was a Dayton Audio DAEX25CT-4. It was driven via a Fosi Audio TDA7498E amplifier with the signal generated in a Labview script run on a laptop connected to a DAQ card (USB-4431). A monoaxial (PCB 356B21) accelerometer was used as the reference measurement (a_{ref}) taken at a constant 50 mm from the shaker, while a triaxial accelerometer (3 x PCB 353B18 with sensitivity 10 mV/g) was used to measure the acceleration in three axes at a range of distances from the shaker. The triaxial accelerometer was attached to the pipe using wax with the z-axis oriented in the radial direction, x-axis along the pipe axis and the y-axis in the horizontal direction. The sampling rate was 12 kHz in all the experiments so that the maximum frequency of the sine sweep was the Nyquist frequency. Full details of parts used are provided in Appendix A.

In order to understand the repeatability of the shaker as a sound source a series of experiments were run. In the first of these, the triaxial accelerometer was placed on top of the shaker, to see the vibrational response of the shaker at the source. In the second experiment, 5 measurements were taken with the triaxial accelerometer 1 m from the shaker, with the shaker and accelerometers not moved between repeats. When compared with the first experiment, this shows the effect of the shaker coupling to the pipe on the acoustic response to the shaker, as well as showing the repeatability of measurements at a distance. This experiment was repeated twice more, with the shaker moved between experiments, to see how repeatably the shaker could be attached. For each of these experiments a background measurement was taken, with no output sent to the shaker.

Table 4.3: Summary of measurements conducted investigating the repeatability of the shaker as a sound source

Experiment	Description	Repeats
1	Triaxial accelerometer on shaker	5 + 1 background
2	Triaxial accelerometer 1 m from shaker, attachment (i)	5 + 1 background
3	Triaxial accelerometer 1 m from shaker, attachment (ii)	5 + 1 background
4	Triaxial accelerometer 1 m from shaker, attachment (iii)	5 + 1 background

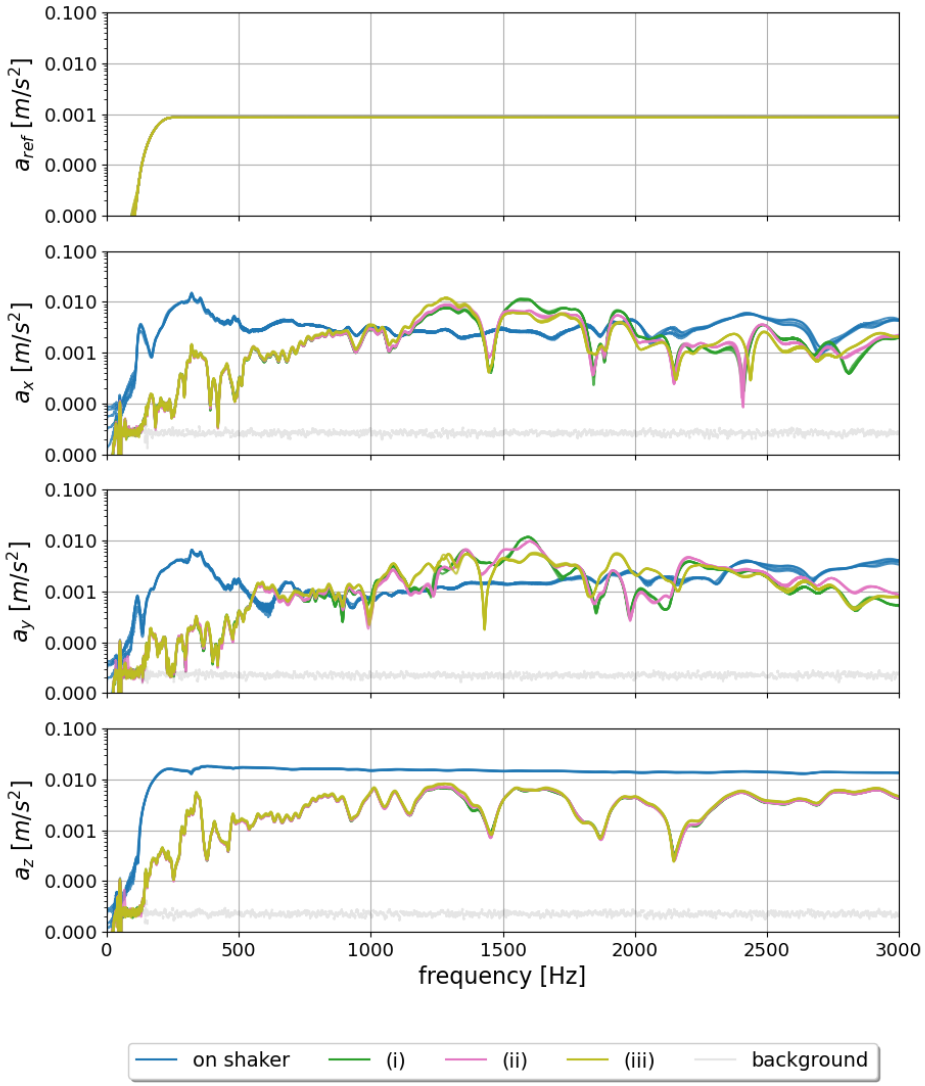

Figure 4.19: The variability in the acceleration spectra recorded on the monoaxial accelerometer 0.05 m from the shaker and triaxial accelerometer at 0.5 m from the shaker. 10 repeats are overlaid in different colours, the background measurements are shown in black.

These experiments are summarised in Table 4.3.

The results of these experiments are shown in Figure 4.19. The response on the shaker (a_{ref}) is consistent between repeats and between experiments, with a linear output from 200 Hz. The response on the shaker when measured using the triaxial accelerometer (the blue traces) is similarly linear in the z axis, unsurprising given that the monoaxial accelerometer was measuring the acceleration in this axis. In an ideal set up the shaker would only vibrate in the z axis; consideration of the x and y measurements show that this is very much not the case here, with a significant proportion of the energy going into vibration in these axes. This effect is particularly pronounced between 200 and 400 Hz. Some work was conducted to reduce these off-axis vibration by shortening the attachment of the shaker to the collar, and adding weight to the shaker, but no effective solution could be found.

Moving on to consider the acceleration measured 1 m from the shaker, it can be seen that the

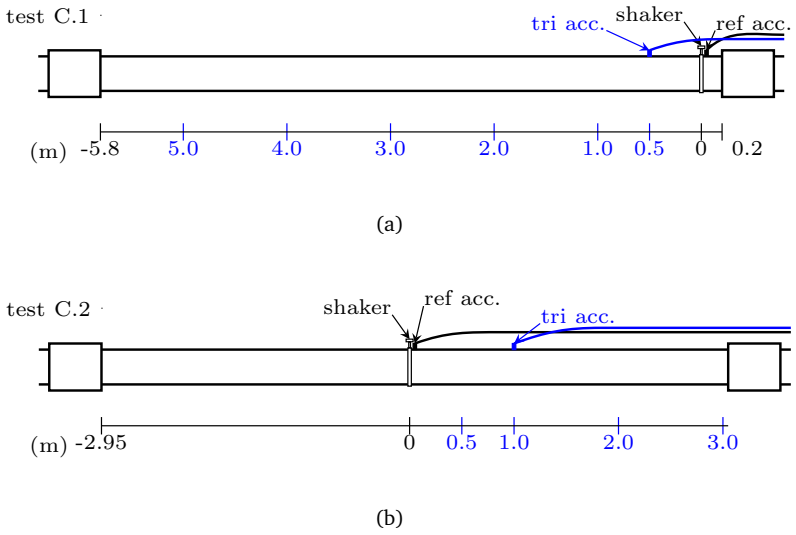

Figure 4.20: The locations of the shaker and triaxial accelerometers for the two sets of measurements taken on segment C of the pipe loop.

linearity with frequency is significantly reduced, with variations of an order of magnitude across this frequency range in all three axes. The z acceleration is most consistent across the frequency range, although there are still significant losses in amplitude due to resonances, e.g. at 1,450, 1,850 and 2,150 Hz. The x and y accelerations measured on the pipe increase from 10^{-4} to 10^{-2} $\mathrm{m/s^2}$ over the range 200 to 1,500 Hz, before stabilising (to an extent). This means that at frequencies of less the 500 Hz a_x and a_y are an order of magnitude less than a_z. a_z shows a remarkably level of repeatability, both between shaker attachments (i), (ii) and (iii) and within them. The only slight exception to this is between 1,200 and 1,400 Hz where the three traces can just be distinguished. The x and y accelerations show a similar level of repeatability within shaker attachments, with the 5 repeat measurements being indistinguishable, however, the repeatability between shaker attachments is much poorer. This is particularly true for frequencies greater than 1,500 Hz where the results for the three attachments diverge clearly.

Based on this, it was taken that while the pipe response to the shaker is not linear with frequency, the pipe response is consistent between repeats. Given that re-attaching the shaker led to large differences in a_x and a_y for higher frequencies, any measurements comparing recordings were taken with the shaker in the same position for all recordings.

4.3.3 Attenuation in a straight pipe

Two sets of measurements were taken with the shaker in different positions relative to features on pipe section C (as labelled in Figure 4.17). These are labelled test C.1, where the shaker was 0.2 m from a joint with 5 measurements taken at 1 m increments, and test C.2 where the shaker was in the middle of the pipe section and 3 measurements were taken at 1 m increments. A detailed view of these test positions is shown in Figure 4.20 with the location of the shaker and sensors for each of the sets of measurements taken. The reference accelerometer (a_{ref}) was kept 0.05 m from the shaker, while the position of the triaxial accelerometer was varied, with the locations labelled as shown in Figure 4.20.

The recordings on each axis of the triaxial accelerometer and for the reference accelerometer

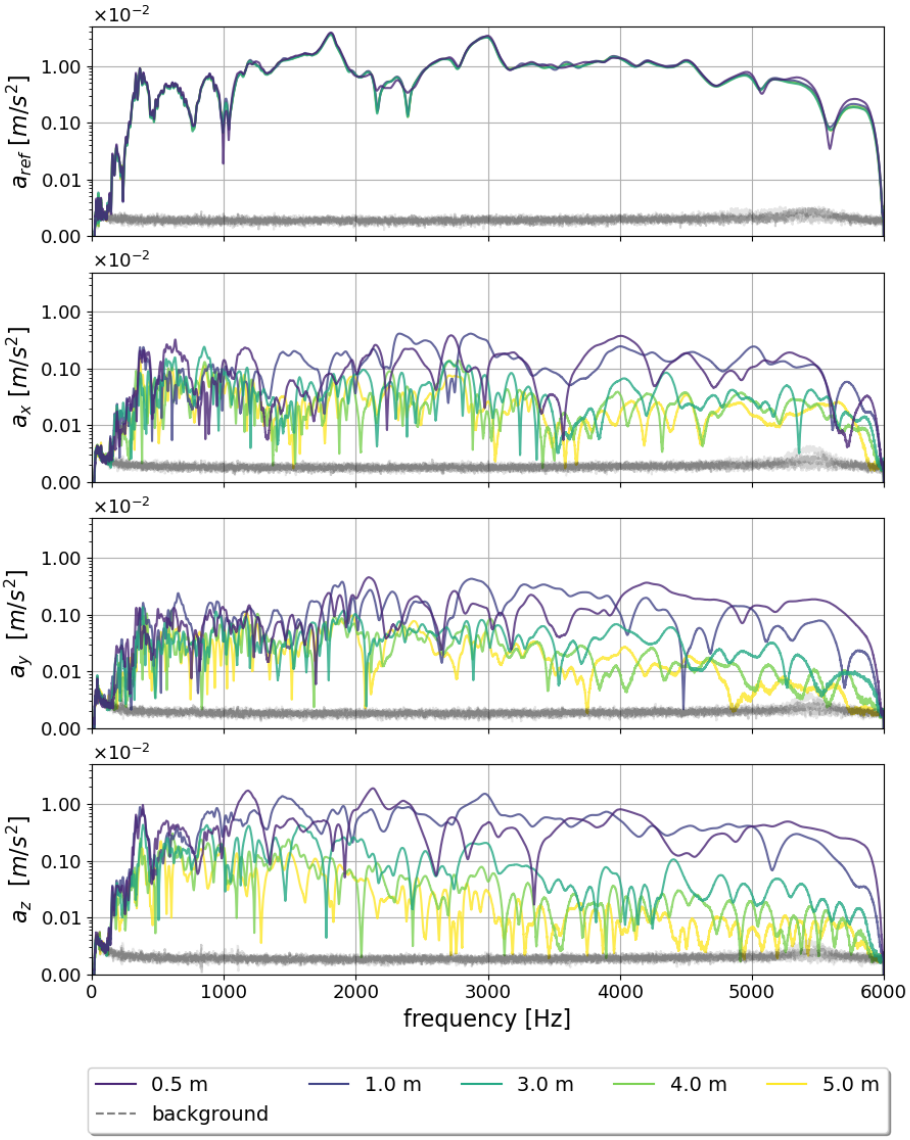

Figure 4.21: The spectra of accelerometer measurements in pipe section C for test C.1, showing the effect of distance on the triaxial acceleration spectra for a straight pipe (b-d), as well as the reference accelerometer spectrum (a). The data has been smoothed with a 101 point savgol filter.

are shown in Figures 4.21 and 4.22 for test C.1. In Figure 4.21 the reference accelerometer (a_{ref}) measurements are consistent between the measurements at different locations, showing that the triaxial accelerometer measurements at different distances can be meaningfully compared, given that the acceleration next to the source was very similar. In contrast to the relatively smooth a_{ref} measurements, it can be seen immediately in Figure 4.21 that the recordings on all three axes of the triaxial accelerometer are very complex, with many nodes and anti-nodes. These are likely to be associated with some complex wave interference pattern due to strong reflections from features in the pipe network. This complexity has been somewhat reduced by applying a 101 point[†] Savitzky-Golay ('savgol') filter [201] to remove very fine detail. This complexity seems to increase with distance from the source, with the measurements 5 m from the source showing a very complex

[†]A 101 point filter was chosen as a balance between removing very fine detail, without compromising the shape of the data. A wider filter could have been used instead of the step function introduced in Figure 4.22 however it was felt that this led to such a change in behaviour that such a smooth function was a misrepresentation of the underlying data. A savgol filter requires an odd number of samples.

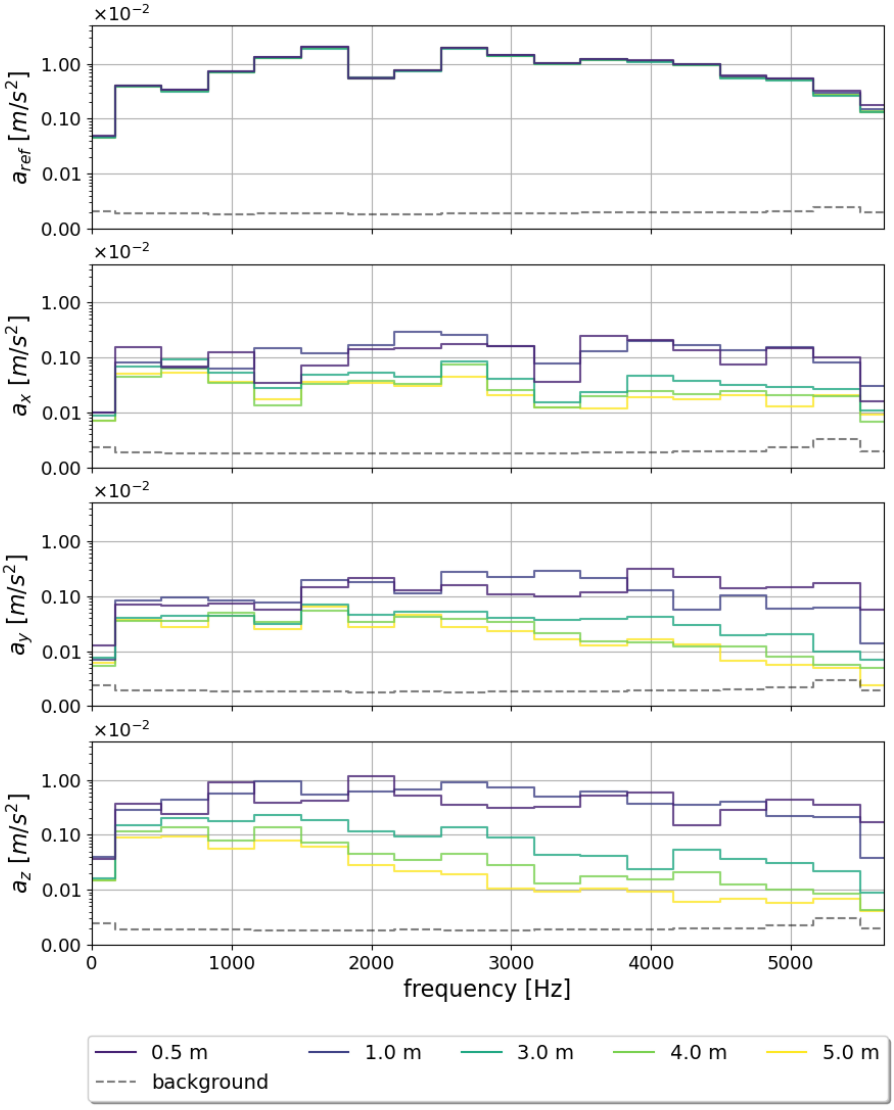

Figure 4.22: The spectra of accelerometer measurements in pipe section C for test C.1, showing the effect of distance on the triaxial acceleration spectra for a straight pipe (b-d), as well as the reference accelerometer spectrum (a). The data has been grouped to every 333 Hz, with the mean of each band plotted.

spectrum, particularly in a_z. In this analysis we are mainly focussing on the changes in behaviour over distance, therefore this level of complexity is unhelpful. To make the data easier to compare over distance, the mean of every 333 Hz[‡] has been found and re-plotted in Figure 4.22.

The z-component of the acceleration shows the clearest reduction in amplitude with distance, particularly for higher frequencies with $f > 1,000$ Hz. The x-component attenuates less, particularly below 2,000 Hz. The attenuation of the y-component of the acceleration is between that found for z- and x-components. However, the amplitude of the x- and y-components is approximately an order of magnitude less that that of z-component. In general, the acceleration amplitude reduces down to that of background noise at 5 m away from the position of impact for $f > 5,000$ Hz.

Calculating the attenuation using Equation 4.5 from these measurements leads to Figure 4.23. The calculated values for 0.5 m and 1.0 m have been excluded since they were much higher (up

[‡]Again, this was chosen based on a balance between maintaining enough detail to gain a sense of the behaviour, while removing the necessary level of fine detail.

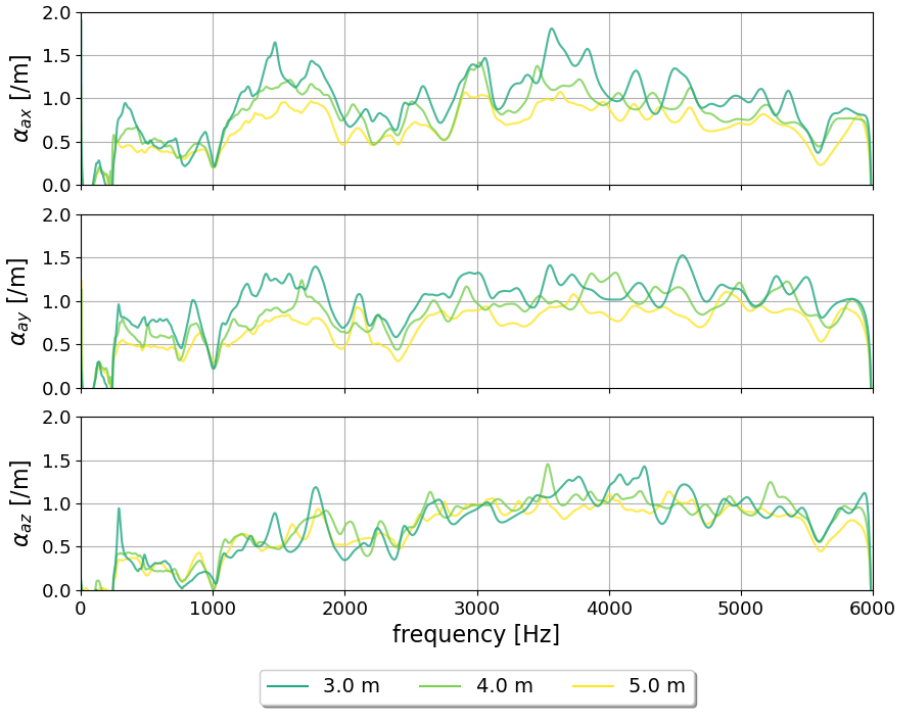

Figure 4.23: The attenuation of accelerometer measurements in pipe section C for test C.1. The data has been smoothed with a 101 point savgol filter to aid in interpretation.

to 5 /m for measurements 1 m from the source and up to 10 /m for measurements 0.5 m from the source). This was considered to be due to near-field effects, rather than an interesting phenomenon for discussion. The attenuation shown in Figure 4.23 varies with measurement location, but follows the same trends in behaviour with frequency. α_{az} shows the most consistency between measurement locations, presumably because the initial amplitude of a_z was higher than for the other two axes. α_{az} is also lower than α_{ax} and α_{ay}, particularly for f < 1,000 Hz, where α_{az} is less than 0.5 /m, while α_{ax} and α_{ay} are between 0.5 and 1.0 /m. All three axes show a trend towards increasing with frequency, bar a small decrease in attenuation at between 2,000 and 2,500 Hz. This is most pronounced for α_{az}. The lower attenuation for f < 1,000 Hz makes this frequency range more practical for acoustic inspection of plastic pipes.

So far, this only considers the effect of distance for a single set of measurements, for the source in a single location. Comparing the measurements at site C.1 and C.2 allows for some of the effects of source location to be seen. The source being close the joint for measurements C.1 allowed for measurements over a larger distance, but the joint is a stiffer section of pipe, so may inhibit the pipe oscillations, in addition to being a large source of reflections. The attenuation calculated for each axis where the triaxial accelerometer was 3 m from the source location is compared for C.1 and C.2 in Figure 4.24, where the data has been grouped into 333 Hz bins for a less cluttered graph. For lower (< 2,500 Hz) frequencies, there is little divergence between the two setups, save perhaps an increase in α_{ay} for location C.1 around 1,500 Hz. α_{az} is very similar across the entire frequency range. α_{ax} and α_{ay} show more of a divergence in behaviour for f > 2,500 Hz, particular around 3,500 and 4,500 Hz respectively. For the x and y axes the attenuation is higher for location C.1 at these higher frequencies. This implies that the joint close to the source has more of an effect on the x and y axes, and only at higher frequencies, with a nearby joint leading to higher

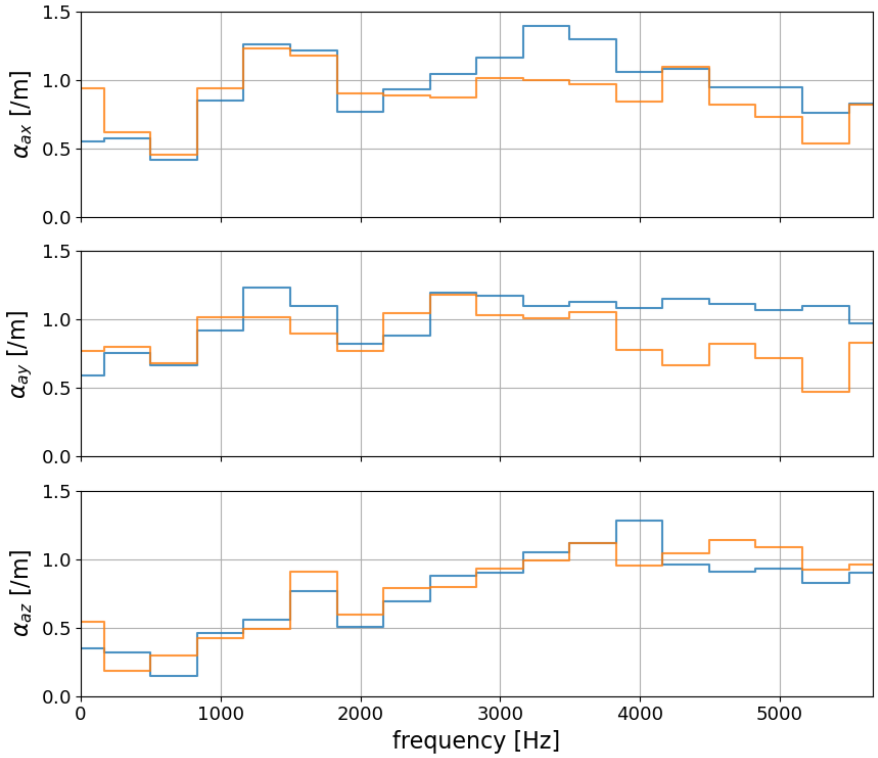

Figure 4.24: Attenuation calculated for each axis for tests C.1 and C.2, both of which measured the triaxial acceleration 3 m from a shaker on a straight MDPE pipe. The results for test C.1 are shown in blue and those for test C.2 in orange. The average of every 333 Hz has been taken to aid in interpretation.

attenuation. Intuitively it makes sense that an electrofusion joint would inhibit the longitudinal and torsional motion more than the radial expansion of the pipe.

These experiments have shown that there is significant attenuation on a plastic pipe, even over 3 m, with a reduction in amplitude down to background levels over 5 m. This attenuation is highly frequency dependent, with frequencies of less than 1,000 Hz showing a lower attenuation in all axes than for higher frequencies. It has also shown how a nearby electrofusion joint impacts the sound transmission through a pipe, this is taken further in the following subsections.

The sound source used for this work was not ideal, given the poor transmission from the source to the pipe wall demonstrated in Figure 4.19, making it difficult to say how much of fine variations in frequency across this section have been due to the shaker vs. a highly frequency dependent attenuation profile of the plastic pipe. It seems likely that a large proportion of this came from the sound source, but that does not explain the increase in variability for a_z in Figure 4.21 with distance from the source. Furthermore, a wide band sinusoidal sweep is clearly not representative of the noise made by a leak. However, it was felt that gaining information on the frequency dependence of the attenuation was of more worth than the attenuation of specific leak, particularly given the large variation in leak noise seen in Chapter 3. The minimum frequency of these investigations was limited by the capabilities of the shaker, which struggled to produce repeatable pipe wall accelerations for frequencies less than 200 Hz, given that the attenuation was lowest for lower frequencies it would be beneficial to decrease this lower frequency limit.

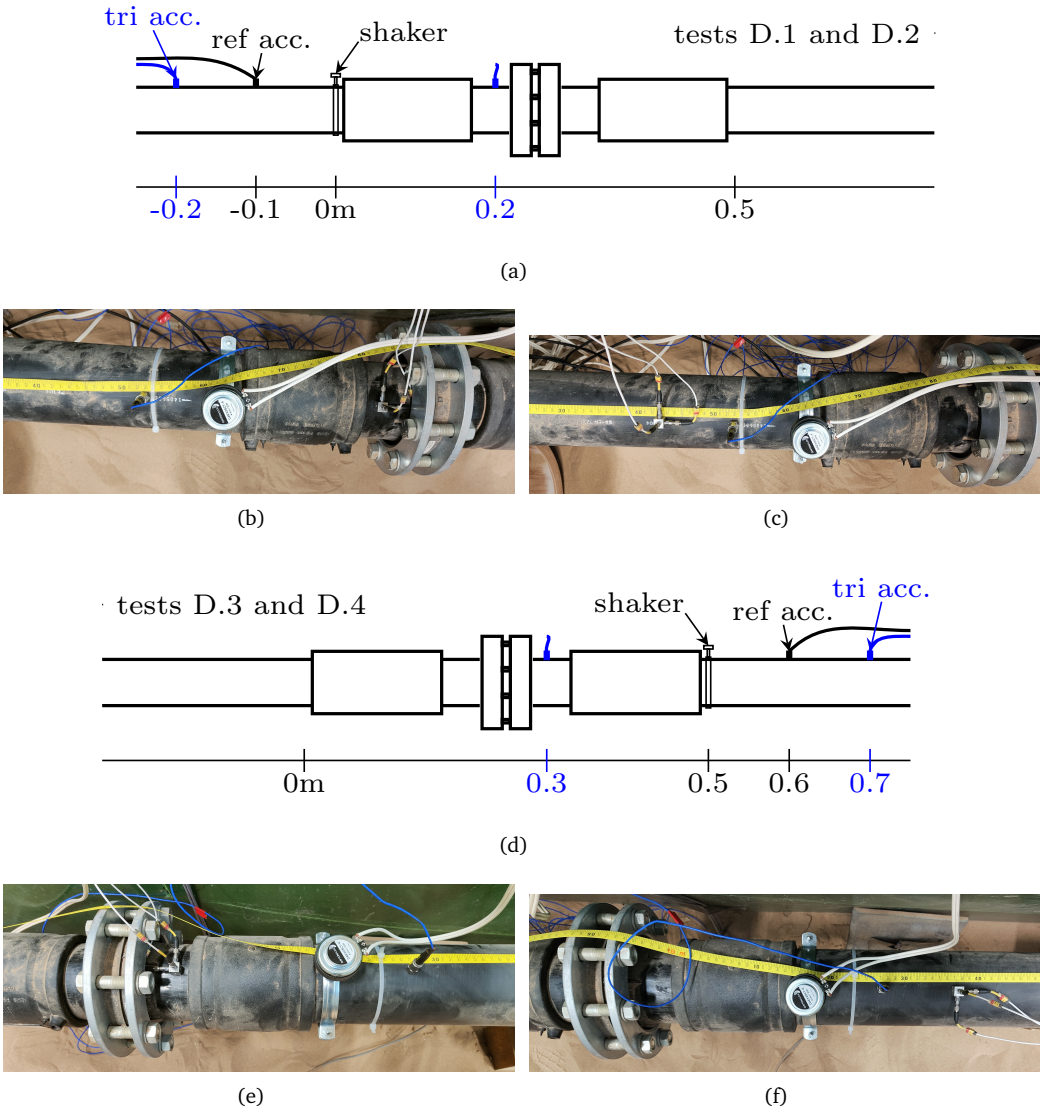

Figure 4.25: Location of shaker and accelerometers for measurements across an electrofusion joint, showing (a) the schematic for tests 1 and 2, (b) a picture of test 1, (c) a picture of test 2, (d) the schematic for tests 3 and 4, (e) a picture of test 3 and (f) a picture of test 4.

4.3.4 Attenuation across an electrofusion joint

Electrofusion joints are very common on PVC pipes. On the test rig used here they occur every 6 m, in the 'wild' they would be more widely spaced than that, but still occur every time two plastic pipes are joined together. The attenuation over two joints was measured, and compared with measurements taken with the shaker in the same place but the accelerometers moved such that there was a straight line to the shaker rather than a joint in the middle. Schematics and images of each of the four measurement location are shown in Figure 4.25. The shaker was placed close to the joint to reduce attenuation between the shaker position and the start of the feature of interest, this was based on the high attenuation seen in Section 4.3.3. Its position was also chosen to match the relative proximity of the shaker and feature in later experiments, where the possible positions for the shaker were more limited. Unfortunately, this does mean that the measurements are in the extreme near field of the source - future work might consider a larger separation.

A comparison of the spectrum in each location is shown in Figure 4.26, given the significant

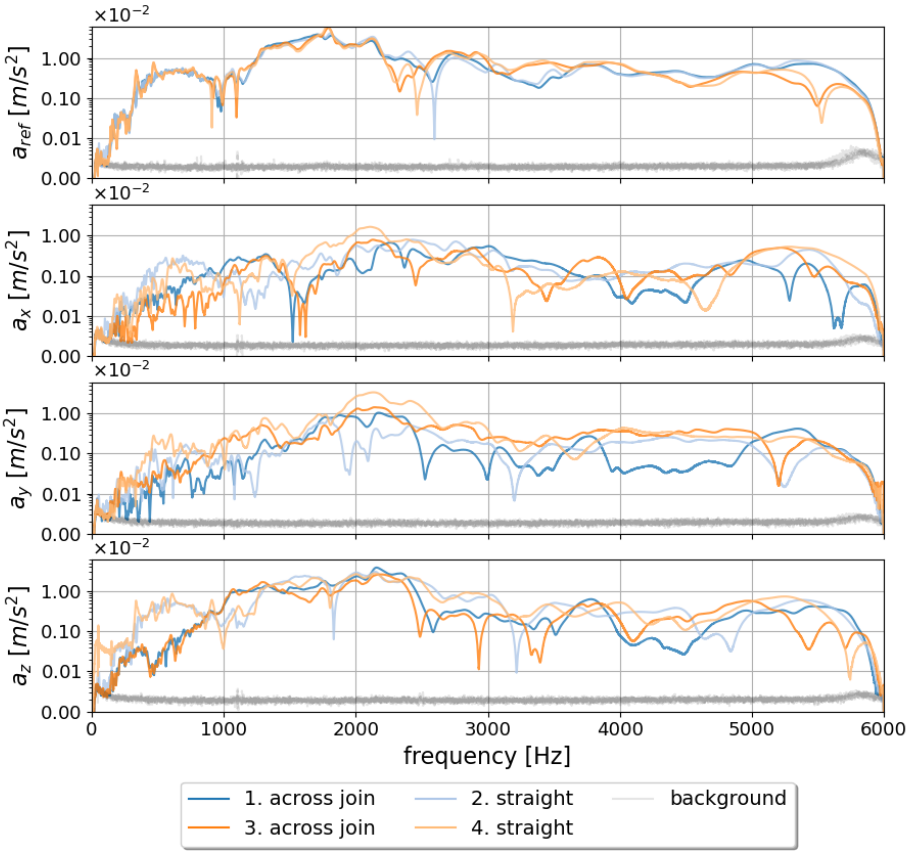

Figure 4.26: Spectrum of recordings for each accelerometer axis comparing the effect across two electrofusion joins with comparable measurements on a straight pipe. This means the shaker is in the same place for tests 1 and 2, was then moved and then is in the same place for tests 3 and 4. The tests are numbered as per Figure 4.25. The data has been smoothed using a 101 point savgol filter.

effect of shaker location on the pipe response, these graphs have been coloured by shaker location, with the measurements along the straight section shown as paler, 'background' traces, while the measurements across the joint are shown in the foreground. It can be seen in Figure 4.26 (a), that moving the shaker only had a large effect for frequencies above 2,500 Hz.

The joint has the largest attenuating effect on the radial (z) acceleration, particularly for frequencies less than 1,000 Hz. Over the length of the joint the signal amplitude is not reduced to the background level, but does diminish by a factor of 10 for a_z for f between 500 and 800 Hz. This is most pronounced at 500 Hz. In contrast the radial acceleration for f between 900 and 1,250 Hz is positively affected by the presence of the joint, with higher attenuation on the unobstructed pipe. For frequencies from 1,250 to 2,250 Hz the presence of the joint has minimal effect. At frequencies greater than this it is difficult to tell where the differences are due to the shaker attachment varying vs. the presence of a joint, although in general up to 4,000 Hz the joint does lead to some reduction in the signal received.

The torsional (y) acceleration is less affected by the joint, and is smaller in general. There is some loss of amplitude for $f < 1,000$ Hz, and there are some sharp discrete drops in amplitude when the joint is in the middle of the measurements, e.g. at 400, 600 Hz. For higher frequencies there is less agreement between the two datasets but generally the joint has little effect on a_y. The axial (x) acceleration is also barely affected by the joint. The low (<1,000 Hz) frequencies are

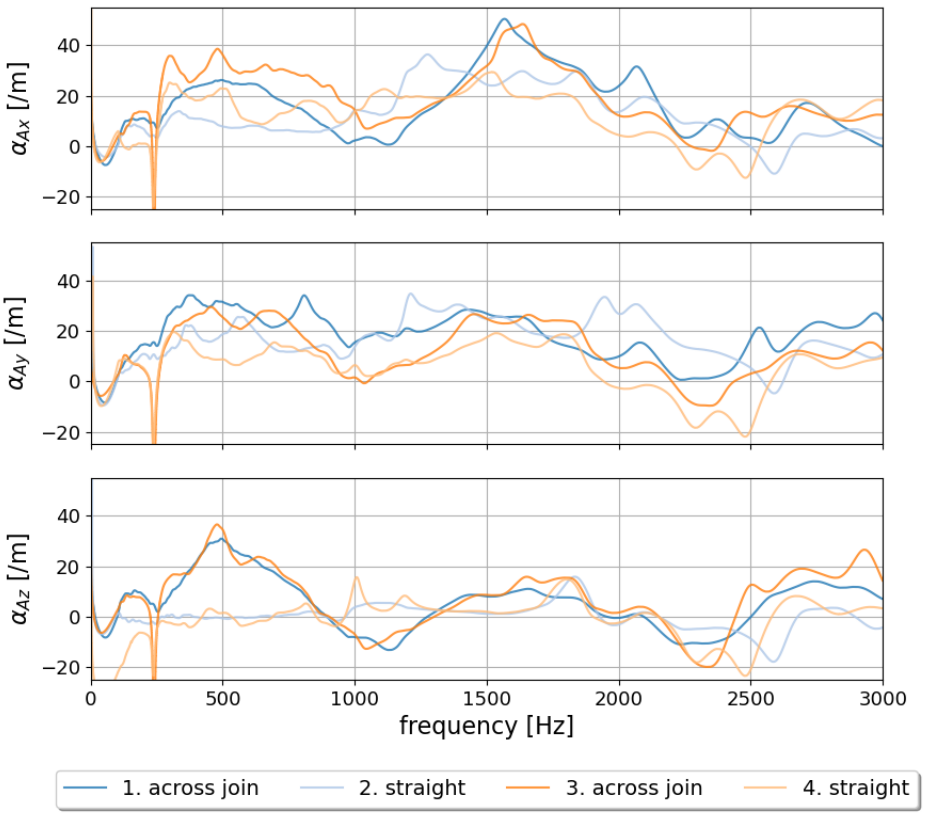

Figure 4.27: Attenuation calculated with respect to the reference accelerometer (a_{ref}). Results have been smoothed using a 2501 point savgol filter.

more affected by the presence of the joint, but in this case the effect is much smaller. Between 1,000 and 1,500 Hz it is the straight pipe where a_x loses most amplitude and for $f > 1,750$ Hz there is little difference.

The attenuation calculated using Equation 4.5 is shown in Figure 4.27, with the attenuation calculated with respect to the reference acceleration measured for each test. It has been smoothed with a more aggressive 2501 point[§] savgol filter. As could be seen in the previous figure, the joint has the largest attenuating effect on a_z below 1,000 Hz. At other frequencies and for other axes the effect of the joint is less clear.

The accuracy of these calculations of α_a are believed to be compromised by the extreme near-field in which they have been recorded, so while trends in behaviour can be determined, more extensive testing would be required to understand the quantitative effect of the joint.

These measurements have demonstrated the benefit of measuring the acceleration on more than one axis as different components of the acceleration are more affected by the join.

[§]Again, this has been chosen based on a balance of being able to see trends in behaviour, while not removing too much detail. A savgol filter requires an odd number of points.

4.3.5 Attenuation across a flange joint

Flange joints comprise a metal gasket sandwiched between two flange plates, held together by bolts, a picture is provided in Figure 4.28(a). The ends here have been connected to the main pipe using electrofusion joints. There are many of these on the test rig used; they are less common on the network at large, but do happen, particularly between pipes of different materials.

Measurements were taken at four locations across a joint (Figure 4.28(b)), with the shaker 0.25 m from the join. The accelerometer was positioned such that these measurements provide information about the effect of the flange joint (positions B and C) as opposed to the effect of the pipe only (positions A and D). The spectra recorded at each location are shown in Figure 4.29 and the attenuation calculated with respect to the measurements 0.24 m from the joint is shown in Figure 4.30 for each axis.

Looking at the recordings at the two positions before the flange joint (0.24 m and 1.0 m) in Figure 4.29, the recording at 0.24 m from the source is larger than that 1.0 m from the source in most cases. The exceptions to this are at localised reductions in frequency, such as that at 2,400 Hz in a_x, and for frequencies less that 1,000 Hz, where there is very little difference in magnitude of the acceleration in any axis. a_y shows more of a frequency dependence in magnitude for these two measurements, with the measurements at point D reducing by an order of magnitude from 1,000 Hz to 4,000 Hz.

The measurements from the other side of the flange joint show that the joint has a significant impact, with a_x and a_z reducing by an order of magnitude over the majority of this frequency range. a_y also reduces over the flange joint when compared with the measurement 0.24 m from the source, however the difference is no greater than that of the measurements at -1.0 m with 1 m of straight pipe in the intervening distance instead, particularly for $f > 2{,}500$ Hz, where the acceleration at -1.0 m was particularly reduced. The joint has a smaller impact around 1,000 Hz on all axes, with all three axes showing almost no change from the acceleration at -1.0 m. Comparing

(a)

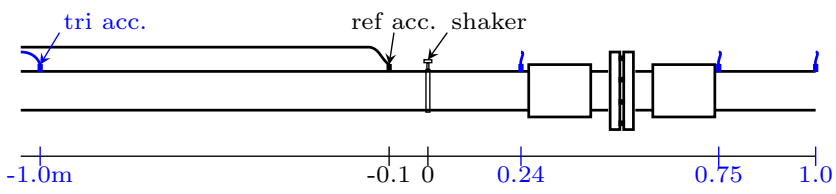

(b)

Figure 4.28: Flange joint. (a) Picture of example flange joint, (b) measurement locations. The measurement was taken 0.24 m from the shaker to avoid clashing with the joint.

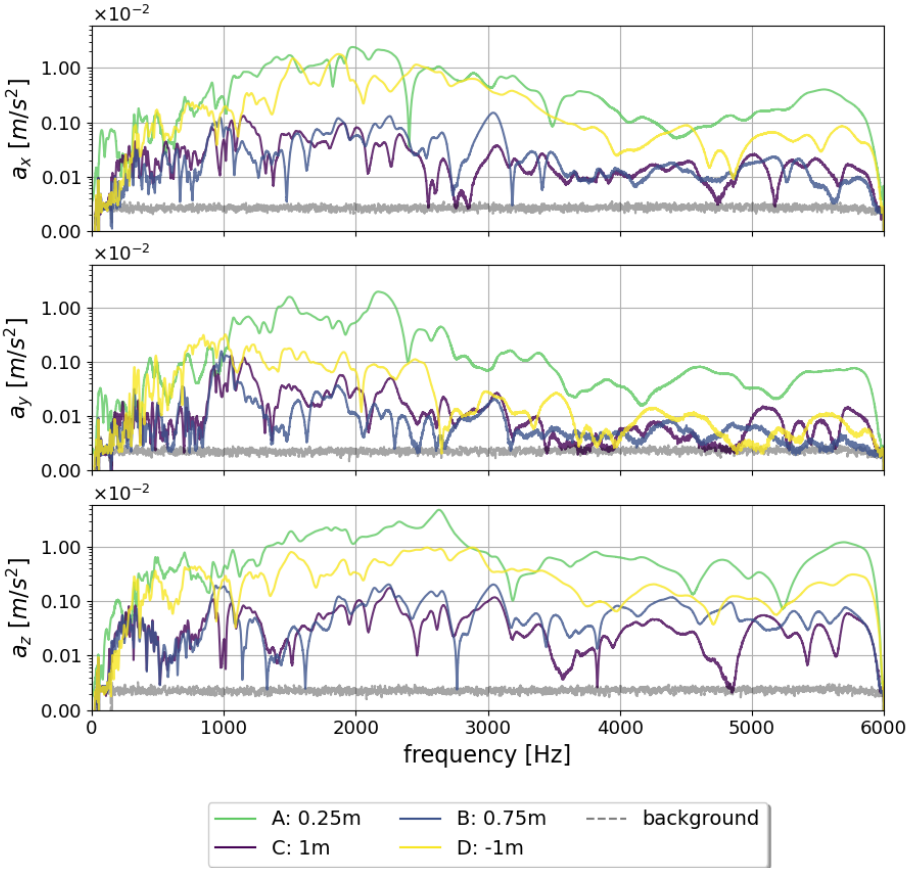

Figure 4.29: Spectrum of recordings for each accelerometer for measurements across a flange join, with the positions in the legend corresponding to those in Figure 4.28(b). The data has been smoothed with a 101 point savgol filter.

the measurements at 0.75 and +1.0 m, both of which are past the flange joint, in general there is little attenuation between these two, however what differences there are are very frequency dependent. For $f < 1{,}000$ Hz there is almost no difference, but for frequencies greater than this the transmission between the two is inconsistent.

The attenuation for each position, calculated with respect to the recording at 0.24 m from the shaker, is shown in Figure 4.30. As with the calculated attenuation across the electrofusion join, these measurements are too close together to be in the far field. It is believed that this, in combination with the large number of reflections in the system, is the cause of the high level of complexity in the signal, which led to an aggressive smoothing function being applied. This shows the same trends just discussed, with the attenuation of a_z being generally higher across the joint for all frequency ranges.

Again, this demonstrates the difficulty in measuring leak noise when dependent on transmission through such joins. The difficulties lie not only in the reduction in amplitude, but also in the strong frequency dependence of the attenuation. This would undermine any frequency-based approach to leak classification.

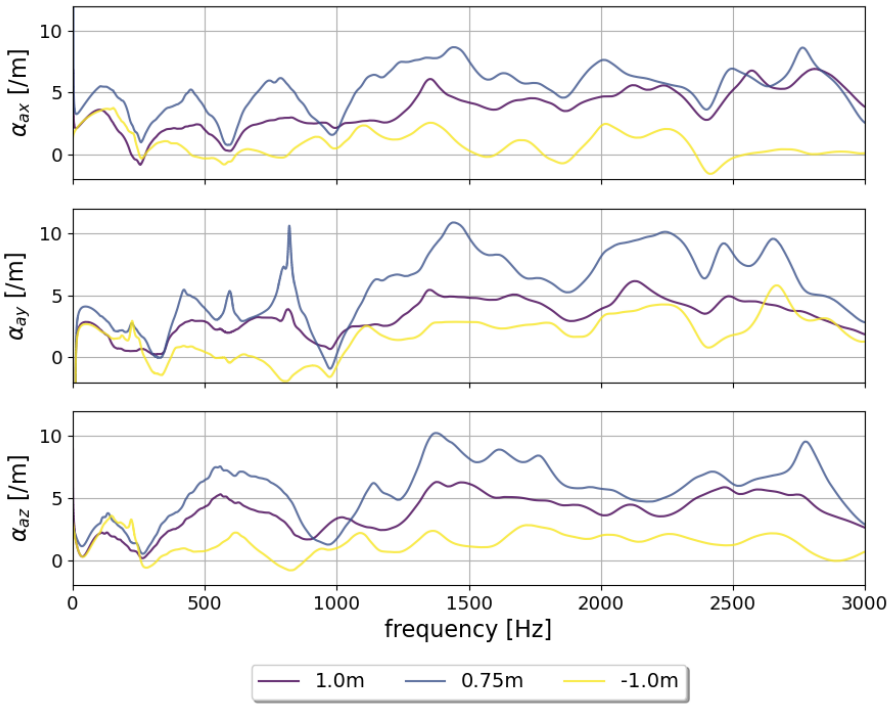

Figure 4.30: Attenuation calculated with respect to the measurements 0.24 m from the shaker. Results have been smoothed using a 2501 point savgol filter.

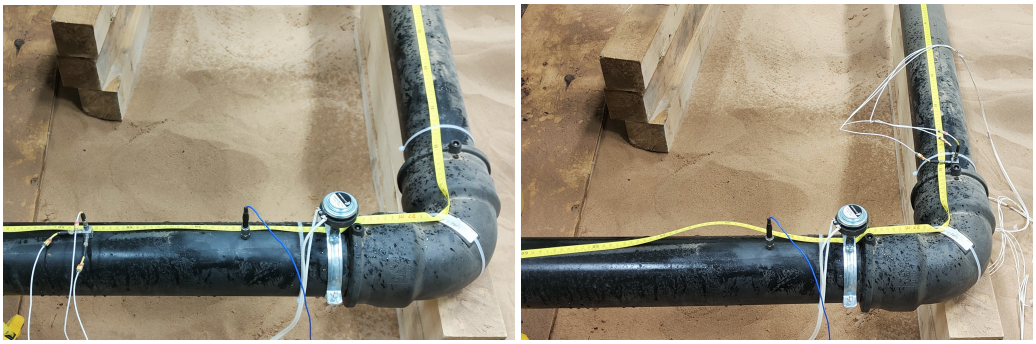

(a) (b)

Figure 4.31: Location of shaker and accelerometers for measurements across a 90 degree join, showing (a) the positions of the shaker and accelerometers for measurements along a straight pipe section and (b) around the corner, with the monoaxial accelerometer acting as a reference.

4.3.6 Attenuation around a corner

A similar set of measurements to those described in the previous section were performed for the 90 degree bend shown in Figure 4.31, this is segment E of Figure 4.17. In this case the shaker was kept in the position shown and the accelerometers were moved such that they were 0.3 m from the shaker along a straight length of pipe and then 0.3 m from the shaker around the corner, shown in Figures 4.31(a) and (b) respectively. The reference accelerometer was not moved.

A comparison of the spectra for the recordings of a straight pipe and across the corner is shown in Figure 4.32. Again, the reference acceleration for both sets of measurements is almost indistinguishable, save a few points between 2,500 and 3,000 Hz where the measurements for the straight

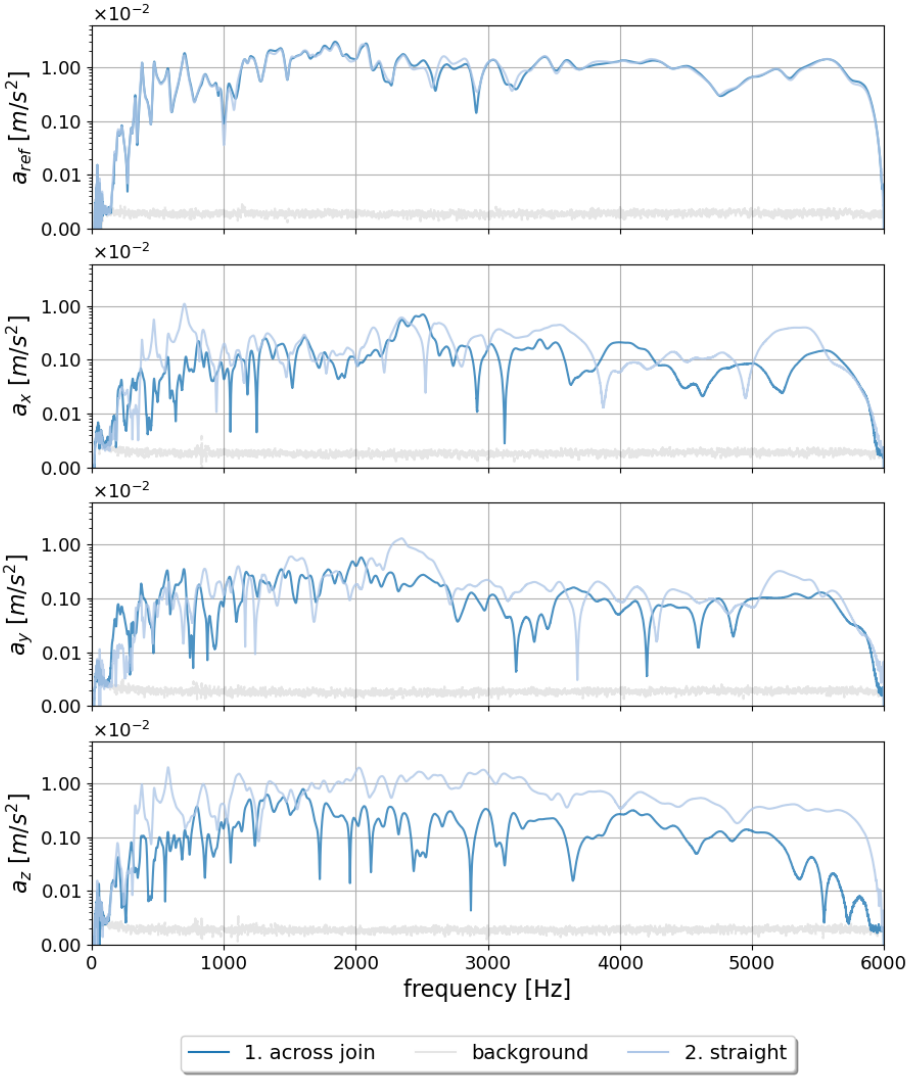

Figure 4.32: Spectrum of recordings for each accelerometer across a corner joint, comparing acceleration measured 0.3 m from the shaker along a straight pipe and across a corner joint. The data has been smoothed with a 101 point savgol filter.

pipe are marginally larger. This means the measurements taken by the triaxial accelerometer can be compared with confidence.

The x and y components of acceleration have very similar magnitudes between the two measurements, of around 10^{-3} $\mathrm{m/s^2}$. There is some attenuation of a_x across the corner for $f < 1,000$ Hz, and a general change in behaviour for $f > 2,000$ Hz where the measurements in the two scenarios do not overlay each other well. a_z again exhibits the most attenuation due to the corner. For most of the frequency range tested a_z measured across the corner is approximately 1/10 that measured along the straight pipe section. There is less of a drop for frequencies between 800 and 1,200 Hz, and around 4,000 Hz, but the corner still has an attenuating effect. The final feature of note here is the increased 'spikiness' of the frequency response, particularly in a_z but also in a_x for f less than $1,250$, where the data exhibits sharp drops in amplitude at discrete frequencies.

The attenuation calculated with respect to a_{ref} is shown for each axis in Figure 4.33, where the same trends just discussed can be seen. The corner has the largest effect on α_{az}, with a consistent increase in α_{az} except for $1250 < f < 1700$ Hz, where the corner has little effect. The corner

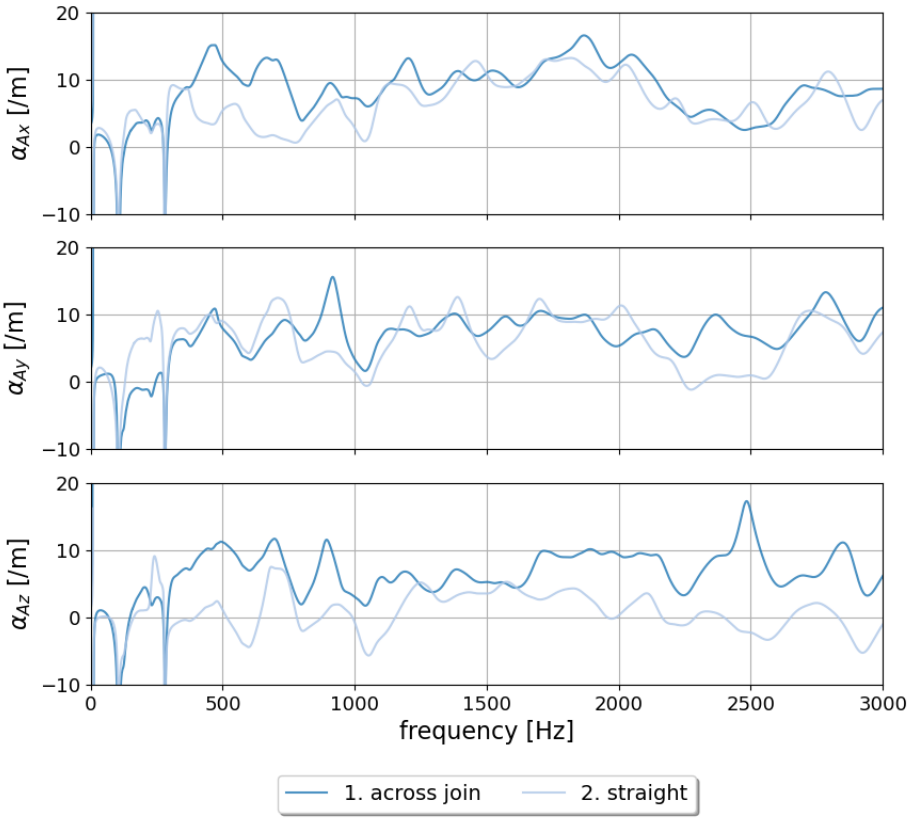

Figure 4.33: Attenuation calculated with respect to the reference accelerometer (a_{ref}) for the measurements around a corner described in Section 4.3.6. Results have been smoothed using a 2501 point savgol filter.

increases the α_{ax} between 400 and 800 Hz, but otherwise has little effect on α_{ax} or α_{ay}

Based on these measurements, the corner has more of an attenuating effect than the electrofusion joint across most of the frequency range, although it is less attenuating for $f < 1,000$ Hz. It has slightly less of an effect than the flange joint over the entire frequency range, although it, too increases the number of strongly attenuated frequencies, leading to increased 'spikiness' in the spectrum.

4.3.7 Attenuation underground

Finally, the effect of burying the pipe was considered. This is arguably the most important aspect to be considered, given most pipes are buried, although it has already been investigated elsewhere, e.g. in [38, 59, 62, 63].

The layout of this experiment is shown in Figure 4.34(a), where this is pipe section A of the network shown in Figure 4.17. The shaker was placed underground, 4.0 m from where the pipe emerges from the ground, as shown in Figure 4.34(b). Measurements were taken from 4.0 m away from the impact with an accelerometer placed on the pipe at another excavated section, a photograph of this is provided in Figure 4.34(c). These were compared with the measurements on

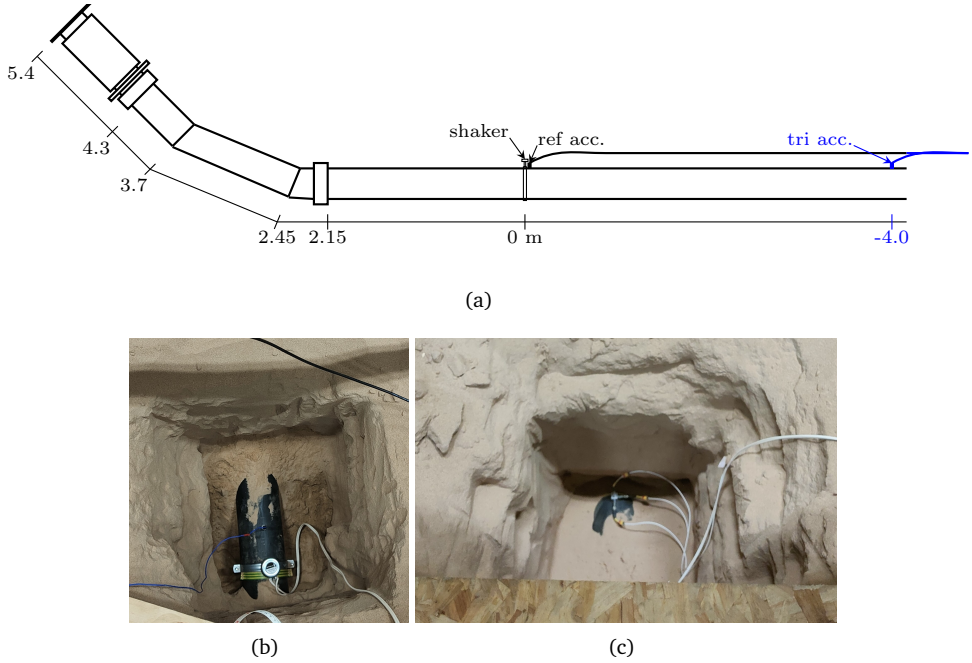

Figure 4.34: The test layout for measurements of the attenuation in a buried pipe, showing (a) a schematic of the setup, (b) the shaker attachment and (c) the accelerometer attachment.

pipe section C, described in Section 4.3.3, for measurements 4 m apart on an above-ground pipe.

The spectra of these two recordings, both 4.0 m from the shaker are shown in Figure 4.35, with the acceleration 0.05 m from the shaker included as a reference. a_{ref} is more dissimilar for these two cases than for the other experiments in this section. The magnitude is generally within $\pm 0.1 \times 10^{-2}\ m/s^2$, except at specific frequencies where the frequency drops, e.g. 2,160 and 2,400 Hz for the above ground measurements and 3,150 and 4,300 Hz for the below ground measurements. There is also a much lower amplitude between 250 and 400 Hz at a_{ref} for the below ground measurements. These differences are likely due to the increased challenge of tightening the jubilee clip for the shaker on the below ground experiment.

These discrepancies in a_{ref} are of less concern once the measured triaxial acceleration is considered: the acceleration measured on the below ground section is indistinguishable from the background measurements for all but a few cases. The differences in a_{ref} cannot justify such a large change in behaviour. In all three axes it looks as though there is a deviation in acceleration from the background for f between 60 and 100 Hz. However, closer inspection reveals that there is a similar increase in the background acceleration for the below ground measurements. Once this has been discounted as background noise, the only measurements which are above the background for the below ground case is a_z for frequencies between 525 and 600 Hz. Even here the loss in amplitude compared with the above ground case is two orders of magnitude.

Even with an anticipated increase in attenuation when the pipe is buried, this is an extreme change in behaviour between the below and above ground measurements. It should be noted that the magnitude of this attenuation does match that of the measurements in Section 3.4 which considered the attenuation of the noise profile of a leak over 4 m underground. Further work is needed here, measuring the below ground acceleration at shorter intervals or with more sensitive accelerometers and hydrophones to fully understand what is happening and to get a true value of the attenuation in the buried HDPE pipe. The sound source should be moved inside the pipe, since

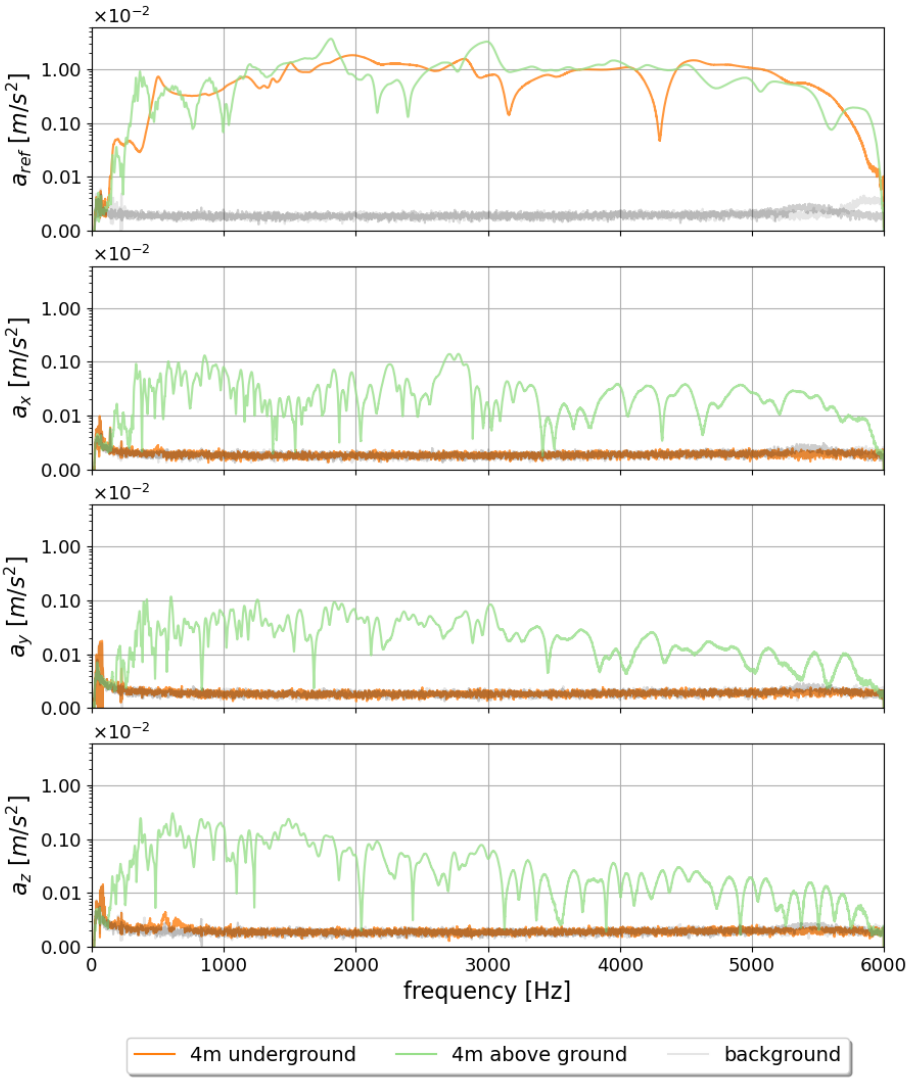

Figure 4.35: Spectrum of recordings for each accelerometer for above and below ground measurements.

the sand close to the shaker will have inhibited its ability to move the pipe wall.

4.4 Summary

In this chapter, the use of acoustics to extract the properties of plastic pipes has been attempted, including finding the age of the pipe from calculation of E. The complications and complexities of this endeavour have been shown, particularly the large errors in measuring the speed of sound in the pipe and the commensurate effect on leak localisation using traditional methods.

Further, the significant attenuation experienced by sound in plastic pipes has been measured. It has been shown how frequency dependent the attenuation in plastic pipes is, with greater attenuation at higher frequencies, including a 100-fold reduction in amplitude seen for transmission down 5 m of a straight, above-ground pipe at 5 kHz. The effect of various common features on the network has been explored, with flange joints having the largest attenuating effect of those studied and corners the least. The significant attenuation in buried pipes has also been shown. Low ($< 1,000$ Hz) frequencies were found to travel furthest on straight pipes, even though these were most affected by features on the pipe. This is most likely because higher order modes are attenuated more with distance, but the dominant breathing mode at low frequencies is strongly attenuated by breaks in the continuity of the pipe wall.

Based on these results, it was concluded that while acoustic loggers located at key points on the network may work for metal pipes and for very noisy or nearby leaks on plastic pipes, they are unlikely to be sufficient on their own to find smaller leaks on plastic pipes. The following chapters present an alternative methodology for use in highly attenuating pipes.

Chapter 5

Detection of Pipe Wall Damage with Low-Frequency Acoustics

The previous chapters have provided an introduction to the theory of sound wave propagation in water-filled pipes for the detection of existing leaks. However, the advent of smart no-dig and core drilling technologies, such as described in [221, 222], means that detecting the early signs of pipe wall damage has become an important research question as an enabler for optimal use of these no-dig maintenance solutions. Currently, detailed pipe wall inspection mainly requires ultrasonic scanning of the pipe wall [223, 224]. This gives a very accurate view of the pipe wall, but is slow and requires a good connection between the sensor and the pipe wall. Ultrasonic guided waves can also be used to detect defects in the pipe wall, although it lacks sensitivity with distance [225].

In this chapter, novel sensing options are investigated, that move beyond on-pipe accelerometers and hydrophones such that smaller leaks and defects can be detected. The use of the fluid velocity coupled with low-frequency acoustics is posited as a method of detecting damage to the pipe wall. This technology can be delivered with mobile robots such as that proposed by pipebots [181]. This technology is more practical for large scale pipe inspection than ultrasonic sensor technologies because it is based on sound waves with wavelengths that are much greater than the pipe diameter. These waves propagate considerable distance with little attenuation and do not experience the typical coupling problems associated with ultrasonic waves which limit the rate at which scanning can be undertaken, and the pipe conditions which it can inspect. The volume of data produced by this kind of low frequency acoustic scanning is also significantly lower than that produced by a full ultrasonic survey. It is proposed that this method would be used as a preliminary investigation method, to find regions of interest which could then be inspected in more detail either visually or ultrasonically. On a robotic platform, these three inspection methods could be used in conjunction for increased efficiency in terms of scan speed and data storage.

The problem of defect detection is a problem not only on the WDN but also on rising mains. From an inspection point of view, rising mains are more similar to pressurised water pipes than gravity sewers in some ways: any inspection vehicle needs to be resistant to pressurised fluids and acoustic propagation is in a pressurised water column. From the perspective of prototype testing, rising mains offer a more appealing prospect than the WDN due to the less demanding regulations for access (e.g. water quality is not a concern). As such, at this point this thesis shifts focus from water pipes to rising mains. The theoretical work should apply equally to both, but experimental work from here on has been conducted exclusively on rising mains.

5.1 Investigating the acoustic environment of rising mains

As a first step to understanding the situation, work was conducted measuring the acoustics of live rising mains. The data set described here was collected with the assistance of Wessex Water on a pair of large diameter rising mains which were known to be in need of repair - there have been three bursts on the pipes since 2014. These measurements allowed us to gain an insight into the acoustic environment of rising mains, in particular the effect of the pumping cycle used to move material through the pipes. Depending on the volume and consistency of pump noise between and within pipes, the pump noise has the potential to be useful as the sound source for acoustic analysis of the pipe.

5.1.1 Experimental setup

The Wessex Water site consists of two rising mains which travel next to each other in a tunnel for 6+ kilometers under a town with limited access points. The access point chosen was a large chamber accessible by manhole.

Measurements were taken using two PCB 393B04 accelerometers, with a sensitivity of 1 V/g. The accelerometers were attached at 3 different locations within the chamber, with one accelerometer placed on top of the pipe and the other to the side. Two of these measurement locations were on the 800 mm diameter pipe, in the centre of the chamber and within the tunnel, the other measurement was on the 1,100 mm pipe within the tunnel. Pictures of each of the three measurement locations are shown in Figure 5.1.

Within the chamber, the pipes were buried in concrete up to 1/3 of their height, whereas within the tunnel the pipes were resting on the floor. The measurement in the access chamber was to determine whether the change in conditions due to the larger surroundings and the encasement in concrete had a significant impact on the pipe wall vibrations. The measurements in the tunnel are assumed to be more representative of the acoustics of the majority of the pipe length; these measurement positions are only 1 m from the access chamber due to safety-related access restrictions.

(a) (b) (c)

Figure 5.1: Location of accelerometers when measuring pump noise on the large diameter rising mains managed by Wessex Water: (a) 800 mm diameter pipe, in centre of access chamber, (b) 800 mm pipe, in tunnel, (c) 1,100 mm pipe, in tunnel.

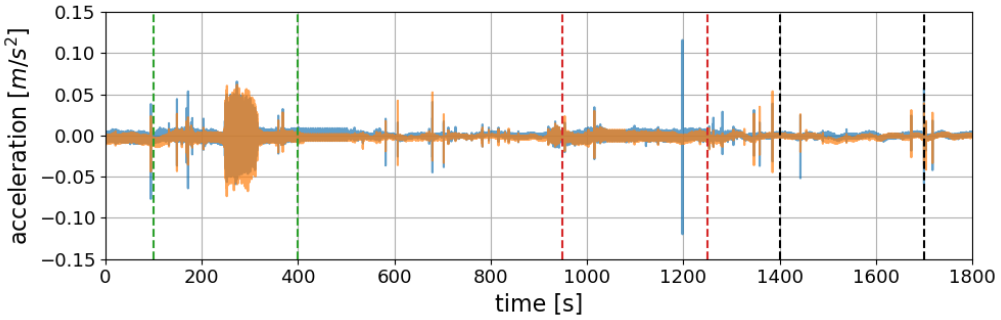

(a)

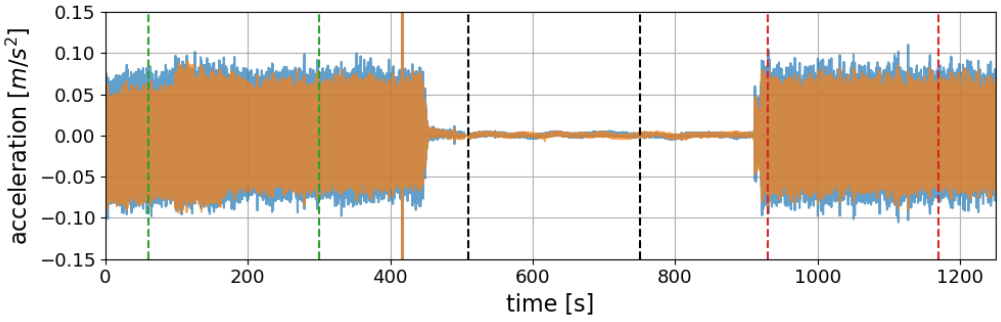

(b)

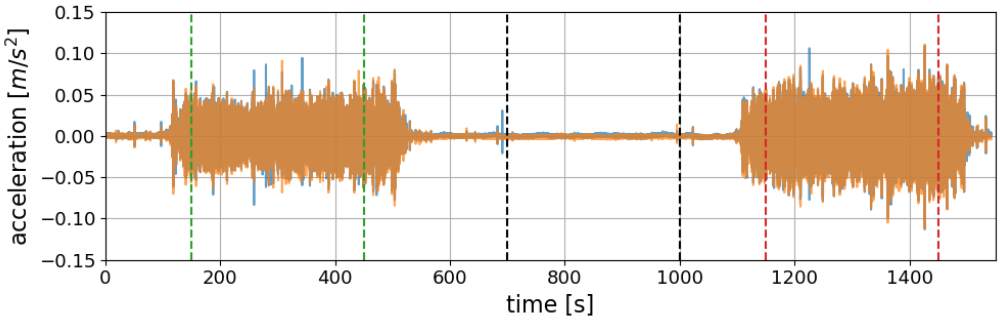

(c)

Figure 5.2: Recordings for each location on the Wessex Water pipes: (a) location a, 800 mm pipe within chamber, (b) location b, 800 mm pipe in tunnel, (c) location c, 1,100 mm pipe in tunnel. The measurement at the top of the pipe is shown in blue, the measurement at the side of the pipe in orange. The bounds of the regions of interest are marked by vertical dashed lines, the colour of which correspond to those used in the following plots.

This proximity to the semi-buried pipe sections may mean that there are more acoustic reflections within the pipe than in a longer straight section, however the discontinuities in the pipe at joints are likely to be a larger contributor to complexities in the acoustic environment.

The data was recorded using LabView via a NI DAQ (4431). The data was captured at a 2,000 Hz sample rate. The accelerometers were attached to the pipes magnetically.

Throughout this analysis, the different measurement locations are labelled a-c as per Figure 5.1.

5.1.2 Results

The time series recorded at each of the three locations on the Wessex Water pipes is shown in Figure 5.2 with a wide filter, from 10 to 990 Hz, applied to remove spurious data beyond the sam-

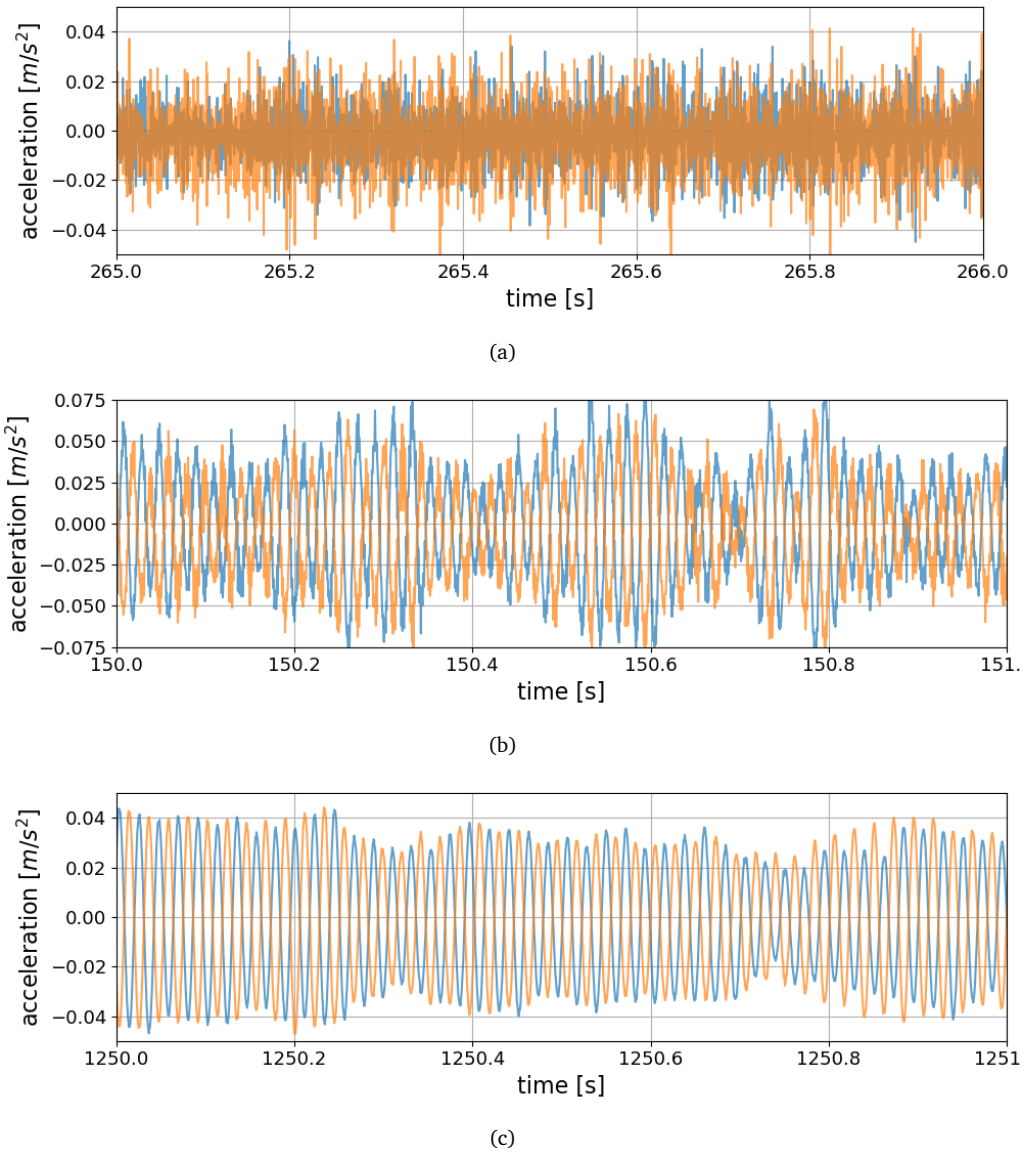

Figure 5.3: Recordings for each location on the Wessex Water pipes, zoomed in to see the behaviour during a period when the pumps were running: (a) location a, 800 mm pipe within chamber, (b) location b, 800 mm pipe in tunnel, (c) location c, 1,100 mm pipe in tunnel. The measurement at the top of the pipe is shown in blue, the measurement at the side of the pipe in orange. Note the change in scale on the y axis.

pling rate of the data, and to remove very low frequency noise. The noise from the pumps is clearly visible in subplots 5.2(b) and (c), with a marked increase in amplitude. The time stamps of these regions have been compared with logs from the pumping station and they do correspond to the timings of the pumps turning on and off. There is some increase in amplitude in the recording at location (a) (Figure 5.2(a)) when the pumps were turned on, although there is more background noise at this location and a lower acceleration measured due to the pumps. Again, the pumping station logs have been used to designate the regions between the coloured dashed lines as containing pump noise. The significantly lower wall acceleration measured at location (a) as opposed to (b) and (c) may be because at this position the pipe is buried up to half its height in concrete, which would reduce the freedom of the pipe wall. In each of these time series, two sections have been selected within the pump noise for further analysis, along with one section outside of the pump noise to serve as a reference measurement of the background noise. The boundaries of these

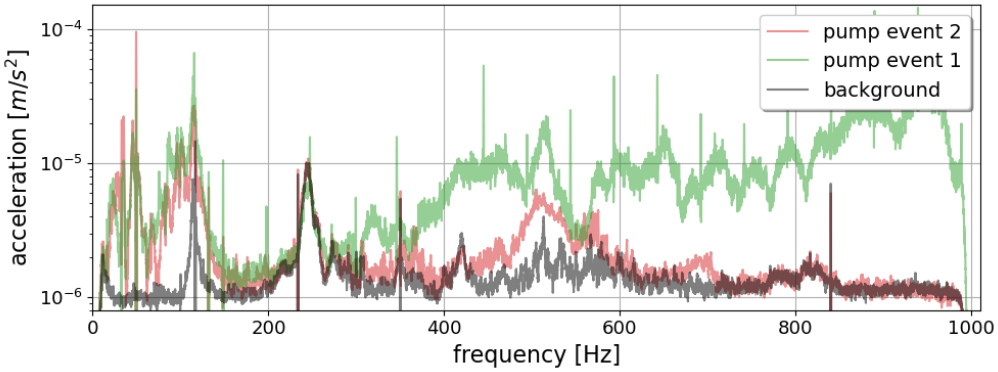

(a)

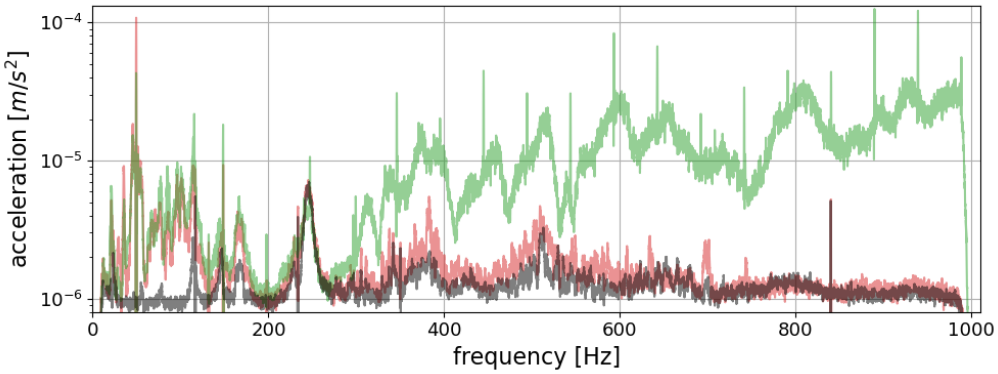

(b)

Figure 5.4: Spectrum calculated for each of the regions designated in Figure 5.1(a), coloured by region. Here (a) shows the result for the accelerometer on top of the pipe while (b) shows the result for the accelerometer on the side of the pipe.

regions are shown with dashed lines in each subplot, the colours of which match the traces used in Figures 5.4, 5.5 and 5.6.

A small section of each of these plots is shown in Figure 5.3, showing a section of the time series where the pumps are on. In Figures 5.3(b) and (c) the measurements at the two accelerometers are out of phase for the entirety of the segment. Inspection of the rest of the time series shows this behaviour continuing while the pumps are on. There is a higher frequency component in Figure 5.3(b) which does not overwhelm the behaviour. This is in strong contrast with the time series recorded at location (a) (Figure 5.3(a)), where the signal is dominated by much higher frequencies and there is no such relationship between the phase of the signals from the two accelerometers.

The spectrum of each of the regions where the pumps were known to be on was calculated, along with a section of the same length as a reference background measurement. These are shown for each of the three locations in Figures 5.4, 5.5 and 5.6.

As expected given the visibly tonal nature of the time domain signals in Figure 5.3, the spectra for locations (b) and (c) (Figures 5.5 and 5.6 respectively) show a peak at 50 Hz which is approximately an order of magnitude larger than any other frequency components in these spectra. This peak is very similar for both of the two pump events at each location. The spectra recorded at location (b) (Figure 5.5) show a much wider peak around 50 Hz than the recordings at location (c), with an acceleration amplitude of more the 1×10^{-4} m/s^2 (an equivalent of $\sim 0.3 \times 10^{-6}$ m/s in terms of the radial acoustic velocity) for most of the range from 15 to 60 Hz, and an amplitude

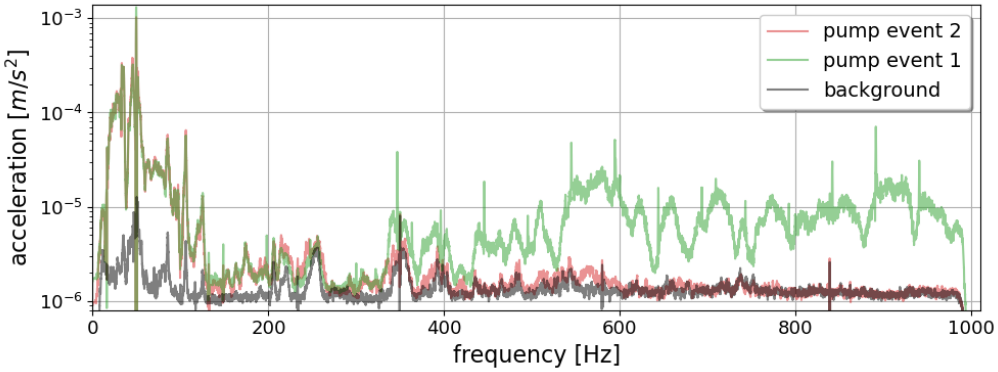

(a)

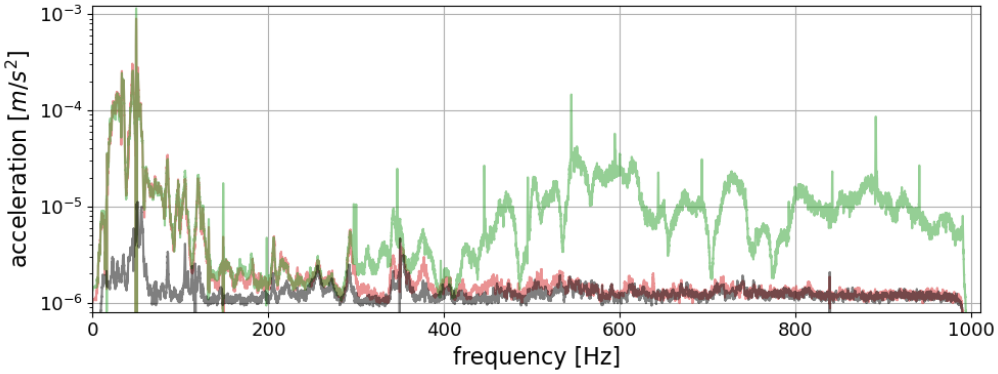

(b)

Figure 5.5: Spectrum calculated for each of the regions designated in Figure 5.1(b), coloured by region. Here (a) shows the result for the accelerometer on top of the pipe while (b) shows the result for the accelerometer on the side of the pipe.

an order of magnitude above the background for the range 15 to 100 Hz. The two spectra from location (c) (Figure 5.6) show a similar narrow peak at 50 Hz. Both of these locations are in the tunnel with (b) on the 800 mm diameter pipe and (c) on the 1,100 mm diameter pipe. Without more results it is difficult to say whether the difference in behaviour on the two pipes is due to specifics of how the accelerometers were attached or due to the difference in pipe geometry.

At higher frequencies, pump event 1 at location (b) (Figure 5.5) shows a strong divergence from the background noise, while pump event 2 shows almost no change in behaviour from the background for frequencies greater than 200 Hz. Again, without more information it is difficult to determine the cause of these discrepancies, although it seems likely that there was some other noise source present during pump event 1. In retrospect, further measurements taken at a distance from the pipes would have been a useful point of reference, in order to filter out transitory background noise sources. The recordings taken at location (c) (Figure 5.6) show more consistent high frequency components between the two pump events, with several broad peaks that are clearly above the background measurements, for example at 200, 330, 490 and 660 Hz, as well as above 760 Hz.

Returning to the measurements at location (a), which Figure 5.3(a) has shown is more complex than the measurements at locations (b) and (c), Figure 5.4 shows the spectra for the pump events at this location. There is some tonal behaviour at 50 Hz, however the peak amplitude at 50 Hz is only 1×10^{-4} m/s^2 here, as opposed to 1×10^{-3} m/s^2 at locations (b) and (c). Furthermore, the background has much higher amplitude components, for example at 120 Hz and at 245 Hz, than

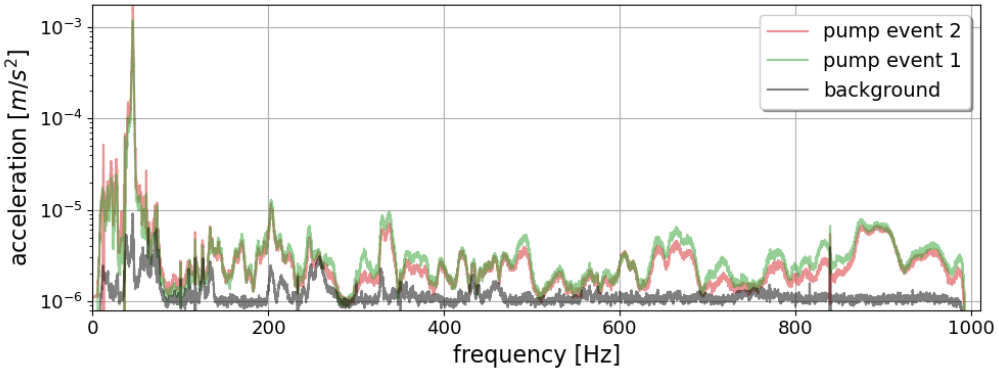

(a)

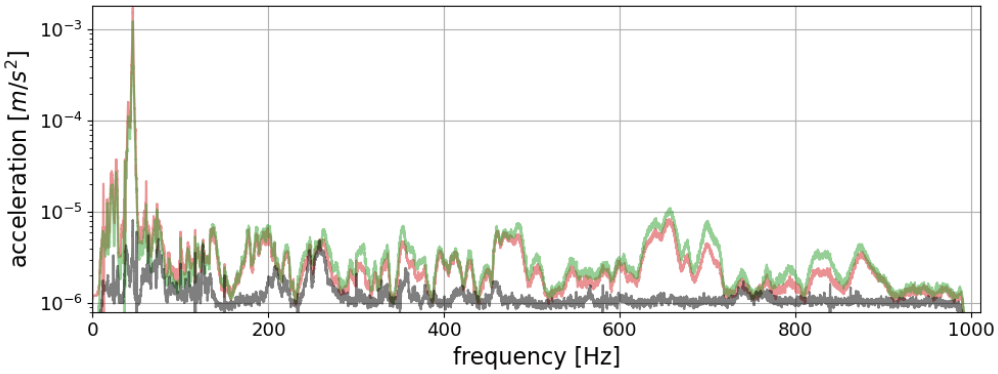

(b)

Figure 5.6: Spectrum calculated for each of the regions designated in Figure 5.1(c), coloured by region. Here (a) shows the result for the accelerometer on top of the pipe while (b) shows the result for the accelerometer on the side of the pipe.

for the other two locations. The higher amplitude of the background components is probably due to the pipe being half buried in concrete, due to which it is coupling more strongly to background noise sources. It is interesting that there is a similar increase in amplitude for frequencies above 400 Hz in pump event 1 as was seen in Figure 5.5 for location (b), adding credence to the theory that this is caused by another transitory but repeating background noise source, which could be road noise.

The spectra at the two accelerometers, positioned on the top and side of the pipe in subfigures (a) and (b) respectively for Figures 5.4, 5.5 and 5.6 show small differences in their spectra, but in general are very similar.

To summarise, these experiments with the wall acceleration on pipes several kilometres from a pumping station have shown a tone at 50 Hz measured at 6 locations covering different pipe diameters, surroundings and positions around the pipe circumference. The background noise was significantly louder for the half-buried pipe, making the tonal behaviour impossible to see in the time series analysis, although it was visible in a frequency analysis of the data. Beyond this difference in the background noise, there was also the broader peak seen for the larger diameter pipe, stretching from 15 to 100 Hz (Figure 5.5) as opposed to the narrow peaks in the spectra seen at 50 Hz for the other two locations. Without further measurements it is difficult to determine the cause of this signal.

To understand this behaviour better it would be useful to take reference measurements close to

the pump, in order to understand how the pump noise is changing from the source to this detection point. Similarly, it would be useful to measure at more points at varying distances from the pumps. As ever, longer measurements allowing more of an understanding of transient background noise sources as well as measuring more pump cycles would be beneficial.

5.1.3 Summary

Based on these recordings, it is clear that should pump noise be used as a sound source, any receiver would need to be focusing on very lower frequencies, of around 50 Hz since this is where the majority of the pump noise is. Conversely, should a different noise source be used these frequencies clearly propagate for large distances, rendering them similarly worth consideration, although in this case steps would need to be taken to remove 'background' pump noise from any recordings.

These conclusions are based on a single pump source and two similar pipes, therefore while these low frequencies can be used as a focus for initial investigations, further work is required to corroborate the use of low frequencies. Nevertheless, the results of these experiments suggest that the pipe wall vibration is detectable at these frequencies with a standard measurement accelerometer, i.e. the corresponding fluid acceleration and acoustic velocity can also be measured inside the pipe with a suitable accelerometer device suspended in fluid.

5.2 Finding a parameter sensitive to defects

The work of the previous section has highlighted low frequencies as a viable avenue of exploration for long distance inspection of rising mains, either using a synthetic sound source or the pump noise itself, since these low frequencies are clearly propagating effectively through the pipe system. However, accelerometers mounted on the pipe wall are not an ideal means of inspecting the pipe system, for all the reasons highlighted in Chapter 2. In addition to this, the accelerometers used in Section 5.1 were much more sensitive than the accelerometers normally used for leak detection.

In order to investigate alternatives to measuring the wall acceleration, the modelling work from Chapter 3 was modified and extended to consider the effect of defects on the in-pipe acoustics. From this, the parameter most sensitive to the presence of defects could be determined. Chapter 6 reports on the experimental work undertaken to verify these results.

This section focuses on a COMSOL Multiphysics®[193] model of a 310 mm diameter ductile iron (DI) pipe, with wall thickness 10 mm. This is representative of a reasonable proportion of the rising main network, and matches the pipe available for further testing as described in Chapter 6. The effect of deviating from these dimensions and materials is considered in Section 5.4.

5.2.1 The model

To investigate the system further, a numerical model of a pipe was created in COMSOL Multiphysics®. Initially this was a defect-free pipe, of diameter 800 mm, which was compared with the measurements taken in Section 5.1 to determine a realistic source amplitude. The diameter of the model was then reduced to 310 mm to match the pipe available for testing and two different shapes of defect were introduced to the pipe wall. The effect of these defects on the acoustic environment considered. From this decisions could be made for designing a more sensitive sensor for defect detection in pipes.

The model is an extension of the work already described in Section 3.1, so is not described in detail again here. The radial acceleration on the pipe is shown in Figure 5.7 for a planar source located at -20 m with a range of amplitudes from 10 to 1,000 Pa on a pipe with radius 800 mm and length 56 m. Adjusting the amplitude of this source led to the choice of 600 Pa as the source excitation pressure, since this led to a wall acceleration of the same order as the 0.02 $\mathrm{m/s^2}$ measured in Section 5.1.

This model was adjusted to match more closely the pipe available for testing, the relevant parameters are provided in Table 5.1 and Figure 5.8(a) shows a schematic of the setup. This table includes the dimensions of the two defects modelled: a hole in the pipe wall and thinning of the pipe wall. The length of the pipe in the model was set to 56 m to make it greater than the acoustic wavelength and to help control the reflections from the pipe ends while maintaining fast solve times. An analysis of the mesh chosen is provided in Appendix E.

Three pipe models were set up and run:

i) an intact pipe without any wall defects,

ii) a pipe with localized wall thinning to 1/3 of its normal thickness,

iii) a pipe with a wall hole of radius 0.01 m.

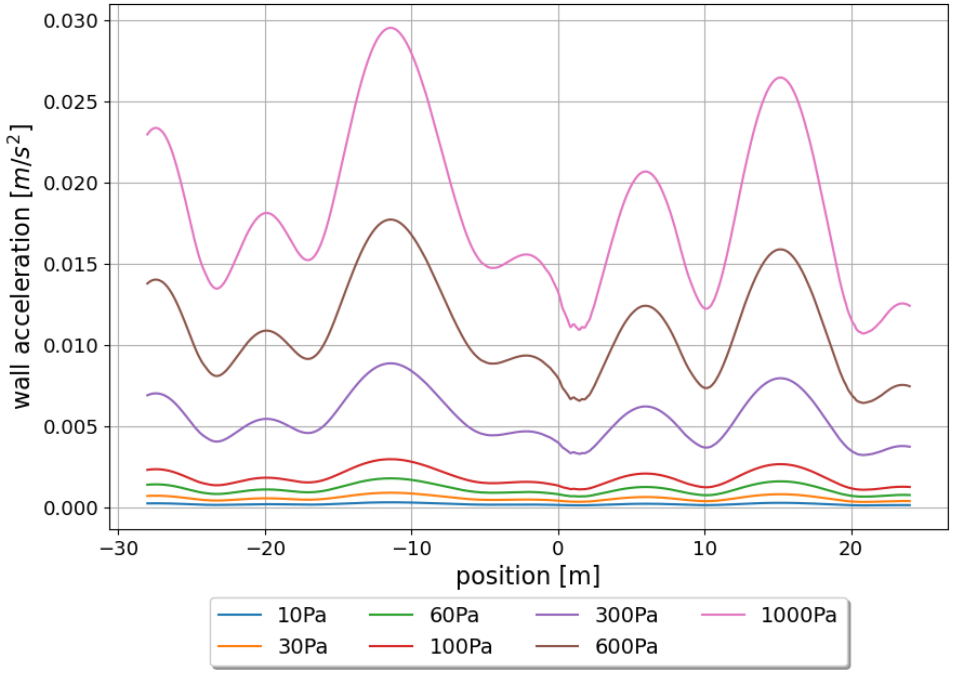

Figure 5.7: Radial acceleration on the surface of an 800 mm pipe with planar sound sources of the amplitude provided.

Table 5.1: The values of key parameters used in the COMSOL Multiphysics model.

property	value	unit	comment
Young's modulus	172	GPa	pipe material:
loss factor	0.0015	-	DI
Poisson's ratio	0.275	-	
density	7150	kg/m^3	
Young's modulus	1	GPa	pipe material:
loss factor	0.05	-	HDPE
Poisson's ratio	0.4	-	
density	950	kg/m^3	
length	56	m	pipe dimensions
inner diameter	0.31	m	
wall thickness	10	mm	
hole diameter	15	mm	1/20 pipe diameter
cutout depth	6.6	mm	2/3 pipe thickness

A section of the mesh around the defects are shown in Figures 5.8(b) and (c) for model configurations (ii) and (iii). The construction of the hole in the pipe wall was a simple case of removing a cylinder of the appropriate thickness from the pipe wall. The pipe wall thinning was constructed by removing a sphere of radius

In all of these models the frequency response to a planar pressure source operating at 170 Hz was considered. At this frequency the wavelength in water is approximately 8.6 m, considerably greater than the pipe's diameter of 0.31 m. This frequency was chosen based on an analysis of the sensitivity of multiple frequencies, provided in Section 5.4.2.

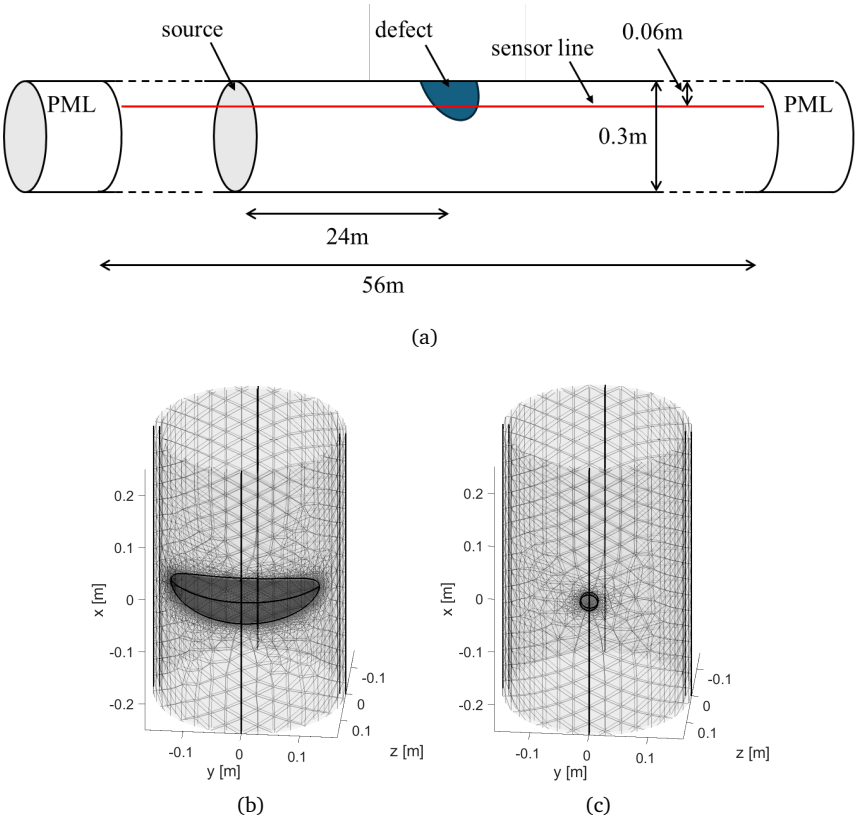

Figure 5.8: The model. (a) shows a schematic of the model, (b) and (c) show the mesh around the two defects modelled: thinning of the pipe wall and a hole in the pipe wall respectively.

Table 5.2: The maximum percentage change in the absolute value each variable, v, shown in Figure 5.9 for each type of defect. Calculated as the maximum difference in v along the axial coordinate divided by the maximum of v along that coordinate.

defect	a_{wall}	p	v_x	v_y	v_z
hole	5.0	0.7	0.4	410	45
cutout	0.4	0.2	0.2	7800	37

5.2.2 FEM results

The amplitude and phase of the pipe wall acceleration, pressure in the fluid column and the acoustic velocity in all three axes were compared. This comparison is provided in Figure 5.9 for each of the three cases modelled, along with a quantitative comparison of the maximum difference caused by each type of defect for each parameter in Table 5.2. The acoustic pressure and velocity components shown were calculated along a line in the fluid offset 0.06 m from the defective pipe wall (this is the distance used in the experiment described in Chapter 6, and is shown in Figure 5.8(a)).

It should be noted that the described model does not account for the attenuation in the fluid and pipe wall, however for metal pipes this effect should be minimal.

The results presented in Figures 5.9 (a), (b) and (c) demonstrate that the wall acceleration, a_{wall}, acoustic pressure, p, and axial fluid velocity, v_x, are relatively insensitive to the presence of these defects. This can be seen in Table 5.2 where the maximum difference caused by a defect over the length of the pipe is less than 1% of the amplitude of each parameter in all cases except a_{wall}, where it is less than 5%. In contrast, the horizontal fluid velocity, v_y, (Figure 5.9 (d)) shows a

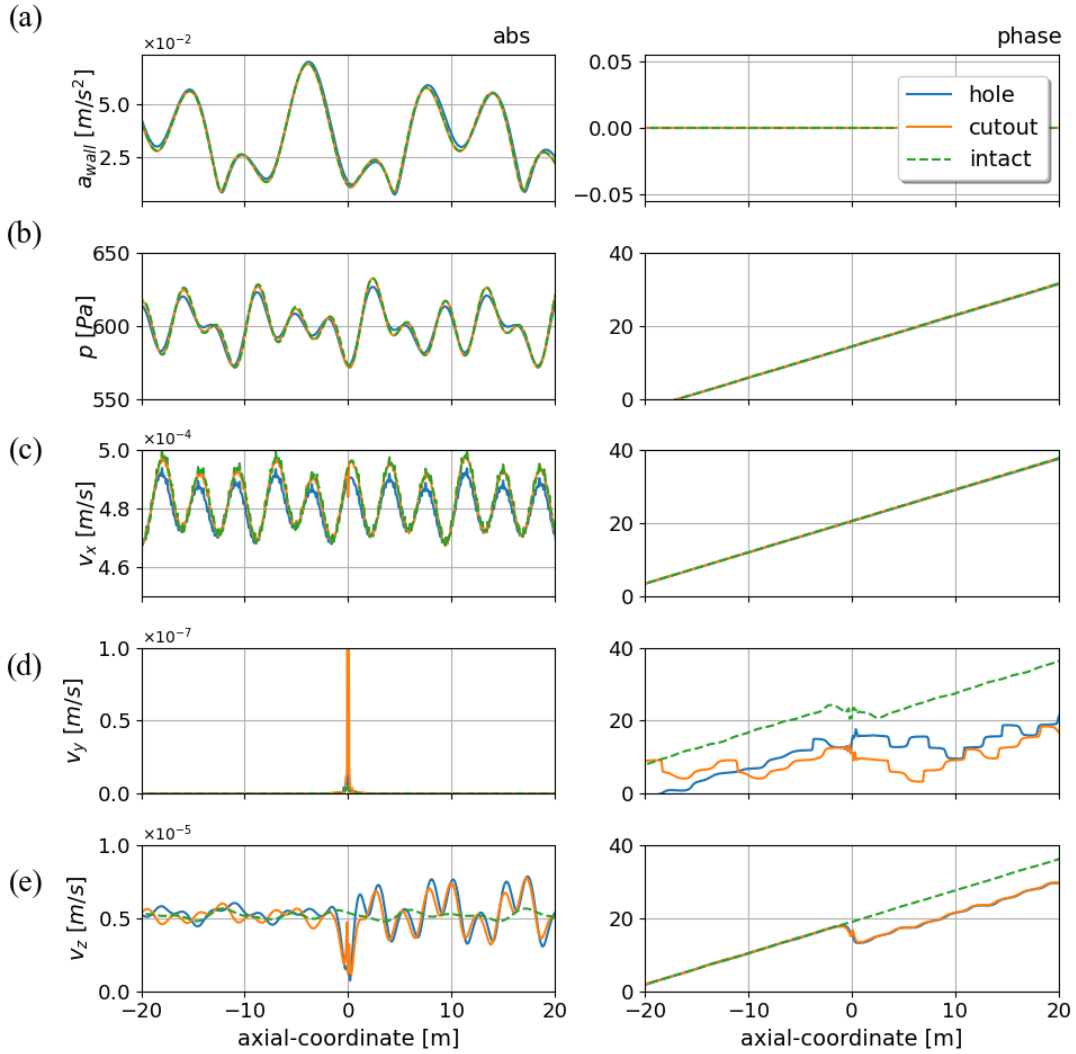

Figure 5.9: The results from the numerical simulation for sound propagation along an 'infinite' pipe with and without a defect. The amplitude and phase are shown for: (a) the wall acceleration; (b) the acoustic pressure; (c) the axial component of velocity (v_x); (d) the horizontal component of velocity (v_y); and (e) the vertical/radial component of velocity (v_z). The results in (b-e) are for a receiver line that runs 0.06 m from the edge of the pipe closest to the defect. The defect is at 0 m and the planar sound source is at -24 m, oscillating at 170 Hz.

pronounced localised increase in its amplitude and much less localised change in the phase when a defect is present. Similarly, the amplitude of the vertical component of the acoustic velocity vector in the fluid, v_z (see Figure 5.9 (e)) shows a marked change in behaviour in the presence of a defect: its amplitude increases considerably and oscillates as a function of the axial position, x, while there is a phase shift in v_z downstream of the defect. The change in amplitude of v_z can be detected at a significant distance to either side of the defect, although it is again most pronounced downstream from the defect. The maximum percentage change in v_z due to a defect is significant: between 30% and 50% depending on the type of defect (see Table 5.2). Given the pipe geometry, v_y and v_z were combined to form a 'radial' velocity, which is the amplitude of the velocity on the pipe cross-section, where

$$v_r = \sqrt{v_x^2 + v_y^2} \tag{5.1}$$

To understand better the behaviour of the pressure and velocities, the amplitude of these quantities were plotted across a section of the pipe as shown in Figure 5.10. These plots show that the acoustic pressure (Figures 5.10(a), (b) and (c)) is visibly unaffected by the presence of a defect across the entire width of the pipe so that it would be difficult or impossible to use this information to detect the wall thinning or perforation. On the other hand, the v_r shows a clear change in its behaviour when the defect is present (Figures 5.10(d) and (f)) as opposed to when there are no defects on the pipe (Figure 5.10(e)). In the presence of the defect the symmetry of the system is broken in the entire region shown, and close to the defect there is strong increase in the velocity. This localised increase is different for the two defects, with the hole (Figure 5.10(d)) showing a larger increase than the pitting defect (Figure 5.10(f)). The same information is shown for slices across the pipe in Figures 5.11 and 5.12.

These results all rely on measuring changes in the velocity of the order 10^{-5} m/s, for velocities that are of a similar order. This will require a sensitive velocity sensor, in addition to minimal background noise due to external sources such as road noise and fluid motion through additional features on the pipe. The magnitude of these external sources on the background fluid velocity has not been studied previously; doing so will form an important future step in the development of the acoustic velocity vector as a method for detecting defects in pipes.

5.3 An analytical consideration

Here we take a brief detour to consider these findings, that the radial component of the fluid acceleration is more sensitive to defects than the pressure or axial acceleration.

For waves with frequencies below the ring frequency, defined in Equation 2.6, the fluid-borne waves are planar. A planar wave travelling along the x-axis can be expressed in terms of pressure as

$$p(x,t) = p_0 e^{i(\omega t - kx)} \tag{5.2}$$

Extending this to find the total pressure, p_t, near a damaged region requires incorporating the acoustic field due to scattering from the defect p_s, so

$$p_t(x,y,z,t) = p(x,t) + p_s(x,y,z,t). \tag{5.3}$$

At low frequencies $|p_s| \ll |p|$ it can be challenging to detect the presence of a defect using the pressure alone. If, instead, we consider the acoustic velocity

$$\boldsymbol{v} = \frac{\boldsymbol{\nabla p}}{i\omega\rho_f}, \tag{5.4}$$

with ρ_f as the density of the fluid, we can see that, combining equations (5.3) and (5.4), the total velocity in the y and z directions comes from the scattering defect, while the x velocity component is a combination of the planar and scattered velocities. The amplitudes of v_y and v_z are negligibly small in the pipe without a defect because of the form of eq. (5.2). The presence of the defect in the pipe wall causes v_y and v_z to increase significantly, as is illustrated in the following sections, to become measurable with an AVVS.

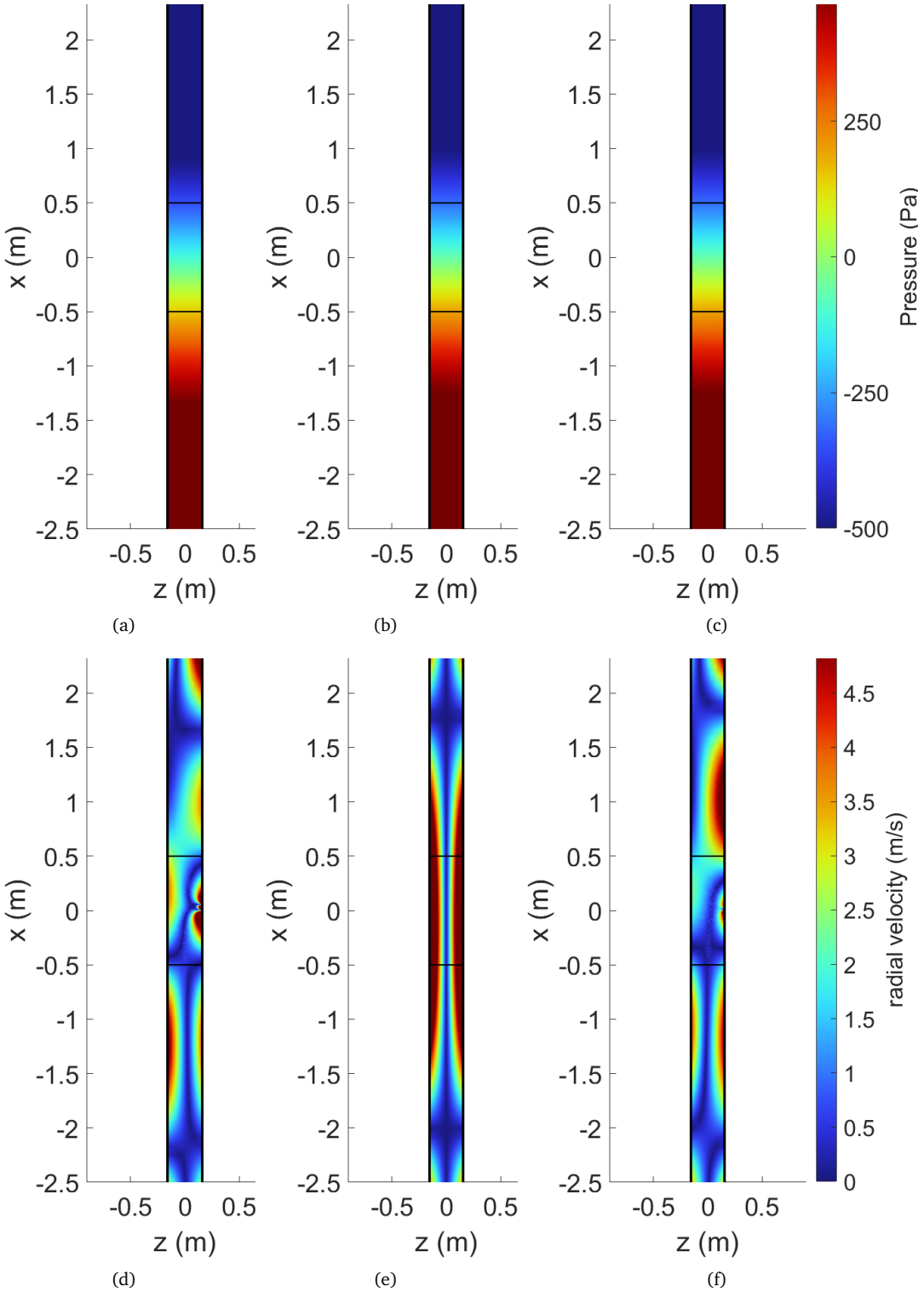

Figure 5.10: The results from numerical simulations with a 170 Hz planar source, for sound propagation showing the amplitudes of the acoustic pressure (a-c) and radial fluid velocity (d-f) for a cut plane through the middle of the pipe, showing 2.2 m to either side of the defect at 0 m. (a) and (d) the effect of pipe wall thinning. (b) and (e) pipe with no defect. (c) and (f) the effect of the hole in the pipe wall.

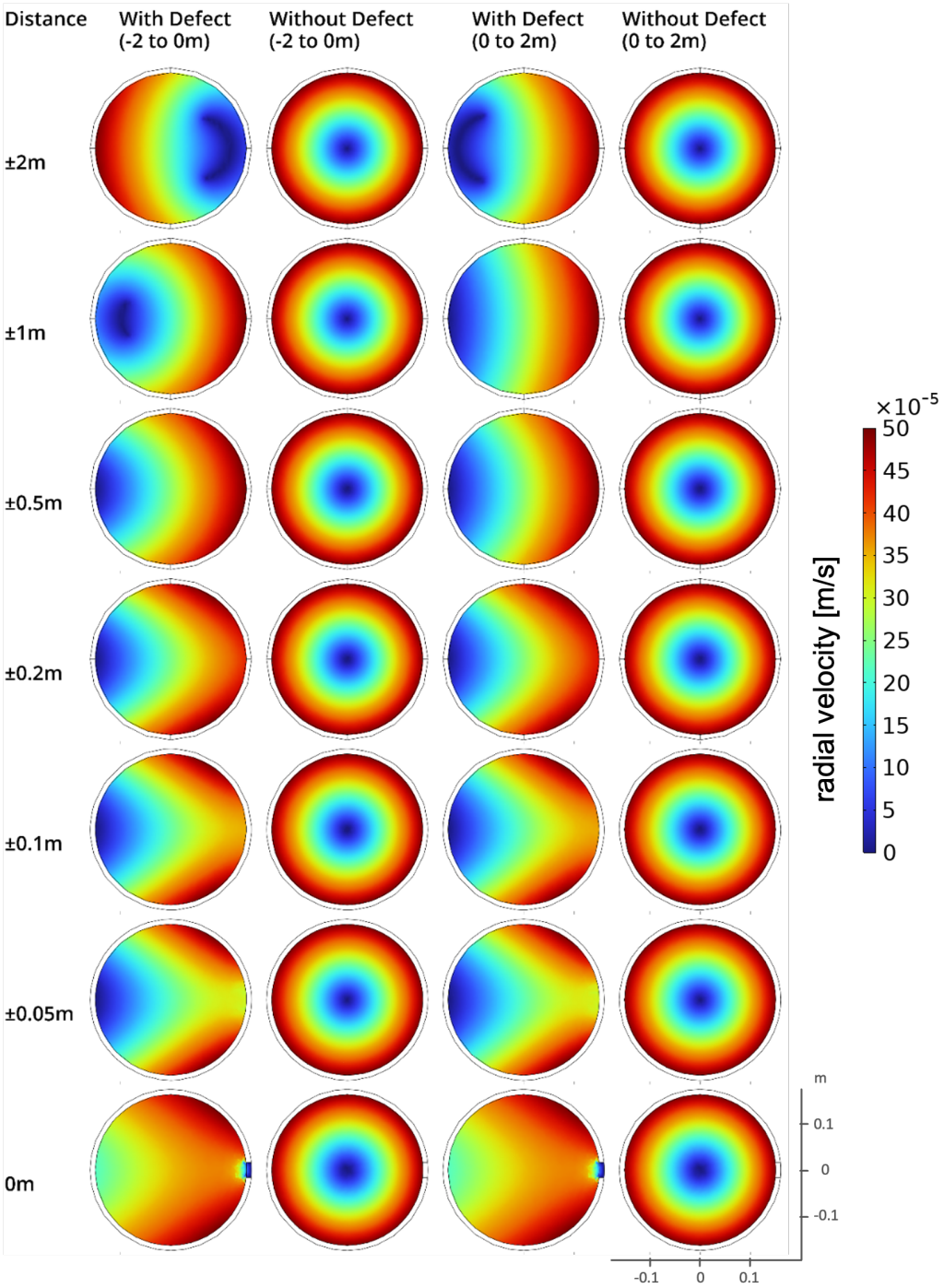

Figure 5.11: The results from numerical simulations for sound propagation with a 170 Hz planar source, showing the amplitude of the radial velocity at slices across the pipe for a pipe with a hole in the side.

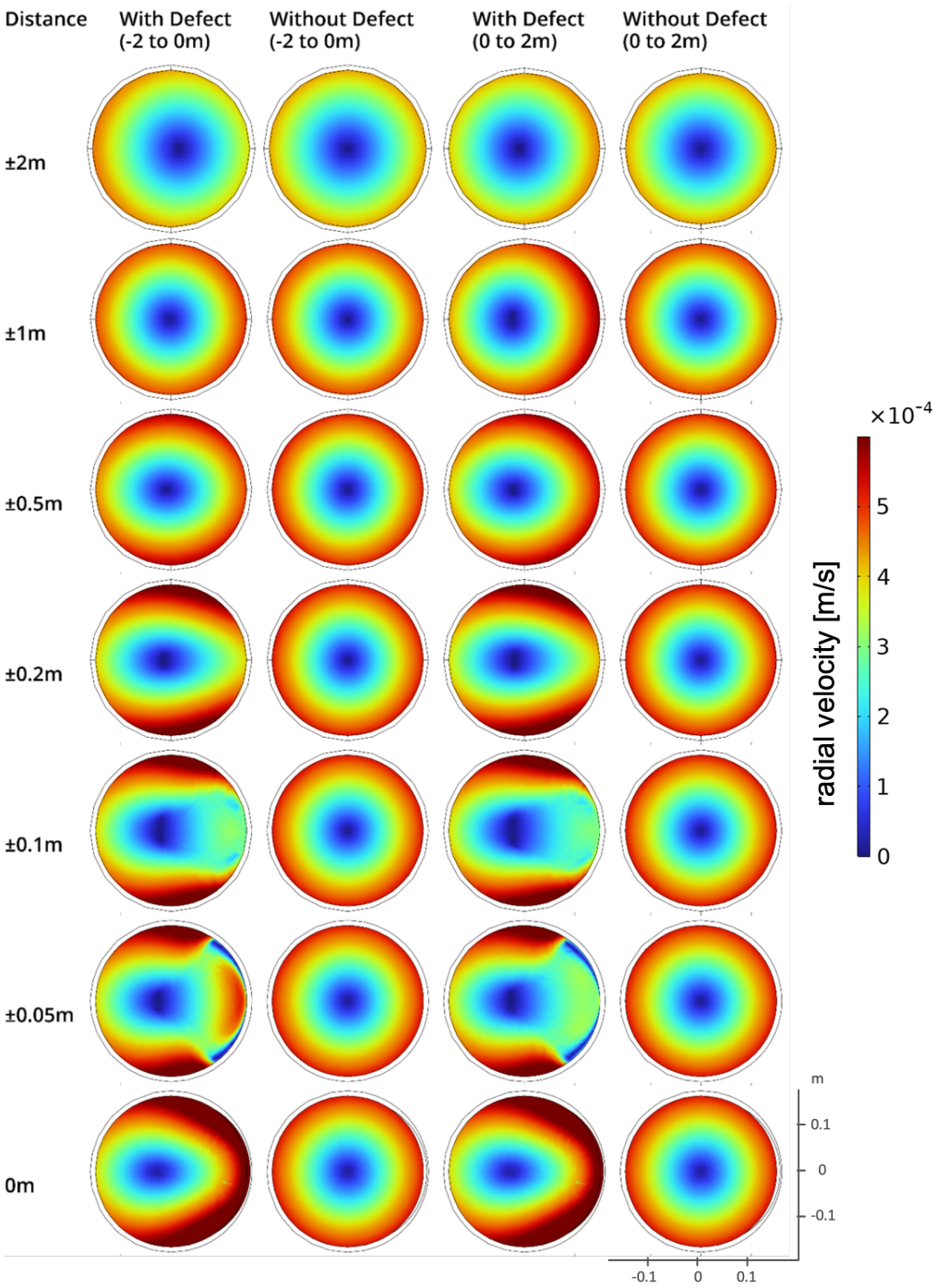

Figure 5.12: The results from numerical simulations for sound propagation with a 170 Hz planar source, showing the amplitude of the radial velocity at slices across the pipe, for a pipe with a pitting defect in the side.

5.4 The sensitivity of the radial velocity as a method for defect detection

The above results stand as a proof of concept. It was considered beneficial to run similar models investigating the effects of pipe material, dimensions and source frequency. Each of these are covered in the following sections. The pipe length was found to have minimal effect - as should be the case if the PMLs are set up appropriately to model an infinite pipe.

5.4.1 Pipe material

The model covered in section 5.2 was run for a pipe made of HDPE and DI, with the wall thinning defect described previously. The material properties are those provided in Table 3.2. A comparison of the radial velocity across a slice of the pipe, cutting through the defect is shown in Figures 5.13 and 5.14 for a model of a 50 m long pipe, with source frequencies of 65 and 170 Hz and pipe diameter of 310 mm. For each frequency and pipe material, the result for the wall thinning defect is displayed next to the result for an intact pipe.

The presence of the defect has a clear effect in all four of these cases. The impact is clearest in the DI pipe, with a localised increase in radial velocity close to the defect for both source frequencies shown here. For the 65 Hz source this is an increase from a consistent background v_r of approximately 2×10^{-6} m/s to approximately 1×10^{-5} m/s within 0.1 m of the defect. For the 170 Hz source there is a higher amplitude standing wave in the pipe in the background case,

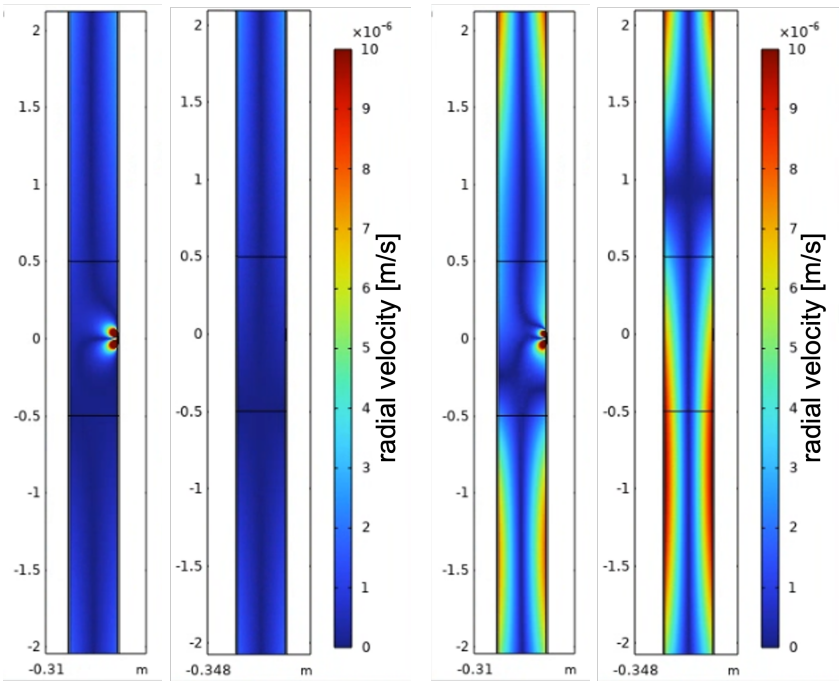

Figure 5.13: Radial velocity predicted for an HDPE pipe with diameter 310 mm, length 50 m, with a source located at -10 m from the defect at 0 m. (a) shows the results with a 65 Hz source and a pitting defect at 0 m, (b) a 65 Hz source and no defect, (c) a 170 Hz source and a pitting defect at 0 m, (d) a 170 Hz source and no defect. Note the change in range between figures.

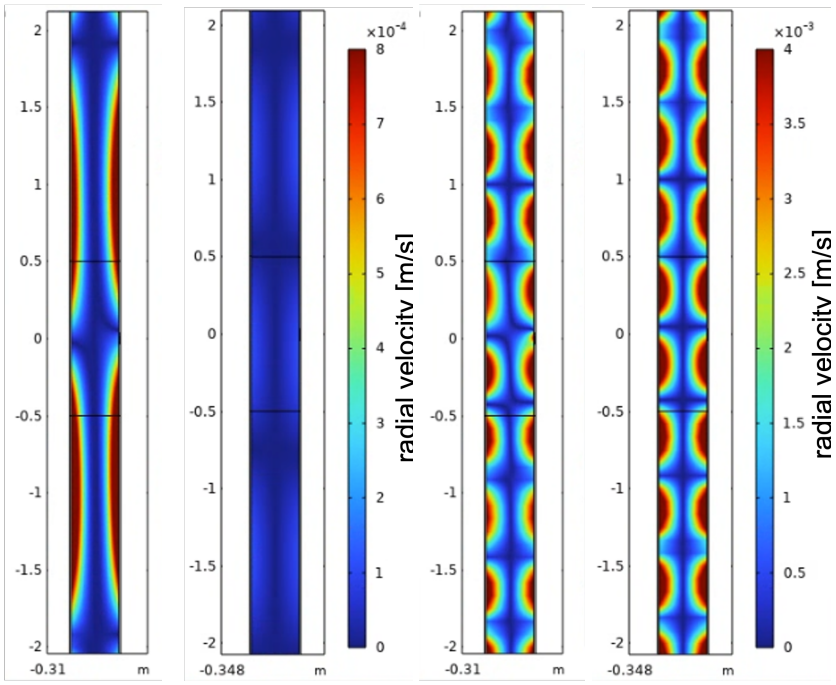

(a) (b) (c) (d)

Figure 5.14: Radial velocity predicted for an HDPE pipe with diameter 310 mm, length 50 m, with a source located at -10 m from the defect at 0 m. (a) shows the results with a 65 Hz source and a pitting defect at 0 m, (b) a 65 Hz source and no defect, (c) a 170 Hz source and a pitting defect at 0 m, (d) a 170 Hz source and no defect. Note the change in range between figures.

however the antinode of this standing wave is shifted by 1 m from its position in the intact pipe to coincide with the location of the defect. The defect itself leads to a similar increase in v_r to approximately 1×10^{-5} m/s within 0.1 m of the defect. The shift in antinode for the 170 Hz source may be detectable in a pipe with strong internal reflections such that an obvious standing wave is set up, however the large number of reflections in a complex pipe network would be more likely to obscure the signal from the defect itself. The strong localised increase in v_r for the 65 Hz source is more likely to be detectable, although given that it does not influence the entire pipe cross section at the defect position, any sensor would need to scan close to the pipe wall (within 0.1 m in this case). This should be considered in any sensor design decisions.

The impact of the defect on the HDPE pipe (Figures 5.14(a), (b), (c) and (d)) is more subtle and may prove more difficult to detect. For the 65 Hz source, substantially higher amplitude standing waves are set up in the pipe when there is a defect in the pipe wall, with the antinode of these waves sitting at the location of the defect. In the model, these higher amplitudes continue for the length of the modelled pipe. There is no localised increase in v_r close to the defect for the HDPE pipe with a 65 Hz source. For the 170 Hz source in the HDPE pipe, the antinode of the standing wave also shifts slightly to align with the defect. In this case, the antinode was close to the defect position in the intact pipe, consequently, this shift is more difficult to see, demonstrating an obvious issue with such a means of defect detection. There is also a localised increase in v_r, from 0.5×10^{-3} m/s to 4×10^{-3} m/s within 0.05 m of the defect. This should be observable to a sensor scanning along the edge of the pipe given that the antinode of the standing wave has also aligned with the defect. However, it is a more subtle difference than those predicted to occur in a DI pipe.

Both of these models indicate that the impact of the defect is localised, such that any sensor would need to scan close to the pipe wall (within 0.05 m). They also indicate that different source frequencies may be appropriate for different pipe materials, with a 65 Hz source showing a clearer defect 'signature' for DI, while a 170 Hz source shows a more identifiable effect for an HDPE pipe.

5.4.2 Wider frequency range

The choice of frequency up to this point has been based on the field work reported in Section 5.1, which was a very small survey of pump noise in a specific pair of rising mains which cannot be taken as representative.

The previous section considered the response of HDPE and DI pipes to a wall defect with a 65 Hz and a 170 Hz source and has demonstrated that different frequency ranges are likely to be of interest for different pipe materials. Given that the focus of the remainder of this project is on DI pipes, this section considers the frequency dependence of the response of a DI pipe to a wall defect and to a hole in the pipe wall. The models from Section 5.2 were run for a selection of frequencies between 65 and 1000 Hz. The lower end of these frequencies were chosen to be 65, 130 and 170 Hz, to cover the range 50 to 200 Hz while avoiding multiples of the mains frequency in the UK (50 Hz), which can be a significant source of background noise during experiments.

The results for the radial velocity for slices across the pipe at the position of the wall thinning and hole are shown in Figures 5.15 and 5.16 respectively. The same results for an intact pipe have been plotted as subfigures (i) to (p) in both figures for reference purposes.

Figures 5.15 (a), (b), (c) and (d) (frequencies 65, 130, 170 and 200 Hz) show a similar pattern of behaviour, with a strong increase in the radial velocity close to the thinner area of pipe, extending to approximately half the pipe diameter in all directions. There is also a shift in the standing wave in the pipe, with the minima of the standing wave moving to coincide with the wall thinning. This can also be seen in Figure 5.16 for the hole in the pipe wall, although the increase in radial velocity is even more localised, extending only approximately 0.05 m from the pipe wall.

For frequencies higher than 200 Hz, the standing waves in the pipe tend to overwhelm the signal from the defect. There is still a localised increase in v_r, but it is only visible when the standing wave does not coincide with it, as is the case for the 800 Hz source in Figures 5.15 (g) and 5.16 (g). This would make deploying a sensor to scan along the pipe wall challenging, as the SNR would be low.

Based on this analysis, efforts will continue to focus on very low frequency sources, with frequencies less than 200 Hz.

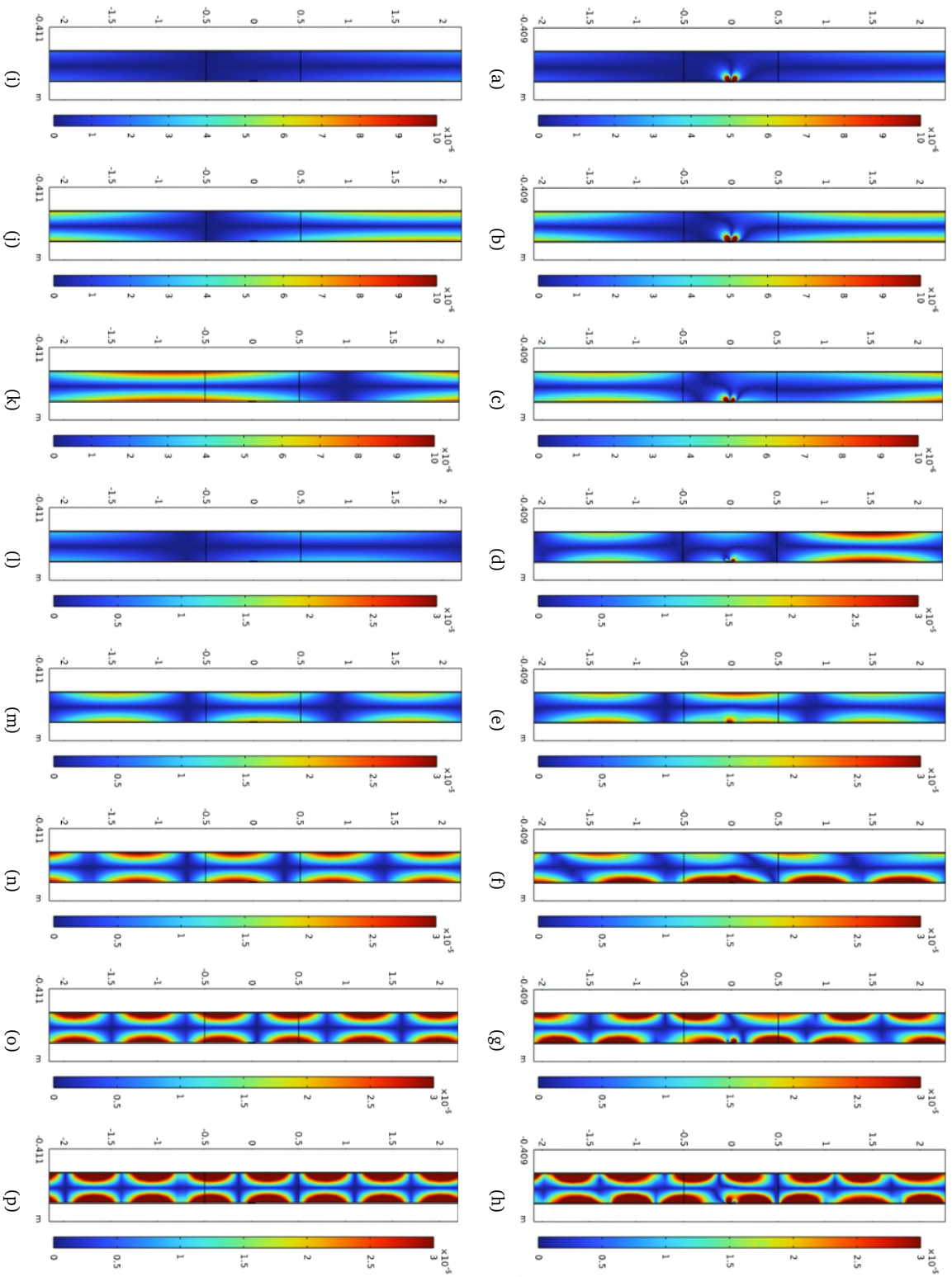

Figure 5.15: Radial velocity profiles for DI pipe for varying frequencies where there is pipe thinning on the side of the pipe. Results for an intact pipe are shown in (i) to (p) for reference. The frequencies in each plot are (a, i) 65 Hz, (b, j) 130 Hz, (c, k) 170 Hz, (d, l) 200 Hz, (e, m) 400 Hz, (f, n) 600 Hz, (g, o) 800 Hz, (h, p) 1,000 Hz. Note the change in scales between 170 and 200 Hz.

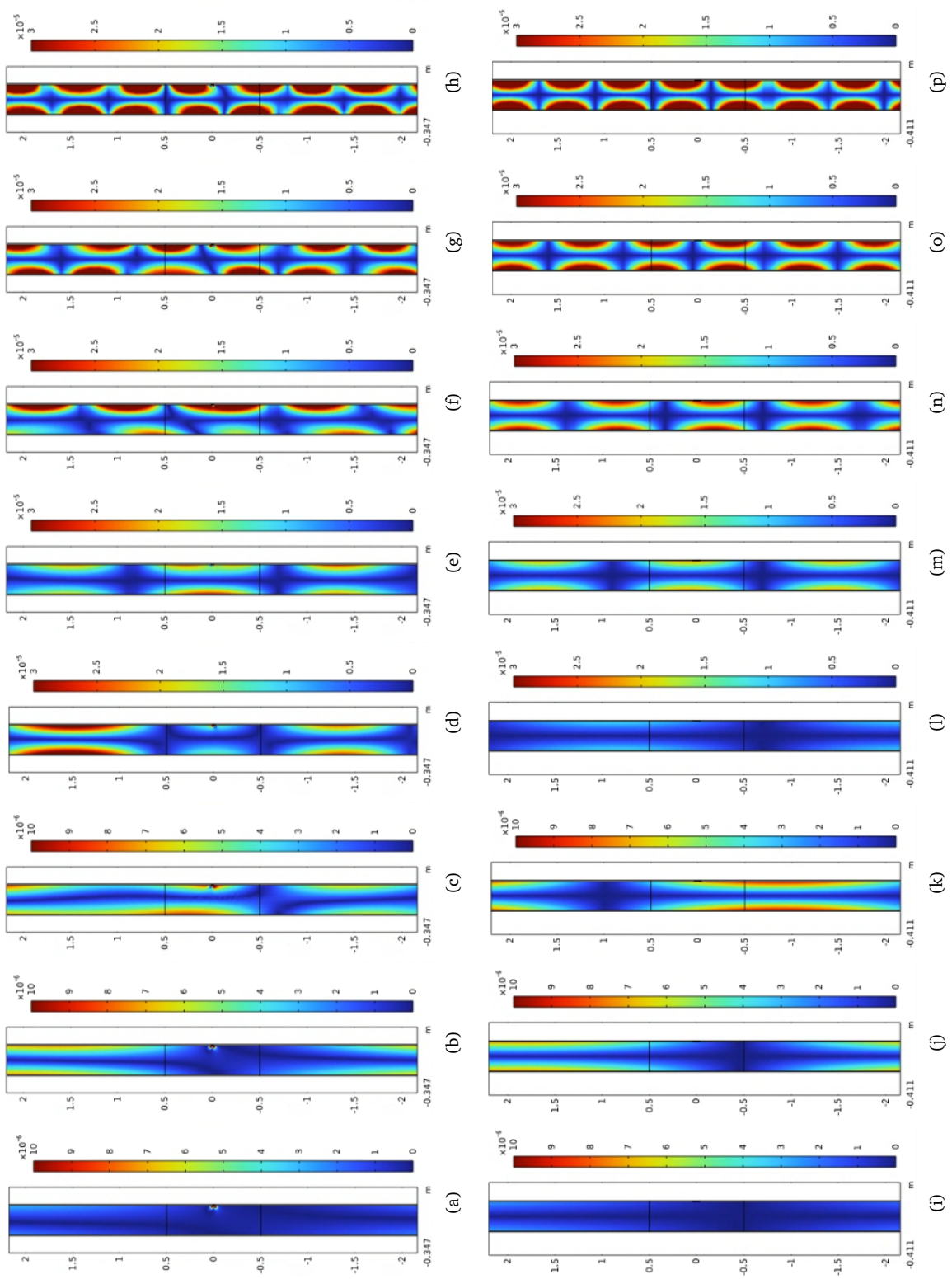

Figure 5.16: Radial velocity profiles for DI pipe for varying frequencies where there is a hole on the side of the pipe. Results for an intact pipe are shown in (i) to (p) for reference. The frequencies in each plot are (a, i) 65 Hz, (b, j) 130 Hz, (c, k) 170 Hz, (d, l) 200 Hz, (e, m) 400 Hz, (f, n) 600 Hz, (g, o) 800 Hz, (h, p) 1,000 Hz. Note the change in scales between 170 and 200 Hz.

5.4.3 Adding soil

Soil was added surrounding the pipe, with material parameters:

$$G_s = 2 \times 10^7 \text{ N/m}^2$$

$$K_s = 5.3 \times 10^7 \text{ N/m}^2$$

$$\rho_s = 2,000 \text{ kg/m}^3$$

The soil surrounded the pipe to 0.5 m in all directions, with a free boundary at its outer edge. This model is for a 310 mm diameter pipe, with a planar source located 10 m from the defect, which is at 0 m. The pipe model is 25 m long with PMLs at either end to simulate an infinite pipe. Only a wall thinning defect, of the same dimensions as previous instances, was simulated here, since the impact of water egress into the soil from a hole in the pipe wall was considered too important to ignore and too complex to simulate accurately using this methodology.

The results for the radial velocity around the defect for a DI and an HDPE pipe are shown in Figures 5.17 and 5.18 respectively. These figures correspond to those shown in Section 5.4.1 (Figures 5.13 and 5.14), which considered the effect of a change in material in an unburied pipe.

Again, there is a clear change of behaviour in the proximity of the defect for both materials and both frequencies.

For the 65 Hz source frequency, the DI pipe shows a pronounced increase in radial velocity up to approximately a pipe radius from the defect (Figure 5.17(a) and (b)). There is also an increase in the amplitude and phase of the standing waves, visible at -2 m and 1 m in these figures. The HDPE pipe (Figure 5.18(a) and (b)) shows much less of an impact of the defect. There is some very localised increase in v_r next to the defect, but no substantial changes to the behaviour in the

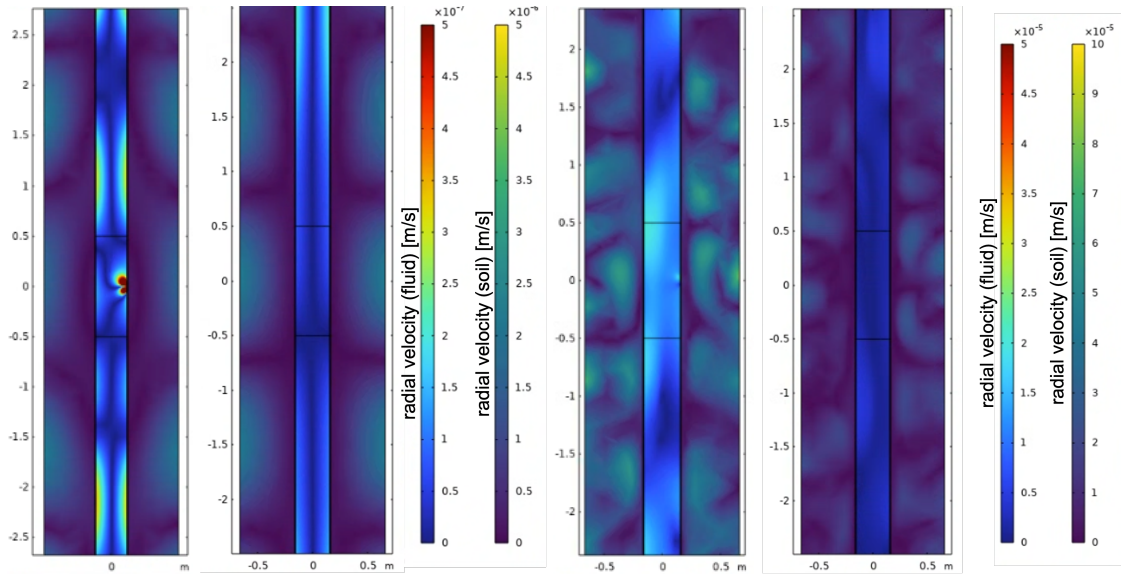

(a) (b) (c) (d)

Figure 5.17: Response of the radial velocity to the presence of a defect for a 300 mm diameter DI pipe with a source 10 m from the defect at 0 m, showing (a) pipe with a defect, source frequency 65 Hz, (b) pipe with no defects, source frequency 65 Hz, (c) pipe with a defect, source frequency 170 Hz, (d) pipe with no defects, source frequency 170 Hz. The colormaps both show the radial velocity, one for the inside of the pipe, the other for the soil outside the pipe, note the changes in scale between these two as well as between the sets of figures.

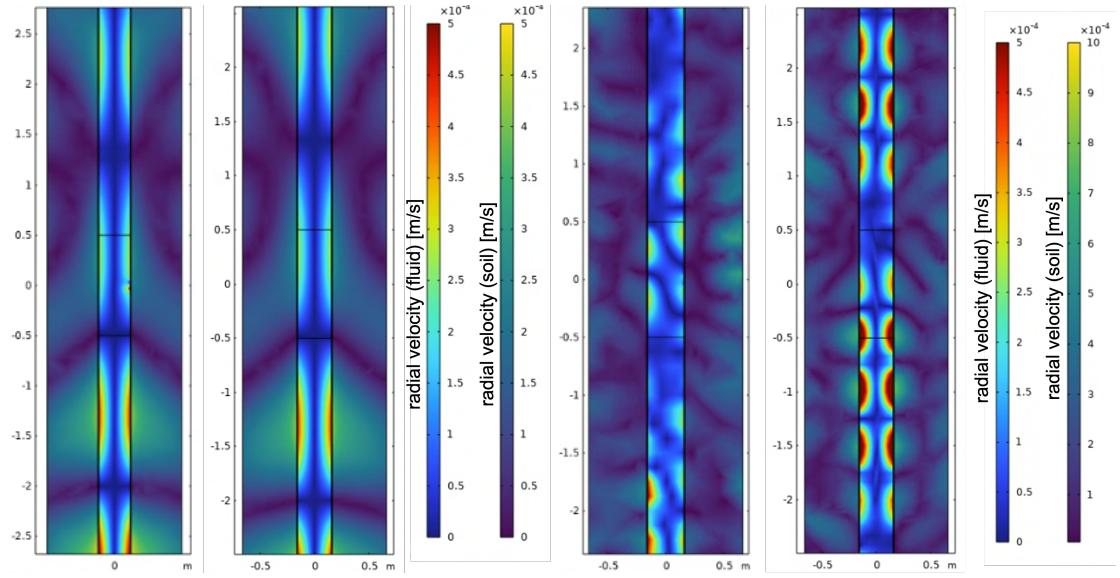

Figure 5.18: Response of the radial velocity to the presence of a defect for a 300 mm diameter HDPE pipe with a source 10 m from the defect at 0 m, showing (a) pipe with a defect, source frequency 65 Hz, (b) pipe with no defects, source frequency 65 Hz, (c) pipe with a defect, source frequency 170 Hz, (d) pipe with no defects, source frequency 170 Hz. The colormaps both show the radial velocity, one for the inside of the pipe, the other for the soil outside the pipe, note the changes in scale between these two as well as between the sets of figures.

rest of the pipe. This is a change from the case where there was no soil surrounding the pipe (Figure 5.14(a) and (b)), where the presence of the defect led to a change in the behaviour of the standing waves in the pipe.

For the 170 Hz source frequency, the DI pipe shows an increase in radial velocity close to the defect (Figure 5.17(c) and (d)). It is interesting that with the introduction of the soil layer the increase in v_r close to the defect is much more localised, but also has more of an impact on the behaviour of the rest of the pipe than for the model where there was no soil (Figure 5.13(c) and (d), with a substantial increase in v_r on the wall opposite the defect. The HDPE pipe (Figure 5.18(c) and (d)) shows a general decrease in amplitude of the standing waves in the pipe, and the symmetry of the standing waves is broken. The defect itself causes a small increase in v_r very close to the defect, but this is overwhelmed by the amplitude of the standing wave. This is very similar to the behaviour seen in Figures 5.14(c) and (d), although the effect on the standing wave is far more pronounced in this case where there is soil.

Based on these results, the soil clearly has an impact. The range of change in behaviour is larger with the soil present than without, with the standing waves in the pipe being significantly distorted for the defective pipe. The defect itself has less of localised effect. This may make it more difficult to detect the defect using a scanning robot-based approach, but more testing is needed to determine this. Testing in a more realistic set up would also be beneficial to test the effect on the standing waves in a more complex pipe, since the standing waves are dominating these results. As with the unburied pipe, the HDPE pipe was more sensitive to the defect for a source frequency of 170 Hz, which the DI pipe was more affected for a source frequency of 65 Hz.

5.5 Summary

Based on the analysis presented here, the radial velocity shows potential as a method of defect detection in pipes. The models indicate that the radial velocity shows an increase in amplitude close to a defect for a metal pipe, with frequencies of less than 400 Hz identified as having the highest signal to noise ratio. Further testing in more environments is required to verify that this SNR is sufficient for detectability when other sources of background noise are present. Coupled with the measurements of pump noise propagation on a working rising main, where frequencies of around 100 Hz showed the most response to the pump, this leads to frequencies of around 100 Hz being proposed for the sound source used for experimental testing of an AVVS for defect detection in a metal pipe. The next chapters test this finding experimentally.

Chapter 6

Experiments with Acoustic Velocity Vector Sensors in a Rising Main

Informed by the findings from the measurements and numerical simulations reported in the previous chapter, a laboratory experiment for two different types of acoustic velocity vector sensors (AVVSs) was designed and carried out to determine how effectively these sensors could detect defects on the pipe wall. This chapter is primarily concerned with the laboratory setup, sensors and experimental results. For completeness, the numerical results from Chapter 5 are compared with the experimental results. The specifics of the experimental setup meant that significant modifications were made to these models before comparing them with the experimental results. These modifications are described and their effect discussed before the numerical results of the modified models are compared with the experimental results.

6.1 Laboratory setup

Measurements were conducted in a 2.0 m long, 0.31 m (internal) diameter ductile iron rising main section exhumed for this purpose by Thames Water. As is common in rising mains, it exhibited significant deterioration of its pipe wall due corrosion and also of its bottom pipe wall surface due to scouring. The pipe wall damage and its arrangement in the water tank are shown in Figure 6.1 - the pipe has been inverted, so the wall damage is visible on the top of the pipe. The points where this scouring has caused holes in the pipe wall have been treated as discrete 'defects' during testing.

The pipe was placed in a large water-tight PVC container (see Figure 6.1). The container was filled with water such that the pipe was fully submerged and covered with water to 0.025 m above its crown. The relevant dimensions of the setup are included in Table 6.1. The same dimensions were used in the COMSOL model discussed in the following section to simulate the specific conditions of the experiment. An underwater speaker (Visaton FR8WP amplified by Fosi Audio TDA7498E) was installed in the centre of the pipe's cross-section at one end of the pipe. The speaker was mounted using four spokes of equal length to fix it in the centre of the pipe cross-section. The speaker mounting is visible in Figure 6.10(b). It was operated at 170 Hz to generate acoustic pressures of a few hundred Pascals. The sensor was moved along the pipe using a tensioned wire at the top of the pipe, taking into account the size of the sensor, this meant that the

(a)

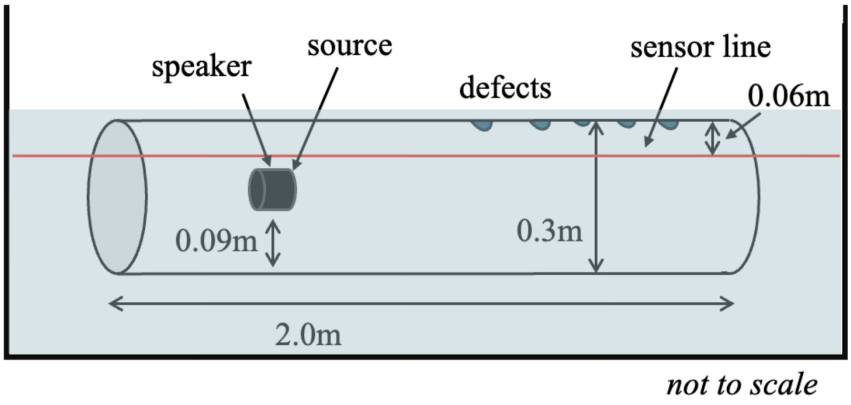

(b)

Figure 6.1: The experimental setup with a 2 m long, 0.31 m (internal) diameter ductile iron pipe in the ICAIR laboratory at Sheffield. The pipe has been inverted so its damaged surface is at the top. (a) shows a picture of the setup while (b) is a schematic showing the key dimensions, including the line along which measurements were taken using each of the sensors.

sensor itself moved along a line 0.06 m from the top of the pipe, as shown by the 'sensor line' in Figure 6.1(b).

Table 6.1: Key dimensions of the experimental setup. All distances are measured with respect to the start of the pipe and the bottom of the pipe (see Figure 6.1(b)). The same parameters are used in the numerical model described in Section 6.2

Property	Value	Unit	Comment
Pipe length	2	m	
Pipe diameter	0.31	m	internal
Speaker location	0.09	m	central to pipe
Speaker length	0.1	m	
Source pressure	450	Pa	at speaker
Tank start location	-0.156	m	
Tank length	2.375	m	
Tank height	0.473	m	
Tank width	0.57	m	
Tank wall thickness	10	mm	
Frame height	0.118	m	
Tank material	PVC		
Young's modulus	2.9	GPa	tank material
Poisson ratio	0.4		(PVC)
Density	1760	kg/m3	
Sensor elevation	0.25	m	from bottom
Hydrophone elevation	0.3	m	of pipe

6.2 Modelling the sensor performance in a laboratory tank

COMSOL MultiPhysics®simulations were carried out to support the experiments reported in this chapter. The simulations presented in Chapter 5 assumed that the pipe was infinitely long and/or surrounded by soil. This section presents a model modified to predict the performance of the AVVSs in the laboratory tank used in the subsequent experiments. The pipe is significantly shorter than infinite, and the pipe is submerged in water within a space-limited tank, this made the models of the infinite pipe a poor match to the experimental setup. The main purpose of these simulations was to determine the requirements for the sensitivity of the AVVSs that would be necessary to detect the pipe wall damage. The simulations were also used to explain the physical meaning of the experimental data.

A schematic of the experimental setup is shown in Figure 6.1(b). There are significant differences between this and an infinite pipe, the most relevant of these are:

- finite pipe length: based on a frequency range of 100-1000 Hz, the wavelength in water is between 1.5 and 15 m, so much larger than the length of this pipe section for the majority of the frequency range.
- pipe surroundings: the pipe is surrounded by water rather than soil or air.
- the pipe and water are enclosed by a tank which is very much within the near field of the source and receiver. This tank is flexible so liable to produce reflections.
- there are many consecutive defects.

The model used is shown in Figure 6.2(b), the values of all the relevant parameters used in the model are provided in Table 6.1. 'Defects', i.e. holes in the pipe walls, have been modelled at the positions of the holes in the pipe used for the experiments. They were generated in the model by removing cylinders from the pipe wall of a radius to match each hole in the pipe used for experiments.

6.2.1 Mesh sensitivity analysis

Two meshes were considered here for the sake of brevity. One is the mesh used in the final model, the other is a significantly finer mesh used to check that the resolution of the mesh used is sufficient to describe the situation. The maximum element size of each component of the model for the two cases is provided in Table 6.2, an image of the mesh in each of the two cases is shown in Figure 6.2.

The calculated value of each parameter of interest (x) is shown in Figure 6.3. This also shows the relative error, $\epsilon_x = (x_{model} - x_{fine})/(x_{fine} + \zeta)$, was calculated for each of the parameters of interest for the mesh used in the main model (x_{model}) and for the finer mesh (x_{fine}), where ζ is a regularisation constant. The maximum relative error was ϵ_p at 0.078, while the lowest was ϵ_{vy} at 0.038 and the other two parameters of interest sat between these two at 0.048 and 0.057 for ϵ_{vz} and ϵ_{vx} respectively. These are relatively high, however an inspection of the relevant graphs (Figure 6.3) shows that the main contributions to these errors are close to the speaker and at minima in the signals. The speaker is intentionally placed at a distance from the measurements, to minimise the near-field effects, therefore the accuracy of the model close to the speaker is not of as much interest as its performance elsewhere. Based on the relative speed of the coarse mesh,

Table 6.2: The maximum element size, in m, for the mesh in each component in the model.

Component	Mesh used	Finer mesh
tank	0.25	0.05
pipe wall	0.25	0.01
pipe interior	0.25	0.01
speaker	0.08	0.01
defect	0.005	0.001

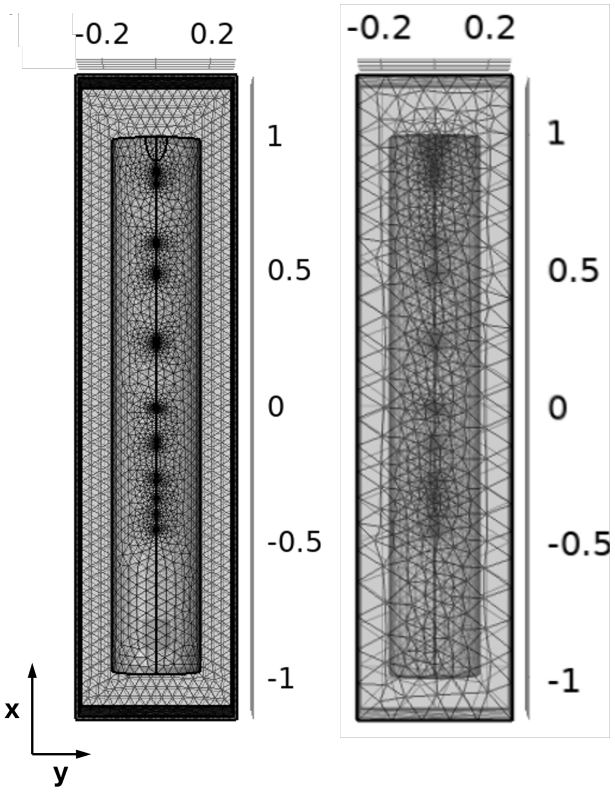

(a) (b)

Figure 6.2: The mesh used for (a) the validation model, which has a much finer mesh, and (b) the main model.

and the fact that this model is for experimental design purposes rather than extensive numerical validation, the relatively coarse mesh was used for comparison with experimental results.

6.2.2 Results

The results for the amplitude of the acoustic pressure and vertical acoustic velocity predicted with the finite element model are shown in Figure 6.4. These plots are for a slice across the pipe, such that the speaker is visible at -0.91 m and the sensor line as defined in Figure 6.1(b) is at the top of the pipe. Isolines have been included to aid in interpretation of the figures.

In Figures 6.4(a) and (b), which show the results for the pressure, there is very little discernible difference between the pressure field for a pipe with defects along the top of the pipe (Figure 6.4(a)) and without (Figure 6.4(b)). The isolines show some small changes in the direction of the pressure gradient at the bottom of the pipe, with the symmetry of the system broken

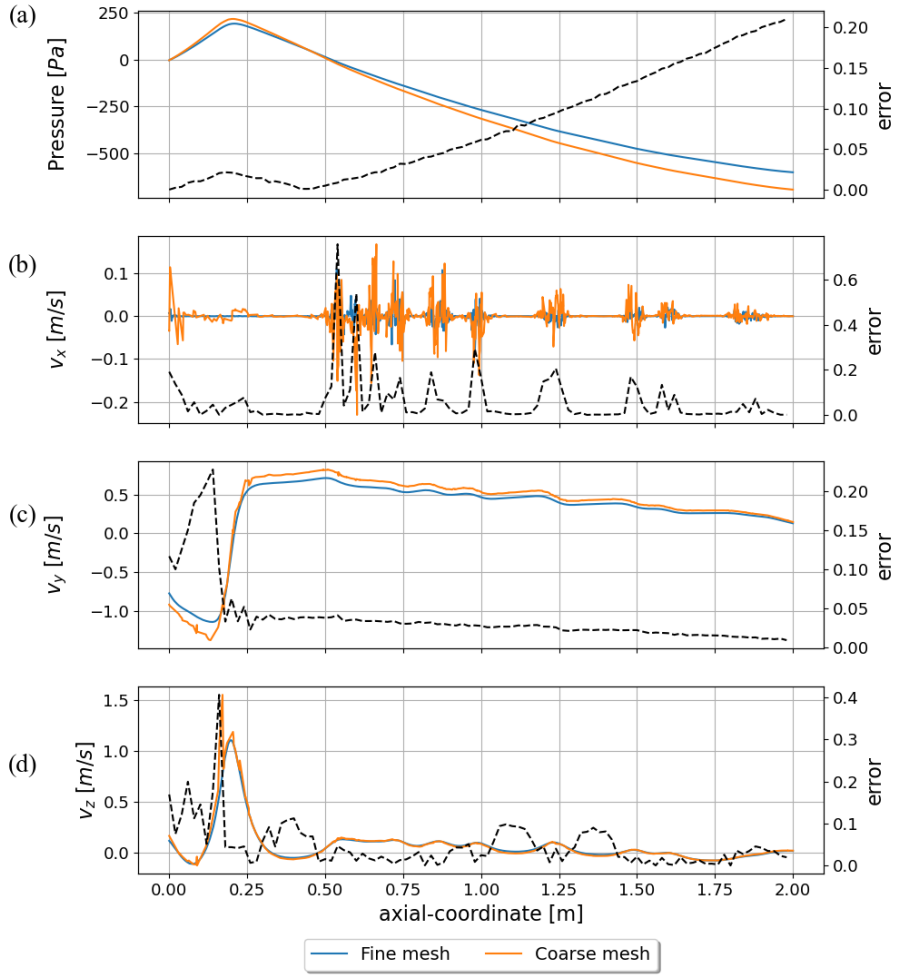

Figure 6.3: Effect of different sized meshes on the model results. The mesh sizes for each section of the model are summarised in Table 6.2. The left hand axis of each graph shows the scale for the blue and orange traces (describing the results for the fine and coarse meshes respectively) while the right hand axis shows the scale for the black dashed line (the error).

in the case with defects, however these changes are very small. The axial velocity has not been plotted since it showed very similar behaviour to p. In contrast, there is a clear change in the horizontal, y, and vertical, z, velocity fields, as shown in Figures 6.4(c)-(f). When there is no defect both v_y and v_z are largely constant. In the case of v_z there is a gradient down the pipe in the z direction, but it is constant down the length of the pipe, while v_y is largely static with only a small increase in the x axis. Once defects are introduced there are large localised increases in both v_y and v_z next to the defects, visible as concentrations of contours along the top of the pipe. These continue away from the pipe wall such that they have a visible effect at the sensor line. In addition to this localised effect they distort the v_z field through the pipe, with a much more static v_z across the z axis than in the case with no defects. This could be utilised in sensing by measuring the velocity around the pipe wall, such that the difference in velocity at the top and bottom of the pipe becomes a factor in determining the presence of defects on the pipe wall.

These results have been plotted for the sensor line (as shown in Figure 6.1(b)) in Figure 6.5. In this graph the differences between the intact and defective pipe is clearer. There is a decrease in the pressure when there are defects, presumably because the holes in the wall act as pressure release points. Regardless of the presence of the defects, the behaviour of the acoustic pressure along the pipe is a smooth function of the axial distance. The presence of the defects in the pipe

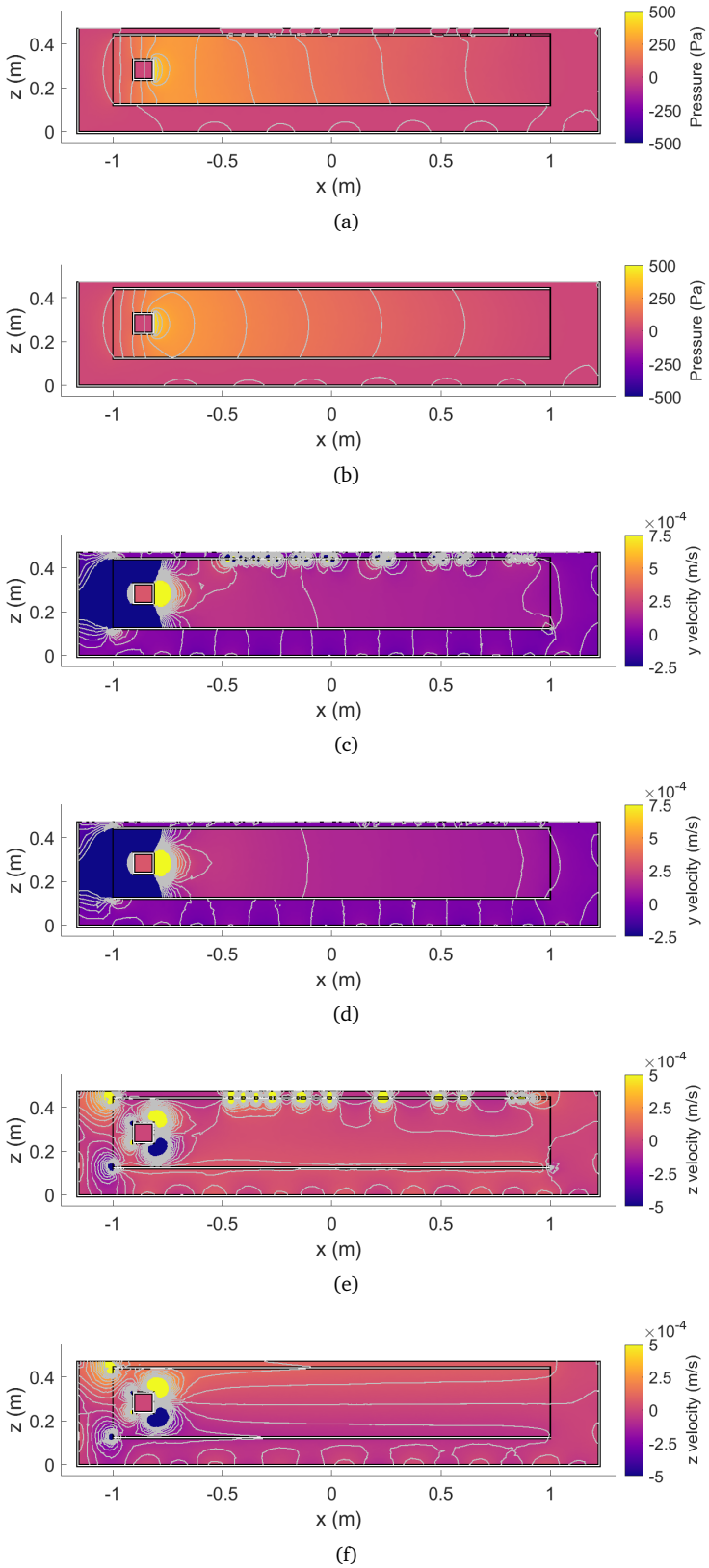

Figure 6.4: A comparison of the acoustic response of the fluid to a 170 Hz source positioned at x =-0.8 m, the response is shown for a vertical cut plane along the centre line of the pipe for (a, b) the acoustic pressure, (c, d) the horizontal component of the acoustic velocity vector and (e, f) the vertical velocity component. (a, c, e) show the acoustic response for a pipe with defects along its upper edge, (b, d, f) show the acoustic response for a pipe rotated by 90° such that the top edge is intact. The isolines are 50 Pa apart for the pressure graphs and 5×10^{-5} m/s apart for the velocity graphs.

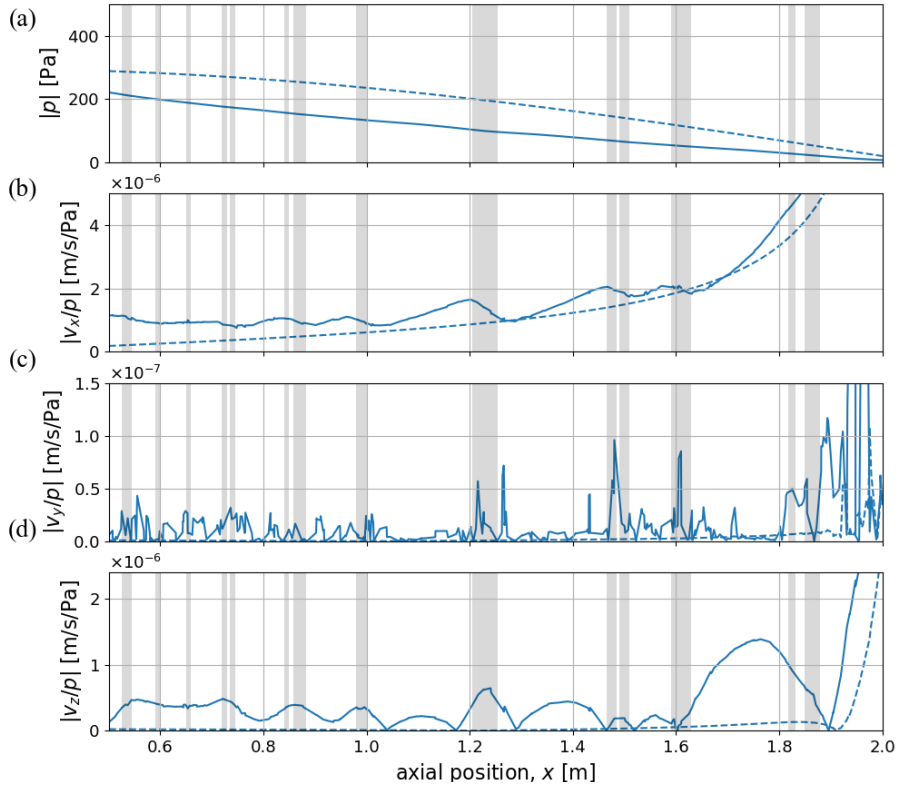

Figure 6.5: Results for defective (solid line) and intact (dashed line) pipe, showing (a) the pressure, then the x-, y- and z-components of velocity normalised by pressure in plots (b) through (d) for a line 0.06 m from the defect surface of the pipe. The locations of holes in the pipe are shown by the grey shaded areas.

causes the amplitude of the acoustic pressure to reduce by approximately 50% across the entire pipe length. However, given that this change is not related to the proximity of the defect, it cannot be used to determine the location of the defect.

The ratio v_x/p shows some change in behaviour in the presence of the defects, with localised increases in the amplitude of the normalised axial velocity, leading to a less smooth measurement along the length of the pipe. In Figure 6.5(c), v_y/p shows large localised increases in amplitude at the defects, this is discussed further in Section 6.3 with comparison to experimental results, and has already been discussed with reference to Figure 6.4(c). The normalised vertical component of velocity (v_z/p) also shows a large difference in behaviour when there are defects in the pipe. In the centre of the pipe, between 0.8 and 1.6 m the increases in amplitude correspond closely with the presence of defects, however at the ends of the pipe this relation reduces, particularly for the large peak at 1.7 m. This is likely due to end effects induced by the finite length of the setup, coupled with the very large defects at the end (1.9-2.0 m) of the pipe. This limitation should be considered during testing and any further application.

In general, these results demonstrate that, as for the case of an infinite pipe, the acoustic velocity is at least an order of magnitude more sensitive to the presence of a defect than the acoustic pressure. Some limitations in the experimental setup have been identified, and as such most of the experimental work will be conducted on the central (1.0-1.6 m) section of the pipe.

6.2.3 Rotated vs defect-free

The only pipe available for testing had a line of defects along the top of the pipe. This meant that a direct comparison with an intact, defect-free pipe was not possible in this experiment, instead the pipe was rotated 90° so that a relatively intact side of pipe that had no holes in the pipe wall was next to the sensor, this is shown in Figure 6.6.

Figure 6.7 shows the results from the model of an intact pipe, vs. the rotated defective pipe used as a proxy for an intact pipe and an unrotated defective pipe, where the defects are next to the sensor. This shows that the rotated pipe is far from an ideal proxy for a truly intact pipe, with the pressure in the defective pipe being the same regardless of whether it is rotated and significantly below the pressure for an intact pipe. The shape of the graph of the axial (x) velocity amplitude for an intact pipe is the same as for the rotated defective pipe, the small difference in amplitude can be explained by the difference in pressure (these velocities have been normalised by the pressure). The horizontal (y) and vertical (z) velocities for the rotated defective pipe bear little resemblance to either the intact pipe or the measurements next to the defect. v_y/p is several times larger for the rotated pipe than for either the intact or defective pipes, particularly at the damaged end ($x > 1.6$ m) and for $0.6 < x < 1.0$ m where there are many consecutive defects. Given that the defects are now aligned with this axis, these predicted increased in the horizontal velocity are not unexpected. While v_y/p and v_z/p are larger for the rotated pipe than for the intact pipe, they

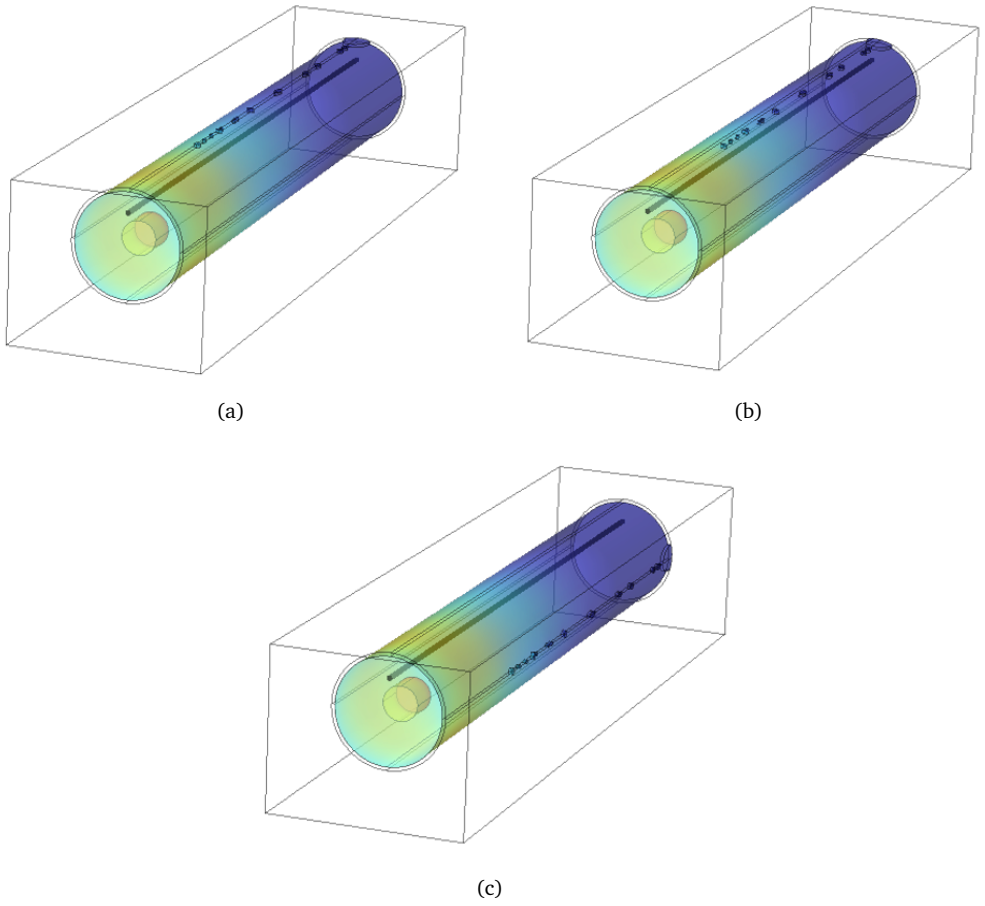

Figure 6.6: Models of the pipe rotations used during the experiment and modelling. The sensor line is shown in black. Pipe shown at (a) 0^o, (b) 9^o and (c) 90^o.

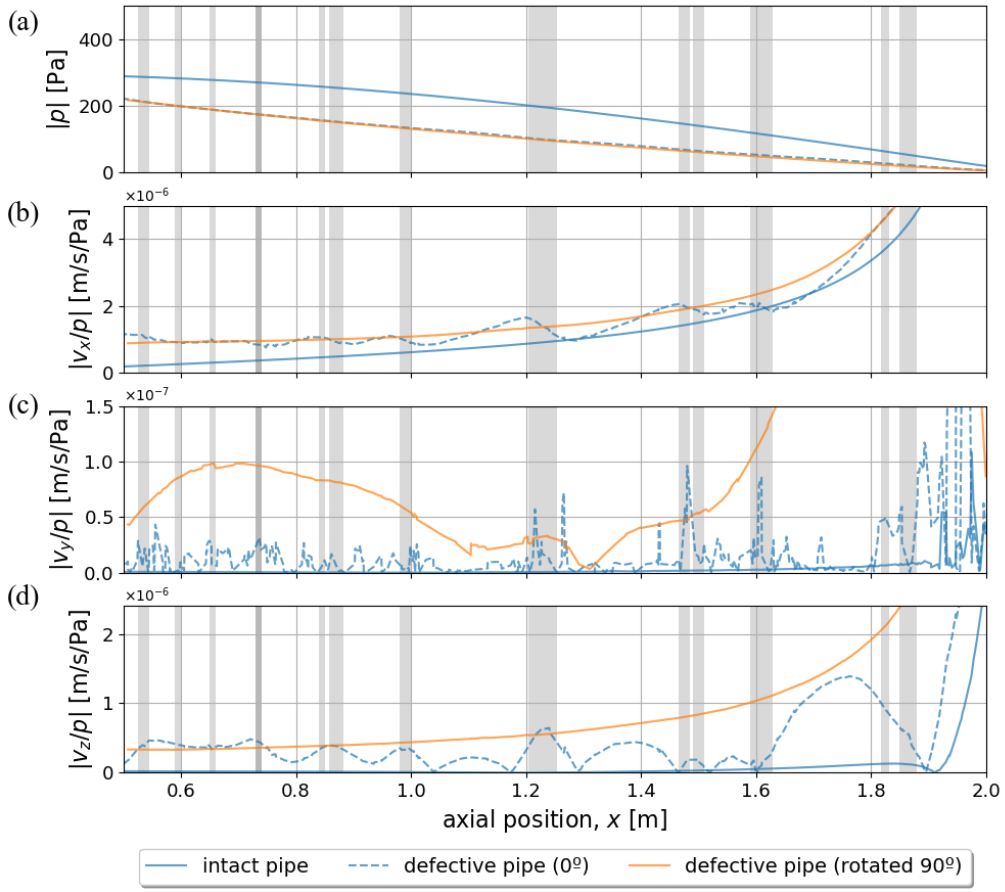

Figure 6.7: Comparison of an actually defect-free pipe with a defective pipe rotated 90º such that the defects are far from the sensor and not rotated such that the defects are right next to the sensor.

still lack the localised changes at the defects exhibited for the model of the defective pipe. Based on this, the rotated pipe was still used as an 'intact' baseline during the experiments.

6.2.4 Model sensitivity analysis

The water level in the tank and visco-elastic properties of PVC panels of which the tank was made are two parameters that can affect the acoustic pressure and velocity predicted with the COMSOL model. An investigation into these effects were carried out accordingly. In this investigation:

i) the elastic properties of the PVC panels was changed from $E = 2.9$ GPa, as used in the main model, to $E = 4.0$ GPa and the pipe walls were modelled as rigid boundary conditions.

ii) the depth of the water in the tank was varied from its base value of 0.025 m to 0.1 m, 0.25 m and 0.5 m above the crest of the pipe.

The results of these permutations were compared against those from a 'baseline' model taken forward into the rest of the chapter. The geometry of the model was not varied from that shown in Figure 6.1(b) and detailed in Table 6.2. Figures 6.8 and 6.9 present the results that illustrate the effect of the tank wall definition and water level in the tank, respectively. The solid lines shown in these figures correspond to the case with the damaged pipe wall, the dashed lines correspond to the case of the undamaged pipe. The velocity amplitudes were normalised by the acoustic pressure for consistency with the rest of chapter.

It can be seen in Figures 6.8(a) and (b) that changing the elastic behaviour of the PVC panels has very little effect on the amplitude of the acoustic pressure and axial velocity component: the

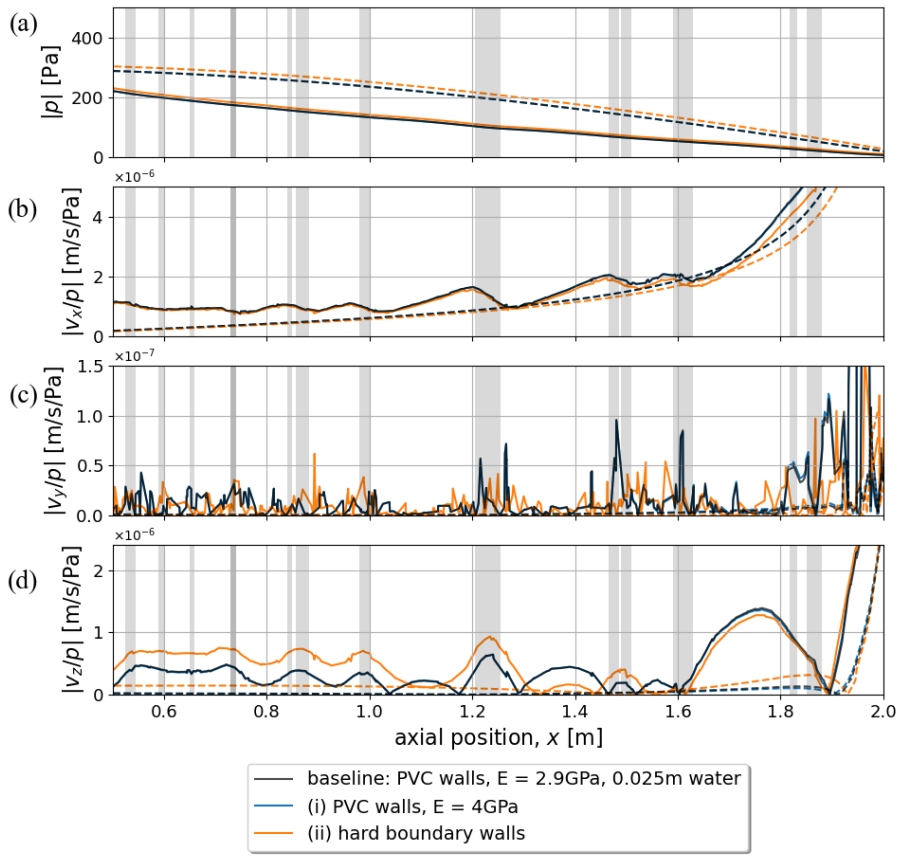

Figure 6.8: Comparison of results for different tank walls, showing the pressure and the x-, y- and z-components of velocity normalised by pressure in plots (a) through (d). The results for a defective pipe are shown with solid lines and the complementary results for an intact pipe are shown with dashed lines.

plots for the two cases are indistinguishable in all four subplots. In contrast, modeling the panels as hard boundaries has a much more pronounced effect on the horizontal (Figure 6.8(c)) and vertical (Figure 6.8(d)) components of the acoustic velocity, particularly as the receiver approaches the source. There is a significant, approximately two-fold, increase in the amplitude of the vertical velocity in the case when the walls of the tank are acoustically rigid for $x < 1.4$ m. The behaviour of the horizontal component of the acoustic velocity is more complex and somewhat random. The difference between the results for $E = 2.9$ GPa and $E = 4.0$ GPa for this velocity component is very small. Since the panels are made of PVC, the model taken forward did not use a rigid boundary, instead letting $E = 2.9$ GPa, a standard value for PVC, the exact value of which has been shown to have little bearing on the results of the model.

Figure 6.9 demonstrates the effect of water level on the four acoustics quantities. In these calculations the tank walls were assumed to be rigid. The acoustic velocities were again normalised by the acoustic pressure. These results suggest that the effect of the water level on the acoustic pressure is small (see Figure 6.9(a)), but stronger than the effect of the value for E (see Figure 6.8(a)). Generally, the acoustic pressure amplitude slightly increases by a few percent with the increased water level. The effect of water level on the amplitude of the three acoustic velocity components is also small, except at distances farther away from the speaker and near the far end of the tank (see Figures 6.9(b-d)). For example, the amplitude of v_z/p can vary by up to a factor of 2 at $x = 1.8$ m (see Figure 6.9(d)). Based on this analysis, the water depth was measured carefully during experiments such that it matched the depth modelled.

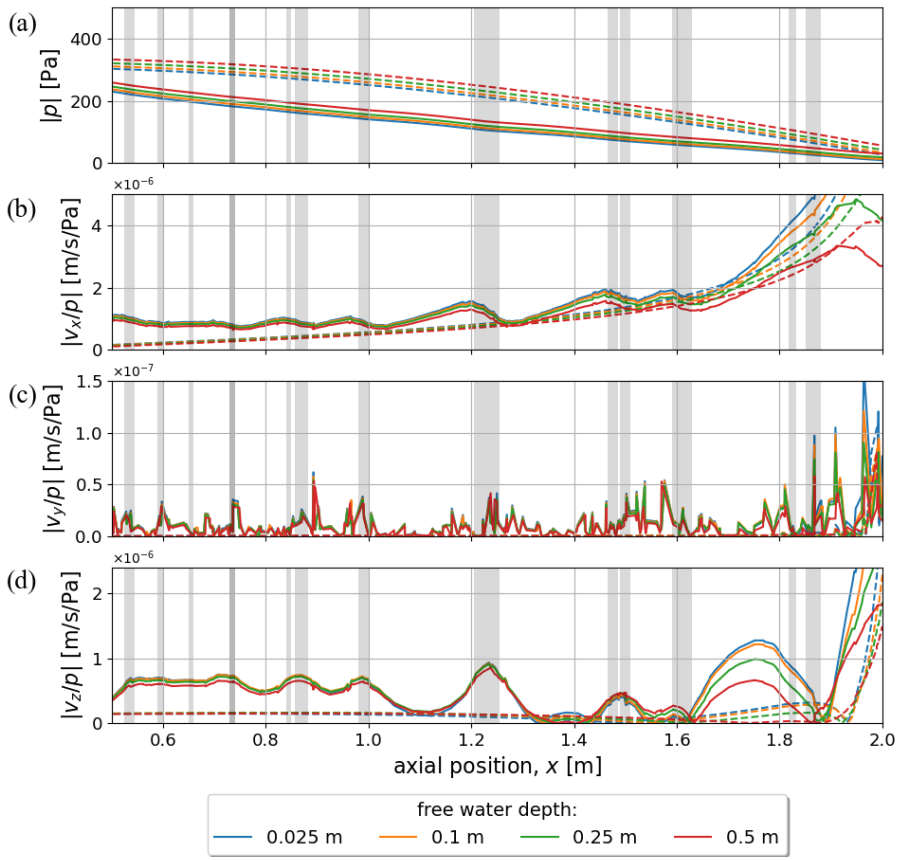

Figure 6.9: Comparison of results for different tank water levels, showing the pressure and the x-, y- and z-components of velocity normalised by pressure in plots (a) through (d). The free water depth has been measured from the crown of the pipe. The results for a defective pipe are shown with solid lines and the complementary results for an intact pipe are shown with dashed lines.

6.3 Sensor 1: suspended triaxial accelerometer

As a starting point for verification of the model results, an off the shelf accelerometer (G-link-200) was adapted to operate underwater as shown in Figure 6.10. The G-link-200 is a battery powered, wireless 3-axis accelerometer, which is designed for vibration monitoring applications. It was chosen for this project primarily based on its high sensitivity, although the cable-less nature of the product did simplify water-proofing and mounting the sensor. For a 2g range, the accelerometer has a sensitivity of 0.19 $\mu\mathrm{m/s}^2$. The system is designed such that it can capture data for a pre-defined period of time, then the data can be downloaded wirelessly.

6.3.1 Experimental setup

The accelerometer was constrained vertically by a piece of string. The elastic bands to either side were to hold it in a known orientation; measurements performed without these were very challenging to extract meaningful data from as the sensor span in place unpredictably. The presence of these bands may reduce the amplitude of axial vibration detected by the accelerometer, but given that the axial motion was predicted to be the largest it was considered an acceptable solution. This sensor was attached to a taut wire such that its vertical position was constant and its axial position could be controlled to within 2 mm. The wire was positioned such that the centre of the accelerometer was 0.06 m from the top of the pipe: the 'sensor line' from Section 6.2. A hydrophone was attached above the accelerometer to measure the pressure, the hydrophone used was a B&K 8103, the signal from which was amplified using a B&K 2693-0S4 conditioning amplifier. The speaker was a Visaton FR8WP in a metal housing for waterproofing and mounting. It was supported by four metal struts, allowing it to be positioned in the centre of the pipe, this is shown in Figure 6.10(b). For these experiments the speaker produced a 5 s tone at 170 Hz. The signal was generated by LabView and sent to the speaker via a DAQ (NI 4431) and an amplifier (Fosi Audio TDA7498E), the same DAQ was used to record the hydrophone signal. The accelerometer data was recorded locally to the accelerometer and extracted using software provided with the sensor. The hydrophone and speaker were operated at a sampling rate of 12,000 Hz while the accelerometer recorded at 2,046 Hz. Full part numbers are provided in Appendix A.

The amplitudes of the axial, a_x, horizontal, a_y and vertical, a_z, components of the fluid acceleration were measured and converted into the acoustic velocity components using the well-known

(a) (b) (c)

Figure 6.10: (a) Sensor used for verification of the model results, shown suspended as during test, positioned just before entry into pipe, with hydrophone visible above the accelerometer, (b) speaker in position for testing, with accelerometer in foreground, (c) schematic of modifications to G-link.

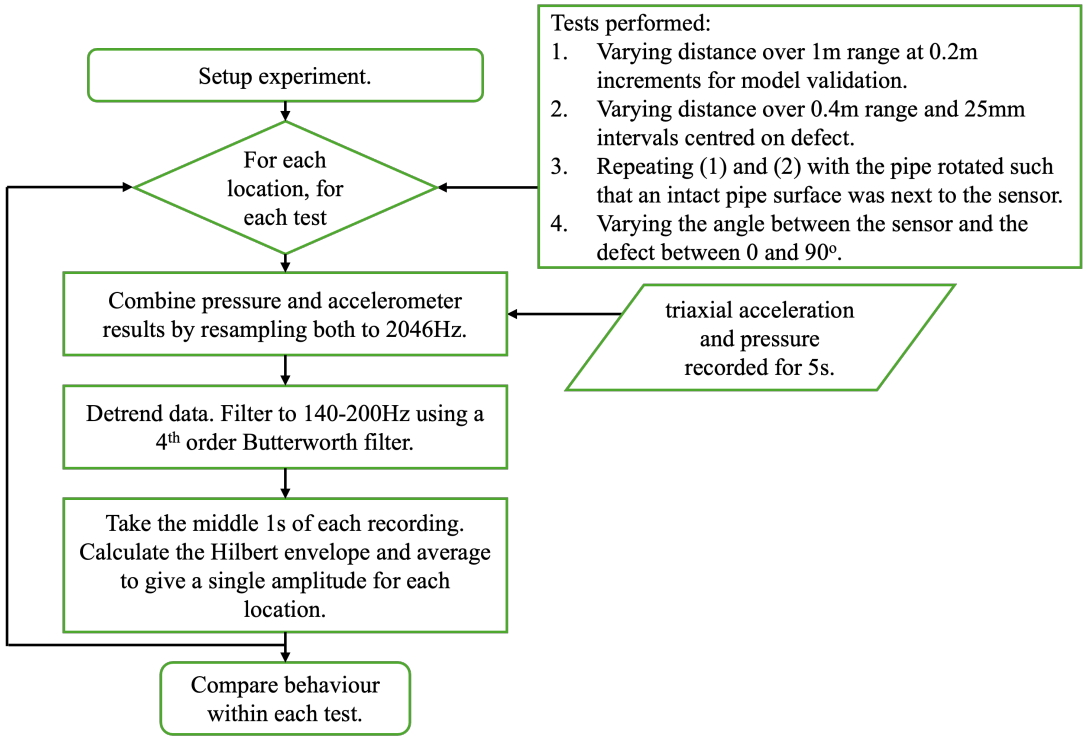

Figure 6.11: Flow chart of experimental process.

relations $v_{x,y,z} = a_{x,y,z}/i\omega$. The results of the numerical simulations described in Section 6.2 suggested that for these acoustic pressures the accelerometer needed to be sensitive enough to detect accelerations of above 10^{-3} m/s^2 (or 9.36×10^{-7} m/s at 170 Hz in terms of the acoustic velocity). The accelerometer chosen for this work had a 20-bit resolution with range ±2 g, giving a sensitivity of 4×10^{-5} m/s^2 (or 3.74×10^{-9} m/s at 170 Hz in terms of the acoustic velocity); more than adequate to detect the changes in the acoustic velocity field.

Measurements were taken for a range of sensor positions and pipe orientations. The position of the sensor was varied using a pulley system which moved the accelerometer along a wire 0.06 m from the top of the pipe. Measurements were taken across a 1 m range at 0.2 m increments to validate the model along the pipe length and across a smaller 0.4 m range centred on a large defect at 0.025 m intervals to investigate the sensitivity of the sensor to defects as a function of distance from the defect. The angle between the sensor and the line of defects was varied by installing a frame under the pipe to enable accurate rotation of the pipe. This allowed the sensor to be exposed to both damaged and undamaged parts of the pipe's wall while moving the sensor along the length of the pipe. It also allowed for an investigation of the sensitivity of the sensor to the presence of a defect with respect to this pipe angle. Ideally the pipe would have been at 0 and 90° for the 'defect' and 'no-defect'/'intact' cases, respectively. However, the geometry of the speaker prohibited measurements at those exact angles. Consequently the closest measurements to the defect were for a pipe angle of 9° and the farthest were for a pipe angle of 89°.

The process used during the experiment, including the signal processing steps, are shown in Figure 6.11. After down-sampling the hydrophone data to match the sample rate of the accelerometer, the data from the two sensors were detrended and filtered in the frequency range between 140 and 200 Hz using a 4th order Butterworth filter to focus on the signal broadcast at 170 Hz. For each position a 5 s recording was taken, from which the average of the Hilbert envelope of the middle 1 s was calculated, to give a single amplitude for each location.

6.3.2 Results

There are four sets of results presented in the following sub-sections. The first compares the variation in measurements, the second set aims to compare the numerical model against experimental data taken over a 1 m length of pipe centred 1.3 m from the end of the pipe. The third set presents data and their variability in close proximity to a defect between 1.025 and 1.425 m. It also presents a comparison with the results of the numerical simulation in this region, thereby supporting the veracity of the observed behaviour of the acoustic pressure and velocity. Finally, the angular dependence of the acoustic velocity measured along the pipe's circumference is studied for two different axial locations in order to assess the sensitivity of the method to orientation.

Repeatability

Figure 6.12 shows the variation in measurements for two locations along the length of the pipe, one close to a defect and one on a relatively intact section of the pipe wall. There were 12 repeat measurements for the location closest to the defect and 9 for the location further from the defect. The acceleration has been normalised by the pressure: this reduces some of the variability caused by the different distances of measurements from the sensor. While the measurements vary by 25% from the mean in the worst cases (particularly the axial direction), it is still possible to clearly separate the cases where there is and is not a defect using the axial or vertical acceleration.

Model calibration

In order to evaluate the accuracy of the model, measurements were taken at 0.2 m intervals along the length of the pipe. To study cases close to and distant from defects, the pipe was rotated to move the line of defects closer to or further away from the sensor. In this experiment the two cases were realised with the pipe rotated to 9° and 89°, respectively. A comparison of the results of the

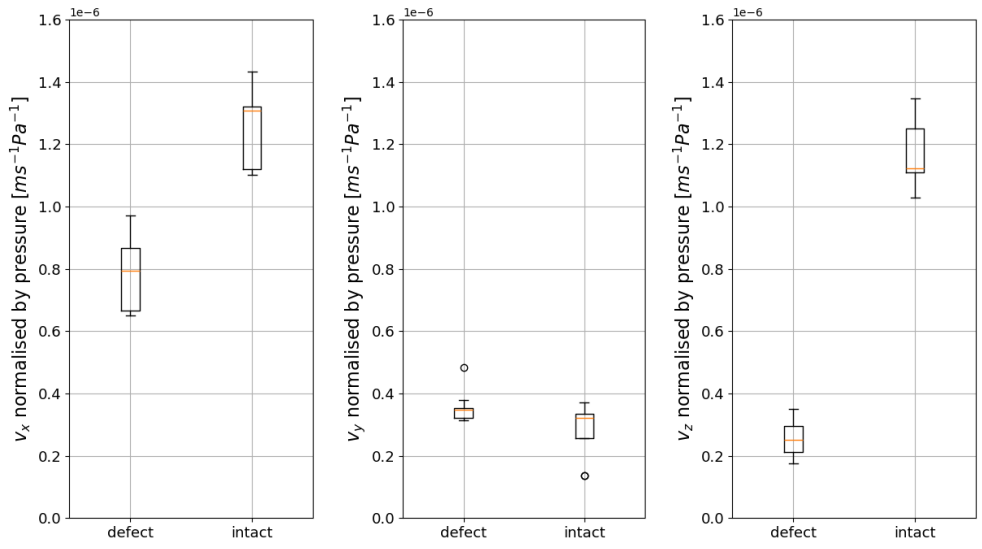

Figure 6.12: Variation in measurements across 10 measurements at 2 locations, one under a defect and one under an intact section of pipe, showing the variation in (a) v_x/p, (b) v_y/p and (c) v_z/p).

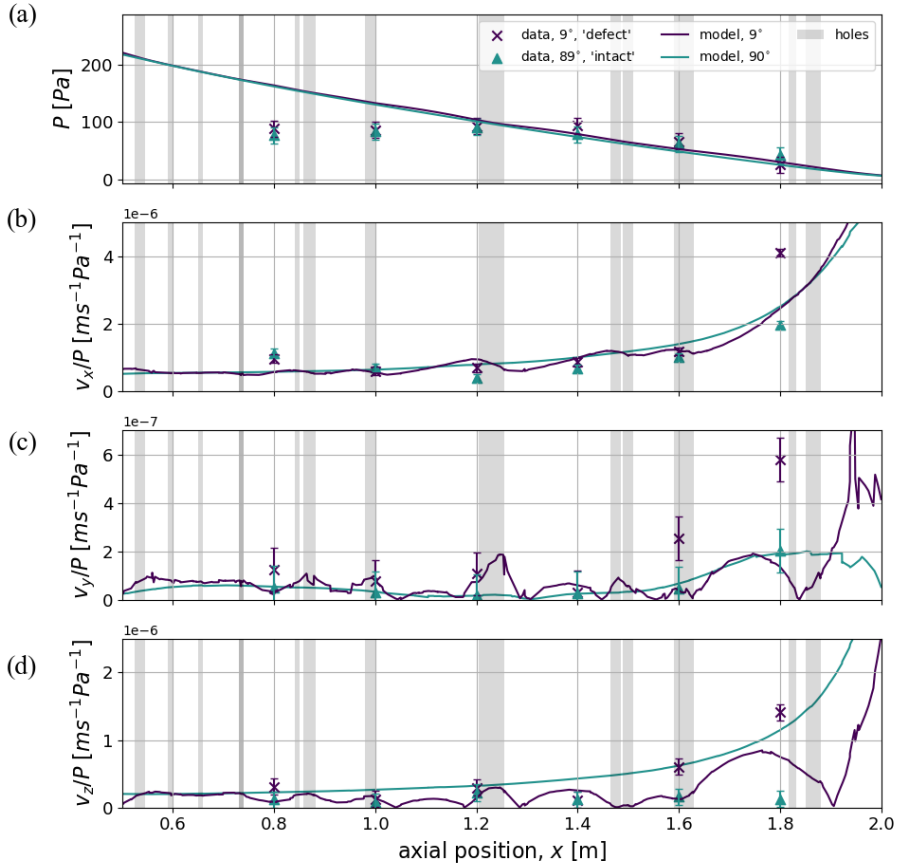

Figure 6.13: A comparison of the measured (markers) and modelled (lines) acoustic quantities. The error bars are calculated as the standard deviation of 2 x 9 repeated measurements on an intact and defective section of pipe. The location of the holes are indicated by the shaded regions in gray. The green Δ markers and lines are the results corresponding to the receiver being next to intact pipe wall. The purple $\times$ markers and lines are for the results corresponding to the receiver being next to the defects.

model and the experiment is provided in Figure 6.13 for the acoustic pressure measurements and for the three components of the acoustic velocity vector normalised by the pressure amplitude.

There is good agreement between model and experiment for the pressure measurements where $x > 1.2$ m. It was determined that the lower amplitude for the measurements at 0.8 and 1.0 m was due to overheating of the speaker; these two measurements were taken last for all repeats. The amplitude of the each acoustic velocity component was normalised by the acoustic pressure amplitude measured at the same time. This removed the drift observed in the speaker output. Aside from the drift in amplitude, the measured pressure are very similar for the two pipe orientations, as expected based on the model. For the first few measurements, from $x = 1.6$ to 1.8 m the amplitude of the measured and predicted pressures are also very similar.

There are strong similarities in the behaviour of the measured and modeled velocities near and away from the line of defects. The axial component of the acoustic velocity, v_x, displays the most similarities between the modeled and measured data, with the dominant behaviour being a clear increase in amplitude along the length of the pipe. The measurements of v_x have a variability (as measured by repeating measurements 9 times at two locations and calculating the standard deviation) of 1.2×10^{-7} m/s/Pa. Given this level of error there is little difference between the axial velocity measured in the presence or absence of the defects, i.e. v_x is relatively unaffected by the

presence of the defects.

In contrast, a key influence of the line of defects on the acoustic field in the pipe is a much more complex variation in the horizontal and vertical components of the acoustic velocity (v_y and v_z) when compared to the case where the sensor is close to an 'intact' section of pipe. The horizontal component of the acoustic velocity vector, v_y, is very sensitive to the presence of the line of defects (compare the purple line and the green line in Figure 6.13). The agreement between the model and experiment deteriorates for $x > 1.6$ m, with the maximum difference of 4.3×10^{-7} m/s/Pa between the model and data at $x = 1.8$ m corresponding to a relative error of 300%. It should be noted that the amplitude of v_y is at least an order of magnitude smaller in comparison with that measured for v_x and v_z, this may make it challenging to measure v_y outside of a laboratory environment, in areas with higher background noise.

The predicted vertical component, v_z, of the acoustic velocity also shows a close agreement between the experimental data and the model for the case when the line of defects was near the sensor and for $x \leq 1.6$ m. For $x > 1.6$ m the measured amplitude of the vertical velocity component is significantly larger than predicted. For most of the measured range, the model over-predicted the amplitude of the vertical velocity component for the case when the sensor is away from the line of defects. The discrepancy is particularly acute for $x > 1.6$ m, where the measured velocity has remained constant but the model predicts an increase towards the end of the pipe.

The consistent discrepancies between the model and data towards the end of the pipe may be due to the increasing deterioration of the pipe condition in that region such that the model is a poor representation the conditions: the model has assumed that the edges of defects are smooth, it can be seen in Figure 6.1 that this is not always the case. Further, the model assumes the internal walls are smooth and of consistent thickness, in fact ultrasonic gauge measurements show that the pipe wall thickness varied from 10.6 to 11.9 mm, and the pipe wall is visibly corroded. Finally, the walls of the water tank caused a large number of reflections resulting in a complicated pattern of standing waves.

Acoustic field near a defect and measurement repeatability

A more granular set of measurements was taken at 0.025 m increments over a 0.4 m range around a 0.05 m diameter hole, 'the defect', at 1.225 m in order to determine how sensitive the acoustic pressure and velocity vector components are to the presence of the defect. The measurements were supported with COMSOL simulations to determine the ability of the model to reproduce the fine structure of the acoustic field in the vicinity of the defect. The results are shown in Figure 6.14 for the sensor installed at 9° (near the defects) and 89° (away from the defect). As in Section 6.3.2, the three velocity components shown in Figures 6.14(b-d) were normalised by the amplitude of the corresponding pressure measurement. The data in this figure are presented with error bars showing the variation in measurements over 3 repeats at each location.

The analysis of the measured and predicted acoustic pressures shown in Figure 6.14(a) suggests that this quantity is insensitive to the presence of the defect. The predicted amplitude of the acoustic pressure reduces with distance from the speaker. This behaviour is not supported with the measured data which are relatively independent of the distance, however the variation in the pressure measurements is relatively large, nearly 50% of the pressure magnitude, making trends difficult to see. It is believed that this is due to the variability in the speaker output described previously.

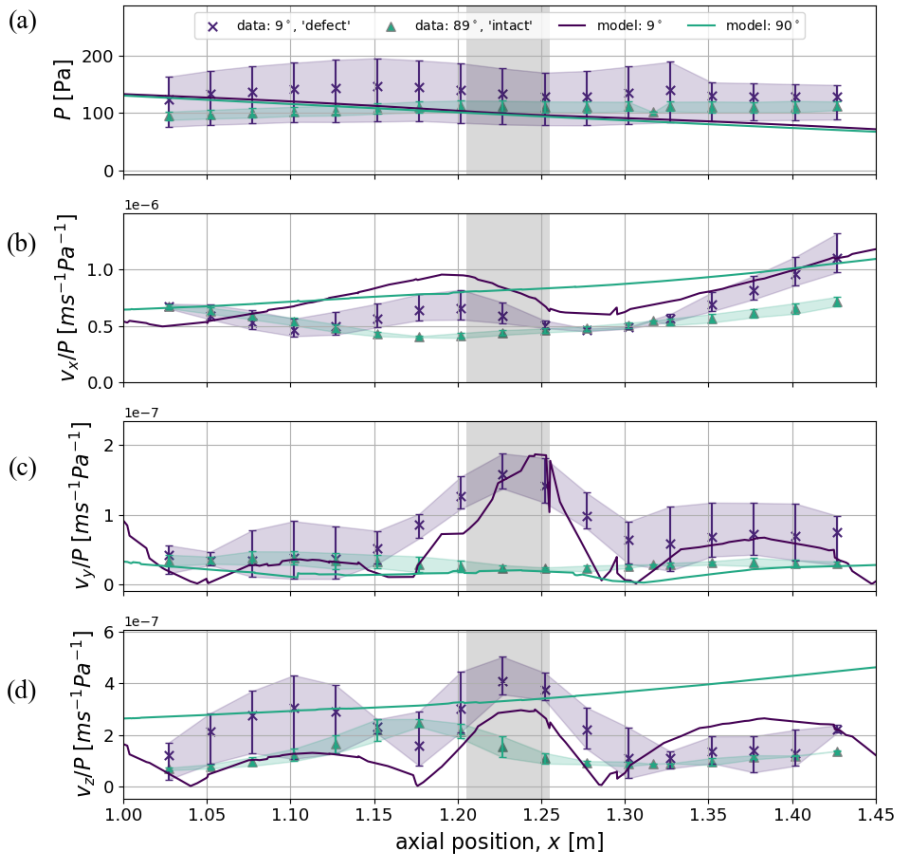

Figure 6.14: A comparison at a higher resolution of the measured (markers) and modelled (lines) acoustic quantities around a 0.05 m hole at $x = 1.225$ m (the shaded region in gray). The green Δ markers and lines are the results corresponding to the receiver being next to intact pipe wall. The purple $\times$ markers and lines are for the results corresponding to the receiver being next to the hole. The error bars show the repeatability of measurements.

The analysis of the measured and predicted acoustic velocities shown in Figures 6.14(b-d) for the amplitude of the three components of the acoustic velocity vector suggests that the model captures well the general behaviour of the measured data at $9°$. The maximum relative error is 220% for the data at $9°$ (for v_z at $x = 1.402$ m).

The defect has a relatively small effect on v_x, in line with the modelled result (see Figure 6.14(b)). The horizontal component of the acoustic velocity, v_y, is sensitive to the presence of the defect as shown in Figure 6.14(c). The data show that its amplitude increased by a factor of 7 when the sensor was placed close to the defect. The model captures particularly well the behaviour of v_y with the maximum relative error being 120% at $x = 1.252$ m for angle $9°$ and the mean relative error being 46%. For this component of the acoustic velocity the model is mostly within the experimental error both near the defect and away from the defect. In the case when the sensor is away from the defect, the behaviour of the model and data is much less complex and relatively independent of the distance.

Similar behaviour can be observed in the v_z data to demonstrate further the potential of using the acoustic velocity to detect the pipe wall thinning. There are more pronounced differences between the modelled and measured values of v_z for $x < 1.15$ m and $x > 1.30$ m (up to a relative error of 220% at 1.402 m for $9°$). There are two possible reasons for these differences. Firstly, the thickness of the pipe was not constant. The level of corrosion and graphitisation in the pipe

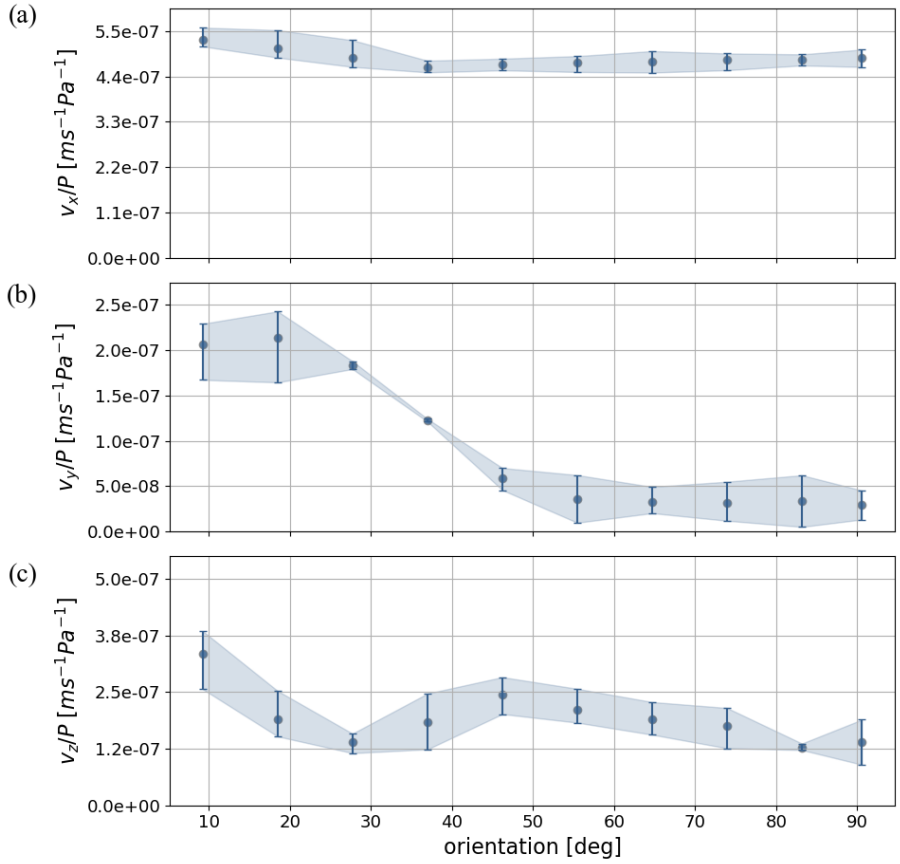

Figure 6.15: The effect of the angle between the sensor and line of defect on the amplitude of the three components of the acoustic velocity vector. The data were taken at $x = 1.227$ m, corresponding to the pipe cross-section with a 0.025 m diameter hole at 0°.

material was not known. The pipe wall thickness was measured using an ultrasonic thickness guage for points on the wall corresponding to each of the data points shown in Figure 6.14. Over this range the pipe wall thickness varied by 1.3 mm with the average being 11.2 mm. Also, the results shown in Section 6.2.4 suggest that the effect of the tank wall can be rather complex to capture accurately with the proposed model because the predicted acoustic pressure and velocity components are dependent on the choice of the Young's modulus for the PVC panel material and the quality of the tank assembly.

Effect of pipe angle

When scanning a pipe in a laboratory or in the field there is no guarantee that the sensor will be aligned perfectly beneath any defects, i.e. within a given pipe cross-section there may be some angle between the defect line and the sensor. An additional experiment was carried out to determine the effect of this pipe angle on the amplitude of the three velocity components measured with the triaxial accelerometer.

The results from this experiment, shown in Figure 6.15 and summarised in Table 6.3, suggest that the horizontal component of the acoustic velocity vector is the most sensitive to the angle at which a defect is approached. The amplitude of this component increases progressively when the angle reduces below 40° (see 6.15(b)). A 5.5-fold maximum increase in the amplitude is observed

	Max.	Angle	**Min.**	Angle	Change
v_x/P	5.3	9.24	4.6	36.97	14%
v_y/P	2.1	18.48	0.29	90.56	150%
v_z/P	3.3	9.24	1.3	83.17	90%

Table 6.3: Summary of variation in each parameter over angle, in x10^{-7} m/s/Pa.

in the v_y data when the sensor is at 9°. The behaviour of the amplitude of the vertical velocity component as a function of pipe angle is more complicated as illustrated in Figure 6.15(c). The maximum v_z amplitude is for the minimum angle of 9°. It is a 3-fold increase with respect to that recorded at 89° and it is approximately 2.5 times greater than the maximum of v_y at 9°. Between these angles v_z oscillates suggesting that it can be possible to use this quantity as an indicator of the wall damage presence even if the sensor is not in the immediate vicinity of it, e.g. at 40-50°. In contrast, the angle has little effect on the amplitude of the axial component of the acoustic velocity, v_x (see Figure 6.15(a)). There is still some increase in v_x when the angle reduces from 89° to 9°, but its amplitude does not change by more than 16% confirming that this velocity component is much less sensitive to the presence of damage.

6.4 Sensor 2: a vector hydrophone

Since the axial acceleration is of less interest here than the vertical and horizontal acceleration an alternative arrangement was trialed. This was a MEMS vector hydrophone, provided by the State Key Laboratory of Dynamic Measurement Technology, China. This work was conducted in collaboration with P. Shi from the State Key Laboratory as well as Y. Yu from the University of Sheffield, this work has been published in [226]*. It consists of a cantilevered cilia-crossbeam and is in principle more sensitive to the acoustic velocity than the accelerometer presented in Section 6.3, but only in two axes. It also contains a pressure sensor. Images of the sensor are provided in Figures 6.16(a) and (b), showing the sensor casing, the cilia crossbeam and the deployment of the sensor. More details on the sensor are provided in [226], including a discussion of the effect of sensor orientation on the results.

6.4.1 Experimental setup

Tests were conducted in the same test rig as described in Section 6.1, with the vector sensor suspended from the same tensioned cable as in Section 6.3. The sensor suspended in the tank is shown in Figure 6.16(c), with the eyelets used the mounting the sensor shown.

The sensor was moved in 50 mm increments along the length of the pipe. A 65 Hz and 170 Hz tone were used with the same speaker setup described in Section 6.1. All data was recorded using the NI DAQ, with data saved using LabView with a 12 kHz sample rate. The data was processed in the same way as depicted in Figure 6.11, excluding the resampling in step 1. This allowed a single metric for each measurement location to be compared.

Due to issues when running the experiment, only the 65 Hz data was recorded for the entire pipe length, as such the 170 Hz data is not presented here.

6.4.2 Results

The results for each of the velocity components, again normalised by pressure, are shown in Figure 6.17 for a 65 Hz source tone. These show a much less convincing correlation with defects than for the accelerometer in Section 6.3. There is a sudden increase in v_y/p at $1.25 \leq x \leq 1.3$ m, and a similar increase at $x = 1.5$ m and for $x \leq 0.75$ m. The increases around 1.5 and 1.25 m correspond to the location of two large defects which are far removed from other defects; these two defects have lengths of 45 and 46 mm respectively, as opposed to the defects further from the speaker, which have maximum length 21 mm. An image of the full length of the pipe, with the defects labelled is provided in Figure 6.16(d). The increase in v_y/p for $x \leq 0.75$ m also corresponds to a region with a large number of defects. Considering v_x/p (Figure 6.17(a), there is a significant decrease in this parameter at the location of the defect at 1.5 m, and another decrease at $x < 0.75$ m where there are multiple defects. However the response of v_x/p is largely flat for the remainder of the pipe length, regardless of the presence of defects.

*The sensor was designed and build by P. Shi and G. Zhang, experiments were conducted by P. Shi, Y. Yu and myself, experimental analysis was conducted by all authors cited in [226]. Modelling work (presented earlier in this thesis) was conducted by myself with analysis and refinement suggestions from Y. Yu and K. Horoshenkov.

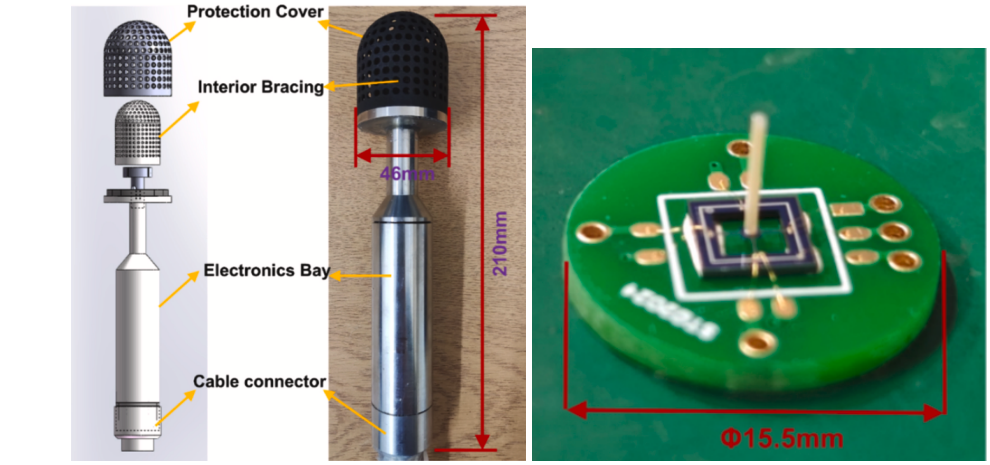

(a) (b)

(c)

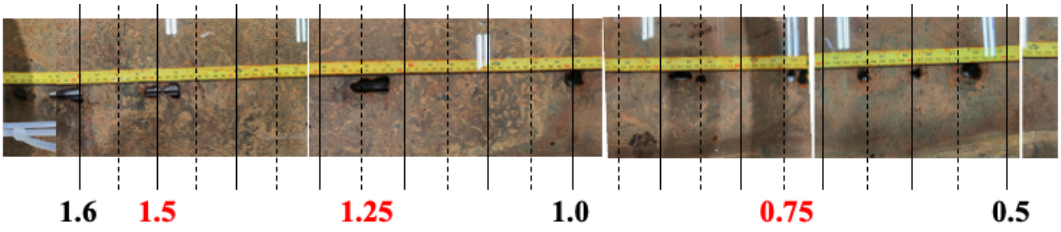

(d)

Figure 6.16: The MEMS vector sensor and experimental setup, showing (a) each component of the MEMS vector sensor, (b) the MEMS vector sensor, (c) the deployment of the vector sensor and (d) the location of each of the defects on the pipe, with the locations of interest from the main text highlighted.

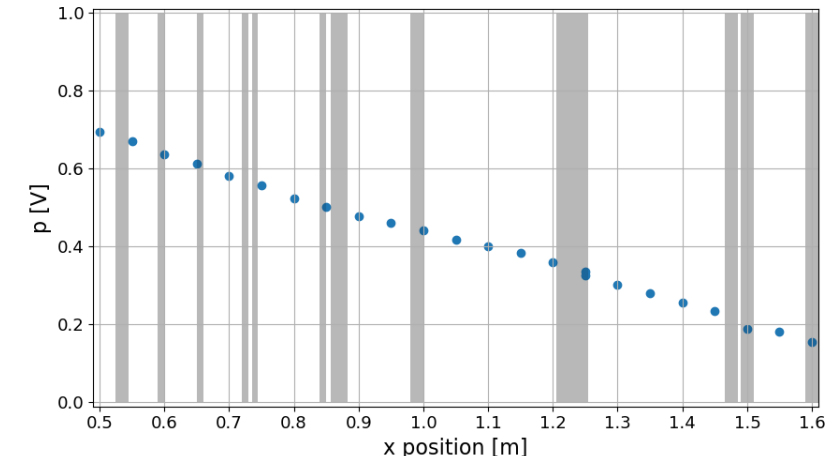

(a)

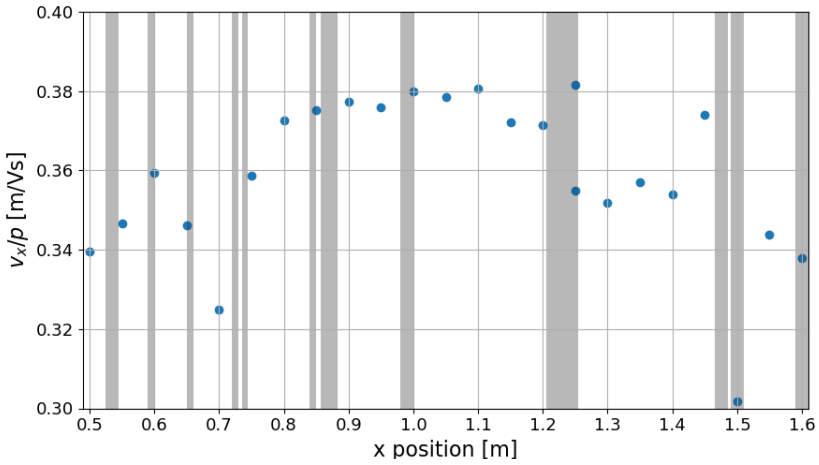

(b)

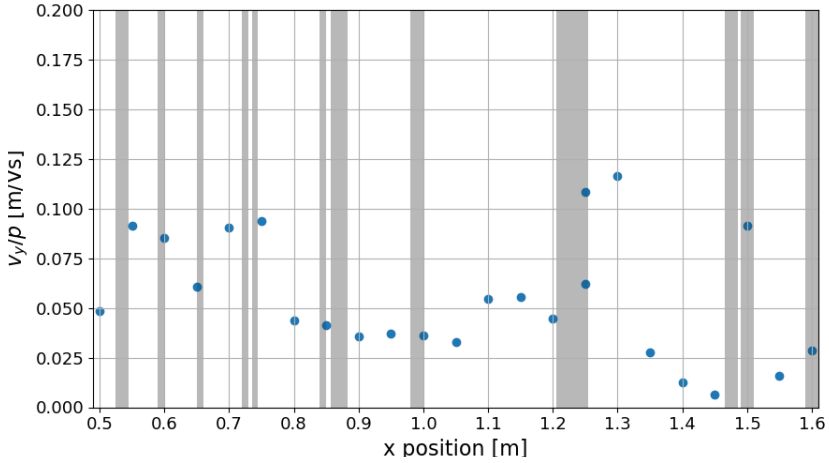

(c)

Figure 6.17: Results for each of the two components of velocity, normalised by the pressure, measured using the vector hydrophone, showing the location of the defects shaded in grey.

6.4.3 Discussion

The results for this sensor are less conclusive than for the sensor described in Section 6.3. There is a reasonable level of correlation between the y-velocity and the location of defects, with all peaks in v_y/p corresponding to the location of defects, although not all defects lead to an increase in v_y/p. Some correlation between v_x/p and the location of defects can be seen, but there are many more defects without a corresponding change in v_x/p. Furthermore, these results are based on a single dataset, with no baseline case recorded for comparison. Unfortunately, the sensor suffered from debilitating water-ingress after the set of results presented here was captured. Should the opportunity arise, further measurements should be taken to validate these results, including taking measurements at smaller intervals close to the defects, once further waterproofing of the electronics has been achieved.

6.5 Summary

In this chapter the efficacy of a triaxial accelerometer based sensor at detecting a small defect in the wall of a pressurised rising main has been demonstrated. The difference between measurements taken close to a defect and those next to an intact section of pipe is within the limits of the repeatability of the sensor measurements, and the deviation in behaviour close to a defect is striking enough to be detectable in a scan along the pipe length. This result has been proven experimentally in a limited setting, for the specific case of small holes in a pipe wall. It has been used to validate the results of numerical models which predicted that the vertical and horizontal components of the acoustic velocity would be more sensitive to small defects in a pipe than the pressure or axial velocity. These models go beyond the results of the experiment and predict that the acoustic velocity vector can be used to find not only small holes in the pipe wall, but also internal and external pitting defects. Further work is required to investigate the limitations of this result experimentally, although the range of the sensor in terms of axial distance from a defect and angle between the sensor and the defect has been shown. This work stands as a proof of concept that this kind of sensor can be used to detect small defects in pipe walls, allowing for improved predictive and preventative maintenance of pipes.

The next stages of this work require testing the triaxial acceleration sensor in a more realistic environment, at which point a more flexible deployment solution is required. The next chapter reports on this.

Chapter 7

Robotic Deployment of Acoustic Velocity Vector Sensors

The previous chapters have shown that some of the acoustic velocity components are sensitive to the proximity of a defect in the pipe wall. This has been shown both numerically, for two types of wall defect, and experimentally for holes in the pipe wall. These experiments were limited by access to the inside of the laboratory pipe; a different method of deployment was considered for inspection of a longer pipe. To this end, work was conducted in collaboration with Synthotech [227], who designed and built an in-pipe robot, including a 'halo' of triaxial accelerometers which could be used to measure the acoustic velocity vector close to the pipe wall while the robot was moving. The robot is shown in Figure 7.1. It is based on a crawler robot, controlled via the yellow cable visible in the right of Figure 7.1. There is also a camera on the robot, with pictures transmitted live via this cable. The six accelerometers are equally spaced around the halo, they have been suspended at a distance from the halo to reduce the halo's impact on the acoustics.

This chapter covers experiments with the robotic platform in the same section of exhumed rising main pipe as introduced in Chapter 6.

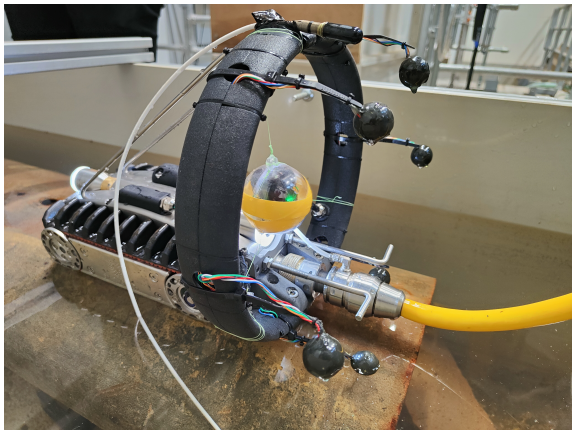

Figure 7.1: The robotic platform used for defect detection, showing the 6 accelerometers on the 'halo', they are encased in black resin to protect them from the in-pipe environment. The accelerometers are labelled anti-clockwise when viewed from the rear, with accelerometer 1 on the bottom left. The sensor described in Section 6.3 was attached for comparison.

7.1 Modelling the effect of the robot

The robot proposed by Synthotech was not insubstantial in size, with a height 1/3 the pipe diameter and a width that filled the pipe, and the effect of this on the in-pipe acoustics was a concern. Based on this the model described in Section 6.2 was modified to include a basic representation of the robot, as shown in Figure 7.2, with the key model properties summarised in Table 7.1. It is assumed that the robot is moving away from the speaker located at -3 m, so the robot body is between the sound source and the halo.

7.1.1 Effect of robot

Initially, let us consider the case where the robot halo is directly under a defect, where the defect is at the top of the pipe ('0^o', as shown in Figure 7.3(b)). The horizontal and vertical components of the velocity have been combined to give a 'radial' velocity

$$v_r = \sqrt{v_x^2 + v_y^2} \tag{7.1}$$

The horizontal and vertical velocities make a different angle to the pipe wall depending on the

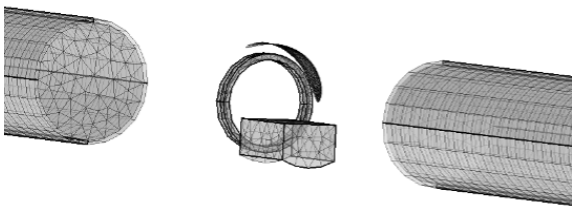

Figure 7.2: Robot as modelled in COMSOL, showing the geometry and mesh close to the robot/defect. The pipe next to the robot has been removed for improved visibility. The defect has been offset by 45^o from the top of the pipe here as part of the analysis of the robot sensitivity in Section 7.1.2.

Table 7.1: Key properties of the model used to investigate the effect of adding a robot to detecting wall defects. The dimensions of the robot are based on a simplified representation of the robot shown in Figure 7.1.

	Property	Value	Units
source	frequency	65	Hz
	location	-3	m
cutout	depth	6.6	mm
	location	0	m
pipe	length	43	m
	radius	150	mm
	thickness	10	mm
	material	ductile iron	
crawler	height	110	mm
	length	245	mm
	width	145	mm
	material	steel	
halo	radius	117	mm
	thickness	15	mm
	material	PVC	
	location	0	m

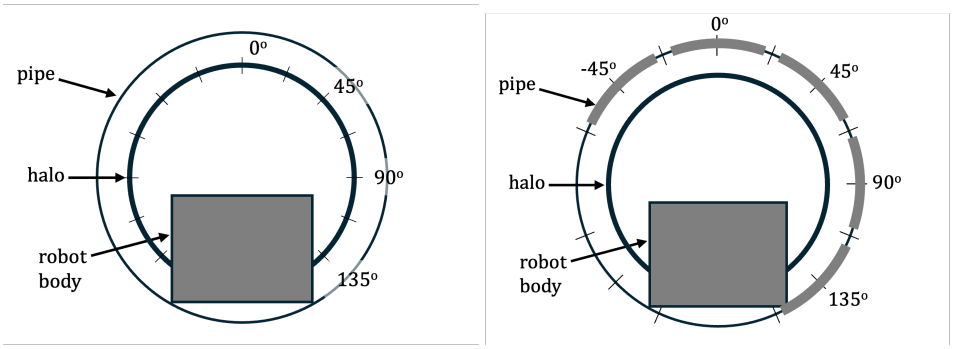

Figure 7.3: Schematics showing (a) the angular measurements around the halo used as the x-axis of Figures 7.4, 7.5 and 7.6 and (b) the location of the defect for the varying angles described in Section 7.1.2, with the approximate extent of the defect shown as the grey line to either side of each angle label.

placement of the sensor around the pipe radius, combining them in this way reduces the complexity of the problem while allowing for meaningful comparisons between sensor positions.

Figure 7.4 shows the radial and axial (v_z) velocities predicted at the halo at 5^o intervals around the halo. The left hand column shows the results with and without a defect with no robot, and the right hand column shows the results with and without a defect with a steel robot and a PVC halo. The positions measured around the halo, and the location of the defect are shown in Figures 7.3(a) and (b) respectively.

The first thing to note is the order of magnitude change in the predicted velocities: when the robot is in the pipe v_r and v_z have similar magnitude of ∼0.01 m/s (Figures 7.4(b) and (d)), whereas when there is no robot in the pipe v_r is ∼0.007 m/s (Figure 7.4(a)) and v_z is ∼0.04 m/s (Figure 7.4(c)). This reflects unsurprising changes in the fluid/halo motion when there is a robot in the pipe: the robot constricts the motion in the z direction, reducing v_z by a factor of 10, and the halo couples the motion of the r and z axes, such that v_r increases by a factor of 100 when measured on the halo as opposed to measurement in a free fluid. As long as the accelerometer on the halo is still sensitive to the presence of a defect these are not insurmountable changes, although the extent of the change (particularly in v_r) certainly justifies the current investigation.

As in Section 6.2, v_z is insensitive to the presence of a defect. There is a small reduction in amplitude at 90^o when the robot is present and there is a defect (Figure 7.4(d)), but it would be difficult to distinguish in practice. In contrast, again in line with findings in Section 6.2, v_r is sensitive to the presence of a defect. When there is no robot, this is an angle-independent increase in v_r (Figure 7.4(a)). With the robot this is heavily angle dependent (Figure 7.4(b)). The angle dependence can be explained in terms of the physics of the setup: the halo is attached to the robot at the bottom (between approximately 100 and 220^o), this coincides with the strong reduction in v_r in Figure 7.4(b). The fact that v_r is still significantly above the baseline (defect free) case for angles outside this range indicates that it can still be used to detect defect on such a contraption.

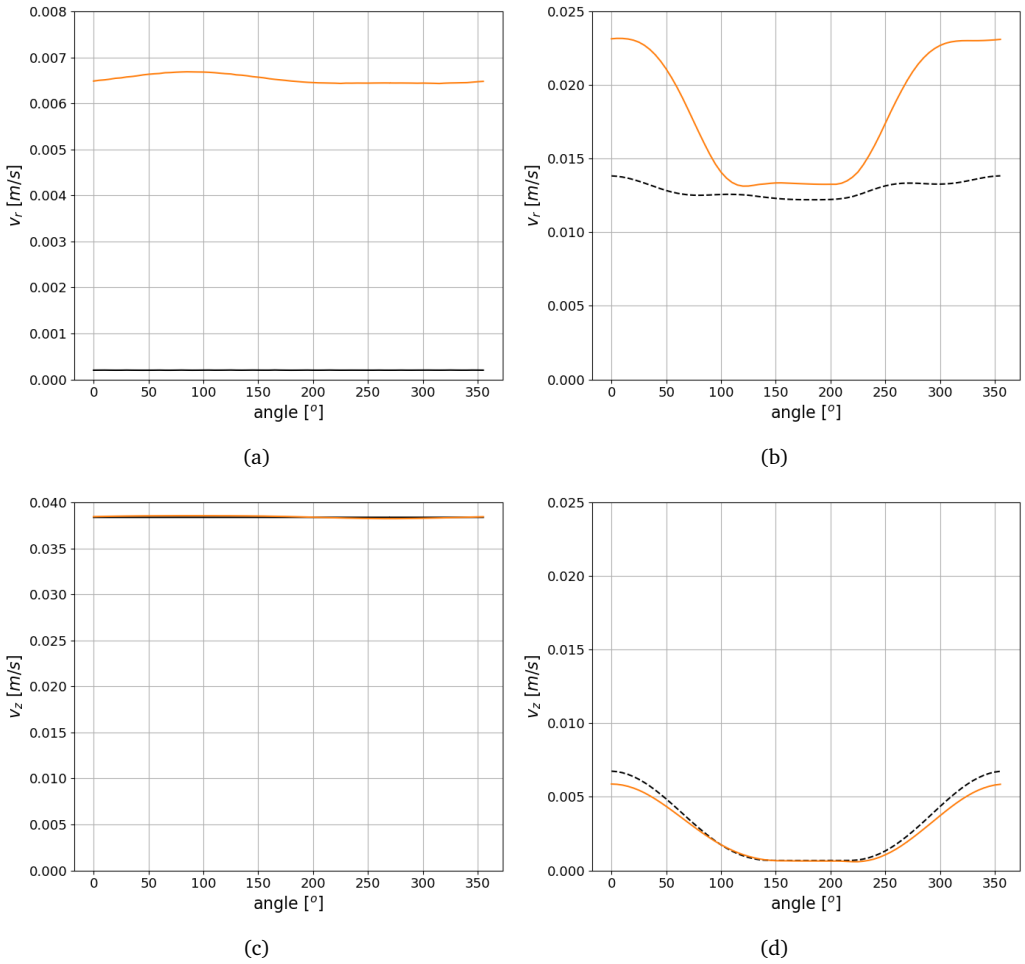

Figure 7.4: Results showing the effect of the robot on the sensitivity of measurements on the halo to the presence of a defect. Each plot shows the results with a defect at 0^o in orange, and the results for an intact pipe in dashed black, the halo is directly below the defect. (a) and (b) show the radial velocity while (c) and (d) show the axial velocity; (a) and (c) show the results without a robot while (b) and (d) show the results with a robot. These results are for points around the halo, with the angles labelled as per Figure 7.3 with 0^o directly above the robot. Note the change in scales on the y-axis.

7.1.2 Effect of defect angle

The situation considered thus far has the defect directly above the robot. Based on the angular response of v_r to this defect, which was strongly curtailed at the base of the halo where it attached to the robot body, the effect of the defect angle with respect to the robot body was investigated. This was achieved by moving the defect around the circumference of the pipe in 45^o increments as shown schematically in Figure 7.3(b). The results of this are shown in Figure 7.5(a) and (b) for the radial and axial velocities respectively.

The axial velocity in Figure 7.5(b) shows small changes in value between the with- and without defect cases, but no deviation in behaviour. The radial velocity (Figure 7.5(a)) shows a distinct change in behaviour for all defect positions. The defect at 0^o, shown in orange, has the most symmetric behaviour, while the asymmetric placement of the defect in the other cases leads to asymmetry in the measured value of v_r. As expected given that the halo is attached to the robot body at the bottom (180^o on this figure), there is very little response to the defect at this point

on the halo for all defect positions. Instead, the largest response is almost exclusively at the top of the halo. The exception to this is for the defect at 90^o to the robot, where there is the smallest response in the halo to the defect, and this is exhibited as a decrease in v_r, rather than the increase seen for other defect angles.

Based on this work, it would be worthwhile investigating alternative configurations of robot and sensor which allow for better sensitivity at all points around the pipe circumference. The poor sensitivity predicted here at 90^o is a cause for concern. It would also be beneficial to see whether alternative positioning of the accelerometers allows the angle of the defect to the robot to be determined from measurements at different points on the halo. The results of this model show a distinct lack of correlation between where around the pipe circumference the defect is, and where on the halo the largest response is; it would be useful for certain types of maintenance work if the location of the defect could be found around the pipe circumference as well as along the pipe length.

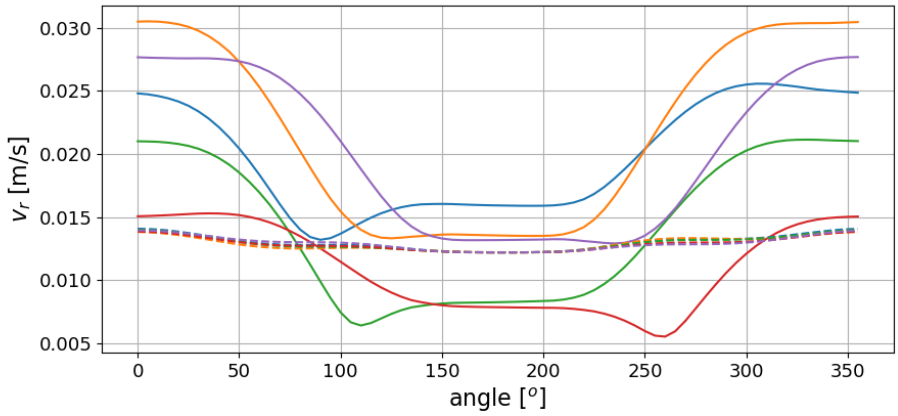

(a)

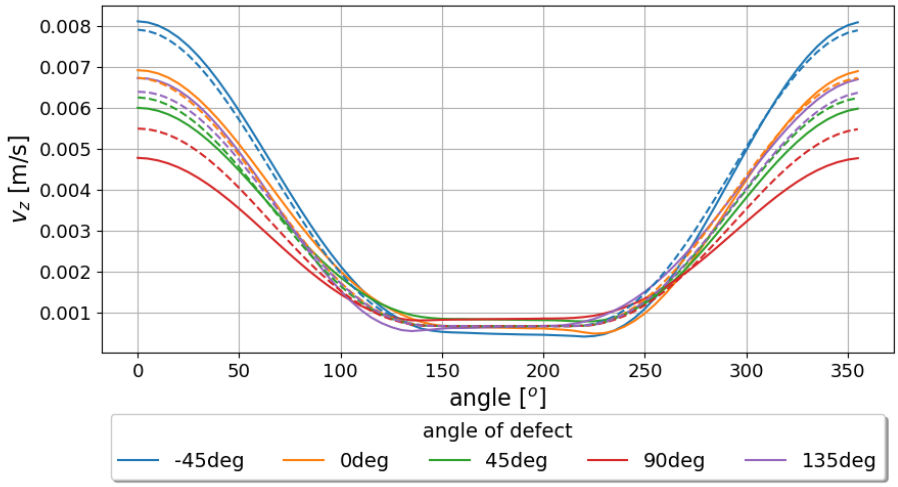

(b)

Figure 7.5: Results showing the effect of the angle of the defect with respect to the robot on the (a) radial and (b) axial velocity. The dashed lines in (a) and (b) are for results without a defect, while the solid lines are for results with a defect. The legend in (b) applies to both (a) and (b), the defect angles are shown schematically in Figure 7.3(b).

7.1.3 Effect of robot position

Extending this work further to consider how the axial position of the robot effects the detection of defects leads to Figure 7.6. This figure shows results for the robot halo positioned between -0.5 and 0.5 m from the defect. This range was chosen since it is expected that it is within this distance that the robot body will have most influence.

Again, the axial velocity, v_z, shows little sensitivity to the defect, regardless of the axial distance between the robot and the defect. v_r is more interesting, showing that the defective pipe is distinguishable from the intact pipe for the entirety of this distance. As expected, the largest response to the defect is when the halo is directly beneath the defect, at which point v_r is 0.031 m/s for measurements at the top of the halo (0^o). Moving the robot away in either direction reduces the

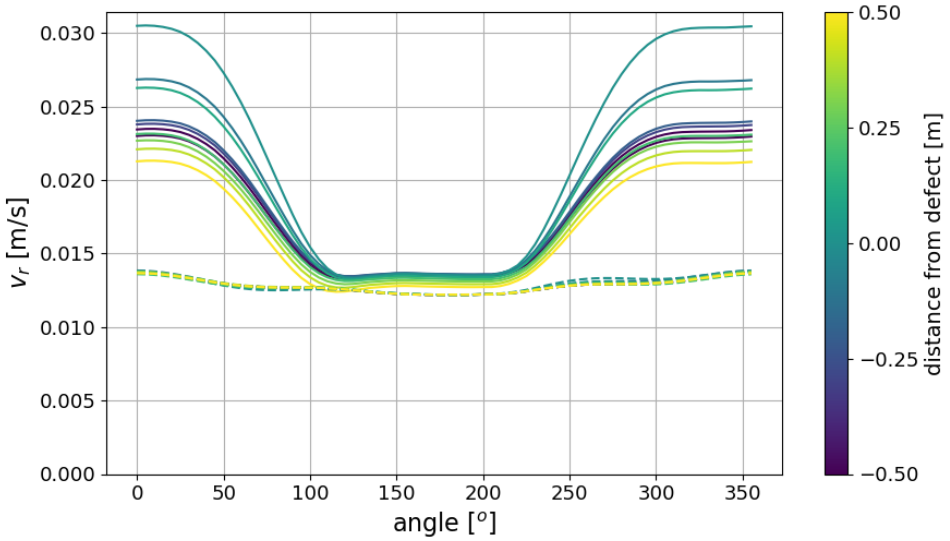

(a)

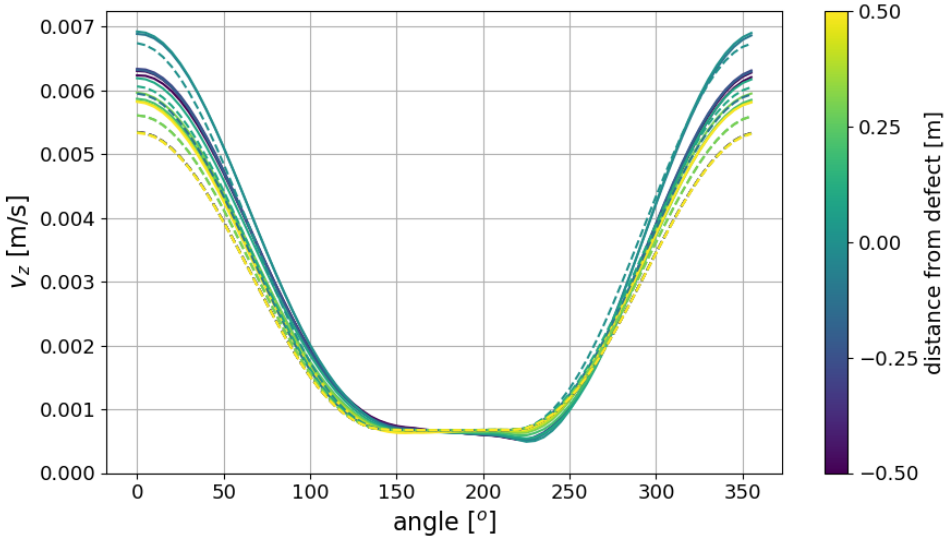

(b)

Figure 7.6: Results showing the effect of the distance of the robot from the defect on the (a) radial and (b) axial velocity. The distance is measured from the halo since this is where the sensors are located. The defect is at 0^o, directly above the robot. The dashed lines are for results without a defect, while the solid lines are for results with a defect.

measured value of v_r to 0.023 m/s at -0.5 m from the defect and 0.021 m/s at +0.5 m from the defect. The more significant decrease when the robot moves to +0.5 m from the defect as opposed to -0.5 m is likely because the robot body is between the speaker and the defect when the halo is +0.5 m from the defect, so reduces the transmission. Based on this, deployment designs should try to ensure that the halo is on the side of the robot closest to the speaker to increase sensitivity.

7.2 Testing the robotic platform

7.2.1 Experimental setup

The robot was deployed in the same pipe as was used in the experiments reported in Chapter 6, with measurements taken at four locations in the pipe. One was on a defect free section of pipe, the other three were directly below defects of various sizes. All the defects were chosen based on their being relatively isolated, to make the acoustic environment as simple as possible. The locations of the four measurements are shown in Figure 7.7, where it is the position of the accelerometers that is being monitored. The size of each of the three defects is provided in Table 7.2. The accelerometers were aligned as shown in Figure 7.7, with the z-axis along the pipe and the x-axis directed vertically. The accelerometers are spaced equidistant from each other around the halo, which is a ring of radius 117 mm, supported by the robot body on its bottom edge.

The same speaker was used as a sound source as in Chapter 6, although here a 5 s, 100 Hz tone was used as the signal. The results were processed as shown previously in Figure 6.11, without the requirement for resampling. The part numbers for the amplifier and speaker are provided in Appendix A. The data was recorded at 12,000 Hz.

Both the hydrophone and the accelerometer from Chapter 6 were attached to the robot, as shown in Figure 7.1. It was originally intended to compare the measurements from these sensors with those collected from the new accelerometers, however the configuration of sensors led to this data being too noisy.

7.2.2 Results

The amplitudes of the radial and axial components of the acceleration at each location are shown in Figure 7.8, with the same results presented on a cartesian and polar plot. The defect is located

Table 7.2: Location and length of each of the defects in Figure 7.7, where the location is the distance from the centre of the defect to the end of the pipe in the left hand side of Figure 7.7.

Defect	Location (m)	Length (m)
1	0.60	0.01
2	0.99	0.02
3	1.23	0.05
No defect	0.57	N/A

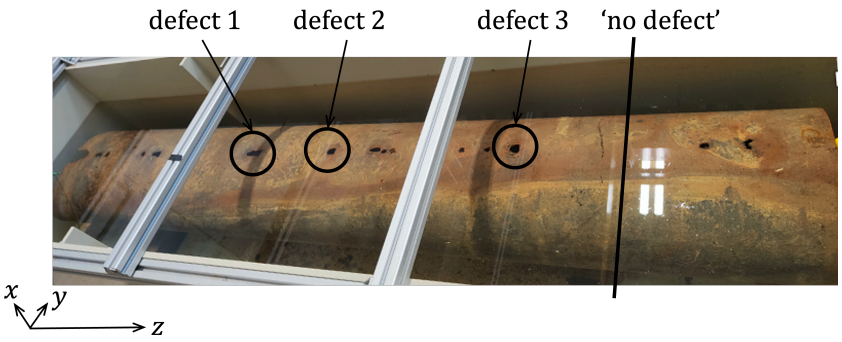

Figure 7.7: Set up for measurements using a robotic platform showing the locations of testing for robotic platform. Locations are labeled by the position of the accelerometers.

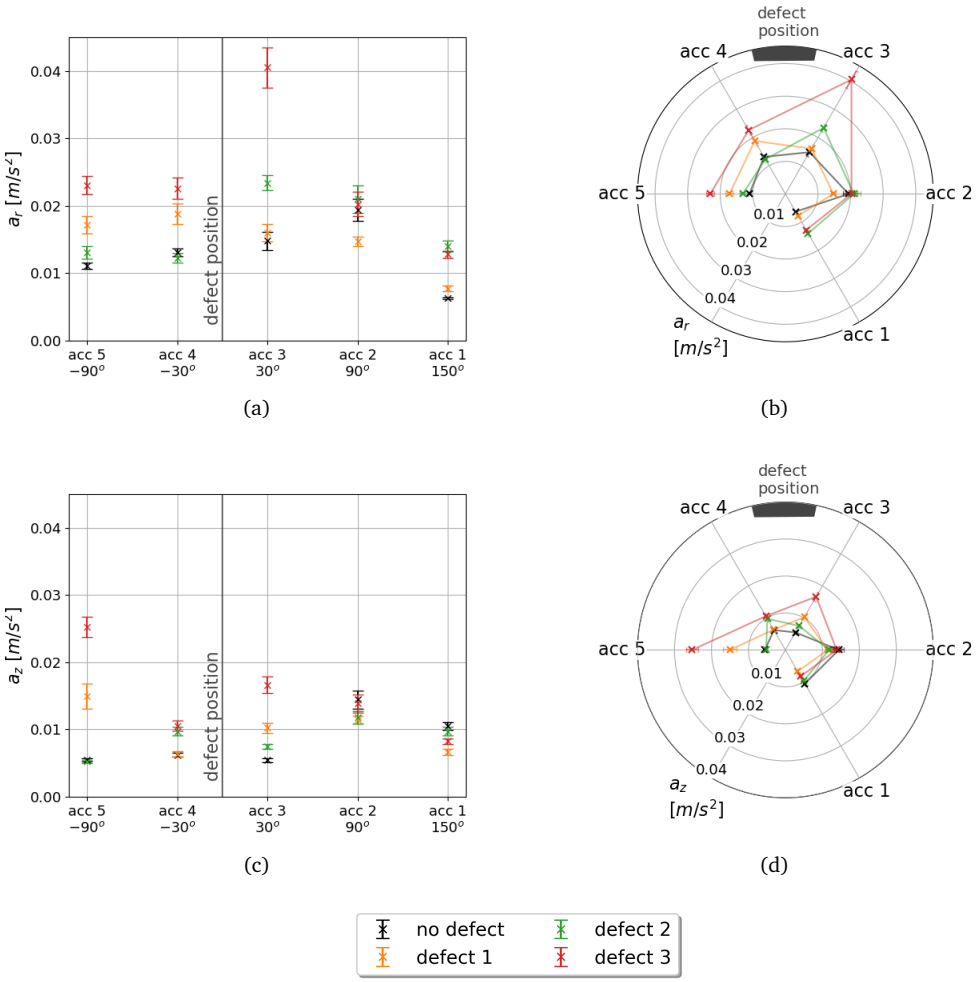

Figure 7.8: Acceleration measured on each axis for each accelerometer around the halo, the same data is shown in two formats. In (a) and (c) the radial and axial accelerations are shown on a cartesian graph, in (b) and (d) the same information is presented on a polar graph with the measurement for each accelerometer shown at the position of that accelerometer on the halo. The legend shown in (e) applies to all subfigures. The error bars are calculated based on the five scans taken at each location and show 1 standard deviation from the mean. The approximate defect position is shown in each figure.

at 0^o, the 'top' of the polar plots. This discussion focuses on the polar plots shown in Figures 7.8(b) and (d), the linear plots provided in Figures 7.8(a) and (c) give an unwrapped view of the relative amplitudes and error bars. The results for each accelerometer around the halo are plotted in Figures 7.8(b) and (d) at the accelerometer location around the halo, with the top of the pipe and the line of defects between accelerometer 3 and 4, at the top of the plots. Accelerometer 6 was not working during this testing, so has been excluded from the presented data. The measurements taken on an intact stretch of pipe are shown in black, with each of the other three defects plotted in a different colour. Five scans were performed at each location, the mean and standard deviation of these measurements form the basis of the error bars in each plot. The location of the accelerometers was determined by the robot designers, future work should consider more accelerometers or rotating the accelerometers to have one at the top of the pipe.

Figures 7.8(c) and (d) show that that the axial acceleration is within a 15 $\mathrm{mm/s^2}$ range around

the halo for all accelerometers except accelerometer 5, and the measurements for each accelerometer are within 5 $\mathrm{mm/s^2}$ of each other for all defect and non-defect measurements, except for accelerometers 3 and 5. The measurement at accelerometer 5, at the side of the pipe, shows a value of a_z at defects 1 and 3 of 2-3 times that at defect 1 and for the intact section of pipe. This is a larger change than is expected at this position in the pipe based on consideration of the results in Section 7.1. Further testing is needed to fully understand this anomaly, but it is most likely caused by the presence of the robot. Accelerometer 3 also shows a slight (approx. 2 times) increase in a_z for defects 1 and 3. This is close to the defect and may be caused by some leakage of the accelerations in the other directions into these measurements; it can be seen in Figure 7.1 that these accelerometers are not as well aligned with the axes of the pipe as for the previous two methods.

Considering a_r in Figures 7.8(a) and (b), which modelling and previous measurements predict will be more affected by defects, this axis does show more of a change between the no-defect and defect measurements. All the accelerometers except accelerometer 4 show an increase in a_r at the defects. The largest changes are measured at defect 3 for accelerometers 3-5 where there is a 2-fold increase in a_r. The increase in a_r measured on accelerometers 3-5 increases from defect 1, which has a length of 0.001 m to defect 2, which has a length of 0.002 m to defect 3 which has a length of 0.005 m, indicating a correlation between the size of the defect and the change in the amplitude of the acceleration. The consistency of the measurements at accelerometer 4 when compared with those at accelerometer 3, implies that either the side of the pipe which accelerometer 4 was measuring was considerably smoother than that of accelerometer 3, or there was some problem with accelerometer 4 since it would be expected that they be similar given the symmetry of the system. This may have been the attachment method: accelerometer 3 has a much looser attachment, as can be seen in Figure 7.1.

Instead of considering the value of the acceleration at each accelerometer, Figure 7.9 considers the range of acceleration around the halo for each axis and defect. Here the 'range' has been calculated as the standard deviation, σ, in acceleration around the halo for each scan, the error bars in the plot show the mean and standard deviation of this range across the scans in each location. The mean range for the measurements on the intact (no-defect) section of pipe has been extended by a dashed line to cover the plot since it acts as a reference point for the other measurements. The first point of interest is how similar the range for the two accelerations is in the no-defect case. The mean accelerations are within 10% of each other and the error bars overlap. This is also the case for defect 1, which the previous analysis has shown did not lead to a significant change in acceleration from the baseline, defect-free, case. In contrast, for defects 2 and 3, the axial acceleration is significantly less than the radial acceleration, at least 3σ in both cases.

Based on this, further investigations are needed to determine why defect 1 was below the sensitivity of this measurement method, when it is similar in size to defect 2. This was the defect furthest from the speaker, so modifying the speaker location could form the first element of this work.

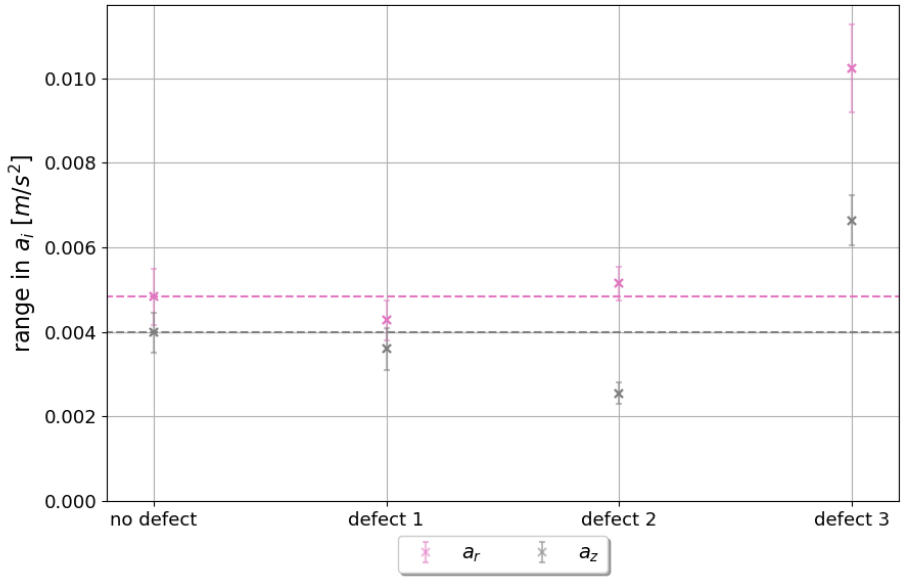

Figure 7.9: Comparison of the range in acceleration around the halo for each defect, showing each acceleration axis in a different colour, with the mean range in acceleration measured for the no defect case extended by a dashed line to cover the rest of the plot.

7.3 Summary

Based on this experiment, there is a reasonably clear correlation between the presence of a defect and the amplitude of the radial acceleration. There is a similar correlation between the presence of a defect and the difference between the axial and radial accelerations, with the axial and radial accelerations being very similar for a defect-free pipe, while the radial velocity is larger than the axial velocity close to a defect. Further testing is required to determine the efficacy of this for detecting defects in a more realistic scenario, and to ascertain the cause of a few oddities in the data, namely the large increase in a_z for accelerometer 1 close to defects, and the lack of response by accelerometer 4. This testing was not conducted at the time due to limited access to the robot.

The work presented in this chapter demonstrates the potential capabilities of this combination of robot and sensor halo. In the test pipe, a_r detected the largest of the defects studied, and with further data to better understand the background noise, it may be that the smaller holes were also detectable. Considerably more work is needed to improve and test this design. The halo design needs further testing to determine the optimal spacing of the accelerometers and the best size of the halo to get close enough to the pipe wall. Ideally this would be some kind of adjustable system, so the accelerometers travel a consistent distance from the pipe wall regardless of pipe radius. The robot needs to be tested in a larger pipe system, with more features and with a blind test to find pipe defects and leaks. It would also be beneficial from a robot localisation perspective to use acoustics to detect features, such as joints, using the robot, which has not been tested or investigated here.

Chapter 8

Conclusions and Recommendations

This thesis has presented a body of work considering the limitations in current acoustic methods for leak detection in plastic pipes before presenting a more sensitive method for detecting leaks and defects in pipes in water distribution networks and wastewater rising mains. Through a combination of numerical modelling and experimental validation, this work has demonstrated that using acoustic velocity vector sensors (AVVSs) to measure the full acoustic velocity vector from an in-pipe platform provides more sensitive diagnostic capabilities than traditional monoaxial or pressure-based acoustic approaches.

Initial investigations demonstrated the variability in acoustic signatures produced by leaks, where the variability was found to be caused by the leak shape as well as back pressure and the distance between the measurement device and the leak location. The use of machine learning methods was initially anticipated to address the scope of this problem, however it was felt that the significant amount of data collection required for such an approach made it impractical within the time-frame of the project, especially since commercial options for such a methodology were already under development. Further work was conducted quantifying the severe and frequency-dependent attenuation of sound in plastic pipes, confirming that only low-frequency waves propagate effectively. It was found that standard pipe features such as joints and burial conditions increase considerably the acoustic wave attenuation and limit further leak signal transmission. These results provide an explanation for the poor performance of conventional correlation methods in plastic pipe systems and underscore the need for proximate, in-pipe measurement approaches ideally based on robotic sensing platforms.

Building upon this understanding of the challenges in detecting waves in plastic pipes at any realistic distance from the sound source using conventional methods, numerical models were used to explore the response of different acoustic velocity components to holes and pitting in pipes of various materials and dimensions. The results showed that the radial velocity components exhibit significant amplitude changes near defects, providing a new basis for acoustic defect and leak detection. This contrasted with the behaviour of the pressure and axial velocity, which were not affected by the proximity of a defect. These predictions were confirmed experimentally using an AVVS inside a section of ex-rising main, where the AVVS successfully identified small holes in the pipe wall.

The final phase of this project concerned the deployment of AVVSs on a robotic platform and the effect of the robot's body on the sensor performance. The results show that a larger hole in the pipe wall leads to a clear response in the acoustic velocity vector. While further work is required

to optimise the sensor geometry and deployment method to improve robustness, and to evaluate its performance in more realistic buried networks, the results establish that such a platform offers a viable route towards autonomous in-pipe inspection.

Overall, this thesis contributes both new physical understanding and technological innovation to the field of leak and defect detection in buried pipes. It advances the state of the art by introducing acoustic vector sensing as a next-generation approach for monitoring plastic and ferrous water pipes, offering improved sensitivity, adaptability, and compatibility with robotic inspection systems. With further refinement, the results of this work can significantly enhance the reliability and efficiency of water infrastructure maintenance in the coming decades and paves the way for no dig in-pipe rehabilitation with autonomous robotics.

8.1 Proposed Future Work

This work has justified and conducted tests on an acoustic velocity vector-based approach to robotic pipeline inspection. The proposed next steps based on this work include:

1. **Further, systematic measurement of the attenuation in pipes over different features**. This has been started in this thesis, with Chapter 4 measuring the attenuation across multiple features in a plastic pipe loop. However, these measurements were conducted on a pipe network designed for other purposes, with many additional features which led to multiple reflections, interference within the system and often short pipe sections between features, which limited the distance over which reliable measurements could be conducted. These measurements should be repeated on simpler pipe sections in the acoustic far-field for improved accuracy. The sound source used in these experiments was also not ideal, since it was limited at low frequencies and led to a non-linear excitation on the pipe at all frequencies. Finally, the measurements taken should be compared with predictions from theory and numerical simulations.

2. **Testing of the proposed AVVS methodology on a more realistic pipe setup**. Initially this would be a longer pipe section with the fluid only inside the pipe, and either air or soil outside the pipe. It would be beneficial to run tests on different pipe diameters, pipe materials and with a variety of defects of various sizes. The numerical work should also be extended to cover this increased scope of investigations. These experiments should culminate in work on a larger pipe network, including blind detection of defects, the location of which is not known during processing.

3. **Further validation of the robotic platform**. The next stages of this work should consider the ideal placement of a sound source with respect to the robot, as well as testing the robot on a more realistic section of pipe. This testing should be continued for a range of pipe materials and dimensions, with a range of defects tested. The aim of these tests should be to ensure the AVVSs perform on a robotic platform in a similar way to on their own, and to test the practicalities of the robotic deployment. For example, its range, any traction issues it might have, etc.

4. **Optimisation of the robot design**. The shape of the robot should be adjusted to minimise its effect on the surrounding fluid and sensor performance. The design of the halo should be optimised to allow free motion of the sensors in the water. The halo design needs further

work to adapt it to potentially varying pipe diameters, where the sensors will either be different distances from the pipe wall, or the size of the halo needs to be adjustable to allow the distance to pipe wall to be maintained. Currently, the robot body is very square, and has a noticeable impact on the projected in-pipe acoustic field, this should be modified into a more acoustically quiet form factor.

5. **Extension of the modelling work to account for the fluid dynamics of the system**. The frequencies being considered allow for static fluids to be used as a first approximation. However, these are not static systems, with typical flow speeds of 1 m/s and leakage being an inherently mobile phenomenon. Modelling work should progress from a purely acoustic model to a fluid dynamics model, this would be a continuation of the work presented by Adesina [228], which used Ansys Fluent to predict leak noise from the fluid dynamics of the system.

6. **Extension of the AVVSs to detect other features in the pipe network**. This work has concentrated on leaks in pipes and defects in the pipe wall, with a focus on holes in the pipe wall. There are many different issues in the pipe network, including different forms of corrosion and bubbles forming within the pipes. A full survey should be done of which are detectable acoustically using this platform.

7. **Integration with complementary sensors**. The work presented here aims to provide information on areas where defects are likely to be. The use of such low frequencies limits the resolution of detection, therefore any robotic platform using this would probably want to have a higher resolution tool to more accurately inspect the issue. This might be a camera or some kind of ultrasonic sensor. More information is needed on the limits of the sensor proposed in this thesis before complementary sensors could be identified. Once the best choice of sensor suite is determined, significant development would be required on power management, data processing and memory consumption optimisation.

Appendix A

Part numbers

Table A.1: Part numbers of equipment used during this thesis. The chapters in which the equipment was used has been provided.

Description	Part number	Documentation	Chapters
hydrophone	B&K 8103	[229]	4
hydrophone amplifier	B&K Nexus 2693-0S4	[230]	4
data acquisition card (DAQ)	USB-4431	[231]	3, 4
monoaxial accelerometers	PCB 353B04	[232]	3, 4
triaxial accelerometers	3 x PCB 353B18	[233]	4
high resolution monoaxial accelerometers	PCB 393B04	[234]	5
impact hammer	PCB 086C03	[235]	4
shaker	Dayton Audio DAEX25CT-4	[236]	4
speaker	Visaton FR8	[237]	6, 7
amplifier (for shaker and speaker)	TDA7498E	[238]	4
underwater triaxial accelerometer	G-link-200	[239]	6

Appendix B

Mesh analysis for modal analysis of MDPE pipe

The model used to generate the results in Sections 3.1 and 4.1 was a 2D axisymmetric model. A free triangular mesh was used for the pipe interior, and a mapped mesh for the pipe wall.

To validate the mesh, three parameters within the mesh were changed:

1. the number of mesh elements in the pipe wall thickness, n_{wt}
2. the number of mesh elements in the pipe wall circumference, n_{wc}
3. the largest element size allowed in the pipe interior, m_p

An example of a mesh with $n_{wt} = 5$, $n_{wc} = 24$ and $m_p = 8$ mm is shown in Figure B.1.

The effect of varying each of these parameters is shown in Figure B.2. It can be seen that the number of mesh elements in the pipe wall thickness (m_{wt}) has minimal effect on the results, as does changing the minimum element size in the pipe interior (m_p). Increasing the number of elements around the pipe wall circumference (n_{wc}) does have an effect, mainly at higher frequencies and in the evanescent modes. Based on these results a value in the centre of each of these ranges has been determined to give a good representation of the solution.

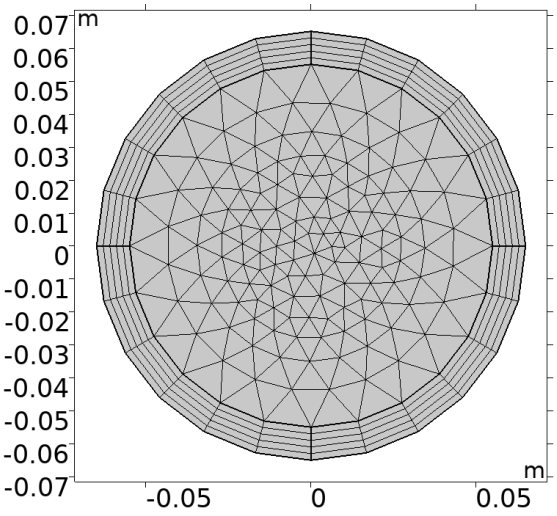

Figure B.1: Example of mesh used in model with $n_{wt} = 5$, $n_{wc} = 24$ and $m_p = 8$ mm.

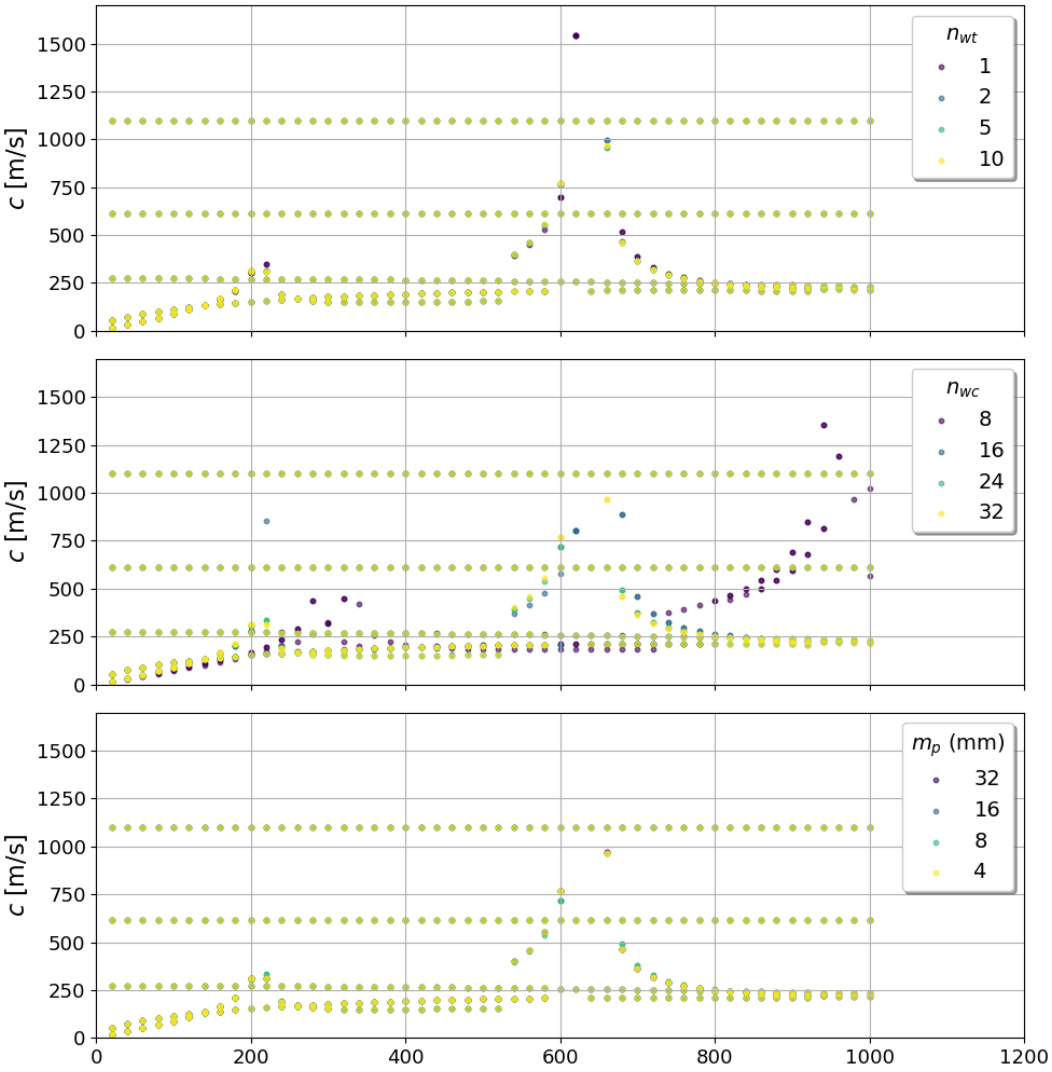

Figure B.2: Effect of varying the size of each part of the mesh, with the legends in each figure showing the value being changed. The other two variables are held at their finest value while the third is changed.

Appendix C

Estimating the storage modulus acoustically

The dispersion relation for axisymmetric wave propagation in a fluid filled pipe surrounded by soil can derived from the equations of motion for the fluid and soil. The dispersion relation in terms of displacement amplitudes, U_z, U_θ and U_r is described by:

$$\left\{[Q] + \frac{(1-\nu^2)R^2}{Eh}\left([L][K]^{-1} + P\begin{bmatrix}0 & 0 & 0\\ 0 & 0 & 0\\ 0 & 0 & -1\end{bmatrix}\right)\right\}\begin{bmatrix}U_z\\ U_\theta\\ U_r\end{bmatrix} = 0 \tag{C.1}$$

By way of introduction to each of the terms in this equation a very brief outline of the derivation of this equation is provided, however the reader is referred to Appendix A of [205] for a more complete derivation.

For a pipe shell, the equation of motion can be written as

$$[Q][U_j] = 0 \tag{C.2}$$

where $[Q]$ is a matrix differential operator acting on the displacement. The choice of $[Q]$ depends on the shell theory being used, here that from the Donnel-Mushtari theory is appropriate [240]:

$$Q = \begin{bmatrix}\Omega^2 - k_z^2R^2 - n^2\frac{(1-\nu)}{2} & k_zRn\frac{(1+\nu)}{2} & -k_zR\nu i\\ k_zRn\frac{(1+\nu)}{2} & \Omega^2 - k_z^2R^2\frac{(1-\nu)}{2} - n^2 & ni\\ -k_zR\nu i & ni & -\Omega^2 + 1 + \frac{h^2}{12R^2}(n^2 + k_z^2R^2)^2\end{bmatrix} \tag{C.3}$$

with $\Omega = \omega R\sqrt{\rho(1-\nu^2)/E}$ for a mode of order n ($n = 0$ for axisymmetric modes). Here $E = E'(1 + \eta i)$ is the complex modulus for a storage modulus E' and loss factor η, k_z is the axial wavenumber and ω is the angular frequency. The values of these used during testing are shown in Table 4.1.

Including the pipe-soil interface requires consideration of the pressure exerted by the pipe shell on the soil. This can be derived for a homogeneous, isotropic, linear elastic soil by combining Navier's wave equation with Hooke's law to find

$$\begin{bmatrix}\sigma_{rz}\\ \sigma_{r\theta}\\ \sigma_{rr}\end{bmatrix} = [L][K]^{-1}\begin{bmatrix}U_z\\ U_\theta\\ U_r\end{bmatrix} e^{in\theta}e^{i(\omega t - k_z z)} \tag{C.4}$$

where σ_{ij} are the stresses in the soil acting from direction i to direction j, $[L]$ is a matrix summarising the stresses in the soil and $[K]$ is a matrix expressing the soil displacement. The components of $[L]$ and $[K]$, for an axisymmetric wave where the dependence on θ is removed are:

$$K_{11} = -k_z \mathrm{H}_n(k_d^r r)i \tag{C.5}$$
$$K_{13} = -\frac{1}{r}k_\tau^r \mathrm{H'}_n(k_\tau^r r) - (k_\tau^r)^2 \mathrm{H''}_n(k_\tau^r r) + \frac{1}{r^2}n^2 \mathrm{H}_n(k_\tau^r r) \tag{C.6}$$
$$K_{31} = k_d^r \mathrm{H'}_n(k_\tau^r r) \tag{C.7}$$
$$K_{33} = -k_z k_\tau^r \mathrm{H'}_n(k_\tau^r r)i \tag{C.8}$$

$$L_{11} = -2\mu_s k_z k_d^r \Pi'_n(k_d^r r)i \tag{C.9}$$
$$L_{13} = -\mu_s(k_z^2 k_\tau^r H'_n(k_\tau^r r) + \frac{1}{r}(k_\tau^r)^2 H''_n(k_\tau^r r) - \frac{1}{r^2}k_\tau^r H'_n(k_\tau^r r) + (k_\tau^r)^3 H'''_n(k_\tau^r r) - \frac{1}{r^2}n^2 k_\tau^r H'_n(k_\tau^r r) + \frac{2}{r^3}n^2 H_n(k_\tau^r r)) \tag{C.10}$$
$$L_{31} = (\lambda_s + 2\mu_s)(k_d^r)^2 H''_n(k_d^r r) + \lambda_s(\frac{1}{r}k_d^r H'_n(k_d^r r) - \frac{1}{r^2}n^2 H_n(k_d^r r) - k_z^2 H_n(k_d^r r)) \tag{C.11}$$
$$L_{33} = -2\mu_s k_z (k_\tau^r)^2 H''_n(k_\tau^r r)i \tag{C.12}$$

In the above equations H_n and Π_n are Hankel functions of the first and second kind of order n, k_d^r and k_τ^r are radial wavenumbers relating the compressional (k_d) and shear (k_τ) to the axial wavenumber k_z such that $k_x^r = \sqrt{k_x^2 - k_z^2}, x \in (d, \tau)$. This derivation assumes a homogeneous, isotropic, linearly elastic soil such that it can be described by the Lame constants μ_s and λ_s.

It is possible to solve these equations, such that if the radial wavenumber is known the storage modulus of the pipe wall can be calculated. The solution for these equations is presented in [205] for the experimental setup described below. This author presents an alternative methodology in Chapter 4 based on comparison with numerical results from COMSOL®.

Appendix D

Finding the speed of sound from crossing points on impact hammer measurements

In Section 4.2.1, the time difference between the arrival times of impact hammer measurements was proposed as a method of finding c. An example of the time series for such a measurement is shown in Figure D.1. This example shows the results for a threshold of 4x the background noise, where the background noise was calculated as the maximum of the signal for 0.5 s before the impact. This choice of threshold was a crucial element of the process and no sensible way of deciding it could be found.

This is demonstrated in Figure D.2, where thresholds of between 1 and 100 times the background recordings have been applied, and the speed of sound calculated. There is a huge range in the calculated value of c, with no obvious way of differentiating the actual value.

Figure D.3 shows a similar set of results as Figure 4.15, with c calculated from the peaks, with the thresholds given in the legend. It was hoped that this method might allow more visibility of other modes, and to an extent this seems to be the case. The lower thresholds lead to values of c grouped around 800 m/s, as would be expected for the fluid borne mode, while the higher thresholds lead to a value of c similar to that found using the cross-correlation and phase-based methods, of around 400 m/s. This is interesting, however the large span of values limits the practicality of this method. It could be made more manual, and potentially more accurate, by visually inspecting the data to find features related to the impact reaching each meter, however this would be laborious for large data sets and it was felt it was highly liable to bias.

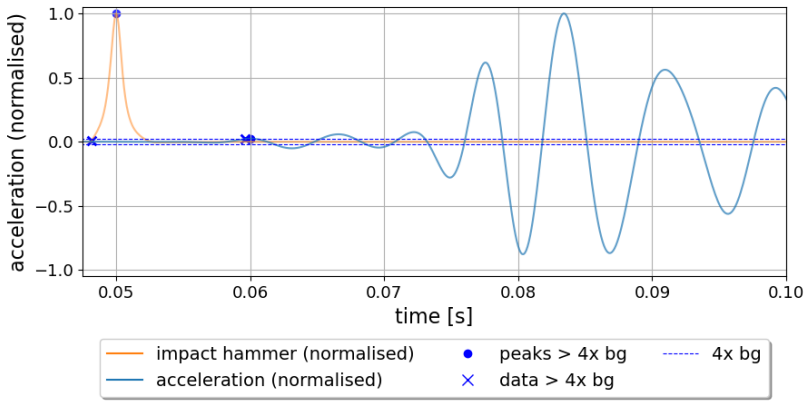

(a)

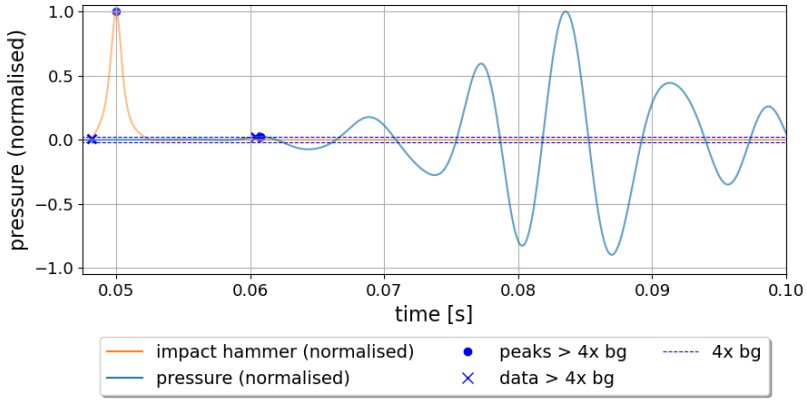

(b)

Figure D.1: An example of identifying the speed of sound based on either the first time a signal crosses a threshold value, or the first peak greater than this threshold, where the thresholds have been determined as a multiple of the background. In these figures the data has been filtered to between 25 and 175 Hz.

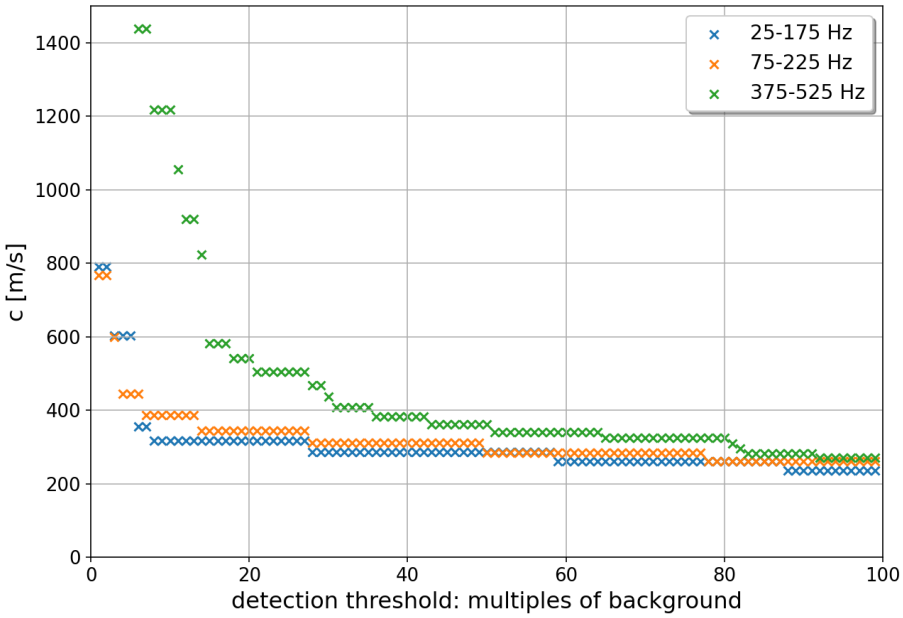

Figure D.2: Speed of sound calculated from the arrival time of impact hammer measurements on the wall acceleration, where the data has been filtered according to the legend, and detection thresholds from 1 to 100x the background measurements have been applied.

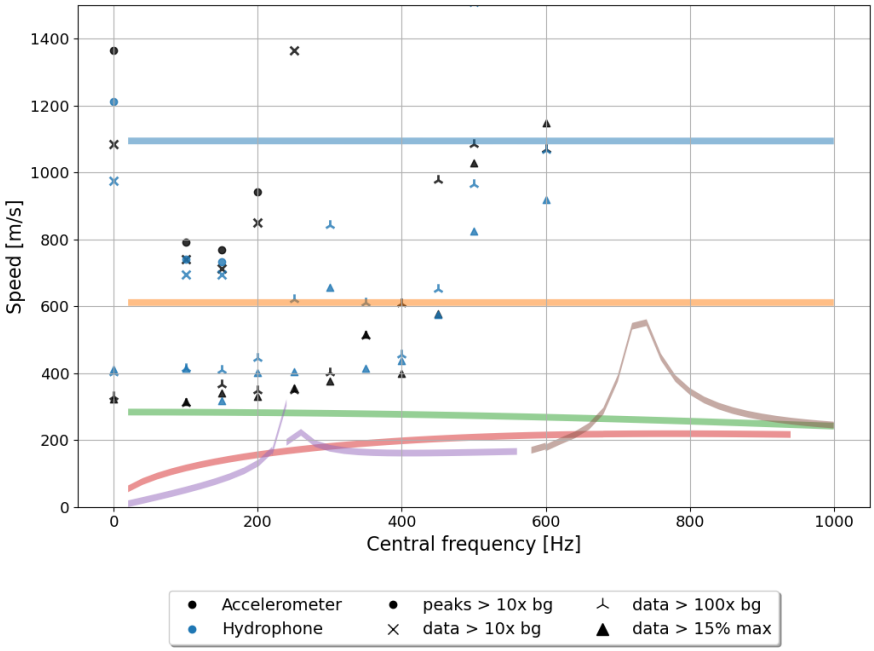

Figure D.3: A comparison of the speed of sound calculated for an example dataset with the impact 8 m from the hydrophone/accelerometer. The speed of sound is plotted against the central frequency of the filter applied to the data for an array of filters, the exact frequency ranges are provided in Table 4.2. The shaded regions show the predicted values of c from Chapter 3, coloured as per Figure 3.1.

Appendix E

Mesh analysis for model of defective pipe

This section describes the steps taken to optimise the mesh for the model described in Chapter 5.

A schematic view of the mesh used in the model described in Section 5.2 is provided in Figure E.1 showing each of the meshing elements. Based on this there are 6 main parameters than can be modified within the mesh:

- m_p, the maximum element size of the free triangular mesh that is swept along the majority of the pipe.
- d_p, the distance between elements in this swept mesh.
- n_w, $n_{w,3D}$, the number of elements in the pipe wall, in the main pipe wall and close to the defect (in the 3D section).
- m_t, the maximum element size of the tetrahedral mesh close to the defect.
- m_d, m_h, the maximum element size on the surface of the defect/at the location of the hole in the pipe.

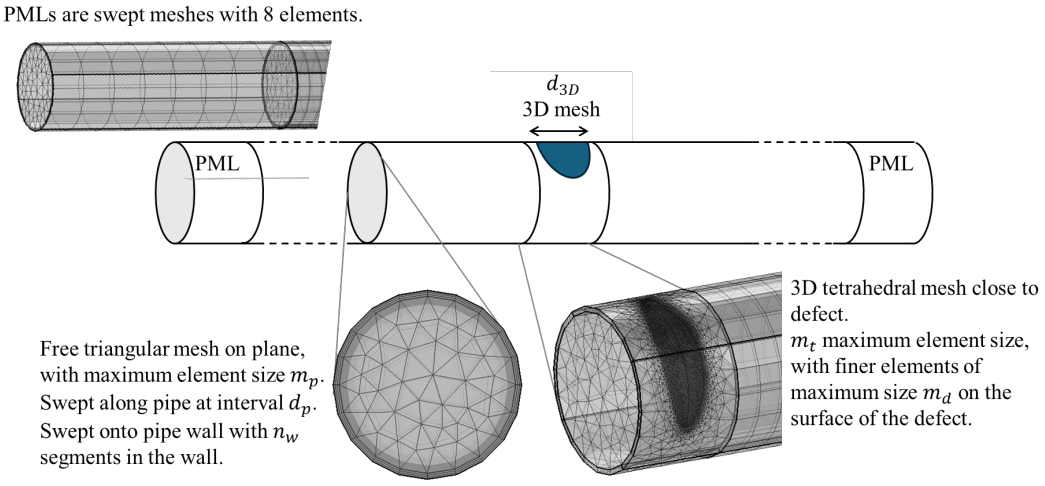

Figure E.1: Schematic of the mesh for the model described in Section 5.2.

Table E.1: A representative selection of the mesh sizes tested for basic model, where R is the radius of the pipe, h is the pipe wall thickness and r is the radius of the hole in the pipe wall.

m_p, m_t	d_p (m)	n_w	$n_{w,3D}$	m_d	m_h	d_{3D} (m)	description
$R/2$	0.3	1	3	h	r	1	very coarse
$R/3$	0.25	1	5	$h/3$	$r/3$	1	coarse
$R/5$	0.25	2	7	$h/4$	$r/5$	1	medium
$R/8$	0.2	3	10	$h/4$	$r/8$	1	ultra-fine
$R/3$	0.25	3	5	$h/3$	n/a	2	fine, long 3D
$R/8$	0.1	5	5	$h/4$	$r/8$	0.25	med., short 3D

- d_{3D}, the length of the 3D mesh.

In order to simplify the problem, we set $m_p = m_t$ in all cases.

The size of the mesh used in each test for each section of the model is summarised in Table E.1, with the results compared in Figure E.2. The error here is calculated as $\epsilon = (x_{model} - x_{fine})/(x_{fine} + \zeta)$, where ζ is a regularisation constant. It can be seen that the error in the results is similar for both the medium and fine meshes, however the fine mesh has lower errors close to the defect for p and v_x, so was chosen for the model described in the main text. The results along the length of the pipe for each parameter are shown in Figure E.3 for a subset of the mesh sizes shown above. The relative error as a function of the mesh size is also shown. Inspection of Figure E.3 shows that the relatively high error in v_y is dominated by a very dissimilar result immediately next to the defect, removing this increases the similarity in the results of the fine and ultra-fine meshes, the remaining high relative error can be explained by the very low values of v_y being measured. There is a similar very localised increase in the error of v_z close to the defect, largely due to the sudden decrease in v_z distorting the error calculation. In general the low level of difference seen between the medium and ultra-fine meshes led to the selection of the medium mesh for the results presented in this paper, as such the final mesh parameters used are:

- $m_p = m_t = R/5$
- $d_p = 0.25$ m
- $n_w = 2$
- $n_{w,3D} = 7$
- $m_d = h/4$
- $d_{3D} = 1$

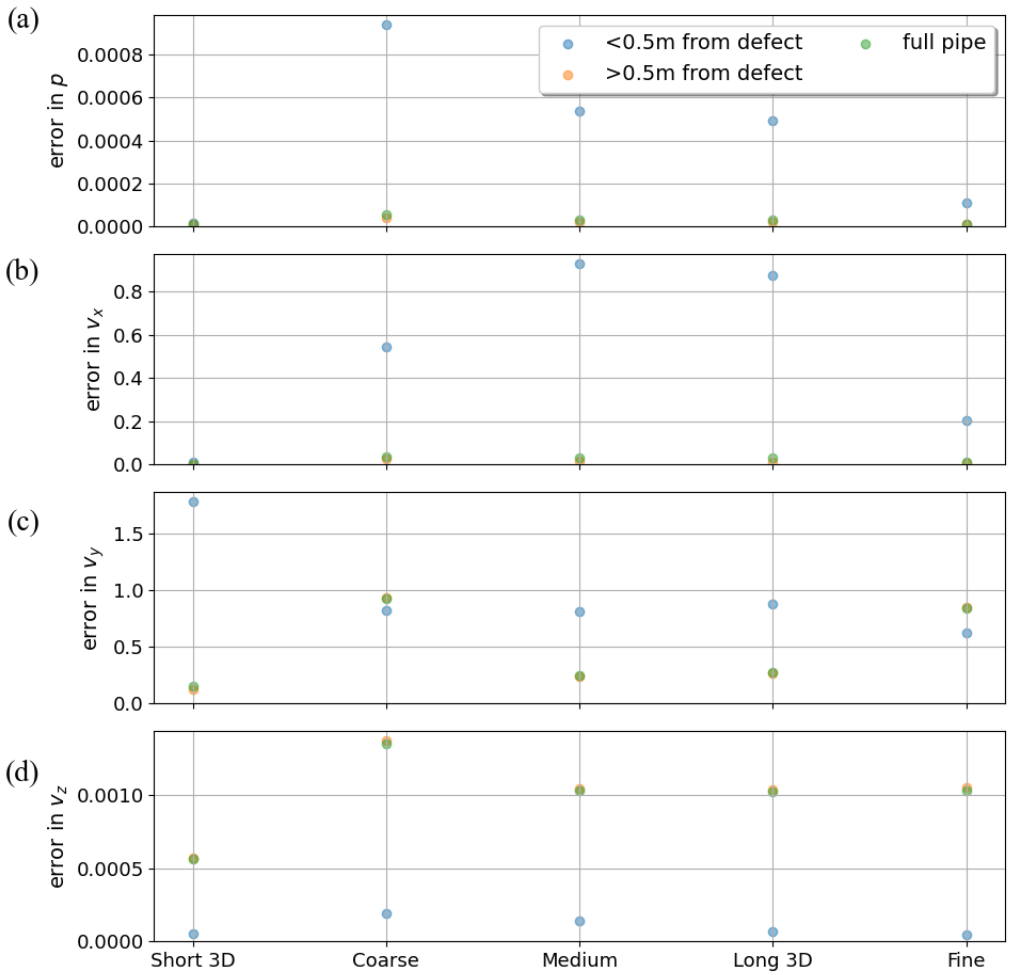

Figure E.2: Effect of different sized meshes on the error in the value of each parameter along the sensor line. The error has been calculated with respect to the 'ultra-fine' model. The mesh sizes for each section of the model are summarised in Table E.1.

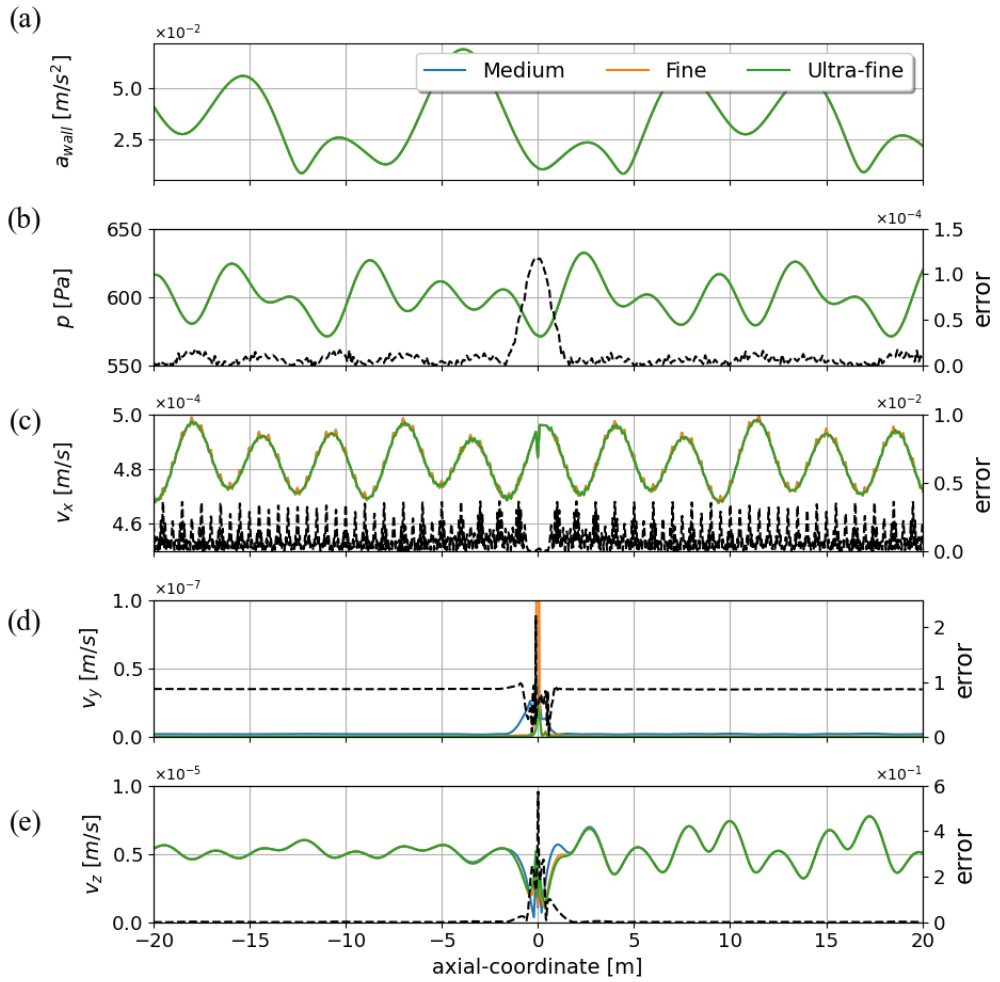

Figure E.3: Effect of different sized meshes on the model results along the sensor line for 3 different meshes. The error is between the fine and ultra-fine meshes. The mesh sizes for each section of the model are summarised in Table E.1.

Appendix F

Sensitivity of acoustic velocity to frequency

In Section 5.4.2, the effect of varying source frequency on the pressure, axial velocity and radial velocity response to a defect was shown.

For the sake of brevity the figures for each frequency are provided here rather than in the main text.

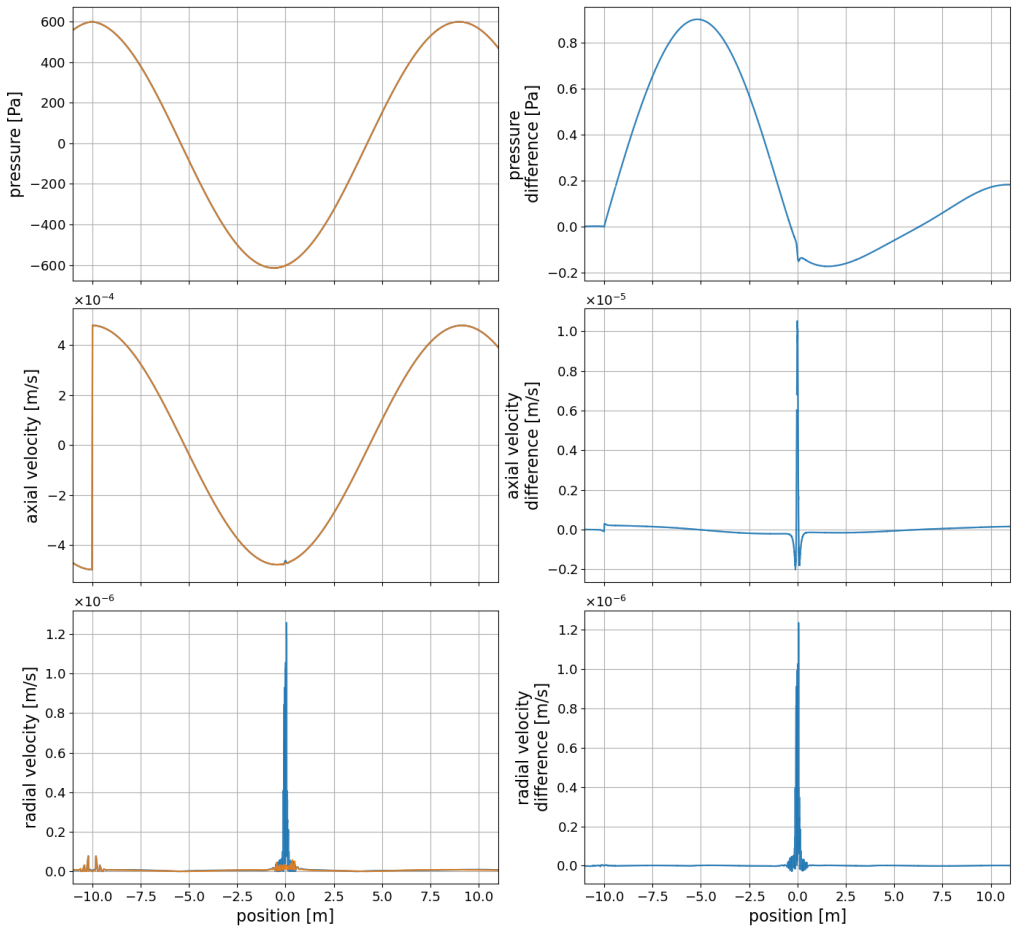

Figure F.1: The results from the numerical simulation for sound propagation along an 'infinite' pipe with (blue) and without (orange) a defect. The amplitude of the pressure, axial velocity and radial velocity are shown in the left hand figures, while the difference between the amplitudes of the with and without defect cases is shown in the right hand figures. The results are for a receiver line that runs 0.06 m from the edge of the pipe closest to the defect. The defect is at 0 m and the planar sound source is at -10 m, oscillating at 65 Hz.

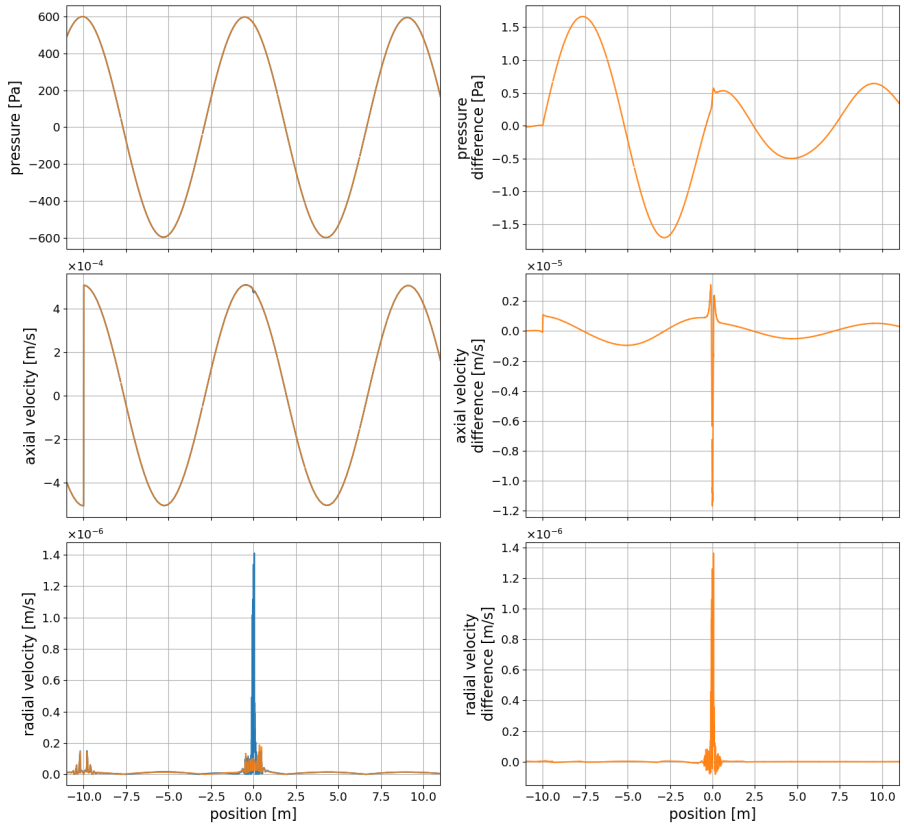

Figure F.2: The results from the numerical simulation for sound propagation along an 'infinite' pipe with (blue) and without (orange) a defect. The amplitude of the pressure, axial velocity and radial velocity are shown in the left hand figures, while the difference between the amplitudes of the with and without defect cases is shown in the right hand figures. The results are for a receiver line that runs 0.06 m from the edge of the pipe closest to the defect. The defect is at 0 m and the planar sound source is at -10 m, oscillating at 130 Hz

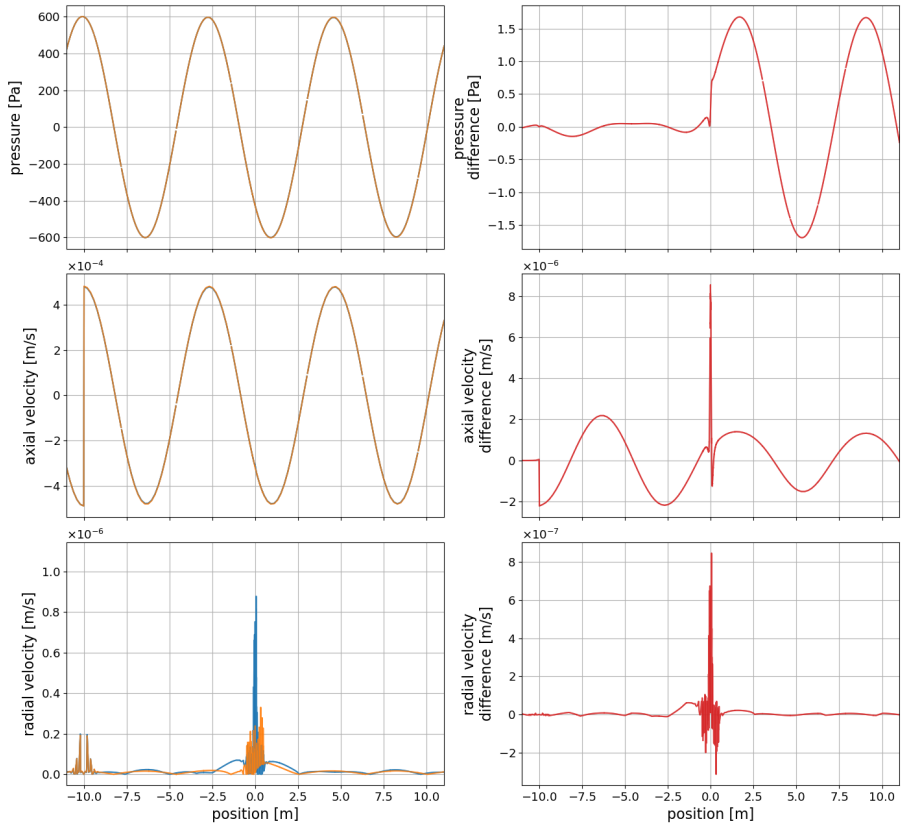

Figure F.3: The results from the numerical simulation for sound propagation along an 'infinite' pipe with (blue) and without (orange) a defect. The amplitude of the pressure, axial velocity and radial velocity are shown in the left hand figures, while the difference between the amplitudes of the with and without defect cases is shown in the right hand figures. The results are for a receiver line that runs 0.06 m from the edge of the pipe closest to the defect. The defect is at 0 m and the planar sound source is at -10 m, oscillating at 170 Hz

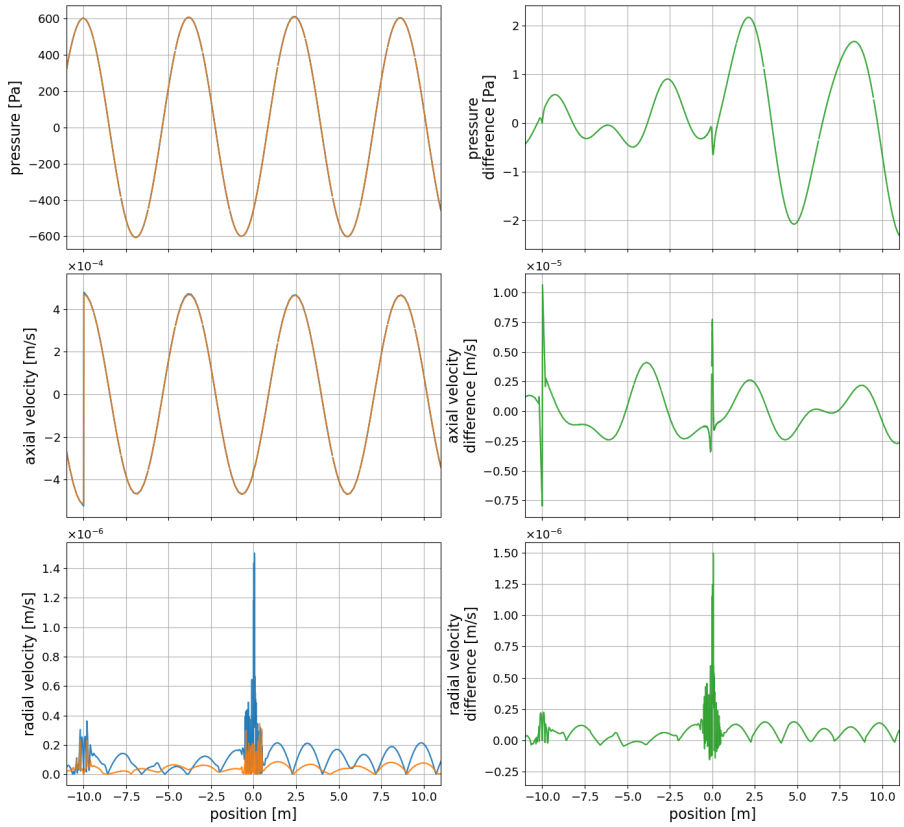

Figure F.4: The results from the numerical simulation for sound propagation along an 'infinite' pipe with (blue) and without (orange) a defect. The amplitude of the pressure, axial velocity and radial velocity are shown in the left hand figures, while the difference between the amplitudes of the with and without defect cases is shown in the right hand figures. The results are for a receiver line that runs 0.06 m from the edge of the pipe closest to the defect. The defect is at 0 m and the planar sound source is at -10 m, oscillating at 200 Hz

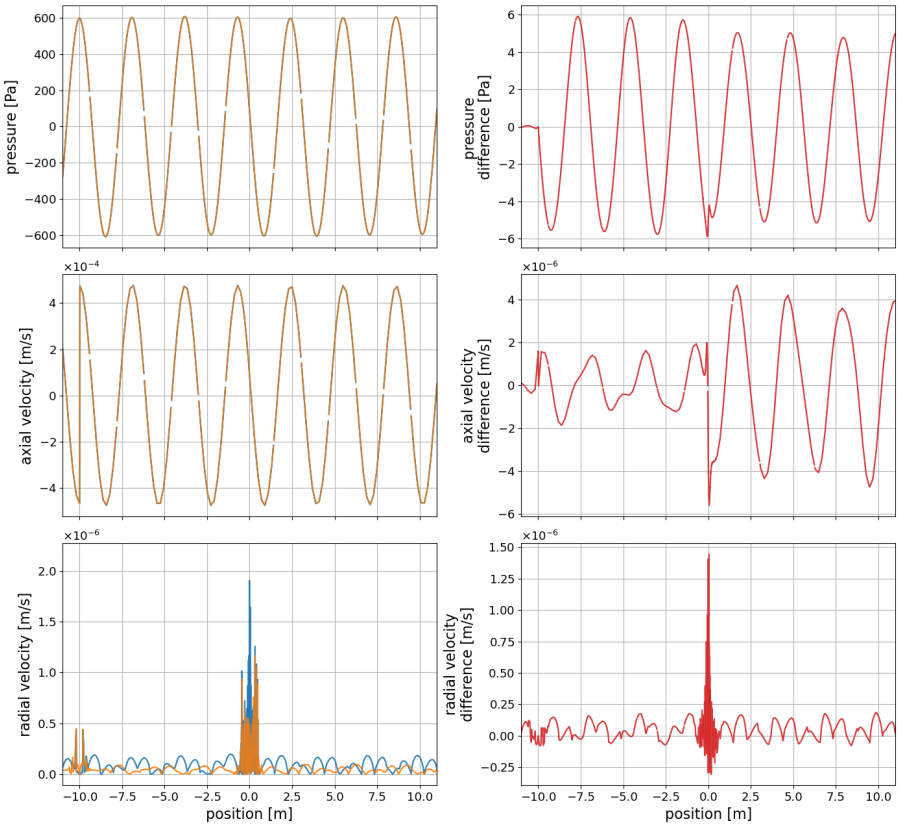

Figure F.5: The results from the numerical simulation for sound propagation along an 'infinite' pipe with (blue) and without (orange) a defect. The amplitude of the pressure, axial velocity and radial velocity are shown in the left hand figures, while the difference between the amplitudes of the with and without defect cases is shown in the right hand figures. The results are for a receiver line that runs 0.06 m from the edge of the pipe closest to the defect. The defect is at 0 m and the planar sound source is at -10 m, oscillating at 400 Hz

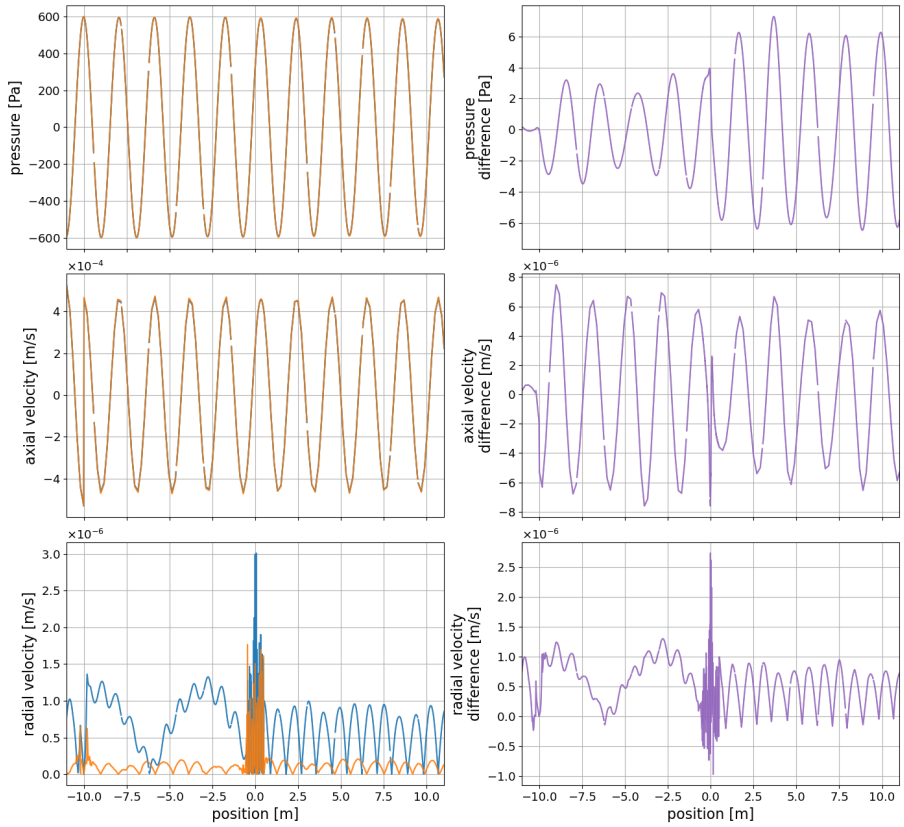

Figure F.6: The results from the numerical simulation for sound propagation along an 'infinite' pipe with (blue) and without (orange) a defect. The amplitude of the pressure, axial velocity and radial velocity are shown in the left hand figures, while the difference between the amplitudes of the with and without defect cases is shown in the right hand figures. The results are for a receiver line that runs 0.06 m from the edge of the pipe closest to the defect. The defect is at 0 m and the planar sound source is at -10 m, oscillating at 600 Hz

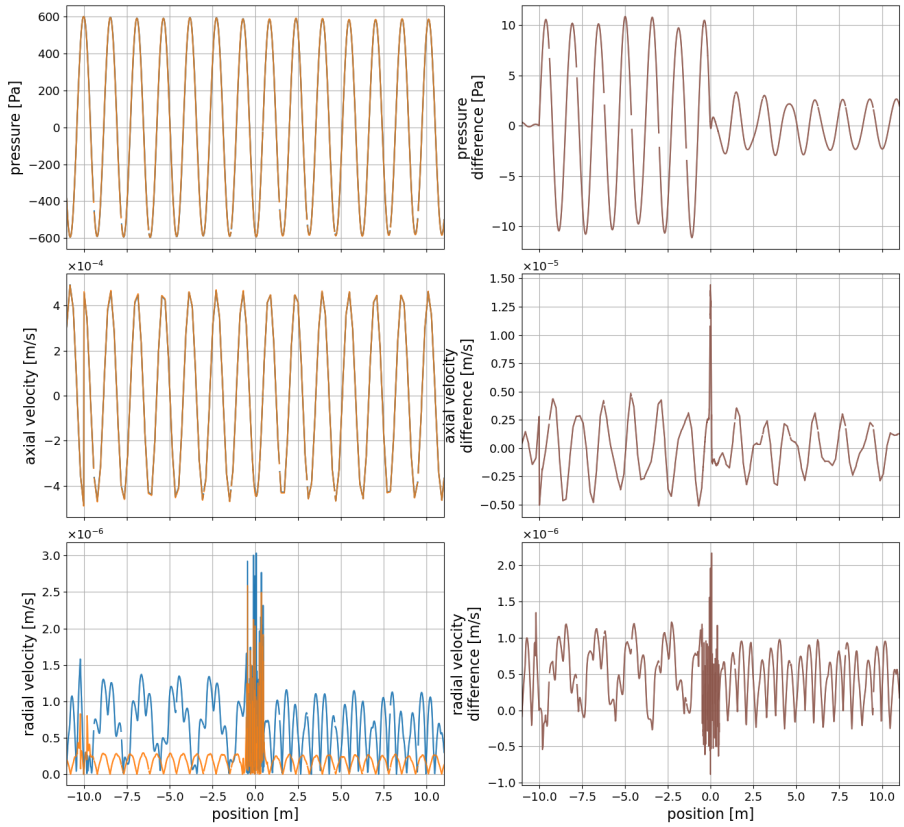

Figure F.7: The results from the numerical simulation for sound propagation along an 'infinite' pipe with (blue) and without (orange) a defect. The amplitude of the pressure, axial velocity and radial velocity are shown in the left hand figures, while the difference between the amplitudes of the with and without defect cases is shown in the right hand figures. The results are for a receiver line that runs 0.06 m from the edge of the pipe closest to the defect. The defect is at 0 m and the planar sound source is at -10 m, oscillating at 800 Hz

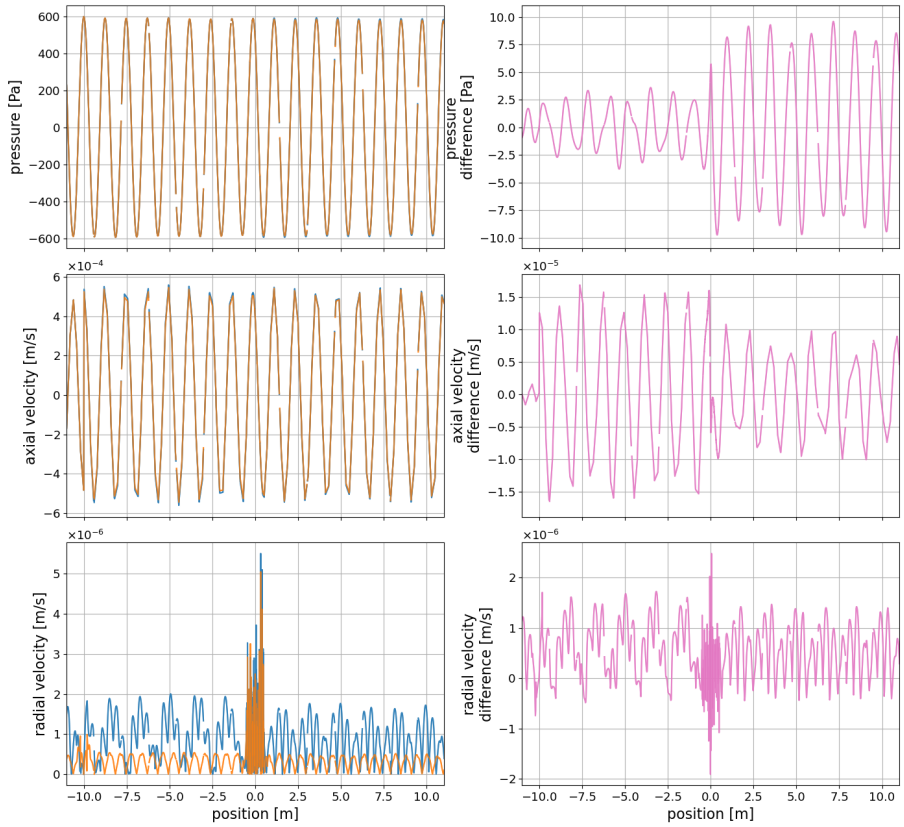

Figure F.8: The results from the numerical simulation for sound propagation along an 'infinite' pipe with (blue) and without (orange) a defect. The amplitude of the pressure, axial velocity and radial velocity are shown in the left hand figures, while the difference between the amplitudes of the with and without defect cases is shown in the right hand figures. The results are for a receiver line that runs 0.06 m from the edge of the pipe closest to the defect. The defect is at 0 m and the planar sound source is at -10 m, oscillating at 1,000 Hz

Bibliography

[1] National Infrastructure Commission. “Preparing for a drier future: England’s water infrastructure needs”. In: *National Infrastructure Commission, London, United Kingdom* (2018).

[2] OfWat. *Leakage in the water industry*. 2022. URL: https://www.ofwat.gov.uk/leakage-in-the-water-industry/. Accessed 21/03/2025.

[3] EurEau. *Europe’s Water in Figures: An overview of the European drinking water and waste water sectors*. 2021. URL: https://www.eureau.org/resources/publications/eureau-publications/5824-europe-s-water-in-figures-2021/file. Accessed 21/03/2025.

[4] Ofwat. *Service and delivery report*. 2019. URL: https://www.ofwat.gov.uk/regulated-companies/company-obligations/outcomes/service-and-delivery-2019-20/. Accessed 24/11/2025.

[5] S. Hamilton and B. Charalambous. *Leak Detection: Technology and Implementation*. IWA Publishing. 2013.

[6] pipebots. *pipebots*. URL: http://pipebots.ac.uk. Accessed: 11/04/2025.

[7] OfWat. *No dig leak repair - from concept to reality*. URL: https://waterinnovation.challenges.org/winners/no-dig-leak-repair/. Accessed: 14/10/2025.

[8] Z. Liu and Y. Kleiner. “State of the art review of inspection technologies for condition assessment of water pipes”. In: *Measurement: journal of the International Measurement Confederation* 46.1 (2013), pp. 1–15.

[9] Y. Yu, A. Safari, X. Niu, B. Drinkwater, and K. V. Horoshenkov. “Acoustic and ultrasonic techniques for defect detection and condition monitoring in water and sewerage pipes: A review”. en. In: *Applied acoustics* 183.108282 (Dec. 2021), p. 108282.

[10] J. Butterfield. “Deriving further information from the leak signal in water distribution pipes”. PhD thesis. University of Sheffield, 2018.

[11] D. K. O’Day. “Organizing and analyzing leak and break data for making main replacement decisions”. In: *Journal-American Water Works Association* 74.11 (1982), pp. 588–594.

[12] J. Mora-Rodríguez, X. Delgado-Galván, H. M. Ramos, and P. A. López-Jiménez. “An overview of leaks and intrusion for different pipe materials and failures”. In: *Urban water journal* 11.1 (2014), pp. 1–10.

[13] A. C. Twort, D. D. Ratnayaka, and M. J. Brandt. *Water Supply, 5th Edition*. Oxford, England: Butterworth-Heinemann, 2000.

[14] Water Services Association of Australia. *Failure Modes in Pressurised Pipeline Systems*. 2003. URL: https://sswm.info/sites/default/files/reference_attachments/WSAA%202003%20Common%20Failure%20Modes%20in%20Pressurised%20Pipeline%20Systems.pdf. Accessed 24/11/2025.

[15] J. W. Male, A. Slutsky, and T. Walski. "New York Water Supply Infrastructure Study; Volume V; Analysis of Replacement Policy". In: *US Army Engineer Waterways Experiment Station (WES)* (1990).

[16] R. Newport. "Factors influencing the occurrence of bursts in iron water mains". In: *Aqua* 3 (1981).

[17] K. F. Makris, J. Langeveld, and F. H. L. R. Clemens. "A review on the durability of PVC sewer pipes: research vs. practice". In: *Structure and Infrastructure Engineering: Maintenance, Management, Life-Cycle Design and Performance* 16.6 (2020), pp. 880–897.

[18] E. Drenth. "Towards condition based asset management of uPVC pipes". PhD thesis. University of Twente, Dec. 2015.

[19] H. Visser, T. C. Bor, M. Wolters, L. Warnet, and L. Govaert. "Influence of physical aging on impact embrittlement of uPVC pipes". In: *Plastics, rubber and composites* 40.5 (2011), pp. 201–212.

[20] A. Volynskii, A. Efimov, and N. Bakeev. "Structural aspects of physical aging of polymer glasses". In: *Polymer Science Series C* 49.4 (2007), pp. 301–320.

[21] K. F. Makris, J. G. Langeveld, and F. H. Clemens. "Extensive testing on PVC sewer pipes towards identifying the factors that affect their operational lifetime". In: *Structure and Infrastructure Engineering* 18.12 (2022), pp. 1601–1613.

[22] R. Hermkens, M. Wolters, J. Weller, and R. Visser. "PVC pipes in gas distribution: still going strong!" In: *14th International Plastic Pipes Conference 2008*. 2008.

[23] OfWat. "Funding approaches for leakage reduction". In: *OfWat* (2019).

[24] A. S. Braga, C. V. S. Fernandes, and S. Braga. "Leakage Modeling Through Empirical Equations: An Experimental Approach:(021)". In: *WDSA/CCWI Joint Conference Proceedings*. Vol. 1. 2018.

[25] I. Idelchik. *Handbook of Hydraulic Resistance, 3rd Edition*. JAICO Publishing House, 2003.

[26] M. Ferrante, C. Massari, B. Brunone, and S. Meniconi. "Leakage and pipe materials". In: *Water Distribution Systems Analysis 2010*. 2010, pp. 1140–1145.

[27] A. Cassa, J. Van Zyl, and R. Laubscher. "A numerical investigation into the effect of pressure on holes and cracks in water supply pipes". In: *Urban Water Journal* 7.2 (2010), pp. 109–120.

[28] J. E. Van Zyl and C. R. I. Clayton. "The effect of pressure on leakage in water distribution systems". In: *Proceedings of the Institution of Civil Engineers-Water Management*. Vol. 160. 2. Thomas Telford Ltd. 2007, pp. 109–114.

[29] T. Walski, B. Whitman, M. Baron, and F. Gerloff. "Pressure vs. flow relationship for pipe leaks". In: *World Environmental and Water Resources Congress 2009: Great Rivers*. 2009, pp. 1–10.

[30] B. Greyvenstein and J. E. van Zyl. "An experimental investigation into the pressure - leakage relationship of some failed water pipes". In: *Journal of Water Supply Research and Technology–AQUA* 56.2 (Mar. 2007), p. 117.

[31] NumPy. *Discrete Fourier Transform*. URL: https://numpy.org/doc/2.2/reference/routines.fft.html. Accessed: 06/06/2025.

[32] M. Pal. "Leak detection and Location in Polyethylene Pipes". PhD thesis. Loughborough University, 2008.

[33] J. D. Butterfield, G. Meyers, V. Meruane, R. P. Collins, and S. B. M. Beck. "Experimental investigation into techniques to predict leak shapes in water distribution systems using vibration measurements". en. In: *Journal of hydroinformatics* 20.4 (July 2018), pp. 815–828.

[34] S. Fox, J. Boxall, and R. Collins. "Derivation and Validation of a Leakage Model for Longitudinal Slits in Polyethylene Pipes". In: *Journal of Hydraulic Engineering* 144.7 (2018).

[35] M. Ferrante. "Experimental Investigation of the Effects of Pipe Material on the Leak Head-Discharge Relationship". In: *Journal of Hydraulic Engineering* 138.8 (2012), pp. 736–743.

[36] J. D. Butterfield, R. P. Collins, and S. B. M. Beck. "Influence of pipe material on the transmission of vibroacoustic leak signals in real complex water distribution systems: Case study". en. In: *Journal of pipeline systems engineering and practice* 9.3 (Aug. 2018), p. 05018003.

[37] A. S. Papastefanou, P. F. Joseph, and M. J. Brennan. "Experimental investigation into the characteristics of in-pipe leak noise in plastic water filled pipes". In: *Acta acustica united with acustica: the journal of the European Acoustics Association (EEIG)* 98 (2012), pp. 847–856.

[38] J. M. Muggleton and J. Yan. "Wavenumber prediction and measurement of axisymmetric waves in buried fluid-filled pipes: Inclusion of shear coupling at a lubricated pipe/soil interface". In: *Journal of sound and vibration* 332.5 (2013), pp. 1216–1230.

[39] J. E. van Zyl, M. O. A. Alsaydalani, C. R. I. Clayton, T. Bird, and A. Dennis. "Soil fluidisation outside leaks in water distribution pipes – preliminary observations". en. In: *Institution of Civil Engineers. Proceedings. Water Management* 166.10 (Nov. 2013), pp. 546–555.

[40] J. M. Muggleton, M. J. Brennan, and P. W. Linford. "Axisymmetric wave propagation in fluid-filled pipes: wavenumber measurements in in vacuo and buried pipes". en. In: *Journal of sound and vibration* 270.1-2 (Feb. 2004), pp. 171–190.

[41] F. C. L. Almeida, M. J. Brennan, P. F. Joseph, S. Dray, S. Whitfield, and A. T. Paschoalini. "Towards an in-situ measurement of wave velocity in buried plastic water distribution pipes for the purposes of leak location". In: *Journal of sound and vibration* 359 (2015), pp. 40–55.

[42] N. Humphrey, M. Loveday, and S. Tooms. "Leak detection on plastic pipes". In: *UKWIR (Ref: 12/WM. 08/47)* (2012), pp. 1–101.

[43] Y. Gao and Y. Liu. "Theoretical and experimental investigation into structural and fluid motions at low frequencies in water distribution pipes". In: *Mechanical systems and signal processing* 90 (2017), pp. 126–140.

[44] F. Almeida, M. Brennan, P. Joseph, S. Whitfield, S. Dray, and A. Paschoalini. "On the acoustic filtering of the pipe and sensor in a buried plastic water pipe and its effect on leak detection: an experimental investigation". In: *Sensors* 14.3 (2014), pp. 5595–5610.

[45] W. A. Wassef, M. N. Bassim, M. Houssny-Emam, and K. Tangri. "Acoustic emission spectra due to leaks from circular holes and rectangular slits". In: *The journal of the Acoustical Society of America* 77.3 (1985), pp. 916–923.

[46] F. C. L. d. Almeida, M. J. Brennan, P. F. Joseph, S. Dray, S. Whitfield, and A. T. Paschoalini. "Measurement of wave attenuation in buried plastic water distribution pipes". In: *Strojniski Vestnik* 60.5 (May 2015), pp. 298–306.

[47] J. M. Muggleton and M. J. Brennan. "The design and instrumentation of an experimental rig to investigate acoustic methods for the detection and location of underground piping systems". In: *Applied Acoustics* 69.11 (2008), pp. 1101–1107.

[48] P. Tayefi, S. B. M. Beck, and R. A. Tomlinson. "The fatigue performance of electrofusion tapping tees subject to contamination". en. In: *International journal of pressure vessels and piping* 171 (Mar. 2019), pp. 271–277.

[49] O. Hunaidi, W. Chu, A. Wang, and W. Guan. "Detecting leaks in plastic pipes". en. In: *Journal - American Water Works Association* 92.2 (Feb. 2000), pp. 82–94.

[50] J. E. van Zyl, A. O. Lambert, and R. Collins. "Realistic Modeling of Leakage and Intrusion Flows through Leak Openings in Pipes". In: *Journal of Hydraulic Engineering* 143.9 (2017), pp. 04017030–04017030.

[51] R. Ben-Mansour, M. A. Habib, A. Khalifa, K. Youcef-Toumi, and D. Chatzigeorgiou. "Computational fluid dynamic simulation of small leaks in water pipelines for direct leak pressure transduction". In: *Computers & fluids* 57 (2012), pp. 110–123.

[52] A. Papastefanou. "An experimental investigation of leak noise from water filled plastic pipes". PhD thesis. University of Southampton, Apr. 2011.

[53] W. Chalgham. "Simulation of sound wave propagation inside a spherical ball submerged in a pipeline". In: (2016).

[54] O. Hunaidi and W. T. Chu. "Acoustical characteristics of leak signals in plastic water distribution pipes". In: *Applied acoustics* 58.3 (1999), pp. 235–254.

[55] Y. Gao, M. J. Brennan, P. F. Joseph, J. M. Muggleton, and O. Hunaidi. "A model of the correlation function of leak noise in buried plastic pipes". In: *Journal of sound and vibration* 277 (Oct. 2004), pp. 133–148.

[56] O. Scussel, M. J. Brennan, F. C. L. Almeida, J. M. Muggleton, E. Rustighi, and P. F. Joseph. "Estimating the spectrum of leak noise in buried plastic water distribution pipes using acoustic or vibration measurements remote from the leak". In: *Mechanical systems and signal processing* 147 (2021), pp. 107059–107059.

[57] F. C. L. Almeida, M. J. Brennan, P. F. Joseph, Y. Gao, and A. T. Paschoalini. "The effects of resonances on time delay estimation for water leak detection in plastic pipes". In: *Journal of sound and vibration* 420 (2018), pp. 315–329.

[58] S. Dray, M. Loveday, and S. Tooms. "Leak detection on plastic pipes". In: *UK Water Industry Research* (2012).

[59] M. J. Brennan et al. "On the effects of soil properties on leak noise propagation in plastic water distribution pipes". In: *Journal of sound and vibration* 427 (Aug. 2018), pp. 120–133.

[60] O. Scussel, M. J. Brennan, J. M. Muggleton, F. C. L. Almeida, and A. T. Paschoalini. "Estimation of the bulk and shear moduli of soil surrounding a plastic water pipe using measurements of the predominantly fluid wave in the pipe". In: *Journal of applied geophysics* 164 (2019), pp. 237–246.

[61] Y. Gao, Y. Liu, and J. M. Muggleton. "Axisymmetric fluid-dominated wave in fluid-filled plastic pipes: Loading effects of surrounding elastic medium". In: *Applied acoustics* 116.C (Jan. 2017), pp. 43–49.

[62] M. K. Kalkowski, J. M. Muggleton, and E. Rustighi. "Axisymmetric semi-analytical finite elements for modelling waves in buried/submerged fluid-filled waveguides". In: *Computers & structures* 196 (2018), pp. 327–340.

[63] Y. Gao, F. Sui, J. M. Muggleton, and J. Yang. "Simplified dispersion relationships for fluid-dominated axisymmetric wave motion in buried fluid-filled pipes". In: *Journal of Sound and Vibration* 375 (2016), pp. 386–402.

[64] R. J. Pinnington and A. R. Briscoe. "Externally applied sensor for axisymmetric waves in a fluid filled pipe". In: *Journal of Sound and Vibration* 173.4 (1994), pp. 503–516.

[65] A. Martini, M. Troncossi, and A. Rivola. "Leak detection in water-filled small-diameter polyethylene pipes by means of acoustic emission measurements". In: *Applied Sciences* 7.2 (2017).

[66] A. Martini, M. Troncossi, and A. Rivola. "Vibroacoustic Measurements for Detecting Water Leaks in Buried Small-Diameter Plastic Pipes". In: *Journal of pipeline systems engineering and practice* 8.4 (2017).

[67] Xylem. *Pure Technologies Sahara Inline Tethered Inspection Platform*. URL: https://www.xylem.com/en-us/brands/pure-technologies/technologies/sahara-inline-tethered-inspection-platform/. Accessed: 10/03/2025.

[68] Xylem. *Pure Technologies SmartBall Inline Free-swimming Inspection Platform*. URL: https://www.xylem.com/en-uk/products--services/pipeline-assessment/smartball-inline-free-swimming-inspection-platform/. Accessed: 17/03/2025.

[69] Echologics/Mueller. *Leakfinder-ST: Advanced Acoustic Leak Detection System*. URL: https://www.echologics.com/products/leakfinderst. Accessed: 20/03/2025.

[70] R. Nestleroth, S. Flamberg, W. Condit, J. Matthews, L. Wang, and A. Chen. "Field Demonstration of Innovative Condition Assessment Technologies for Water Mains: Leak Detection and Location". In: *United States Environmental Protection Agency* (2012).

[71] A. E. Khalifa, R. Ben-Mansour, K. Youcef-Toumi, and C. Choi. "Characterization of in-pipe acoustic wave for water leak detection". In: *Volume 8: Mechanics of Solids, Structures and Fluids; Vibration, Acoustics and Wave Propagation*. ASMEDC, Jan. 2011.

[72] Y. A. Khulief, A. Khalifa, R. B. Mansour, and M. A. Habib. "Acoustic Detection of Leaks in Water Pipelines Using Measurements inside Pipe". In: *Journal of pipeline systems engineering and practice* 3.2 (2012), pp. 47–54.

[73] S. Kumar, A. E. Khalifa, A. Deshpande, and K. Youcef-toumi. "In-pipe Acoustic Characterization of Leak Signals in Plastic Water-filled Pipes". In: *AWWA Annual Conference and Exposition 2010* (2010).

[74] S. Fox, R. Collins, and J. Boxall. "Physical investigation into the significance of ground conditions on dynamic leakage behaviour". In: *Journal of Water Supply: Research and Technology - AQUA* 65.2 (2016), pp. 103–115.

[75] J. D. Butterfield, A. Krynkin, R. P. Collins, and S. B. M. Beck. "Experimental investigation into vibro-acoustic emission signal processing techniques to quantify leak flow rate in plastic water distribution pipes". en. In: *Applied acoustics* 119 (Apr. 2017), pp. 146–155.

[76] J. D. Butterfield, V. Meruane, R. P. Collins, G. Meyers, and S. B. M. Beck. “Prediction of leak flow rate in plastic water distribution pipes using vibro-acoustic measurements”. en. In: *Structural health monitoring* 17.4 (July 2018), pp. 959–970.

[77] M. Pal, N. Dixon, and J. Flint. “Detecting & locating leaks in water distribution polyethylene pipes”. In: *WCE 2010 - World Congress on Engineering 2010* 2 (2010), pp. 889–894.

[78] S. Moore. “A review of noise and vibration in fluid-filled Pipe systems”. In: *2nd Australasian Acoustical Societies Conference, ACOUSTICS 2016* 2.November (2016), pp. 701–710.

[79] Y. Liu et al. “A comprehensive review of acoustic methods for locating underground pipelines”. In: *Applied Sciences (Switzerland)* 10.3 (2020).

[80] C. R. Fuller. “The input mobility of an infinite circular cylindrical elastic shell filled with fluid”. In: *Journal of sound and vibration* 87.3 (1983), pp. 409–427.

[81] C. R. Fuller and F. J. Fahy. “Characteristics of wave propagation and energy distributions in cylindrical elastic shells filled with fluid”. In: *Journal of sound and vibration* 81.4 (1982), pp. 501–518.

[82] C. R. Fuller. “The effects of wall discontinuities on the propagation of flexural waves in cylindrical shells”. In: *Journal of sound and vibration* 75.2 (1981), pp. 207–228.

[83] J. M. Muggleton, M. J. Brennan, and R. J. Pinnington. “Wavenumber prediction of waves in buried pipes for water leak detection”. en. In: *Journal of sound and vibration* 249.5 (Jan. 2002), pp. 939–954.

[84] J. M. Muggleton and M. J. Brennan. “Axisymmetric wave propagation in buried, fluid-filled pipes: Effects of wall discontinuities”. In: *Journal of sound and vibration* 281 (2005), pp. 849–867.

[85] A. Demma, P. Cawley, M. Lowe, and B. Pavlakovic. “The effect of bends on the propagation of guided waves in pipes”. In: *Journal of pressure vessel technology* 127 (2005), pp. 328–335.

[86] T. Graf and J. Pan. “Determination of the complex acoustic scattering matrix of a right-angled duct”. en. In: *The journal of the Acoustical Society of America* 134.1 (July 2013), pp. 292–299.

[87] Y. Tong and J. Pan. “Reciprocity in the scattering coefficients of acoustic waveguide modes”. en. In: *The journal of the Acoustical Society of America* 134.3 (Sept. 2013), pp. 1731–1734.

[88] Z. Li, L. Jing, W. Wang, P. Lee, and R. Murch. “Guided acoustic wave interaction with flanged junctions in water-filled steel pipelines”. en. In: *The journal of the Acoustical Society of America* 144.5 (Nov. 2018), p. 2824.

[89] O. Scussel, A. Seçgin, M. J. Brennan, J. M. Muggleton, and F. C. L. Almeida. “A stochastic model for the speed of leak noise propagation in plastic water pipes”. In: *Journal of sound and vibration* 501 (2021).

[90] M. D. Kafle, S. Fong, and S. Narasimhan. “Active acoustic leak detection and localization in a plastic pipe using time delay estimation”. In: *Applied Acoustics* 187 (2022), p. 108482.

[91] R. Kirby and W. Duan. “Guided wave propagation in cylindrical ducts with elastic walls enclosing a fluid moving with a uniform velocity”. In: *Wave motion (North-Holland Publishing Company)* 85 (2019), pp. 1–9.

[92] Mistras. *Guided Wave Testing (GWT) Services*. URL: https://www.mistrasgroup.com/united-kingdom/how-we-help/field-inspections/advanced-ndt/automated-ultrasonic-testing/guided-wave-testing/. Accessed: 17/03/2025.

[93] M. J. Lowe, D. N. Alleyne, and P. Cawley. "Defect detection in pipes using guided waves". In: *Ultrasonics* 36.1-5 (1998), pp. 147–154.

[94] C. Aristégui, M. Lowe, and P. Cawley. "Guided waves in fluid-filled pipes surrounded by different fluids". In: *Ultrasonics* 39.5 (2001), pp. 367–375.

[95] R. Long, M. Lowe, and P. Cawley. "Attenuation characteristics of the fundamental modes that propagate in buried iron water pipes". In: *Ultrasonics* 41.7 (2003), pp. 509–519.

[96] Z. Liu and Y. Kleiner. "State of the art review of technologies for pipe structural health monitoring". In: *IEEE sensors journal* 12.6 (2012), pp. 1987–1992.

[97] R. Puust, Z. Kapelan, D. A. Savic, and T. Koppel. "A review of methods for leakage management in pipe networks". In: *Urban water journal* 7.1 (2010), pp. 25–45.

[98] X. Wan, P. K. Kuhanestani, R. Farmani, and E. Keedwell. "Literature Review of Data Analytics for Leak Detection in Water Distribution Networks: A Focus on Pressure and Flow Smart Sensors". In: *Journal of Water Resources Planning and Management* 148.10 (2022), p. 03122002.

[99] O. M. Aamo. "Leak detection, size estimation and localization in pipe flows". In: *IEEE Transactions on Automatic Control* 61.1 (2015), pp. 246–251.

[100] H. Anfinsen and O. M. Aamo. "Leak detection, size estimation and localization in branched pipe flows". In: *Automatica* 140 (2022), p. 110213.

[101] Gutermann. *Aquascope 2 - Universal Leak Locator and Acoustic Listening Device*. URL: https://en.gutermann-water.com/product/aquascope-3-leak-locator-and-acoustic-listening-device/. Accessed: 21/03/2025.

[102] R. A. Cody, B. A. Tolson, and J. Orchard. "Detecting leaks in water distribution pipes using a deep autoencoder and hydroacoustic spectrograms". en. In: *Journal of computing in civil engineering* 34.2 (Mar. 2020), p. 04020001.

[103] FIDO Tech. *FIDO AI*. URL: https://fido.tech. Accessed: 20/03/2025.

[104] Gutermann. *ZoneScan820*. URL: https://en.gutermann-water.com/product/zonescan-820-correlating-radio-loggers-and-zonescan-smart-software/. Accessed: 20/03/2025.

[105] D. Lyon. "The Discrete Fourier Transform, part 6: Cross-correlation." In: *J. Object Technol.* 9.2 (2010), pp. 17–22.

[106] M. Shehadeh, J. A. Steel, and R. L. Reuben. "Acoustic emission source location for steel pipe and pipeline applications: The role of arrival time estimation". In: *Proceedings of the Institution of Mechanical Engineers, Part E: Journal of Process Mechanical Engineering* 220 (2006), pp. 121–133.

[107] P. Virtanen et al. "SciPy 1.0: Fundamental Algorithms for Scientific Computing in Python". In: *Nature Methods* 17 (2020), pp. 261–272.

[108] D. Becker. *Leak detection in water distribution networks by correlation: sound velocity as a possible source of error*. Tech. rep. Accessed: 2025-09-04. Hermann Sewerin GmbH, 2015. URL: https://www.sewerin.com/fileadmin/redakteure/Fachbeitraege/Leckortung%20im%20Trinkwasserrohrnetz/Leak%20detection%20in%20water%20distribution%20networks%20by%20correlation_web.pdf.

[109] O. Hunaidi. "Acoustic leak detection survey strategies for water distribution pipes". In: *Construction Technology Update* 79 (2012), pp. 1–5.

[110] A. Martini, M. Troncossi, and A. Rivola. "Automatic Leak Detection in Buried Plastic Pipes of Water Supply Networks by Means of Vibration Measurements". In: *Shock and vibration* 2015 (2015), pp. 11–15.

[111] H. V. Fuchs and R. Riehle. "Ten years of experience with leak detection by acoustic signal analysis". In: *Applied acoustics* 33.1 (1991), pp. 1–19.

[112] Gutermann. *HISCAN - Permanent Trunk Main Monitoring*. URL: https://en.gutermann-water.com/product/hiscan-permanent-trunk-main-monitoring/. Accessed: 20/03/2025.

[113] Ovarro. *Phocus 3*. URL: https://ovarro.com/en/global/solutions/monitoring--control-devices/data-loggers--leak-noise-loggers/leak-noise-loggers--correlators/3/phocus/2/phocus-3/. Accessed: 20/03/2025.

[114] Ovarro. *Eureka*. URL: https://ovarro.com/en/global/solutions/monitoring--control-devices/data-loggers--leak-noise-loggers/leak-noise-loggers--correlators/3/eureka/2/. Accessed: 20/03/2025.

[115] Ovarro. *Enigma*. URL: https://ovarro.com/en/global/solutions/monitoring--control-devices/data-loggers--leak-noise-loggers/leak-noise-loggers--correlators/3/enigma/2/. Accessed: 20/03/2025.

[116] A. Anastasopoulos, D. Kourousis, and K. Bollas. "Acoustic emission leak detection of liquid filled buried pipeline". In: *Journal of Acoustic Emission* 27 (2009).

[117] A. H. Muntakim, A. S. Dhar, and R. Dey. "Interpretation of acoustic field data for leak detection in ductile iron and copper water-distribution pipes". en. In: *Journal of pipeline systems engineering and practice* 8.3 (Aug. 2017), p. 05017001.

[118] H. Iqbal, S. Tesfamariam, H. Haider, and R. Sadiq. "Inspection and maintenance of oil & gas pipelines: a review of policies". In: *Structure and Infrastructure Engineering* 13.6 (2017), pp. 794–815.

[119] J. Galleher and D. Kurtz. "Evaluation of an Un-tethered free-swimming acoustic leak detection technology". In: (July 2008), pp. 1–10.

[120] Xylem. *Pure Technologies PipeDiver Condition Assessment Platform*. URL: https://www.xylem.com/en-uk/products--services/pipeline-assessment/pipediver-condition-assessment-platform/. Accessed: 21/03/2025.

[121] D. M. Chatzigeorgiou, A. E. Khalifa, K. Youcef-Toumi, and R. Ben-Mansour. "An in-pipe leak detection sensor: Sensing capabilities and evaluation". In: *Volume 3: 2011 ASME/IEEE International Conference on Mechatronic and Embedded Systems and Applications, Parts A and B*. ASMEDC, Jan. 2011.

[122] D. Wu, D. Chatzigeorgiou, K. Youcef-Toumi, and R. Ben-Mansour. "Node Localization in Robotic Sensor Networks for Pipeline Inspection". In: *IEEE Transactions on Industrial Informatics* 12.2 (2016), pp. 809–819.

[123] D. Chatzigeorgiou, K. Youcef-Toumi, and R. Ben-Mansour. "Design of a novel in-pipe reliable leak detector". In: *IEEE/ASME Transactions on Mechatronics* 20.2 (2015), pp. 824–833.

[124] D. M. Chatzigeorgiou, R. Ben-Mansour, A. E. Khalifa, and K. Youcef-Toumi. "Design and evaluation of an in-pipe leak detection sensing technique based on force transduction". In: *Volume 4: Dynamics, Control and Uncertainty, Parts A and B*. American Society of Mechanical Engineers, Nov. 2012.

[125] Y. Wu, E. Mittmann, C. Winston, and K. Youcef-Toumi. "A practical minimalism approach to in-pipe robot localization". In: *Proceedings of the ... American Control Conference. American Control Conference* (2019), pp. 3180–3187.

[126] D. L. Chandler. *Finding leaks while they're easy to fix*. URL: https://news.mit.edu/2017/robot-finds-leaks-water-pipes-0718. Accessed: 21/03/2025.

[127] Y. Wu, K. Kim, M. F. Henry, and K. Youcef-Toumi. "Design of a leak sensor for operating water pipe systems". In: *IEEE International Conference on Intelligent Robots and Systems* (2017).

[128] D. Chatzigeorgiou, S. Mekid, R. Ben-Mansour, A. Khalifa, and K. Youcef-Toumi. *Leak detection apparatus*. US Patent 9,285,290, filed on March 15, 2016.

[129] W. You, K. Youcef-Toumi, K. S. Kim, M. F. Henry, and R. B. Mansour. *In-pipe leak detection systems, devices, and methods*. Filed on November 24, 2020. Nov. 2020.

[130] Y. Wu, A. Noel, D. D. Kim, K. Youcef-Toumi, and R. Ben-Mansour. "Design of a maneuverable swimming robot for in-pipe missions". In: IEEE, 2015, pp. 4864–4871.

[131] Y. Wu, D. Chatzigeorgiou, K. Youcef-Toumi, and M. Zribi. "Modeling and parameter estimation for in-pipe swimming robots". In: (2015), pp. 2007–2013.

[132] E. H. A. Duisterwinkel, E. Talnishnikh, D. Krijnders, and H. J. Wörtche. "Sensor Motes for the Exploration and Monitoring of Operational Pipelines". In: *IEEE transactions on instrumentation and measurement* 67.3 (2018), pp. 655–666.

[133] E. H. Duisterwinkel, G. Dubbelman, E. Talnishnikh, J. J. Bergmans, H. J. Wörtche, and J.-P. M. Linnartz. "Go-with-the-flow swarm sensing in inaccessible viscous media". In: *IEEE sensors journal* 20.8 (2019), pp. 4442–4452.

[134] Xylem. *Leak and air pocket detection case study: Aquaedotto Campano, Italy*. 2021. URL: https://www.xylem.com/siteassets/support/case-studies/case-studies-pdf/case-study-ischia-5.4.21.pdf. Accessed: 10/03/2025.

[135] D. Kumar, D. Tu, N. Zhu, R. A. Shah, D. Hou, and H. Zhang. "The free-swimming device leakage detection in plastic water-filled pipes through tuning the wavelet transform to the underwater acoustic signals". In: *Water* 9 (2017).

[136] S. Kazeminasab, M. Aghashahi, and M. K. Banks. "Development of an inline robot for water quality monitoring". In: *5th International Conference on Robotics and Automation Engineering* (2020).

[137] E. A. Shrimpton, D. Hunt, and C. D. Rogers. "Robots in drinking water: A pipe dream?" In: *Cambridge Prisms: Water* 2 (2024), e10.

[138] Ovarro. *Eureka5 User Manual*. 2022. URL: https://ovarro.com/content-media/assigned/103018/Eureka5%20User%20Manual.pdf. Accessed 24/22/2025.

[139] Y. Gao, M. J. Brennan, and P. J. Joseph. “Detecting leaks in buried plastic pipes using correlation techniques: Part 2. On the selection of acoustic/vibration sensors”. In: January (2004), pp. 3659–3662.

[140] O. Scussel, M. J. Brennan, J. M. Muggleton, F. C. L. de Almeida, and A. T. Paschoalini. “On the dynamic loading effects of soil on plastic water distribution pipes and its significance for leak detection using acoustics”. In: *Volume 11: Acoustics, Vibration, and Phononics*. American Society of Mechanical Engineers, Nov. 2018.

[141] J. Yu and E. Kojima. “Methods for measuring the speed of sound in the fluid in fluid transmission pipes”. In: *SAE Technical Paper Series*. 2000-01-2618. 400 Commonwealth Drive, Warrendale, PA, United States: SAE International, Sept. 2000.

[142] O. Scussel et al. “On the Significance of Parameter Uncertainties for Prediction of Leak Noise Wave Speed in Buried Pipes”. In: *Journal of Physics: Conference Series*. Vol. 2909. 1. IOP Publishing. 2024, p. 012009.

[143] J. M. Muggleton, M. J. Brennan, R. J. Pinnington, and Y. Gao. “A novel sensor for measuring the acoustic pressure in buried plastic water pipes”. en. In: *Journal of sound and vibration* 295.3-5 (Aug. 2006), pp. 1085–1098.

[144] F. K. de Lima et al. “Estimating the Velocity of Leakage Noise Propagation for Leak Detection in an Underground Water Pipes”. In: *Proceedings of the VI Symposium of Intelligent Materials and Control*. 2018.

[145] N. Uchendu, J. M. Muggleton, and P. R. White. “Assessing the quality of the time delay estimate in acoustic leak localisation”. In: *Journal of Sound and Vibration* 597 (2025), p. 118811.

[146] O. Hunaidi, A. Wang, M. Bracken, T. Gambino, and C. Fricke. “Acoustic methods for locating leaks in municipal water pipe networks”. In: *International Water Demand Management Conference* (2004), pp. 1–14.

[147] Y. Gao, M. J. Brennan, and P. F. Joseph. “A comparison of time delay estimators for the detection of leak noise signals in plastic water distribution pipes”. In: *Journal of sound and vibration* 292 (2006), pp. 552–570.

[148] A. F. Colombo, P. Lee, and B. W. Karney. “A selective literature review of transient-based leak detection methods”. en. In: *Journal of hydroenvironment research* 2.4 (Apr. 2009), pp. 212–227.

[149] B. Brunone, F. Maietta, C. Capponi, A. Keramat, and S. Meniconi. “A review of physical experiments for leak detection in water pipes through transient tests for addressing future research”. In: *Journal of Hydraulic Research* 60.6 (2022), pp. 894–906.

[150] R. Long, P. Cawley, and M. Lowe. “Acoustic wave propagation in buried iron water pipes”. In: *Proceedings. Mathematical, physical, and engineering sciences* 459 (2003), pp. 2749–2770.

[151] Guided Ultrasonics Ltd. *Technology Overview*. URL: https://www.guided-ultrasonics.com/technology/. Accessed: 17/03/2025.

[152] M. J. Lowe and P. Cawley. “Long range guided wave inspection usage–current commercial capabilities and research directions”. In: *Department of Mechanical Engineering, Imperial College London: London, UK* (2006), pp. 1–40.

[153] E. Leinov, M. J. Lowe, and P. Cawley. “Ultrasonic isolation of buried pipes”. In: *Journal of Sound and Vibration* 363 (2016), pp. 225–239.

[154] P. S. Lowe, H. Lais, V. Paruchuri, and T.-H. Gan. “Application of ultrasonic guided waves for inspection of high density polyethylene pipe systems”. In: *Sensors* 20.11 (2020), p. 3184.

[155] J. Bosch, A. Hugger, J. Franz, S. Falter, and Y. Oberdörfer. “Phase array technology for automated pipeline inspection”. In: *Business Briefing: Exploration & Production: The Oil & Gas Review* (2004), pp. 1–4.

[156] Baker Hughes. *UltraScan: Crack capabilities overview*. URL: https://www.bakerhughes.com/sites/bakerhughes/files/2021-07/19004_BH_PPS_ILI_US_POS_1912CRACKCAPAB-Landscape-A2.pdf. Accessed: 17/03/2025.

[157] Mistras. *Phased Array Ultrasonic Testing (PAUT)*. URL: https://www.mistrasgroup.com/united-kingdom/how-we-help/field-inspections/advanced-ndt/automated-ultrasonic-testing/phased-array/. Accessed: 17/03/2025.

[158] J. Zhang, X. Niu, A. J. Croxford, and B. W. Drinkwater. “Pipe inspection using guided acoustic wave sensors integrated with mobile robots”. In: *NDT & E International* 139 (2023), p. 102929.

[159] M. J. Bianco et al. “Machine learning in acoustics: Theory and applications”. In: *ArXiv* 3590.2019 (2019).

[160] J. D. Butterfield, R. P. Collins, and S. B. M. Beck. “Feature extraction of leaks signals in plastic water distribution pipes using the wavelet transform”. In: *Volume 13: Vibration, Acoustics and Wave Propagation*. American Society of Mechanical Engineers, Nov. 2015.

[161] B. Zhou, V. Lau, and X. Wang. “Machine-Learning-Based Leakage-Event Identification for Smart Water Supply Systems”. In: *IEEE internet of things journal* 7.3 (2020), pp. 2277–2292.

[162] M. J. Bianco, S. Gannot, and P. Gerstoft. “Semi-supervised source localization with deep generative modeling”. In: *arXiv [eess.AS]* (May 2020).

[163] J. Alves Coelho, A. Glória, and P. Sebastião. “Precise water leak detection using machine learning and real-time sensor data”. en. In: *IoT* 1.2 (Dec. 2020), pp. 474–493.

[164] X. Fan, X. Zhang, and X. (B. Yu. “Machine learning model and strategy for fast and accurate detection of leaks in water supply network”. en. In: *Journal of infrastructure preservation and resilience* 2.1 (Dec. 2021).

[165] T. Ravichandran, K. Gavahi, K. Ponnambalam, V. Burtea, and S. J. Mousavi. “Ensemble-based machine learning approach for improved leak detection in water mains”. en. In: *Journal of hydroinformatics* 23.2 (Mar. 2021), pp. 307–323.

[166] Q. Zhuang, J. M. Lorenzi, H.-J. Bungartz, and D. Hartmann. “Model order reduction based on Runge–Kutta neural networks”. en. In: *Data-Centric Engineering* 2.e13 (2021).

[167] T. Dawood, E. Elwakil, H. M. Novoa, and J. F. G. Delgado. “Artificial intelligence for the modeling of water pipes deterioration mechanisms”. In: *Automation in Construction* 120 (Dec. 2020).

[168] A. Paleyes, R.-G. Urma, and N. D. Lawrence. “Challenges in deploying machine learning: A survey of case studies”. In: *arXiv [cs.LG]* (Nov. 2020).

[169] T. Yu, X. Chen, W. Yan, Z. Xu, and M. Ye. “Leak detection in water distribution systems by classifying vibration signals”. In: *Mechanical Systems and Signal Processing* 185 (2023), p. 109810.

[170] Gutermann. *ZoneScanAI Correlating NB-IoT Leak Logger with Artificial Intelligence*. URL: https://en.gutermann-water.com/product/zonescan-ai-correlating-iot-leak-logger/. Accessed: 20/03/2025.

[171] W. Kaewwaewnoi, A. Prateepasen, and P. Kaewtrakulpong. "Investigation of the relationship between internal fluid leakage through a valve and the acoustic emission generated from the leakage". In: *Measurement: journal of the International Measurement Confederation* 43.2 (2010), pp. 274–282.

[172] P. Chen, P. S. K. Chua, and G. H. Lim. "A study of hydraulic seal integrity". In: *Mechanical systems and signal processing* 21.2 (2007), pp. 1115–1126.

[173] M. Ahadi and M. S. Bakhtiar. "Leak detection in water-filled plastic pipes through the application of tuned wavelet transforms to Acoustic Emission signals". en. In: *Applied acoustics* 71.7 (July 2010), pp. 634–639.

[174] N. Uchendu, J. M. Muggleton, and P. R. White. "Wavelet-based and data-adaptive methods for time delay estimation in acoustic leak detection". In: *Mechanical Systems and Signal Processing* 221 (2024), p. 111727.

[175] J. Latif, M. Z. Shakir, N. Edwards, M. Jaszczykowski, N. Ramzan, and V. Edwards. "Review on condition monitoring techniques for water pipelines". In: *Measurement* 193 (2022), p. 110895.

[176] RapidView. *Panoramo 4K Camera Systems*. URL: https://rapidview.com/products/panoramo-4k/. Accessed: 17/03/2025.

[177] S. Robotics. *One powerful multi-functional crawler with multiple job-specific modules*. URL: https://www.sewerrobotics.com/. Accessed: 11/04/2025.

[178] S. Moradi, T. Zayed, F. Nasiri, and F. Golkhoo. "Automated anomaly detection and localization in sewer inspection videos using proportional data modeling and deep learning–based text recognition". In: *Journal of Infrastructure Systems* 26.3 (2020), p. 04020018.

[179] T. Xu, L. Xu, X. Li, and J. Yao. "Detection of water leakage in underground tunnels using corrected intensity data and 3D point cloud of terrestrial laser scanning". In: *IEEE Access* 6 (2018), pp. 32471–32480.

[180] W. Duan, R. Kirby, J. Prisutova, and K. V. Horoshenkov. "On the use of power reflection ratio and phase change to determine the geometry of a blockage in a pipe". In: *Applied Acoustics* 87 (2015), pp. 190–197.

[181] O. I. Fund. *Pipebots for Rising Mains - Technology Development Phase 2*. URL: https://waterinnovation.challenges.org/winners/pipebots-for-rising-mains-2/. Accessed: 09/04/2025.

[182] T. Nguyen et al. "Autonomous control for miniaturized mobile robots in unknown pipe networks". In: *Frontiers in Robotics and AI* 9 (2022), p. 997415.

[183] L. Liu and J. M. Aitken. "Hfnet-slam: An accurate and real-time monocular slam system with deep features". In: *Sensors* 23.4 (2023), p. 2113.

[184] A. R. Towlson, A. J. Croxford, and B. W. Drinkwater. "Ultrasonic nondestructive characterization of blockages and defects in underground pipes". In: *IEEE Transactions on Ultrasonics, Ferroelectrics, and Frequency Control* 69.8 (2022), pp. 2540–2554.

[185] Y. Yu, K. V. Horoshenkov, G. Sailor, and S. Tait. "Sparse representation for artefact/defect localization with an acoustic array on a mobile pipe inspection robot". In: *Applied Acoustics* 231 (2025), p. 110545.

[186] H. Saheban and Z. Kordrostami. “Hydrophones, fundamental features, design considerations, and various structures: A review”. In: *Sensors and Actuators A: Physical* 329 (2021).

[187] J. Nickles et al. “A Vertical Array Of Directional Acoustic Sensors”. In: *OCEANS 92 Proceedings: Mastering the Oceans Through Technology*. Vol. 1. 1992, pp. 340–345.

[188] M. Hawkes and A. Nehorai. “Acoustic vector-sensor beamforming and Capon direction estimation”. In: *IEEE Transactions on Signal Processing* 46.9 (1998), pp. 2291–2304.

[189] X. Shen, M. Bao, Z. Chen, J. Zhao, and Y. Gao. “Fourth-order cumulant-based acoustic imaging via small-aperture acoustic vector-sensor array”. In: *IEEE Transactions on Instrumentation and Measurement* 73 (2024), pp. 1–12.

[190] J. Fischer, M. Orescanin, P. Leary, and K. B. Smith. “Active Bayesian Deep Learning With Vector Sensor for Passive Sonar Sensing of the Ocean”. In: *IEEE Journal of Oceanic Engineering* 48.3 (2023), pp. 837–852.

[191] M. Hawkes and A. Nehorai. “Effects of sensor placement on acoustic vector-sensor array performance”. In: *IEEE Journal of Oceanic Engineering* 24.1 (1999), pp. 33–40.

[192] B. A. Cray and A. H. Nuttall. “Directivity factors for linear arrays of velocity sensors”. In: *The journal of the acoustical society of America* 110.1 (2001), pp. 324–331.

[193] COMSOL AB, Stockholm, Sweden. *COMSOL Multiphysics® v. 6.3*. URL: www.comsol.com. Accessed 28/03/2025.

[194] P. Cui et al. “Characteristics of compression wave propagation and energy absorption effects in dry sandy soil”. In: *Scientific Reports* 14.1 (2024), p. 31625.

[195] P. Bigg. “Density of water in SI units over the range 0-40 C”. In: *British Journal of Applied Physics* 18.4 (1967), p. 521.

[196] NPL. *Technical guides - speed of sound in pure water*. URL: http://resource.npl.co.uk/acoustics/techguides/soundpurewater/. Accessed: 16/04/2025.

[197] T. Strek. *Finite element modelling of sound transmission loss in reflective pipe*. IntechOpen, 2010.

[198] Sonelastic. *Modulus of elasticity and Poisson’s coefficient of polymeric materials*. URL: https://www.sonelastic.com/en/fundamentals/tables-of-materials-properties/polymers.html. Accessed: 04/06/2025.

[199] Azo Materials. *An Introduction to Ductile Iron*. URL: https://www.azom.com/properties.aspx?ArticleID=797. Accessed: 04/06/2025.

[200] *On the role of vibro-acoustics in leak detection for plastic water distribution pipes*. Vol. 199. Elsevier Ltd, 2017.

[201] SciPy. *SciPy.signal Savitsky-Golay filter*. URL: https://docs.scipy.org/doc/scipy/reference/generated/scipy.signal.savgol_filter.html. Accessed: 10/09/2025.

[202] University of Sheffield. *ICAIR, Integrated Civil and Infrastructure Research*. URL: https://icair.ac.uk/. Accessed: 18/08/2025.

[203] S. Tariq, B. Bakhtawar, and T. Zayed. “Data-driven application of MEMS-based accelerometers for leak detection in water distribution networks”. In: *Science of The Total Environment* 809 (2022), p. 151110.

[204] X. Fan and X. Yu. “An innovative machine learning based framework for water distribution network leakage detection and localization”. In: *Structural Health Monitoring* 21.4 (2022), pp. 1626–1644.

[205] K. F. Makris, J. G. Langeveld, F. H. Clemens-Meyer, J. Watts, H. Begum, and K. V. Horoshenkov. "Sonic assessment of physical ageing of plastic pipes". In: *Journal of Sound and Vibration* 544 (2023), p. 117393.

[206] A. Rainer et al. "What does NDE need to achieve for cast iron pipe networks?" In: *Infrastructure Asset Management* 4.2 (2017), pp. 68–82.

[207] H. A. Visser. "Residual lifetime assessment of uPVC gas pipes". PhD thesis. University of Twente, 2020.

[208] L.-A. Fillot, P. Hajji, C. Gauthier, and K. Masenelli-Varlot. "Thermomechanical history effects on rigid PVC microstructure and impact properties". In: *Journal of applied polymer science* 104.3 (2007), pp. 2009–2017.

[209] R. Flores, J. Perez, P. Cassagnau, A. Michel, and J. Cavaillé. "α Mechanical relaxation in poly (vinyl chloride): effect of ageing and crosslinking". In: *Polymer* 35.13 (1994), pp. 2800–2807.

[210] B. E. Read, G. D. Dean, P. Tomlins, and J. Lesniarek-Hamid. "Physical ageing and creep in PVC". In: *Polymer* 33.13 (1992), pp. 2689–2698.

[211] A. Demčenko. "Development and analysis of noncollinear wave mixing techniques for material properties evaluation using immersion ultrasonics". PhD Thesis - Research UT, graduation UT. Netherlands: University of Twente, Oct. 2014.

[212] H. Hernandez Delgadillo. "Ultrasonic inspection of drinking water mains". PhD Thesis - Research UT, graduation UT. Netherlands: University of Twente, Oct. 2019.

[213] D. G. Ivey, B. Mrowca, and E. Guth. "Propagation of ultrasonic bulk waves in high polymers". In: *Journal of Applied Physics* 20.6 (1949), pp. 486–492.

[214] S. Koda, K. Yamashita, K. M. K. Matsumoto, and H. N. H. Nomura. "Characterization of polyvinylchloride by means of sound velocity and longitudinal modulus measurements". In: *Japanese journal of applied physics* 32.5S (1993), p. 2234.

[215] Y. Gao, J. M. Muggleton, Y. Liu, and E. Rustighi. "An analytical model of ground surface vibration due to axisymmetric wave motion in buried fluid-filled pipes". In: *Journal of Sound and Vibration* 395 (2017), pp. 142–159.

[216] I. E. DIN. "Plastics–Methods for determining the density of non-cellular plastics–Part1: Immersion method, liquid pyknometer method and titration method (ISO1183-1: 2004); German version ENISO1183-1: 2004". In: (2004).

[217] SciPy. *tukey window*. URL: https://docs.scipy.org/doc/scipy/reference/generated/scipy.signal.windows.tukey.html. Accessed: 07/10/2025.

[218] F. Harris. "On the use of windows for harmonic analysis with the discrete Fourier transform". In: *Proceedings of the IEEE* 66.1 (1978), pp. 51–83. DOI: 10.1109/PROC.1978.10837.

[219] SciPy. *sosfiltfilt*. URL: https://docs.scipy.org/doc/scipy/reference/generated/scipy.signal.sosfiltfilt.html. Accessed: 07/10/2025.

[220] M. Etchessahar, S. Sahraoui, L. Benyahia, and J. Tassin. "Frequency dependence of elastic properties of acoustic foams". In: *The Journal of the Acoustical Society of America* 117.3 (2005), pp. 1114–1121.

[221] Origin. *Fix leaks with minimal disruption*. URL: https://www.origintech.co.uk/no-dig. Accessed: 16/06/2025.

[222] E. Zaneldin, O. Al Khatib, and W. Ahmed. “Investigating the use of no-dig technologies for underground utilities in developing countries”. In: *Innovative Infrastructure Solutions* 5 (2020), pp. 1–12.

[223] F. Zou and F. B. Cegla. “On quantitative corrosion rate monitoring with ultrasound”. In: *Journal of Electroanalytical Chemistry* 812 (2018), pp. 115–121.

[224] F. Honarvar, F. Salehi, V. Safavi, A. Mokhtari, and A. N. Sinclair. “Ultrasonic monitoring of erosion/corrosion thinning rates in industrial piping systems”. In: *Ultrasonics* 53.7 (2013), pp. 1251–1258.

[225] R. Raišutis, O. Tumšys, E. Žukauskas, V. Samaitis, L. Draudvilienė, and A. Jankauskas. “An inspection technique for steel pipes wall condition using ultrasonic guided helical waves and a limited number of transducers”. In: *Materials* 16.15 (2023), p. 5410.

[226] P. Shi, Y. Yu, J. Watts, G. Zhang, and K. V. Horoshenkov. “An application of a MEMS vector hydrophone for condition assessment of a water supply pipe”. In: *Applied Acoustics* 231 (2025), p. 110449.

[227] Unknown. *Synthotech*. URL: https://synthotech.com/. Accessed: 28/03/2025.

[228] O. A. Adesina. “On the mechanisms of leak noise generation in water-filled pipes”. PhD thesis. University of Southampton, 2024.

[229] HBK. *Family 8103*. URL: https://www.hbkworld.com/en/products/transducers/acoustic/hydrophones/8103. Accessed: 14/11/2025.

[230] HBK. *Product data: the NEXUS range*. URL: https://www.bksv.com/media/doc/bp1702.pdf. Accessed: 14/11/2025.

[231] NI. *USB-4431*. URL: https://www.ni.com/en-gb/shop/model/usb-4431.html?srsltid=AfmBOoorwoJJuxBZ1ban5BB275MsZCswRFFmtPOvUeKk7GXBFDjZJuSJ. Accessed: 14/11/2025.

[232] P. Piezoelectronics. *PCB 353B04*. URL: https://www.pcb.com/products?m=353b04. Accessed: 14/11/2025.

[233] P. Piezoelectronics. *PCB 353B18*. URL: https://www.pcb.com/products?m=353b18. Accessed: 14/11/2025.

[234] P. Piezoelectronics. *PCB 393B04*. URL: https://www.pcb.com/products?m=393b04. Accessed: 14/11/2025.

[235] P. Piezoelectronics. *PCB 086C03*. URL: https://www.pcb.com/products?m=086c03. Accessed: 14/11/2025.

[236] Amazon. *Dayton Audio DAEX25CT-4 Coin Type 25mm Exciter 10W 4 Ohm*. URL: https://www.amazon.co.uk/gp/product/B00M292316/ref=ppx_yo_dt_b_asin_title_o01_s00?ie=UTF8&psc=1. Accessed: 14/11/2025.

[237] R. components. *FR 8 WP Black 8 Ohm*. URL: https://uk.rs-online.com/web/p/speakers/1976435. Accessed: 14/11/2025.

[238] F. audio. *Fosi Audio TDA7498E Stereo Audio Amplifier*. URL: https://fosiaudio.com/products/tda7498e-2-channel-stereo-audio-amplifier-receiver-mini-hi-fi-class-d-integrated-amp-home-speakers-160w-x-2-power-supply. Accessed: 14/11/2025.

[239] HBK. *G-link-200*. URL: https://www.hbkworld.com/en/products/instruments/wireless-daq-systems/wireless-nodes/g-link-200. Accessed 2025-11-14.

[240] A. W. Leissa. *Vibration of shells*. Vol. 288. Scientific, Technical Information Office, National Aeronautics, and Space Agency, 1973.